Monitoring of Long Steel Pipes using Acoustic Emission

Mohamed F. Shehadeh

Submitted for the degree of doctor of philosophy on completion of research in the School of Engineering and Physical Sciences, Mechanical Engineering, Heriot-Watt University

January 2006

Abstract

This thesis relates to the condition monitoring of long steel pipes using acoustic emission (AE). A number of experiments were carried out on pipes with a range of internal and external environments using a linear axial array of sensors with the ultimate aim of locating and reconstituting the time-domain and frequency-domain signatures of AE sources. The AE waves were generated from simulated, discontinuous, continuous, and semi-continuous sources and from real sources generated by impacts and crack propagation.

The simulated source work in different internal and external environments was carried out to develop a generic empirical approach to AE propagation in long steel pipes which acknowledges the distortion of a source disturbance in the time and frequency domains. Generally, the acquired signals have two identifiable components and methods are developed for separating these components automatically and determining their group velocities. A simple model for attenuation is also developed which includes effects brought about by burial of the pipe and /or the nature of the fluid transported (liquid or gas).

In the impact and crack extension tests a variety of intensities were simulated and the effect of type and intensity on time- and frequency-domain characteristics of the source was determined. The overall outcome is the demonstration of the potential of AE for identifying the nature, intensity and location of damaging events, such as crack growth and denting, and for the location and intensity assessment of leaks.

Acknowledgments

This thesis is based on research done at the mechanical engineering department in Heriot-Watt University during 2002-2005. The work has been financed partly by Heriot Watt University and the other part by the AASTMT in Alexandria.

Personally, I prefer to recognise in this acknowledgement those to whom my success is more rightfully attributed, and I apologise in advance for any omissions.

First of all, I would express my gratitude for Prof. Robert L. Reuben. His advice and encouragement, time and assistance during these academic years were invaluable. He motivated me to perform at my best. I consider him as my mentor and will continue to seek his guidance in future.

I shall always remain highly obliged to Dr. J.A. Steel, Dr. M. Elghamry, Dr. P. Nivesrangsan, Mr. R. Douglas, Mr. N.H. Faisal, Mrs A. Blyth, Mr. A. Aziz and all mechanical and electrical technicians for their assistance and insight they had provided through these years. I am delighted to thank all of them for their time and feedback. The opportunity to interact with such talented people has been extremely enlightening.

I thank all my mates, Dr. A. Anas, Dr. S. Elfakhy, Dr. Y. Makkawi, Dr. R. Elagamy, Dr. A. Masaud, H. Abd-Elhaleem, H. Fayad, H. Hotait, for their friendship and all the good time we had together in Edinburgh.

I present these achievements to the soul of my mother for her spiritual guide, my father, my brother, my aunts, mother and father in law and to all my family and friends. None of these would be possible without the support and love of my wife, my beautiful star daughter Rowan and my son Ezz Elden. I love you all and I am so proud of you.

ACADEMIC REGISTRY
Research Thesis Submission

Name*:*	Mohamed F. Shehadeh		
School/PGI:	School of Engineering and Physical Sciences, Mechanical Engineering		
Version: *(i.e. First, Resubmission, Final)*	Final	Degree Sought:	PhD

Declaration

In accordance with the appropriate regulations I hereby submit my thesis and I declare that:

1) the thesis embodies the results of my own work and has been composed by myself
2) where appropriate, I have made acknowledgement of the work of others and have made reference to work carried out in collaboration with other persons
3) the thesis is the correct version of the thesis for submission*.
4) my thesis for the award referred to, deposited in the Heriot-Watt University Library, should be made available for loan or photocopying, subject to such conditions as the Librarian may require
5) I understand that as a student of the University I am required to abide by the Regulations of the University and to conform to its discipline.

** Please note that it is the responsibility of the candidate to ensure that the correct version of the thesis is submitted.*

Signature of Candidate*:*		Date:	20/1/2006

Submission

Submitted By *(name in capitals):*	
Signature of Individual Submitting:	
Date Submitted:	

For Completion in Academic Registry

Received in the Academic Registry by *(name in capitals):*			
Method of Submission *(Handed in to Academic Registry; posted through internal/external mail):*			
Signature:		Date:	

Table of Contents

List of Tables

List of Figures

Nomenclature

$\bar{x}_m$	Average source sensor distance (m)
ρ	Density (kg/m^3)
Δt	Time difference between hits (s)
a	Scale parameter
A	Wave amplitude (V)
A_1	Amplitude of the signal at Sensor 1 (V)
A_2	Amplitude of the signal at Sensor 2 (V)
a_o	Flexural mode
Ap	Approximation signal
b	Shift parameter
D	Distance between Sensor 1 and Sensor 2 (m).
Di	Detail signal
E	Young's modulus
$E(x)$, $E_1(x)$, $E_2(x)$,	AE energy at distance x from the source (V^2.s)
E_0	Energy of the source (V^2.s);
$E_1(x)$	Total energy for air-air condition
$E_2(x)$	Total energy for water-air condition
$E_3(x)$	Total energy for air-wet sand condition
$E_4(x)$	Total energy for water-wet sand condition
f	Frequency (kHz)
h	Thickness (m)
k_1, k_2	Attenuation factor (m^{-1})
K_I	Stress intensity factor (MN.m$^{-3/2}$)
N_f,	Number of rays fired
N_h	Number of rays hitting the sensor
N_r	Number of reflections
R	Cylinder radius (m)
r	propagation distance (m)
R^2	Correlation factor
R_c	Reflection coefficient
$S1$	Trigger sensor position

$S2,S3,S4$	Sensors positions
s_o	Extensional mode
t,t_1,t_2,t_3, t_4	Arrival time (s)
v	Poisson's ratio
V, V_1, V_2, V_3	Wave velocities (m/s)
x	Source sensor distance (m)
x_{act}	Actual source sensor distance
y, y_1, y_2	AE signals
Z_1, Z_2	Acoustic impedance (Kg/m^2s)
z_1,z_2	Source position
α	Attenuation coefficient (dB/m)
θ, β, γ	Angels (deg)
λ	Wave length (m)
$\psi(t)$	Wavelet in time domain

Abbreviations

ADC	Analogue to Digital Converter
AE	Acoustic emission
DAQ	Data acquisition
FFT	Fast Fourier Transform
KE	kinetic energy (J)
LVDT	Linear Variable Displacement Transformer
NI	National instruments
PSD	Power spectral density
PZT	Lead Zirconate Titanate
RMS	Root mean square
STFT	Short Time Fourier Transform
WD	Wavelet Decomposition
WT	Wavelet transform

Chapter 1: Introduction

1.1 Overview

Pipelines and piping systems are important in many industrial fields for transporting both gases and liquids. Release of flammable or toxic materials or even large amount of water can be serious [1-4], and so there is a continuing interest monitoring for evidence of cracking, corrosion and erosion, fatigue crack propagation and leaks. A great many authors have presented AE as suitable technique for continuous automatic monitoring of a wide range of structures, processes and machines [5-8].

1.2 AE Background

AE has been demonstrated, in the last 20 years, to be as a nondestructive testing technique, which can detect growing cracks and discontinuities in structures by monitoring their AE signals. Generally, crack growth and plastic deformation are known to be sources of acoustic emission [9, 10], and discontinuities that enlarge under load generate acoustic emission by virtue of their size, location and orientation. AE has been used in experiments, not only to determine the onset of damage growth and to observe the nature of AE signals for different materials and loading conditions, but also to obtain additional information on the different damage types occurring during the test [11]. AE is therefore important not only in inspection, but also in monitoring and detecting in incipient failure, and much work has been done on damage evaluation, identification of AE sources, and correlation between AE parameters and different types of sources [11-13]. Also, it should be noted that AE differs from most other nondestructive methods in two ways. First, the sonic energy that is detected is released from the test object rather than being supplied by pulsing, as in ultrasonics or radiography. Second, the acoustic emission method is capable of detecting the dynamic processes associated with material

degradation (e.g. cracking, plastic deformation), rather than the symptoms of failure (e.g. increased vibration).

Acoustic emission examination is now reasonably well established for monitoring structures, detecting leaks and incipient failures in mechanical equipment, and for characterising materials behaviour. Some examples of applications [14-17] include:

1- Mechanical property testing and characterisation;
2- Proof testing;
3- On-line monitoring of structures and processes;
4- In-process weld monitoring;
5- Machinery signature analysis; and
6- Leak detection and location.

By definition, on-line monitoring may be continuous or intermittent, and may involve the entire structure or a limited zone only. Finally, the AE method can be used to prevent catastrophic failure of pipes with unknown discontinuities, and to limit the maximum pressure during containment system tests [6]. The detection of progressive and catastrophic failure events is important for the increased safety and reliability of pipes and pipeline systems [6, 18].

1.3 Objectives

So far, little practical work has been done on the characteristics of AE wave propagation on long steel pipes and none, to the knowledge of the author, on the effects of internal and external environments. Therefore, the main aim of this research is to study these characteristics including an identification of time and frequency aspects using simulated and real sources. This is done using a linear array of sensors distributed axially along the pipe.

The scope of investigation includes discontinuous (pencil-lead), continuous and semi-continuous (gas jet) simulated sources and a set of real sources (consisting of dropped weights and crack spreading) in freely suspended pipes in air, with water

inside, and/or with sand of varying degrees of wetness outside. The research objectives can be categorised into two areas:

1- To improve the precision of source location in real situations.
2- To assess the degree of distortion encountered by a wave as it propagates from the source to a distant sensor.

1.4 Thesis Outlines

This thesis consists of six main chapters, with an introduction and conclusions and recommendations.

Chapter 2 reviews relevant literature on AE monitoring, including general aspects of AE propagation and transduction, source location and attenuation, signal processing techniques and monitoring applications, particularly pipelines.

Chapter 3 introduces the experimental apparatus used throughout the thesis, and discusses the experimental approach and procedures.

Chapter 4 applies conventional and novel techniques for source location on plain pipes subject to discontinuous simulated sources. The techniques are compared with a view to establishing the most accurate approach.

Chapter 5 analyses and discusses the results for attenuation effects on pipes with different external and internal environments. A simple model is presented to separate the effects of the pipe and its interfaces on attenuation.

Chapter 6 presents and discusses the results for the continuous and semi-continuous sources. Energy analyses using time and frequency domains, along with appropriate digital filters are used to develop ways of locating such sources.

Chapter 7 analyses and discusses the results of experiments using crack spreading sources. Energy-based models are established for each of these sources and their characteristic temporal aspects noted.

List of Existing and Planned Publications Involving the Thesis Author:

1- Shehadeh, M., Elghamry, M., Steel, J.A. and Reuben, R.L., "*AE Source Location in Long Steel Pipes Using Cross-Correlation and Wavelet Transforms*", Proceedings 17th International Congress on Condition Monitoring And Diagnostic Engineering Management, 2004, Cambridge, pp. 250-259.

2- Shehadeh, M., Elghamry, M., Steel, J.A. and Reuben, R.L., "*Effect Of Internal and External Environment on Acoustic Emission Propagation in Long Steel Pipes*", Proceedings 9th International Mining, Petroleum, and Metallurgical Engineering Conference, Met. Sec., Cairo, 2005, Paper 23.

3- Shehadeh, M., Steel, J.A. and Reuben, R.L., "*Acoustic Emission Source Location for Steel Pipe and Pipeline Applications: the Rôle of Arrival Time Estimation*", in Proceedings IMechE, Part E, J. Process Mechanical Engineering, Vol. 219 (In Press.), 2005.

4- Shehadeh, M., Steel, J.A. and Reuben, R.L.,*" Aspects of AE Attenuation in Steel Pipes in Different Internal-External Environments",* (in preparation).

5- Shehadeh, M., Steel, J.A. and Reuben, R.L., "*Monitoring Continuous and Semi-Continuous Signals in Long Steel Pipe using Acoustic Emission"*, (in preparation).

6- Shehadeh, M., Steel, J.A. and Reuben, R.L., "*AE Generated by Impact and Crack Spreading in Steels*", (in preparation).

Chapter 2: Literature Review

2.1 Introduction

AE is the name given to elastic waves released in solids as a result of rapid localised redistributions of stress, which can be produced by a number of known phenomena, including some failure mechanisms such as fatigue crack propagation. An AE source radiates energy in all directions, and any suitable sensor located sufficiently near to the source will detect the signal, which is generally a complex transient disturbance. The essential problem in AE monitoring is interpreting this complex disturbance in a way that yields information on the condition of the structure, machine, process or component of interest. During the last 20 years, AE analysis has been used and developed in a wide range of applications including: detecting and locating faults in pressure vessels [19] and leakage in storage tanks and piping systems [20], monitoring welding [21] and corrosion-erosion processes [22], detecting partial discharges from components subjected to high voltage [23] and the failure of protective coatings [24].

A vast literature has built up around AE monitoring and this is reviewed in the following way in this chapter. First, the basics of AE propagation and transductions are reviewed leading to a critique of methods used for source location and the value of attenuation studies. This section will culminate in a statement of the state of knowledge of how on AE source signal is distorted as it travels to the sensor. Next, the signal processing techniques traditionally used for AE analysis will be described followed by a critical summary of relevant novel and traditional techniques. Finally, a section on applications will be included, commencing with an identification of the main types of AE source and including a review of applications to pipelines and process vessels.

2.2 Acoustic Emission Wave Propagation and Transduction

Figure 2.1 illustrates the problem of AE monitoring which is to determine as many characteristics of an AE source (its nature, its location, its severity) as possible using signals acquired at one or more surface-mounted transducers. Since AE is an elastic wave, all sources are essentially releases of elastic energy, although this itself may only be a reflection of the monitoring target, such as in the use for particle impacts on the wall of a process vessel. As has been aptly pointed out by Hamstad *et al* [25], there have been numerous studies of AE wave propagation aimed at solving the basic problem of detecting what is the transfer function (time, frequency, amplitude distortion) which is introduced by propagation from the source (for this purpose, defined as the elastic disturbance) to the location of the sensor. Once at the sensor, there is a second transfer function associated with the transduction of the surface elevation to an electrical signal. The third link in the chain, that of translating a physical phenomenon (such as impact or unit of fatigue crack extension) to a transient elastic disturbance relies heavily on a description of these two transfer functions.

However, AE waves can be rather complex, depending on transmission path, geometry and other structural features [26-28], and many attempts have been made to model the AE propagation using classical wave theory [29-32], and to apply such models to practical situations, with only partial success.

AE waves can be attenuated in a number of ways such as during reflection, refraction, scattering and mode conversion [28], some of which result in secondary waves which may themselves be detected by the sensor. In this section, we concentrate on the propagation and transduction of AE waves and we examine the extent to which the extremely complex wave propagation phenomena can be dealt with using simple analytical considerations.

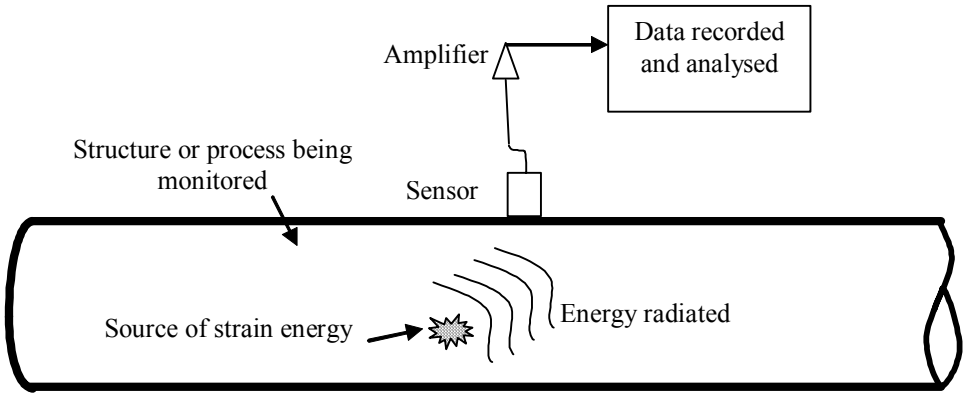

Figure 2.1: Schematic representation of AE monitoring problem

2.2.1 Wave Modes

The most commonly considered AE wave types are dilatational (compression) waves, distortional (shear) waves, surface waves (Rayleigh) and Lamb waves (or plate waves) [10, 33], and separation of modes is generally applicable only for longer source-sensor distances where the wave front is essentially planar [28]. In real structures, AE wave types cannot be controlled, and the different wave types travel over different paths and at different speeds, each of which will depend on the properties of the propagating medium and any surrounding media. As well as the source stimulating an unknown collection of modes, reflection, refraction and mode conversion occur when the wave impinges on boundaries so that some distortion of the source signature is bound to occur. Because different modes may suffer different degrees of attenuation, this further contributes to source distortion.

Elastic waves can only propagate within the body of solid materials as either longitudinal (compression) waves or transverse (shear) waves and hence these are the only types which occur in infinite media. The particle motion in a longitudinal wave is parallel to the wave propagation direction and consists of localised compressions and rarefactions of the medium, Figure 2.2a. Transverse waves are characterised by particle motion which is perpendicular to the wave propagation direction, Figure 2.2b. The velocity of longitudinal waves (c_1) is frequency independent and is given by the following expression:

$$c_1 = \sqrt{\frac{E(1-\nu)}{\rho(1+\nu)(1-2\nu)}} \tag{2.1}$$

where E is Young's modulus of elasticity for the material;

ρ is the density of the material; and

ν is Poisson's Ratio for the material.

By contrast shear waves travel as an oscillatory shearing motion between successive atomic planes normal to the direction of travel. The velocity of shear waves (c_2) is also independent of frequency and is given by the following expression:

$$c_2 = \sqrt{\frac{E}{2\rho(1+\nu)}} \tag{2.2}$$

so that the ratio of the compression wave speed to shear wave speed is always greater than unity, typically around 2 for most metals.

If the wave reaches an interface, some of the incident energy will be transmitted into the adjoining medium, some will be reflected, and some can be propagated along the boundary as a surface-wave [28]. Because the modes of reflected and incident waves are often different it is sometimes useful to think in terms of mode conversion at boundaries even though the transition will not be very sharp.

For semi-infinite media, a third type of wave can also exist, called Rayleigh waves, Figure 2.2c. These waves have some of the characteristics of shear waves and some of compression waves and propagate at a speed a little lower than that of shear waves [28], typically about 0.9 of the shear wave velocity [27].

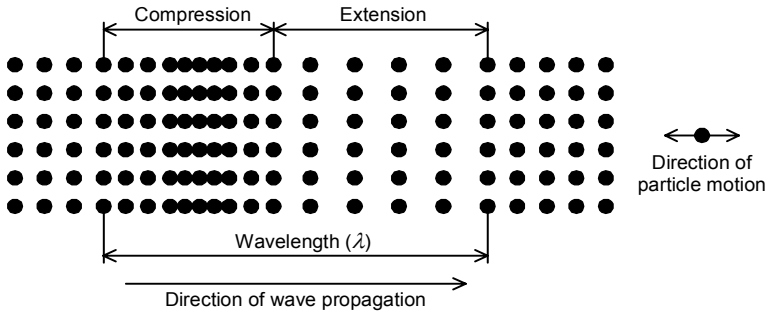

a) Longitudinal wave

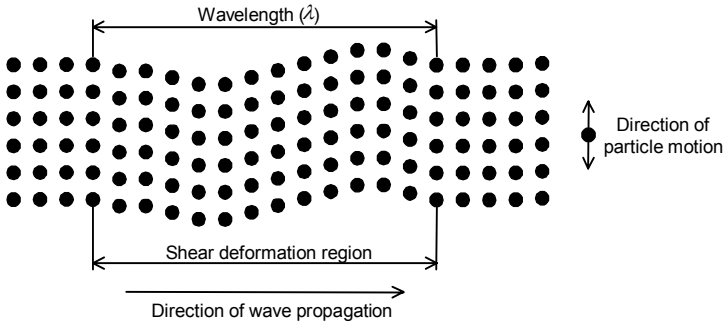

b) Shear wave

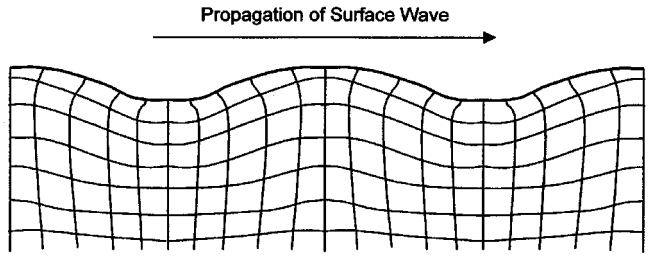

c) Rayleigh wave

Figure 2.2: The main AE wave types in infinite and semi-infinite media

In an infinite medium bounded by two surfaces, such as a plate, the waveforms couple at the surfaces to produce more complex propagation modes called Lamb waves. The two basic wave mode classes are shown in Figure 2.3, normally referred to as symmetric (s_0) or extensional and asymmetric (a_0) or flexural wave modes.

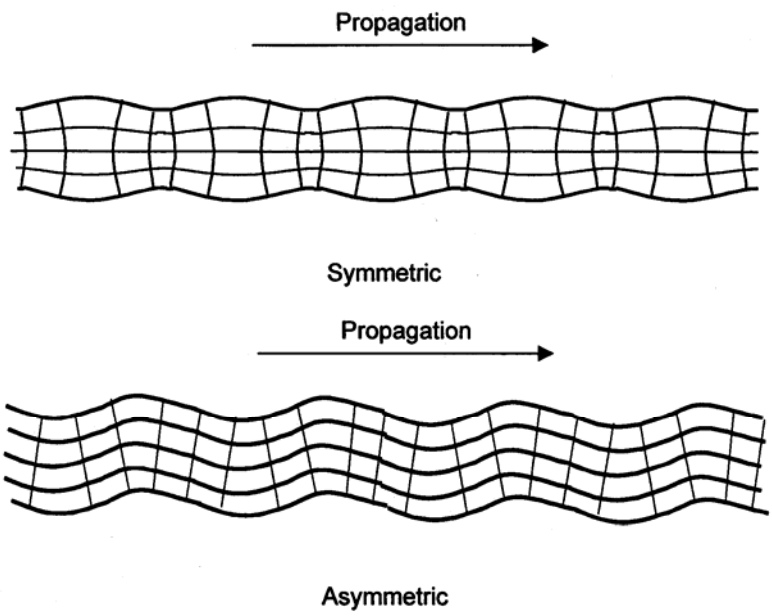

Figure 2.3: Zero-order Lamb wave modes

In Lamb waves, the particles move in ellipses, and the relative magnitudes of the motion parallel and perpendicular to the plate depend on mode and frequency in a complicated manner. Surgeon and Wevers [33] have noted that, of the three classes of wave modes in wave plate theory, only the extensional and the flexural modes can be detected in practice. Also, Gorman and Prosser [34] and Gorman [26] working with aluminium and composite material have showed experimentally that one or two of the Lamb modes are generated in cases where the wavelength (λ) (Figure 2.2a and 2.2b) is much larger than the plate thickness. Also, they noted that the classical plate equation governs the wave motion for waves of wavelength much larger than the thickness of the plate. The wavelength is related to the velocity and frequency by $\lambda=V/f$ [27] and, accordingly, each generated component is different in frequency and velocity and depends on the source type and medium through which AE is propagating [26]. In an isotropic material the in-plane displacement for the extensional mode is governed by the equations [34]:

$$\frac{\partial^2 u}{\partial x^2}+\frac{(1-\nu)}{2}\frac{\partial^2 u}{\partial y^2}+(1+\nu)\frac{\partial^2 v}{\partial x\partial y}=\frac{\rho}{A}\frac{\partial^2 u}{\partial t^2} \tag{2.3}$$

and

$$\frac{\partial^2 v}{\partial y^2} + \frac{(1-\nu)}{2}\frac{\partial^2 v}{\partial x^2} + (1+\nu)\frac{\partial^2 u}{\partial x \partial y} = \frac{\rho}{A}\frac{\partial^2 v}{\partial t^2} \tag{2.4}$$

where x and y are the coordinate axes in the plane of the plate, u and v are the displacements along these axes respectively, v is Poisson's ratio, ρ is the density, and A is given by:

$$A = \frac{Eh}{(1-\nu^2)} \tag{2.5}$$

where E is Young's modulus and h is the thickness. Due to the Poisson effect, the extensional mode may also include of an out-of-plane displacement.

The flexural motion is governed by:

$$D\nabla^4 w + \rho\frac{\partial^2 w}{\partial t^2} = 0 \tag{2.6}$$

where w is the displacement along the z axis which is normal to the plate, and D is the bending stiffness per unit breadth given by:

$$D = \frac{Eh^3}{12(1-\nu^2)} \tag{2.7}$$

Generally speaking, Lamb waves are dispersive [28], the wave velocity being related to the ratio of the plate thickness and wavelength [26]. At higher frequency-thickness products (around 10mm MHz for steel) AE waves can be considered to be non-dispersive, making for easier source location [28]. For example, Holford and Carter [35] and Surgeon and Wevers [33] identify the fact that AE modes in thin plates are dispersive and noted that the arrival times of different frequencies can be used to improve source location accuracy, leading to the possibility of using

a single sensor to locate AE. Also, Jeong and Jang [36] have used the WT of the dispersive AE modes to locate sources accurately, and propose that AE should be identified before signal processing to provide an accurate source location.

For pipelines, wave propagation effects depend on the transmitting structure (mostly shape and material), the fluid contained in the pipe, the surrounding medium and some other environmental aspects, such as temperature and internal gas pressure [20, 28, 37]. The AE energy is partly reflected and partly transmitted when it encounters a boundary with a surrounding medium or the fluid contained in the pipe [28]. The partitioning between transmitted and reflected waves depends on the angle of incidence and relative material acoustic impedances; when the two materials are well matched in acoustic impedance a large proportion of the energy will be transmitted, e.g. steel and water, but, if they are poorly matched, most of the energy will be reflected, e.g. steel and air. The reflected and transmitted waves will generally be of a different nature to the incident wave, normally referred to as mode conversion [10, 28]. For two materials of different acoustic impedance, Z_1 and Z_2, the percentage of energy transmitted, E_t is given by:

$$E_t = \frac{4Z_1Z_2}{(Z_1 + Z_2)^2} \times 100 \tag{2.8}$$

and the percentage of energy reflected, E_r is given by

$$E_r = \left(\frac{Z_1 - Z_2}{Z_1 + Z_2}\right)^2 \times 100 \tag{2.9}$$

where $Z = \rho.V$, and ρ is the material density (kg/m^3) and V is the wave speed (m/s).

When the acoustic impedances of two media are well-matched ($Z_1 \approx Z_2$), the incident wave is largely transmitted to the other medium, as shown in Figure 2.4a. On the other hand, when the acoustic impedances are very dissimilar ($Z_1 >> Z_2$ or $Z_2 >> Z_1$), the incident wave is mostly reflected, as shown in Figure 2.4b. The acoustic impedances of some common materials can be seen in Table 2.1.

Both longitudinal waves and shear waves can be reflected or refracted when they impinge on a boundary. The angles of reflection and refraction depend on wave velocities in the material and can be calculated by Snell's Law:

$$\frac{\sin\theta}{V_1} = \frac{\sin\beta}{V_2} = \frac{\sin\gamma}{V_3} \tag{2.10}$$

where θ, β, and γ are shown in Figure 2.4; and

V_1, V_2 and V_3 are the relevant wave velocities.

Mode conversion can also occur at a boundary when the acoustic impedances of the two media are different and angle of incidence is not normal to the interface, leading, for example, to longitudinal waves transforming to shear waves or shear waves transforming to Rayleigh waves [28]. For example, incident wave (V_1) may be reflected as the same type (V_2) while some is transmitted to the other medium as a different type (V_3), as shown in Figure 2.4c. The angle of incidence of each wave can be determined using Equation 2.10 and the relevant wave velocity.

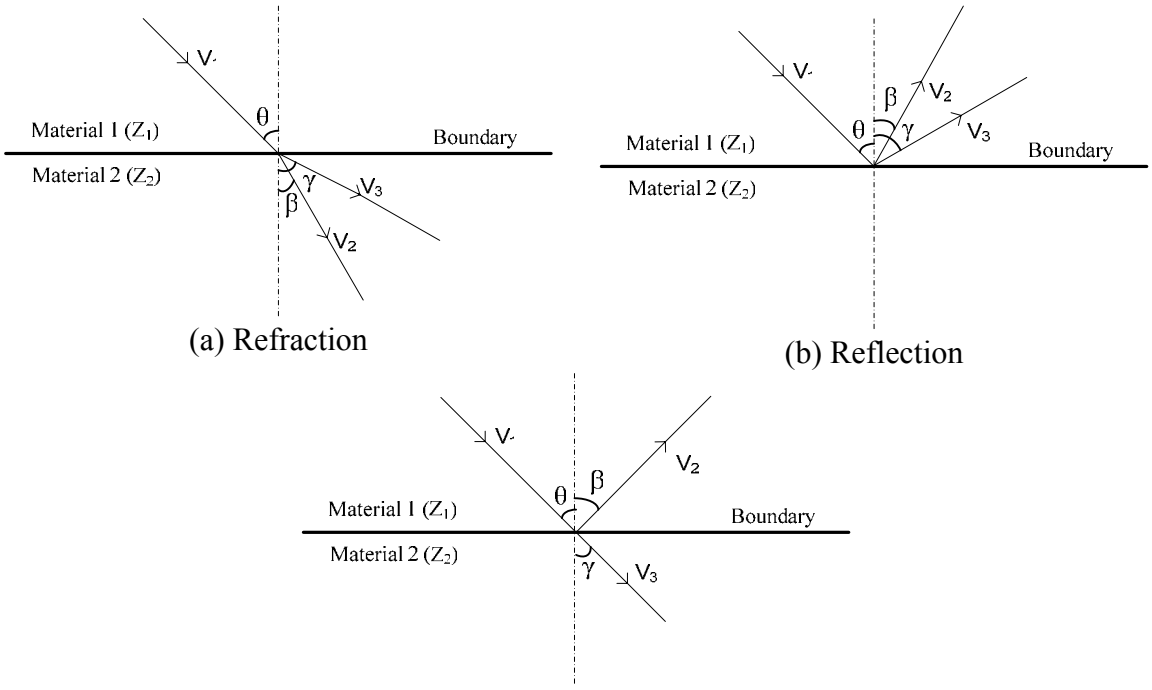

Figure 2.4: Reflection, refraction and mode conversion of waves at boundaries

Material	**Acoustic impedance, $Z \times 10^6$(kg/m^{2}s)**
Dry sand	0.26
Steel	45
Clay (saturated)	1.8
Water	1.5
Air	4.3

Table 2.1: Acoustic impedances of some common materials [27, 38-40]

In long structures the AE energy may propagate through different media being partially transmitted and partially reflected at interfaces, as illustrated schematically in Figure 2.4. Pollock [28] has suggested that the Lamb modes can be considered to be multiply reflecting and mode converting longitudinal and shear waves which may be changed into various other Lamb modes on reflection from the plate ends or be transmitted into the water-filled pipe, the Lamb wave losing energy as compressional waves in the water. Also, Fuller and Fahy [41] have studied the free waves in fluid-filled cylindrical shells and noted that free wave behaviour depends on the thickness of the shell wall and the ratio of the density of the shell material to the density of the contained fluid.

2.2.2 Attenuation

To evaluate and locate AE signals it is often useful to know how much the signal is attenuated in the material or structure of interest. If nothing else, a knowledge of attenuation is essential to ensure that sensors can be placed appropriately on large or complex structures [42, 43]. Attenuation of AE can arise from geometric, absorption, "leakage" or dispersion effects [10, 28].

AE waves generated by a localised source in an infinite medium spread as spherical surfaces in all directions from the source. Geometric attenuation arises from the law

of conservation of energy, where the energy of the wavefront remains constant along the propagation path, and so the amplitude of the wave (A) will decrease inversely with propagation distance (r), $A=k_1/r$. In plates, wave propagation can be considered to be two-dimensional, expanding as a cylindrical wavefront, so the wave amplitude decreases inversely as the square root of the propagation distance (r), $A=k_2/\sqrt{r}$, in order to maintain a constant energy at the wavefront.

In pipelines, the wavefront becomes effectively plane after a short distance and so geometric attenuation is very small. AE waves are also subject to absorption or damping in the propagation medium, where the AE signal amplitude and energy usually fall exponentially with distance. The attenuation coefficient is directly proportioned to the frequency and depends on material properties, and this can lead to a kind of structural filtering where some frequencies are attenuated more than others [28, 35].

Leaking of the wave energy into adjacent media can occur at internal or external boundaries. In pipes, this is particularly significant, since both boundaries are present along the entire propagation path, which can lead to the situation where much of the energy is carried in the fluid inside the pipe [28].

Dispersive attenuation occurs in waves where velocity varies with frequency so that an initial sharp transient will become more spread in time as it propagates. The main practical consequence of dispersive attenuation [28] is for dispersive modes (e.g. asymmetric Lamb modes) to become more attenuated with distance than non-dispersive modes.

In some structures the energy attenuation in one dominant transmission path from source to sensor can be described using a simple absorption law [17]:

$$E(x) = E_0 e^{-kx} \tag{2.11}$$

where $E(x)$ is AE energy at distance x from the source ($V^2.s$);

E_0 is the energy of the source ($V^2.s$);

k is attenuation factor (m^{-1}); and

x is the source-sensor distance (m).

AE wave attenuation is often measured empirically [10, 44, 45] using a logarithmic scale (decibel) [44], where the relative amplitude (A_r) is given by:

$$A_r = 20 \cdot \log_{10}(\frac{A_i}{A_o}) \tag{2.12}$$

where A_i is the maximum signal at a receiver sensor at a distance, x from the source, and A_o is the maximum signal amplitude at the source position. The amplitudes can be measured in volts provided that the amplifiers are consistently calibrated.

Wave attenuation can then be determined from a plot of the relative amplitude versus distance and can be expressed as decibels per unit distance [44], determined by:

$$\alpha = \frac{20}{D} \cdot \log_{10}(\frac{A_2}{A_1}) = \frac{A_r}{D} \tag{2.13}$$

where α is the attenuation coefficient (dB/m),

A_1 is the amplitude of the signal at Sensor 1, (V)

A_2 is the amplitude of the signal at Sensor 2, (V) and;

D is the distance between Sensor 1 and Sensor 2, (m).

A practical example of differential attenuation effects is given by Holford and Carter [35] who recognised two distinct Lamb wave modes in 12m long structural steel girders. The signal was generated by a Hsu-Nielsen source and measured at various source-sensor distances, and it was observed that the non-dispersive mode is essentially an extensional wave, which travels faster than the highly dispersive flexural mode. A low pass filter at 100kHz was used to separate the two modes, since the extensional mode was of predominantly higher frequency. Holford and

Carter [35] also suggested that, for the near-field zone, the higher attenuation was attributed to geometric spreading and, for the far-field zone, the attenuation was caused by absorption or conversion of AE wave energy into heat.

2.2.3 Source Location

Source location is central to AE based inspection, such as proof testing of metallic and composite vessels, and also in monitoring applications including pipe leakage and bridge monitoring [11]. Many applications of source location are on less complicated structures, such as pipes and plates and with sensors that are assumed to be points in time and space. The time of arrival of the AE wave propagating from source to sensor is the main feature that is extracted from the detected signal, and, by measuring this arrival time at various sensors in an array, the position of the source can be determined. The following two sections review the types of geometric algorithms that are used to determine source position given arrival times at the sensors, and this is followed by a discussion of methods used in less clearly-defined cases.

2.2.3.1 1D Source Location

Two sensors are sufficient to calculate the location of a source where the direction and velocity of wave propagation are known. A common equation used for linear source location (Figure 2.5) is [10]:

$$x = \frac{1}{2}(D - \Delta t V) \tag{2.14}$$

where D is the distance between sensors,

V is the constant wave velocity,

Δt is the time difference between hits, and

x is source location measured from the first hit sensor.

For pipes, linear location is most appropriate when the sensor separation is large compared to the diameter of the test object. As this ratio reduces, sources close to

the sensors can be miss-located if they are away from the direct axial line through the participating sensors.

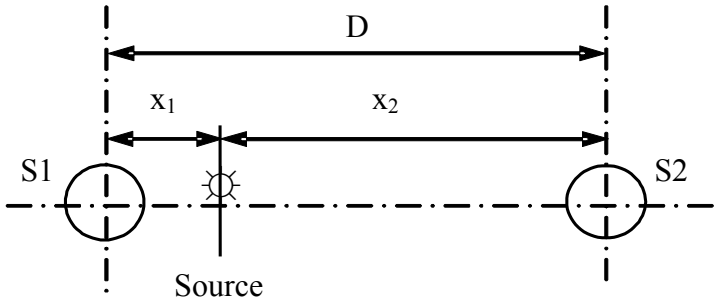

Figure 2.5: Linear source location

Depending on the wall thickness, a source may generate an AE signal which contains Rayleigh, shear and the two basic Lamb wave modes. Since these modes are produced at the same location, but propagate at different velocities, they will arrive at a sensor at different times. For the example of Lamb waves, using the arrival time difference between the extensional and the flexural mode and knowing the propagation velocity of both modes makes it possible to back-calculate the source location with a reduced number of sensors.

Lamb wave arrival time techniques depend on isolating the different frequency components, which travel at different velocities. If the two velocities of the components the higher, V_H, and the lower, V_L, and the time lag (Δt) between their arrivals at a given sensor are measured, then the source to sensor distance (x) is given by [10]:

$$x = \Delta t\left(\frac{V_H V_L}{V_H - V_L}\right) \tag{2.15}$$

It is important to emphasise that application of this technique to a given structure requires a thorough understanding of source behaviour, background noise, wave propagation and attenuation effects as a function of structural details. Prior consideration of the implications of the relationship between structure thickness,

frequency and source velocity, as described by the dispersion curves is vital if the method is to be successfully applied.

2.2.3.2 2D Source Location

Two-dimensional source location can be applied to a plane surface or a curved surface. The simplest analysis assumes an infinite plane and the ideal condition where the stress waves propagating from the source travel at constant velocity V in one direction. If the source is at P1, and two sensors are placed at S1 and S2 (Figure 2.6) the equation of a hyperbola:

$$R = \frac{1}{2}\left(\frac{D^2 - \Delta t^2 V^2}{\Delta t V + D\cos\theta}\right) \tag{2.16}$$

can be written, where any point satisfies the input data (the hit sequence and time difference measurement Δt). Equation 2.16 can be used for most cases of 2D source location on a plate, because any point on the hyperbola satisfies the input data, wave arrival sequence and arrival time difference.

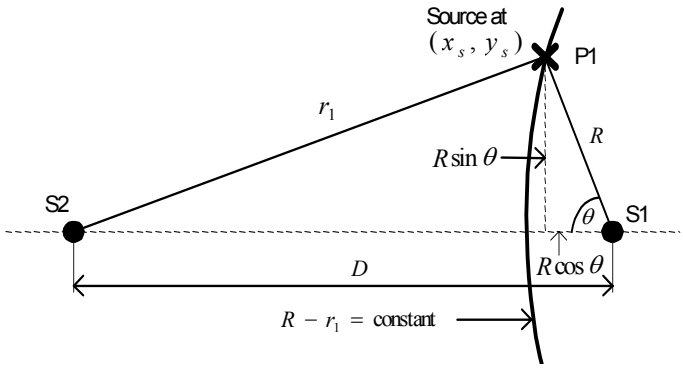

Figure 2.6: Source location in two dimensions

Also, the energy technique can be used to locate the source (essentially for continuous emission) in two dimensions by rearranging the Equation 2.10 as [46]:

$$x_i - x_j = \frac{1}{k}\ln\left(\frac{E(x_i)}{E(x_j)}\right) \tag{2.17}$$

where x_i and x_j are the distances from the AE source to the i^{th} and j^{th} transducer, respectively; *E(x)* is the amplitude of a wave registered by a transducer at a distance *x* from the source; and *k* is the attenuation factor for waves in a given medium.

Barat *et al* [47] have derived an algorithm to locate an AE source at coordinates (R,θ,z) on a cylindrical surface, using three sensors S_o, S_1 and S_2 located at positions $(R,0,0)$, (R,θ_1,z_1) and (R,θ_2,z_2). They expressed the shortest distance between source and sensor on the cylindrical surface by:

$$\delta_1 = \sqrt{R^2(\theta_1-\theta)^2+(z_1-z)^2}-\sqrt{R^2\theta^2+z^2}$$
$$\delta_2 = \sqrt{R^2(\theta_2-\theta)^2+(z_2-z)^2}-\sqrt{R^2\theta^2+z^2} \qquad (2.18)$$

where *R* is the cylinder radius.

If the arrival times (Δt) between the sensors are determined experimentally, and, assuming the AE wave speed to be constant (*V*), the distances between sensors S_o and S_1, S_o and S_2 are:

$$\delta_1 = \Delta t_1 V$$
$$\delta_2 = \Delta t_2 V \qquad (2.19)$$

respectively. Solving Equations 2.18 and 2.19, will allow θ and *z* to be determined and hence the source to be located on the cylindrical surface.

2.2.3.3 Location Methods in Practical Situations

In practical situations, the source is rarely a true step function, and is often distributed in time. Moreover, it is entirely possible that a number of sources will be operating each with its own temporal and magnitude characteristics. Finally, as pointed out by Pollock [28] it is unlikely that any of the 'pure' modes indicated by plate theory will be present although the propagating wave can often be split into components which show characteristics of them. Nivesrangsan *et al* [42] have approached the multi-source problem on the relatively complex structure of a diesel

engine and have demonstrated that characteristic speeds and frequency bands can be used to enhance the quality of information about the relative times and locations of sources.

Continuous sources are rather more difficult to locate, since they generally do not contain any reference events which can be used to determine relative arrival times at sensors. Thus, energy-based methods are most commonly used each sensor being assigned a zone on the structure [10]. The highest output sensor in an array can be used to locate the source, and some improved resolution can be achieved by using the two highest output sensors, Figure 2.7. However, for many real situations it is impractical to deploy enough sensors to make zone location accurate and better source location can be achieved by knowing the attenuation properties of the structure and using these to interpolate for source position between two sensors of highest output using techniques similar to those described in the previous two sections.

If the continuous source has any temporal structure to it, it is possible to use cross-correlation to obtain a time difference, and hence use time and velocity to locate the source, as for burst type emission.

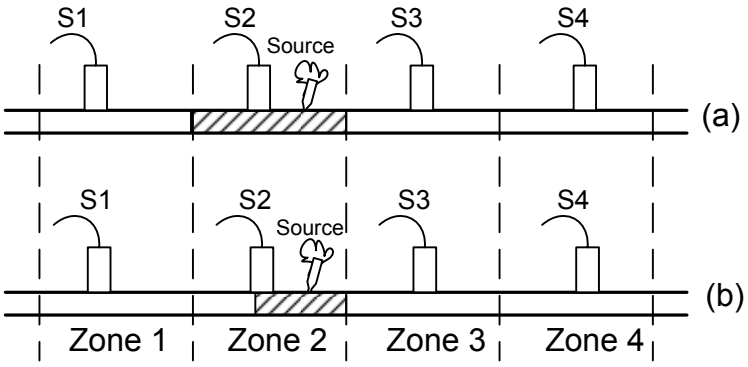

Figure 2.7: Schematic diagram of zone location method (adapted from [10]) where (a) output of sensor 2 is the highest , and (b) output of sensor 2 is highest and that sensor 3 is second highest

2.2.4 Transduction

Generally, AE transducers involve a piezoelectric element, which is most often made from lead zirconate titanate [15]. Commercial transducers are available with different crystal shapes and sizes providing a range of frequency responses. Generally, narrow-band sensors have high sensitivity and broad-band sensors lower sensitivity. The frequency response of the sensor/preamplifier combination depends on the electrical impedance of the sensor element, and calibration is important to match the amplitude and phase response of the sensor to the surface displacement over its frequency range [48].

As well as using an appropriate transducer correct mounting of the sensor on the test object is important [49], using suitable acoustic couplant (e.g. grease or water-based gel), is necessary to improve the reliability of AE detection. Wolfinger *et al* [50], for example, working with fibre reinforced plastic structures, improved the efficiency of a monitoring system by using integrated transducers where the high-pass filter was built in. Also, Grondel *et al* [8] have investigated the Lamb wave modes carried in riveted aluminium plate by stimulating these with a piezoelectric transducer and using calculated dispersion curves to identify an appropriate frequency-thickness product on which to focus AE analysis. They pointed out that optimizing the dimension and frequency response of the piezoelectric elements was essential to achieve success in fatigue monitoring.

2.3 Signal Processing

Recorded AE signals can be broadly categorized into burst, continuous and mixed. Burst signals take the form of discrete transients, as shown in the Figure 2.8a, an example being crack growth. The shape of a burst waveform is often approximated by an exponentially decaying sinusoid. Continuous emission has a random oscillatory appearance as shown in the Figure 2.8 b, and essentially results from the overlapping of multiple burst type signals of indistinguishable amplitude, and a typical example is process “noise” resulting, say, from fluid flow. In most practical

situations, both burst and continuous signals are recorded (Figure 2.8c) where both components may be of interest or one or the other may constitute noise.

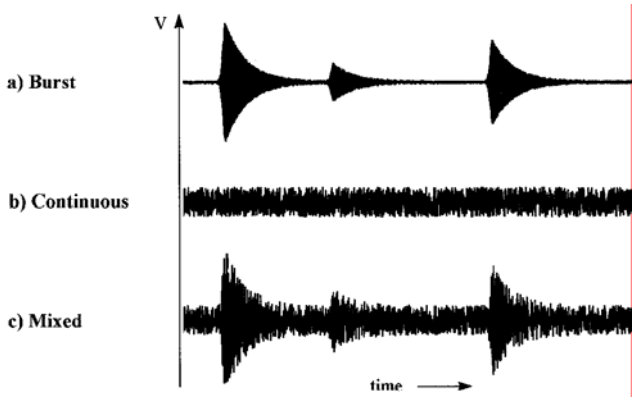

Figure 2.8: Schematic representation of different AE signal types [10]

AE data essentially consist of one or more time series with frequencies in the range of 0.1 to 1 MHz. As such, the features of the signals can be found in the time- and/or frequency domains. Although time domain analysis is widely used in AE applications, and is direct and conceptually simple [51], frequency analysis can often given an indication for the source type and spectral decomposition can be used to distinguish different propagation modes [51, 52]. For example, in support of a patent application, Powell and Dimmick [53] have used a Fast Fourier Transform (FFT) of the detected signal to identify the type of faults in valves each fault having a specific spectral signature. Kwan and Leach [54] have presented a technique for determining the average diameter and average length of glass cylinder particles using spectral peaks of AE of the AE generated whilst the cylinders were undergoing a tumbling motion. On the other hand, Spall *et al* [55] have discussed the difficulties in identifying signals acquired by transducers distant from the source where wave components travel a different speeds, and waveguiding properties in complex structures may distort the signal due to dispersive media, reflections, sensors and multiple paths. To avoid distortion of the signal from pencil lead breaks on a cutting tool, Jemielniak [56] modified a Bruel & Kjær preamplifier type 2637 to lower the gain by a factor of 10 (20 dB), and pointed out that the AE signal should be filtered at the earliest possible stage of processing, just after the unavoidable buffering.

Mathematical transforms are widely applied to raw signals to obtain important information that is not readily available from their time evolutions. The most common tool utilized in signal processing is the Fourier Transform, used to decompose a signal into its frequency components [57]. The Fast Fourier Transform (FFT) is a specific algorithm which converts numerically discrete time domain data into the frequency domain, with very low computation time and avoidance of the round-off errors associated with this computation [58]. Power spectral density (PSD) estimation is another tool, using the FFT to indicate how the signal energy is distributed in the frequency domain [57]. The Welch method is an improved PSD estimator [59] and it is implemented in the MATLAB software used in this work. In order to reduce the variance of the PSD estimate, the Welch method calculates PSD by dividing the time series data into segments (possibly overlapping), and, using by the FFT, can calculate each segment of a modified periodogram and then average these periodograms.

The FFT and PSD require a signal to be stationary, i.e. for the frequency spectrum to be constant in time [60]. For non-stationary signals, a number of time-frequency analysis techniques are readily available such as the Short Time Fourier Transform (STFT) and Wavelet Transform (WT). The STFT is a simple technique which describes the energy distribution of the signal as a time-varying spectrum. The STFT can provide a constant resolution for all frequencies by using same window size for the analysis of the raw signal; accordingly there is a trade-off between time resolution and frequency resolution (Figure 2.9a). The WT also analyses the signal using multi-scaling where the resolution of time and frequency varies in the time-frequency plane (Figure 2.9b), longer time intervals giving more precise low frequency information and shorter time intervals giving high frequency information, thus improving the overall presentation of the time-frequency characteristics.

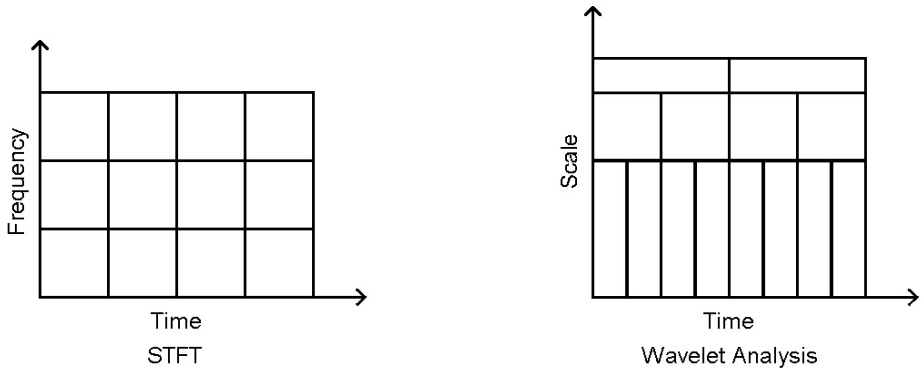

(a) (b)

Figure 2.9: Resolution in (a) the STFT and (b) the WT

The main advantage of the WT over the conventional FFT is that the time domain included in the raw signal is conserved [61, 62]. The WT is implemented in the MATLAB software and it is used in this work to decompose the AE signal into different levels at different frequencies, each level containing some of information of the original signal, with the AE sub-signals being in the time domain [63]. The wavelet transform essentially breaks down a signal into components (wavelets), which vary in scale (stretched or compressed) and in location (shifted) [25, 61, 64]. However, some authors have described wavelet decomposition as splitting the signal into an "approximate" (Ap), low frequency component and a "detail" (Di), high frequency component [65, 66], as shown in Figure 2.10. The wavelet tree method is a generalization of wavelet decomposition that offers a wide range of possibilities for signal analysis [67].

In general, the wavelet transform (WT) is used to decompose any signal into frequency bands producing a high-resolution time and frequency information about the signal by using a variable sized window. The WT is a function of $f(t)$ at time t [64]:

$$WT_f(a,b) = \frac{1}{\sqrt{a}} \int_{-\infty}^{\infty} f(t) \Psi^* \left(\frac{t-b}{a} \right) dt \tag{2.20}$$

where $a > 0$, the superscript * denotes a complex conjugate and t is time. The analysis function for the WT can be defined as the" mother wavelet":

$$\Psi_{a,b}(t) = \frac{1}{\sqrt{a}} \Psi\left(\frac{t-b}{a} \right) \tag{2.21}$$

Its elements are generated by shifting and scaling a basic wavelet *ψ(t)*. The parameters *a* and *b* stand for the scale and shift of the basic wavelet. Also many authors have suggested that the location of the peak value on the (*a*, *b*) plane indicates the arrival time of the signal [25, 61, 64].

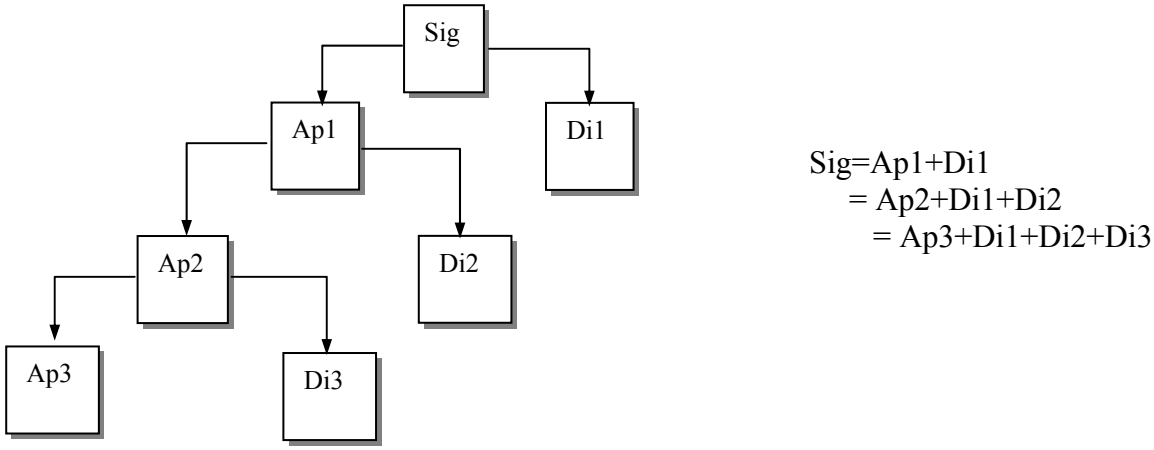

Figure 2.10: Wavelet analysis tree

AE signals normally contain some noise, such as from the environment, which must be removed to aid signal analysis. Time-frequency analysis can be used to describe the AE signal components and hence remove noise. For example, Ng and Qi [63] have presented a wavelet-based AE energy technique, in which they use the ratio of reconstructed energy to total original signal energy to identify the insignificant components in the AE signal without affecting the integrity of the original signal. Using this approach, they were able to correlate the wavelet-based AE energy with fatigue parameters. Also, Kishimoto *et al* [68] and Jeong *et al* [36] have suggested that the wavelet transform with the Gabor wavelet is an effective tool for analysing wave propagation phenomena in structures. The dispersion behaviour of the group velocity can be accurately evaluated by the information extracted using the WT.

Generally, the WT is an effective way to analyse the AE signal and both frequency and time information can be obtained. For example, Qi [69] has noted that the failure modes for composite materials can be quantified and that each failure mode frequency band has a different bandwidth.

2.3.1 AE Signal Energy

As well as the time and frequency changes as a signal propagates from source to sensor, it is important to acknowledge changes in energy, and this can be particularly important for continuous signals where there is no other easy way of locating sources. Generally, the amount of energy emitted from a fault is governed by the dimensions of the structure [12] and also is often used as an indicator of fault severity. The energy associated with an AE signal over a time, *t*, can be determined as follows:

$$E_o = \int_0^t v^2(t) \ \ dt \tag{2.22}$$

where *v(t)* is the amplitude of the AE waveform in volts, *t* is time in seconds, and the AE energy is given in V^2.s.

It is also possible to use a wide range of time-based parameters to characterise the AE signal. For burst signals the amplitude usually rises rapidly to a maximum value and then decays nearly exponentially to the background noise level. The common methods used to obtain the waveform parameters are shown in Figure 2.11 [10, 16, 40], where each parameter is described briefly below.

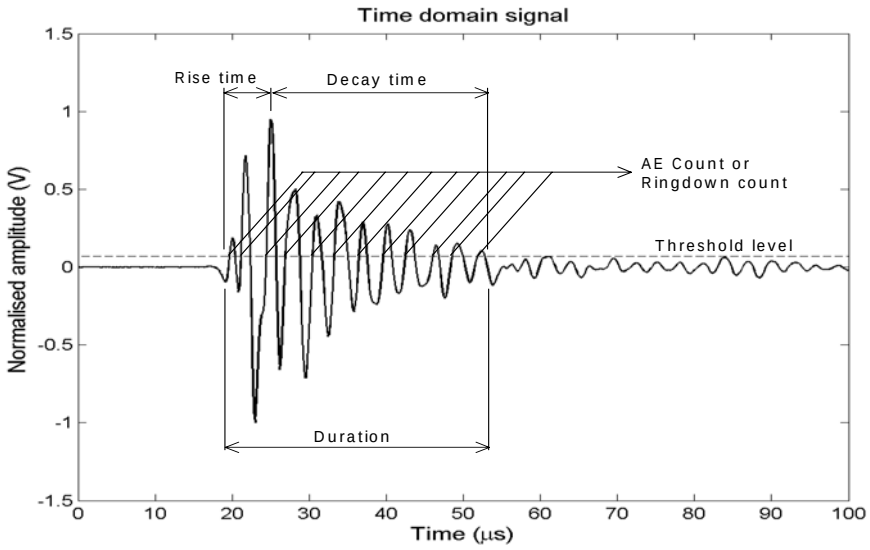

Figure 2.11: AE event and AE waveform parameters

- AE energy is the measurement of the relative energy of an AE signal, which is calculated from the area under the envelope of the square of the signal.
- AE count or ringdown count is the number of times the burst signal amplitude exceeds the preset threshold and count rate is AE count per unit time.
- AE event count is the number of times where a burst signal crosses a preset threshold and AE event rate is the time rate at which AE event counts occur.
- RMS AE is the energy rate or the root mean square of voltage, which is generally an indicator of average AE energy over each averaging time.
- Rise time is the time interval between the first threshold crossing and the maximum amplitude of the burst signal.
- Decay time is the time interval between the maximum amplitude and the last time that the burst signal exceeds the preset threshold.
- Signal duration is the time interval between the first and the last threshold crossing of the burst signal.

These parameters were mostly used in early studies of material properties, material deformation and crack propagation using AE although some variants are used later in this work. Harris and Bell [13] , besides indicating that the AE energy can be

related to other conventional parameters (such as counts and RMS voltage), found energy to be a useful indicator of some degradative phenomena in metals, particularly where signal levels were low. Also, Yoon *et al* [70] and Radon and Pollock [71] have correlated AE energy with energy-based descriptions of various physical phenomena, such as crack extension and dropped weights.

2.3.2 Wave Arrival Time Estimation

In large structures, most AE waves propagate in more than one mode travelling at different speeds so, for pipe applications, it is important to determine arrival times for different components of the wave. AE event source location is based on the arrival times of transient signals measured at a number of transducers. If the propagation velocity is known, the difference in arrival times for an event at sensors a known distance apart can be used to locate the source.

A number of techniques such as cross-correlation, threshold crossing and wavelet transforms have been used [36, 61, 64, 72, 73] for automatic source location. The error in source location depends on any errors in measured arrival time differences. In the case of large structures in different environments, attenuation, reflection, refraction, mode conversion and interference can all distort the shape of the propagating wave. Also, for some waves and media, dispersion effects can cause time of arrival to be triggered at different phase points of the signal.

The most common method for estimating the arrival time is where the arrival time is recorded when the raw signal amplitude first crosses a pre-set threshold. Many authors such as Steven *et al* [72], Ziola and Gorman [74] and Hamstad *et al* [25] have discussed the difficulties of using the first threshold crossing to define the source location, where the threshold needs to be set above the noise level which means that it will not be distinguishable at very long distances. To increase the location accuracy of the threshold method some authors, e.g. [75], have recommended that the large amplitude, high frequency, dispersive components should be filtered out of the raw signal and sufficient gain used to amplify the lower frequency non-dispersive components. This obviously depends upon

identification of dispersive and non-dispersive components, which is not always easy to do on a given new structure, although Gorman [26] has also suggested using the non-dispersive component with a threshold for accurate source location. Also, Gorman [26] used the threshold method to locate sources on a 0.23cm thick, 23cm wide, 46cm long aluminium plate. He suggested that the flexural component should be filtered from the signal and only the extensional wave be used for most accurate location. Floating thresholds have been suggested by Coulter *et al* [73] who have located continuous emission from a fluid leak by allowing the threshold to float with the AE signal and were therefore able to discriminate between the continuous noise and the AE signal spikes. The arrival time difference between these spikes could then be used to locate the leak.

Cross-correlation is a conventional time-based technique for measuring differences of arrival time between two or more sensors. The cross-correlation function is given by:

$$R_{y_1 y_2}(\tau) = \sum_{t=1}^{T} y_1(t) y_2(t+\tau) \tag{2.23}$$

where the variable τ corresponds to the time difference between the signals $y_1(t)$ and $y_2(t)$. The most likely time delay between two complex time series is thus determined by the position of the highest peak in the cross-correlation function, and the peakedness of this function will indicate how much distortion there is between the two time series. Cross-correlation techniques can be used to estimate the arrival time difference between two signals automatically, and are most effective when used with non-dispersive waves and when the wave propagates from source to sensor without reflection [76]. Wang and Chu [67] working with an experimental rotor-bearing rig with a complicated dynamic structure (i.e. friction, impacting and coupling effects) found their cross-correlation results to be considerably enhanced when combined with wavelet decomposition.

Wavelet transform methods are also used to locate sources, for example by Inoue *et al* [77], who produced flexural waves in a simply supported beam by dropping a

steel ball onto the mid span. They then showed that a three-dimensional plot of the magnitude of the WT in time-frequency space has peaks whose locations indicate the arrival times of each component of the wave. Also, Jioa *et al* [64] have also used a WT method to locate sources in a thin steel plate, of dimensions 700mm × 700mm, 2.76mm thick, using a single sensor. They used arrival time difference between the "a" and "b" modes (determined using the peaks in the Gabor wavelet transform) to locate sources with errors of less than 5%. Hamstad *et al* [25], uniquely, have worked with numerically simulated waves, and have noted that the wavelet transform (WT) coefficients (usually local maxima at a frequency, group velocity pair) can be combined to form an a_o/s_o magnitude ratio, where the a_o (flexural) mode is of higher group velocity and lower frequency than the s_o (extensional) mode. This ratio was found to distinguish different source types (in their simulated data), when the sources were all located at the same propagation distance. Combinations of the above-mentioned techniques (i.e. novel technique) can improve the arrival time estimation. For example, Ding *et al* [61], working with composite plates, have noted that wavelet packet decomposition associated with threshold crossing is more effective than cross-correlation for the arrival times of the dispersive, and the highly damped signals involved. They also found a method using maxima in the Gabor wavelet transform to be effective in determining wave speed.

2.4 AE Fault Diagnosis and Monitoring

Many researchers [14, 17, 42, 78-80] have proposed AE as an effective monitoring technique, and there are three ways in which AE can be applied to technological problems; testing and surveillance of structures [81], monitoring and control of machines and processes [82], and materials characterisation [83]. It has been estimated that savings in loss of production and even human cost brought about by modern condition monitoring techniques can amount to as much as 400 times the cost of the equipment [6]. This section will cover applications in monitoring for plastic deformation, fracture, fatigue, impacts and more general process monitoring. Specific pipeline applications will be dealt with in the following section.

Under static loading, AE can be generated by plastic deformation or fracture, or, more commonly, a combination of both. Singh *et al* [84] have worked with steel plates in tension with various types of stress concentration (circular holes) and have found that AE event rates are higher between yield and the UTS and that specimens containing stress concentrators started emitting earlier than those without. Baudouin and Houbeart [85], as part of a study on the effect of plastic deformation on the magnetic properties of electrical steels, carried out some uniaxial tensile tests whilst monitoring the AE generated. They found AE to be concentrated in three bursts of activity: around, and just following, yield; in the advanced stages of work hardening approaching the UTS; and, after the UTS, prior to rupture. They attribute all these burst of activity to intense plastic deformation, and it might be noted that the steels in question have a marked yield point, which is normally associated with unlocking of large avalanches of dislocations from solute atmospheres. Hao *et al* [86] have used AE to monitor the plastic deformation during a deep drawing process, carrying out some prior calibration using uniaxial tensile tests. They developed a model for RMS AE (essentially the AE energy) which has it directly proportional to the product of strain and strain rate, which is similar to an approach used by Carolan *et al* [87] to model the AE associated with metal cutting. Dunegan *et al* [88], have suggested, on the basis of static and dynamic crack extension experiments, that the AE generated is associated with dislocation motion (plastic deformation) in the plastic zone ahead of a crack tip and are credited with the relationship that the total number, N, of AE counts is proportional to the fourth power of the stress intensity factor. Later, Palmer and Heald [89], carried out some basic studies on the application of AE analysis to fracture mechanics of carbon-manganese steels, and have concurred that crack-tip plasticity is an important generating mechanism, and have noted that the total emission count is directly related to plastic zone size which they characterise in terms of the Dugdale strip yielding model, i.e.:

$$N \propto \left[\sec\left(\frac{\pi\sigma}{2\sigma_1} \right) - 1 \right] \tag{2.24}$$

where σ is the applied stress and σ_1 is some characteristic stress, usually the flow stress. Mukhopadhyay *et al* [37], working with notched specimens of stainless steel, have found the power law dependence of the Dunegan crack extension model to vary with specimen thickness (essentially the length of the crack front) thus supporting the Palmer and Heald suggestion to link AE with plastic zone size and hence plastic yielding fracture mechanics which was, of course, not mature at the time of the original work of Dunegan *et al*. On the other hand, some early workers for example Radon and Pollock [71] have considered linear elastic fracture mechanics to be adequate to explain the energy associated with AE during fracture and have related the AE energy to the strain energy release rate, G_c, in brittle fracture.

A large amount of literature exists on the use of AE to detect fatigue crack propagation, stretching back to pioneering work of Dunegan, Harris and co-workers [16, 40], who reported sensitivity of AE to crack growth rates of less than 2.5×10^{-5} mm/cycle, relating AE counts per cycle to the energy released by crack extension, as measured by the peak value of stress intensity factor and crack growth increment. They noted that the nature of the relationship changed as the crack size increased and it went through the plane-stress / plane-strain transition. Later workers, such as Roberts and Talebzadeh [20, 38], Brkovits and Fang [39] and Jiang *et al* [22] have confirmed these findings. Shi *et al* [88], have carried out more detailed studies of the nature of the AE associated with fatigue crack extension, and have identified three different classes of waveform (Figure 2.12) associated with small sub-grain sized cracks at initiation, micro-cracking across grain boundaries and the coalescence of micro-cracks into larger, but still localised, cracks. Larger cracking rates and greater degrees of crack plasticity have been considered by Lindley *et al* [90], Bassim and Emam [91] and Hartbower *et al* [92], the general consensus about the relative importance of fracture and plastic deformation at the crack tip being similar to that found for static fracture above, where consideration of the degree of crack tip plasticity becomes increasingly important as the plastic zone size increases, for example in low-cycle fatigue or with relatively ductile materials.

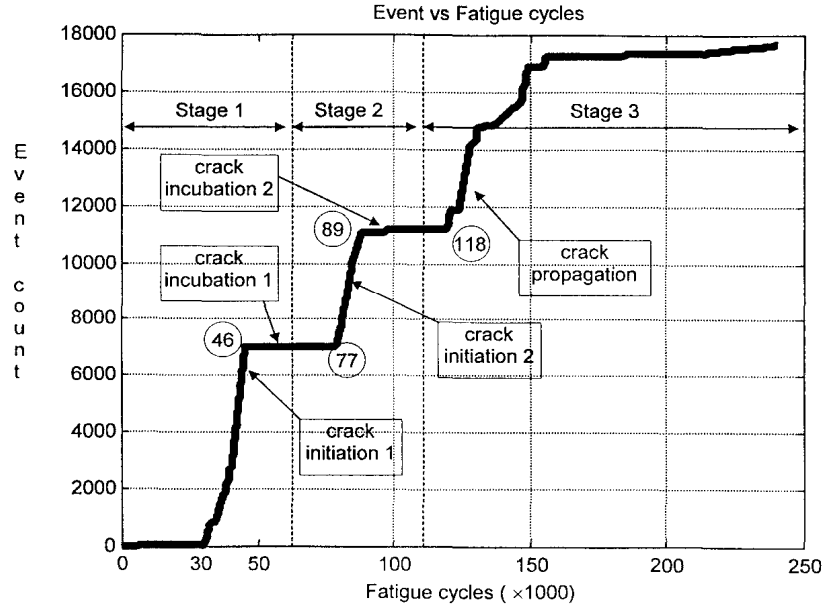

Figure 2.12: Cumulative AE counts fatigue cycles [93]

Impact a significant potential source of damage in many operating systems, and identifying the type and location of damage is important for reliability and safety for structures and processes [3]. Prosser *et al* [94] have studied the AE generated by impact worked on aluminium and graphite/epoxy composites plate using two different types of projectile; a low velocity (0.21 kms^{-1}) impact from a steel projectile fired from an air-gun, and a higher velocity one (1.8 to 7 Kms^{-1}) from a nylon projectile fired using a gas gun. They suggested that quantitative information for assessment, including source location and differentiation between penetrating and non-penetrating impact events, could be obtained but that much more work was required on the effect of projectile type (size and material), projectile velocity, propagation distance and structural shape, before a fully-functioning impact monitoring system for aircraft and spacecraft was possible. Working with a suspended steel plate and a pendulum impactor, Gaul and Hurlebaus [95] have been able to identify an impact location by using the maximum of the wavelet magnitude to calculate the arrival times and hence were able to locate the source of the impact. Their method is mostly concerned with source location and no details were given of the nature of the impact events.

Aside from the specific pipeline applications considered in the next section, a large number of different types of industrial process have been subjected to AE monitoring, including those mentioned above, metal forming [18] and metal cutting [87]. For example, Tonshoff *et al* [96] have applied AE monitoring to determining workpiece quality in hard turning and grinding operations applied to hardened steels. In particular, they have been able to relate sub-surface quality, which influences component life, to RMS AE generated during the process and to residual stress, presumably brought about by a martensitic transformation taking place in the surface layers. Finally, Boyd and Varley [82] have commented on the very wide potential applications of AE in chemical engineering, and have included monitoring of gas-liquid, solids and solids-fluid dispersions, monitoring of chemical reactions and the monitoring of equipment all as potential areas for development.

2.4.1 Pipe and Pipeline System Condition Monitoring

Pipeline condition monitoring can be carried out either to monitor the condition of the pipeline (structural integrity monitoring) or the condition of the process itself (process monitoring). Hence, a monitoring system must be able to recognise structural defects (such as cracks or leaks) and process defects (such as undesirable fluid characteristics, for example erosion or cavitation). When materials characteristics are known, AE assessment can be used as the basis for continuous plant monitoring, increasing structural safety and reducing shutdown costs for inspection. For example, Wood and Harris [14], on the basis of 20-year data on large cryogenic storage vessels, have suggested that remnant life can be predicted and structural integrity classified. Also, Hou *et al* [97] have carried out an experimental study of online AE monitoring of flow and related process parameters for a small diameter pipelines conveying dense slurries of fine silica particles, at varying solids concentration, mass flow and volume flow rate. The results showed that the AE signal can be used to characterise slurry flow and that a characteristic frequency in the power density spectrum of the signal was a manifestation of the speed of the positive displacement pump.

Leaks in pipes and vessels can be detected in two general ways, either by detecting the substance that escapes the vessel, for example by aircraft or satellite

surveillance, or by detecting certain leak-related properties such as pressure drops, acoustic emission, volume balance changes and temperature changes. Conventional continuous monitoring is based on the physical effects which can be measured directly or by calculation from a mathematical model of the pipeline [4, 80, 98]. For example, a nonlinear model to locate multiple leaks in pipelines has been presented by Verd [4], which discretises a spatial variable, such as pressure, into three non-uniform sections of unknown sizes. Generally, leak detection is perhaps the most successful practical application of AE to pipelines [18]. For example , Savic [18] has built a leak simulator consisting of an actual 40 mile long pipeline of internal diameter 6 inches and 1 inch wall thickness. The pipeline was built for ethylene gas with an internal pressure of 1500 psi and was buried in wet soil. In the simulation, the line was filled with nitrogen gas to its working pressure and valves opened to allow a controlled leak to be simulated at selected points along the line. The leaks consisted of round holes and both wide and narrow slits and both the size and shape of the leak was found to influence the "acoustic signals". There are many factors (such as environment) to considered when using AE to locate a source, as mentioned by Rajtar and Muthiah [20], who have studied the capacity of AE to locate a leak position in low pressure, low flow rate, oil and gas production flowlines using AE signal attenuation. They noted that the acoustic emission signal is sensitive to the external and internal environment of the pipeline, i.e. supports, soil properties and fluid viscosity, and the results showed that, at a pressure of 0.68 MPa with sensors placed at 61m and 122m, the AE resulting from a very small simulated leak (of the order of 0.01% of the pipeline flowrate) could be detected. Generally, they provided suggestions on determining how many sensing points will be necessary to monitor the operation of a given length of a pipeline, the practical spacing being a compromise between leak sensitivity and the cost of the detection system. However, AE can not only be used to locate a leak in long pipes, but also can characterise the shape of holes as suggested by Yoshida *et al* [99] who have studied the AE characteristics of pinholes and slits in a 20mm diameter pipe using a range of backing pressures. They found a variety of interesting characteristics in the frequency domain which could be used to determine the size and shape of the breaches in the pipe wall.

2.5 Summary and Identification of Thesis Topic

In this chapter, three main aspects of the state of knowledge of AE technology have been reviewed; AE propagation, signal processing and AE applications. The current work will focus on a specific application, pipelines and pipework, on which there has been limited study outside the principal application of leak detection. The focus of the work will be in what information can be deduced about a source using a small array of sensors disposed axially along the pipe. In order to do this, it is recognised that some contribution to knowledge will be required in the area of propagation and source recognition. Some contribution is also expected in signal processing, although this will be in the combination of established processing methods as opposed to the development of totally new techniques. In propagation, there is room for the clarification of the main "modes" by which AE is carried along pipes and the effects that the internal and external environments have. In source recognition, it is expected that some contribution will ensue in how signals are distorted as they travel from source to sensor, and in the AE characterises of non-leak sources.

Chapter 3: Apparatus and Description of the Experiments

3.1 Introduction

This chapter describes the material specifications, experimental apparatus and procedures used for this work. First the features and specification of apparatus which are common to all experiments are described, and then the details of each of three series of experiments are presented. The first series of experiments were intended to study AE wave propagation and source location, and used a standard Hsu-Nielsen source (pencil lead break) to produce a burst-like signal propagating along a pipe with different internal and external environments. The second series of experiments used both continuous and semi-continuous simulated sources (gas jet) to evaluate detection and source location capabilities for such sources. The final experiments used impact and bending tests to simulated real sources, which were expected to have a specific temporal structure. All experiments were carried out at room temperature using the same pipe sections, and therefore the destructive tests were carried out last.

3.2 Apparatus

A typical AE acquisition system and experimental set-up as used in this work are shown schematically in Figure 3.1. The system generally comprised a test object, an array of two or four AE sensors with their preamplifiers, a signal conditioning unit, a data acquisition card, and a computer with software for controlling the acquisition and storage of data as shown in Figure 3.2.

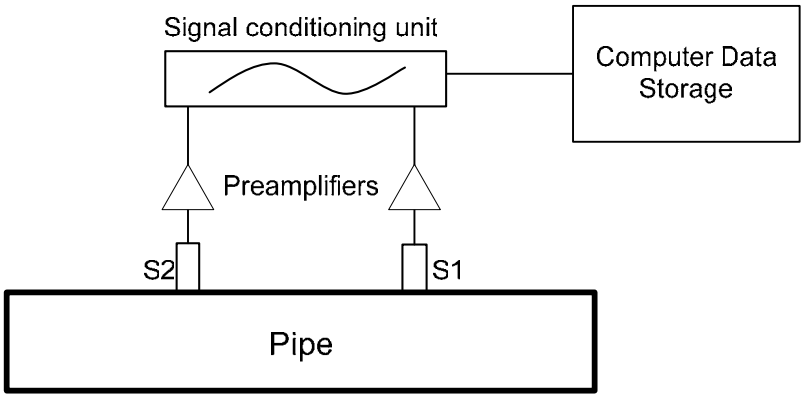

Figure 3.1: Schematic diagram of AE system

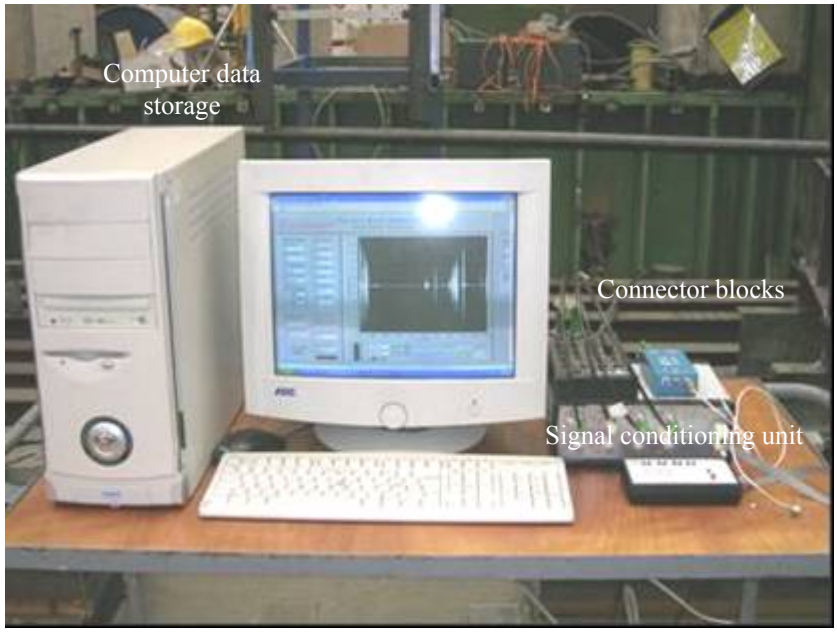

Figure 3.2: Computer data storage with connector blocks and signal conditioning unit

3.2.1 AE Sensors and Coupling

Commercial broadband AE sensors of type Physical Acoustics Micro-80D were used to detect AE. These sensors had a fairly flat frequency response but with two bands of relatively high sensitivity at around 150kHz and 350kHz and are based on lead zirconate titanate (PZT). The AE sensor converts detected waves propagating through the material under examination into a time varying voltage signal. This AE sensor is omni-directional and is sensitive over the frequency range from 175 to

1000kHz, over an operating temperature range from -65 to +177 ^{0}C. The sensors are 10 mm in diameter and 12 mm high and were held onto the test object surface using in-house designed magnetic clamps. In order to obtain good coupling of the AE, the surface was kept smooth and clean and silicone grease was used as couplant to fill any gaps caused by surface roughness and eliminate air gaps which might otherwise impair AE transmission. Calibration certificates for the four sensors used in this work are shown in Appendix A.

3.2.2 Preamplifiers

Preamplifiers of type PAC 1220A were used to amplify the AE signal to a level that can be comfortably transmitted by a short length of coaxial cable and converted by an Analogue to Digital Converter (ADC). They had a switchable 40/60 dB gain and internal bandpass filters from 0.1-1 MHz. The preamplifier was powered by a 28 V power supply and used a single BNC connection for both power and signal.

Signal conditioning units (Figure 3.3) were of in-house construction and were used to power (28 V) the AE sensors and pre-amplifiers. They could also be used to perform analogue RMS processing with the capability of additional amplification or attenuation where necessary.

All of the data acquired in this work were in raw format with the preamplifier gain set at 40dB or 60dB (more often the lower) and the units of AE voltage referred to in the following are corrected to 40dB gain.

3.2.3 Data acquisition (DAQ) system

The experiments in this research were concentrated on acquiring raw AE signals and DAQ was based on an in-house built desktop PC with a 12 bit, National Instruments (NI), PCI-6115 board. This board can be used to acquire simultaneously the raw AE signal at 10M samples/s for up to four channels and uses a full length PCI slot. It is a multifunction analogue, digital and timing device

without on-board switches or jumpers so that it can be configured and calibrated by software.

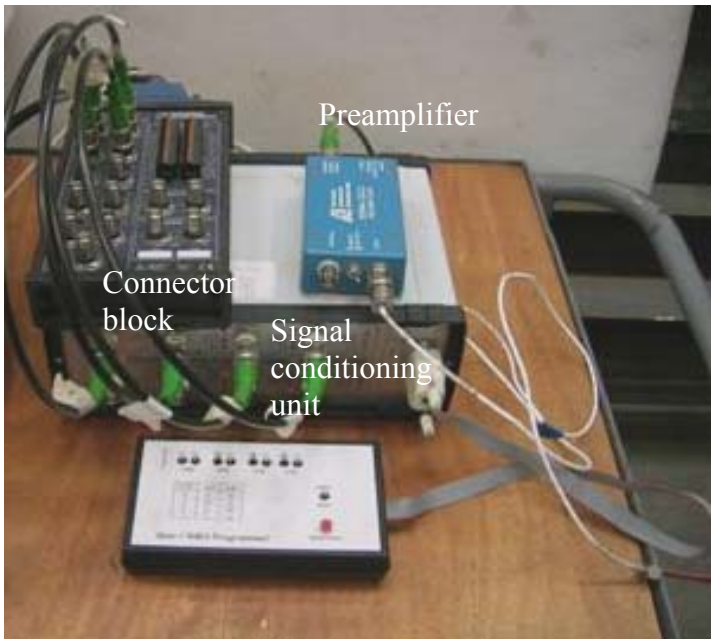

Figure 3.3: Connector block, preamplifier and signal conditioning units

The software-programmable gain can be set to 0.2, 0.5, 1, 2, 5, 10 or 50 and covers an input range from ± 200 mV to ± 42 V. The data can be sampled from 20k samples/s up to 10M samples/s at each channel with a total on board memory of 32 MB. The board supports only differential input configurations and has an over-voltage protection at ± 42 V. For source location applications, it could be used to record raw AE signals (sampled at 5M samples/s) over up to four channels.

3.2.4 Pencil and Guide Ring

A mechanical pencil and an in-house machined guide ring were used to generate simulated AE sources by breaking a 2H pencil lead, the so-called Hsu-Nielsen source. The standard guide ring helps to break the pencil consistently, and ASTM standard (E976–99) [100], recommends that the pencil lead should be the same type (0.3 or 0.5 mm diameter, HB or 2H pencil lead) with a length of 2-3 mm and, accordingly, this research used a 2H, 0.5 mm diameter with a 2mm length of lead

to generate simulated AE sources as shown in Figure 3.4. As far as could be judged visually, the lead was broken under the same conditions, in the same position, using the same length and the same orientation of the pencil for all tests.

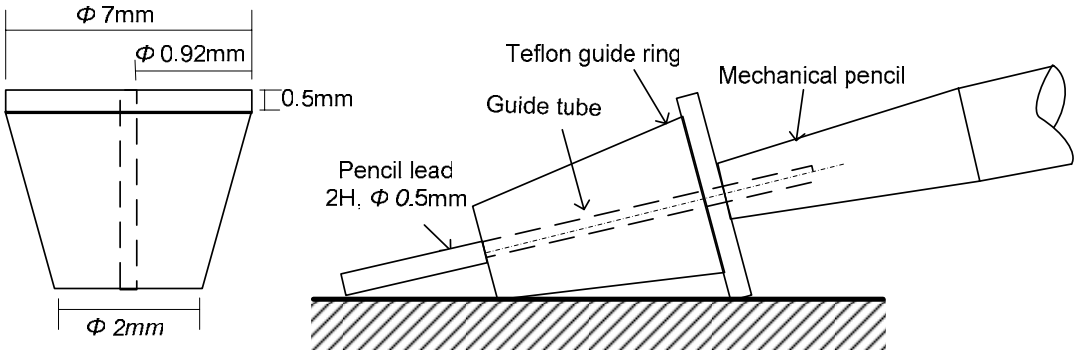

Figure 3.4: Drawing and dimensions of guide rings and pencil [100]

3.2.5 Gas Jet

Continuous AE was generated using a 75 psi gas jet consisting of a nozzle of diameter 0.5mm set at right angle to the surface of the pipe with a stand-off distance of 1mm. The nozzle fitted to the regulator and pressure gauge.

A commercial solenoid valve (SMC SY114) was used to generate pulses of compressed air for a semi-continuous source. This valve is normally closed and opens with a response time of less than 10ms. To operate and control this valve, a control box was made to supply the required of 24V (Figure 3.5), and to control the pulse for a 5ms opening time, flow rate 7.8 l/min, and opening and closing frequency 100Hz, positioned at 10mm from the trigger sensor (S1), which was perpendicular and approximately 1mm apart from pipe surface.

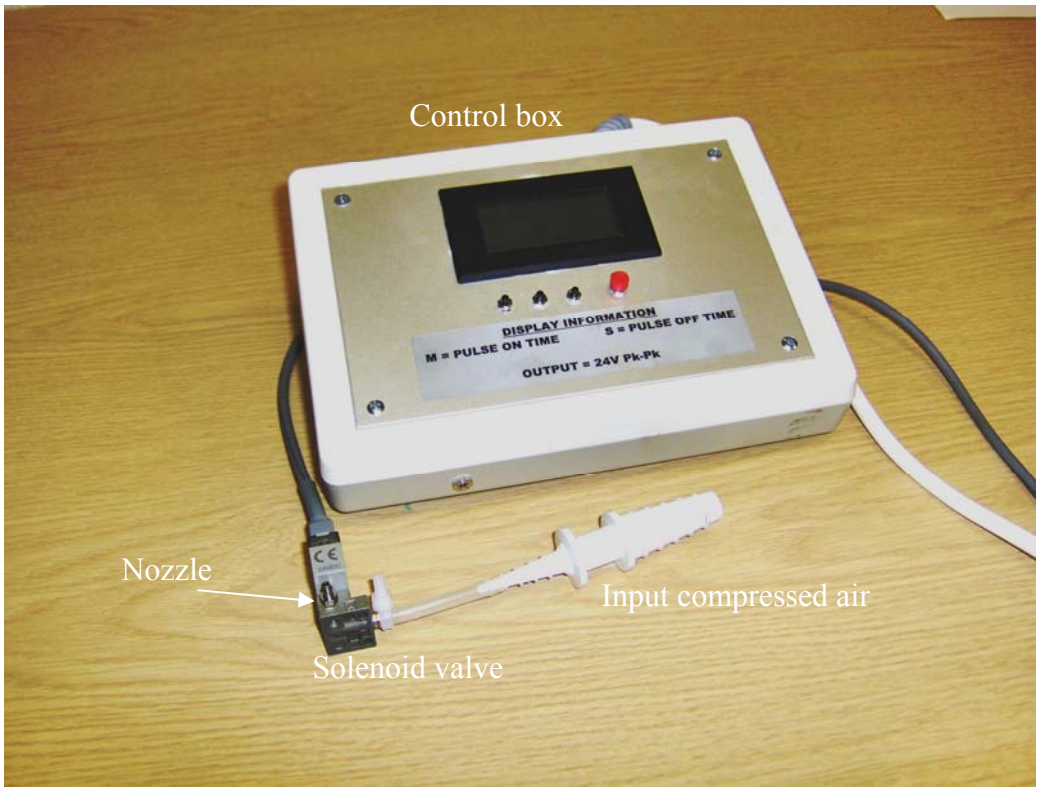

Figure 3.5: Gas jet and solenoid valve

3.3 Computer Software

All experiments were analysed by computer using commercial DA and signal processing software. The software packages used in this research were LabView to control the DAQ system, MATLAB for data handling and some signal processing, and, occasionally, the AGU-Vallen Wavelet algorithm [101] to decompose the signal and analyse the results in the wavelet domain.

LabView was used to control the PCI-6115 board, specifically to control sampling frequency, number of acquired data points per channel, set the number of channels, number of records, input range, pre-trigger data, trigger channel and trigger at up to 74 levels, using a programme developed by Nivesrangsan [40]. The front panel is shown in Figure 3.6, the signals displayed having been acquired from two AE sensors at different positions for a pencil lead break source, for which the upper channel was the trigger sensor.

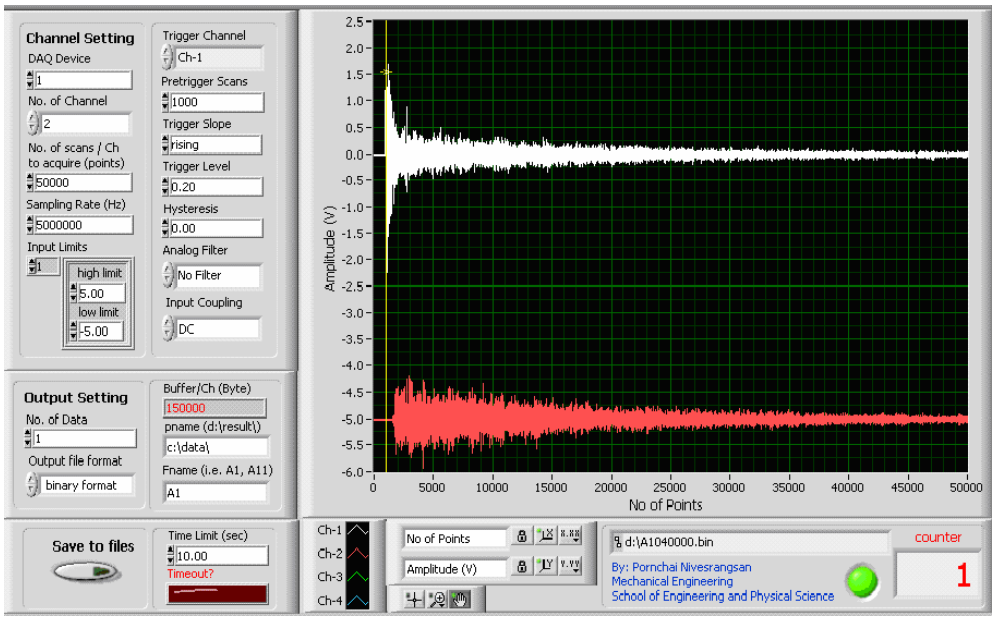

Figure 3.6 : LabView front panel for 2-channel DAQ system

3.4 Experimental Procedures

Series of experiments were carried out to investigate the propagation of AE from simulated (pencil lead break and gas jet) and real (impact and crack spreading) sources to an array of sensors. The overall purpose was to evaluate the potential of AE monitoring to be used in real piping systems, acknowledging the effects that the internal (fluid contained) and external (support, burial) environments may have on the propagation of the waves. To this end, five sets of experiments were carried out where the nature of the source and the environment were varied in a systematic way.

Two lengths of seamless steel (ASTM A106 Grade B) pipe were used in all experiments. The first pipe was 5.5m long, with an external diameter of 168.8 mm and wall thickness of 7.35mm. The second pipe was of a similar material and wall thickness but of external diameter 48.4 mm was also of and length 5.5m. A further two lengths (approximately 5m) of the small diameter pipe were acquired for a separate series of tests (section 3.4.3) and for the destructive tests (section 3.4.5).

3.4.1 Plain Pipe Experiments

Two sets of experiments were carried out with the pipes suspended on wooden blocks in order to obtain a preliminary indication of the type of propagation behaviour shown by a wave generated from a simulated source.

The first of these experiments is shown schematically in Figure 3.7, where the first (trigger) sensor was mounted 300 mm from one end of the pipe, whilst the other sensor was incrementally moved axially along the pipe. The data were sampled at 5 MHz and the pre-amplifier gain was adjusted, if necessary, for the longer distances. Pencil lead breaks were performed on the surface of the pipe beside the trigger sensor, as shown in Figure 3.7. The spacing between the first sensor (S1) and the second sensor (S2) was 20 cm for the first 10 locations, and then increased to 1m for up to 5m spacing, as shown in Figure 3.7. A total of 13 positions were used, the experiment being repeated 10 times at each position.

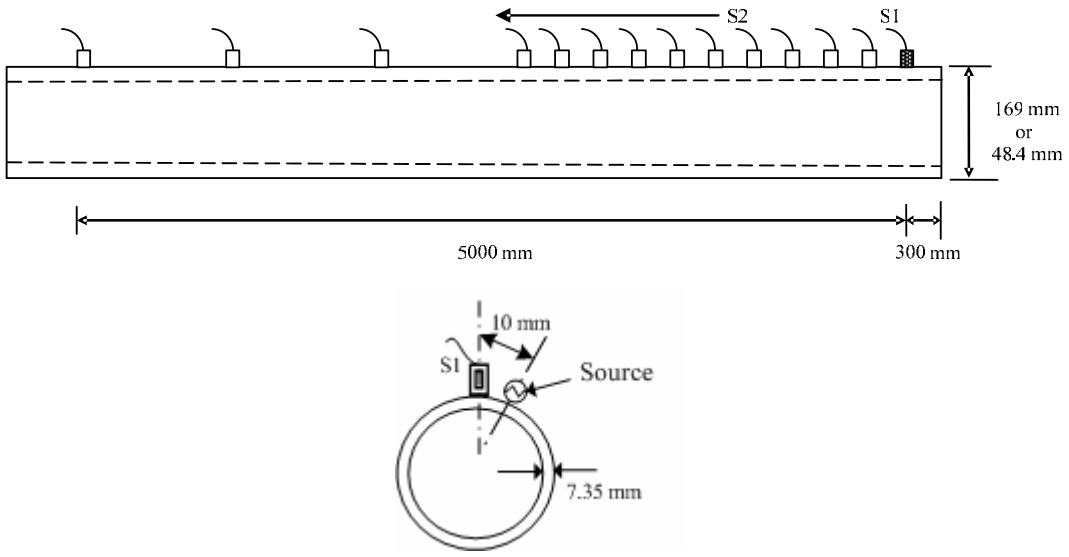

Figure 3.7: Schematic layout of plain pipe experiment for longer source-sensor distances

In order to examine effects at short source-sensor distances compared with the diameter, a second plain pipe experiment was carried out, this time only with large diameter pipe. Four sensors were mounted in an axial linear array pitched approximately 42mm apart (Figure 3.8). Again, the first sensor was the trigger, and the source was 42mm further axially along the pipe from the trigger.

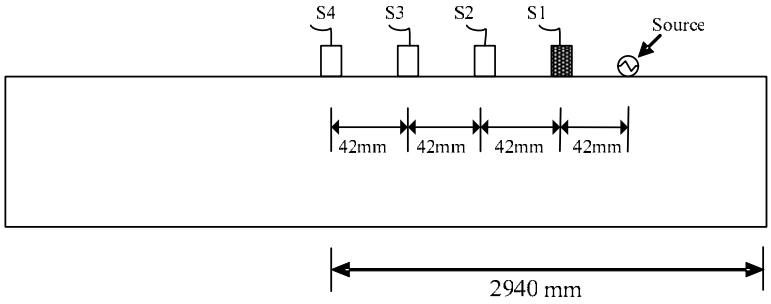

Figure 3.8: Schematic layout of positions for short source-sensor distances

3.4.2 Internal and External Environment Effects on AE Propagation

Two experiments were carried out using the linear array of sensors on the small diameter pipe (Figure 3.7) described in the foregoing section, in order to examine environment interface effects. First, four different interface conditions were investigated; the pipe containing air or water, and surrounded by air (suspended on wooden blocks) or fine wet sand (particle size 180 micron), as shown in Figures 3.9 and 3.10. Second, with the pipe filled with air, six different external conditions were investigated with the pipe surrounded by two different sand sizes, each with three different water contents, as shown in Table 3.1.

For each condition, two sensors were mounted along the 5.5m length, using magnetic clamps and vacuum grease couplant, as shown in Figure 3.11. As before, the first sensor acted as the trigger, and was mounted 300mm from one end of the pipe, whilst the other sensor was incrementally moved along the pipe in line with the first sensor. The spacing between the first sensor (S1) and the second sensor (S2) was 20 cm for the first 10 locations, and then increased to 1m for up to 5m spacing, giving 13 positions in total, the experiments being repeated 10 times at each position.

	180 micron (small size)			**2000 micron (large size)**		
Water content (percentage by weight)	dry	20% (wet)	27% (soaked)	dry	13% (wet)	20% (soaked)

Table 3.1: Specification of sand–water external environments

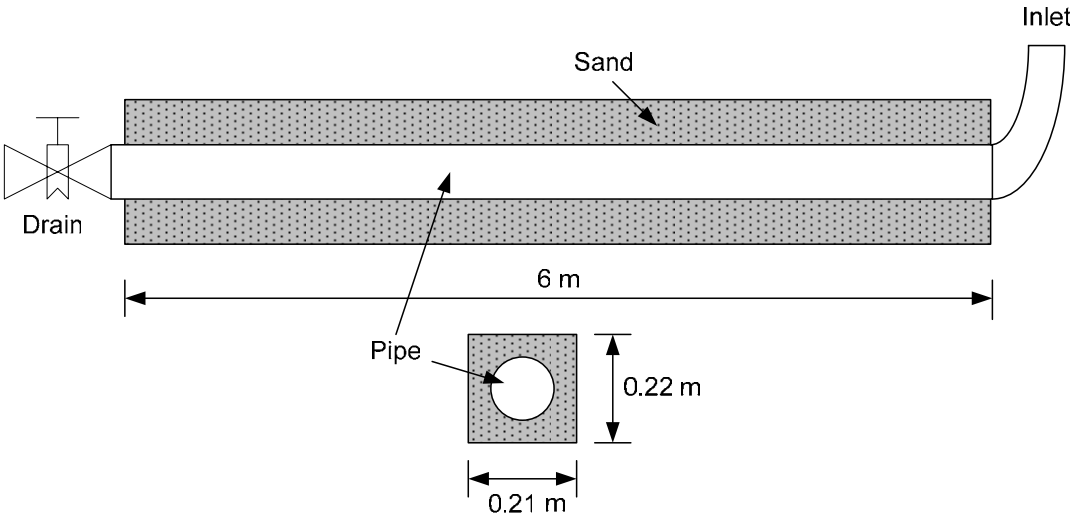

Figure 3.9: Layout of box containing sand

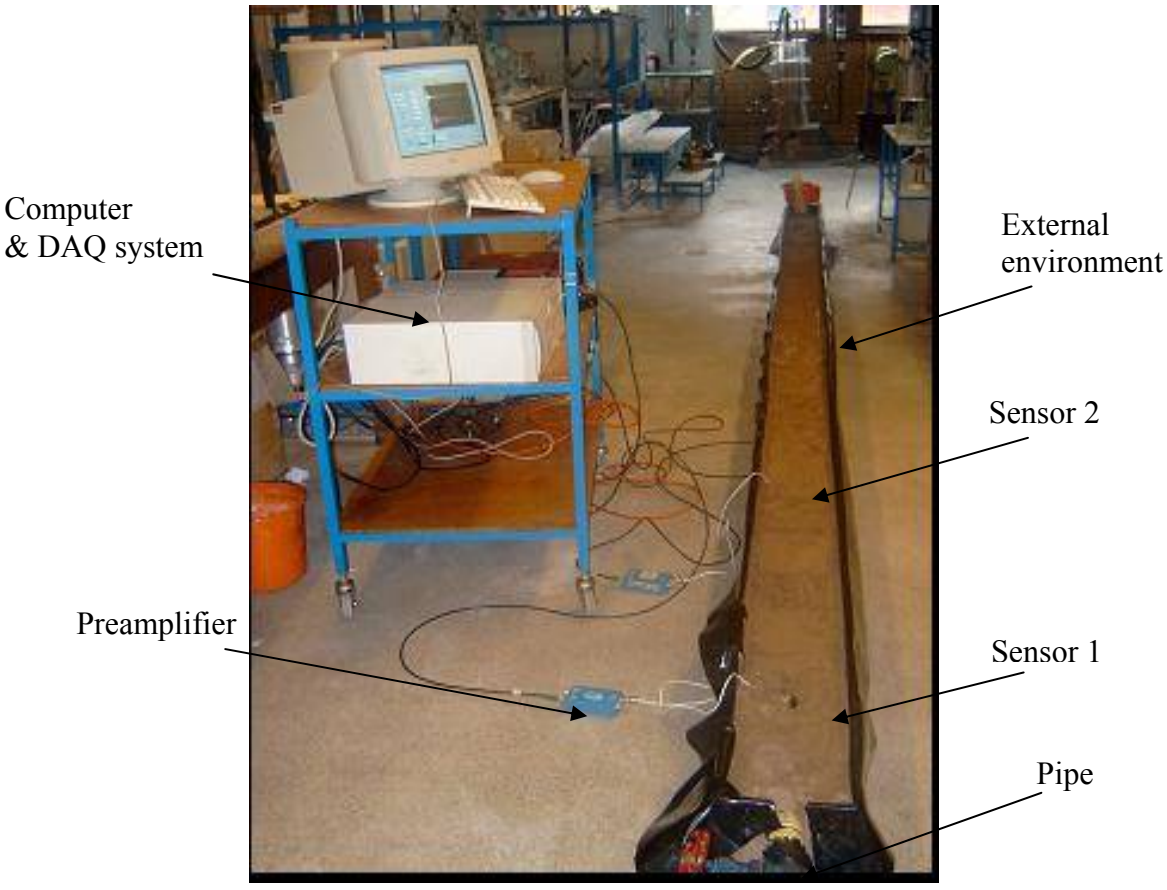

Figure 3.10. Measurement setup for buried tests showing data acquisition system and sensors in position

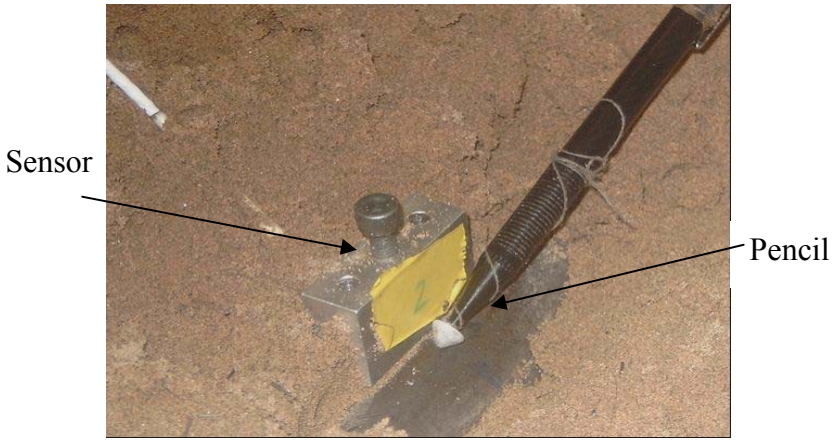

Figure 3.11: Positioning of sensor and source

3.4.3 Continuous and Semi-continuous Source Tests

Two sets of experiments were carried out with the compressed air source, the first using a single 5m length of the small diameter pipe, and the second using three lengths of the small pipe welded together, yielding a total length of 18m.

In the single-length experiments, two sensors were mounted on the pipe, as shown in Figure 3.12. As before, the first sensor (S1) acted as the trigger, and was mounted 300mm from one end of the pipe, whilst the other sensor was incrementally moved along the pipe, in line with the first sensor. The spacing between the first sensor (S1) and the second sensor (S2) was increased in 10cm steps up to 5m. Signals were captured from the compressed air source (Figure 3.12) at a sampling rate of 5MHz for one record of length of 0.01s for each position of S2.

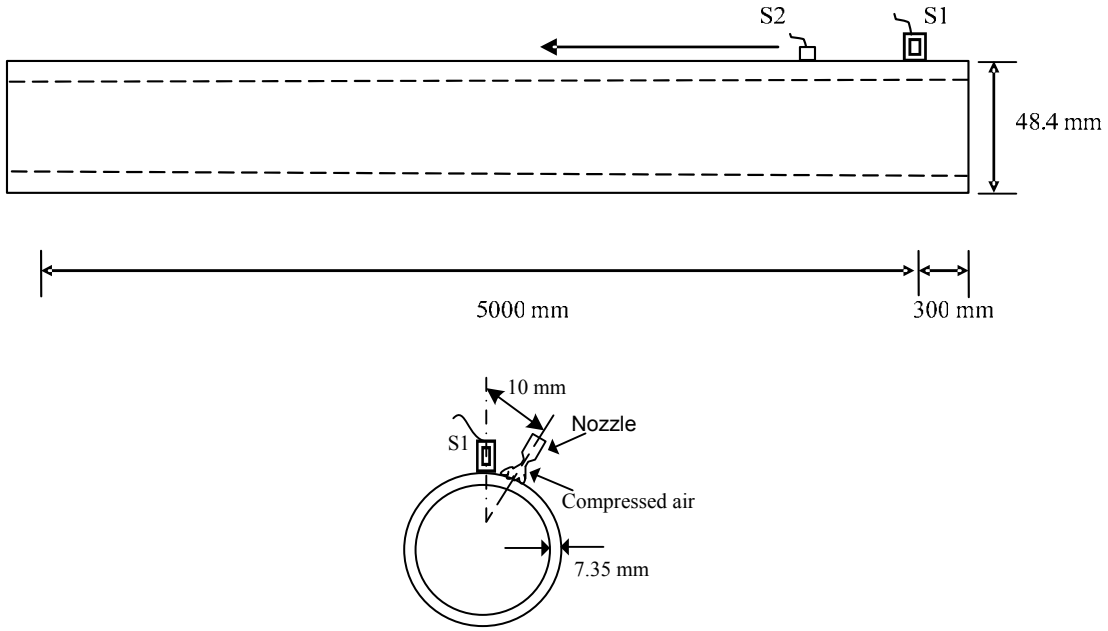

Figure 3.12: Schematic layout of source and sensor positions for continuous source on 5.5m length pipe

For the 18m long pipe experiments, the trigger sensor was mounted 6m from one end, with the simulated source 10mm around the circumference from it. The other sensor was incrementally moved axially along the pipe, in line with the first sensor, its distance being increased in 20cm increments for the first 10 positions, then by 1m increments until 10m spacing, as shown schematically in Figure 3.13. As before, 0.01s segments of continuous AE gas jet data were acquired for each sensor position. For semi-continuous experiments, the signals were captured at S1 and S2 at a sampling rate of 5MHz for five records of length 0.1s. The semi-continuous compressed air (75psi) was through the solenoid valve, (Figure 3.13).

3.4.4 Impact Tests

Three series of dropped-weight tests were carried out on the impact rig shown in Figure 3.14. Only one sensor was used in these experiments mounted on the 5.5m length of the small diameter pipe 1m away from the source. The pipe was mounted on the rig between two simple supports, which were covered with rubber to reduce the noise which might be generated from the interaction of the pipe and its supports. Weights of mass 5kg and 10kg were mounted on an aluminium frame of

weight 1.5kg on which a steel indenter was mounted and the whole assembly was slid down two steel rails from a maximum height of 1.5m.

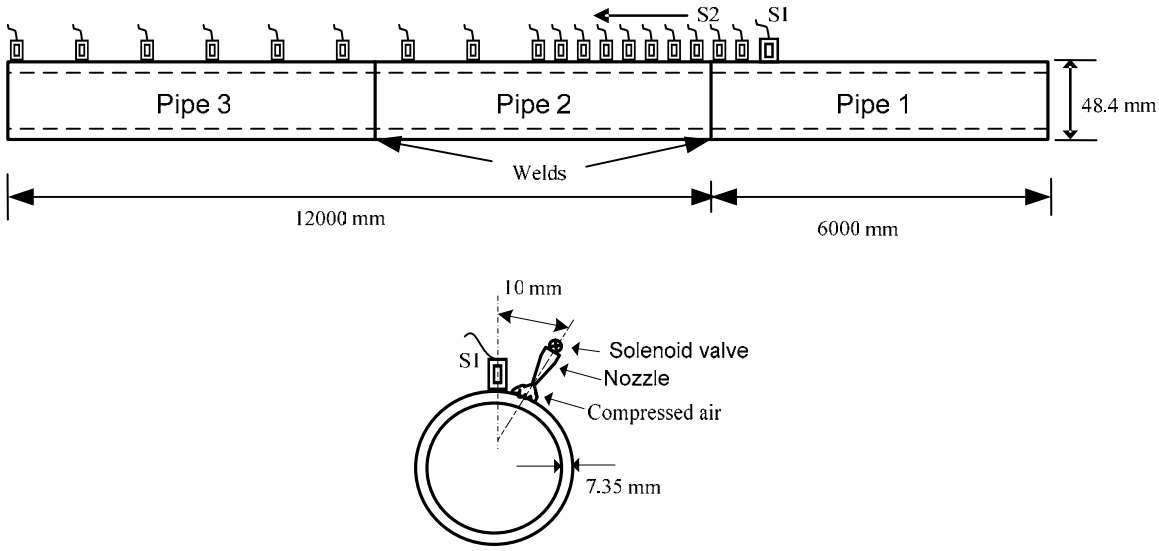

Figure 3.13: Schematic layout of source-sensor positions for 18m length pipe

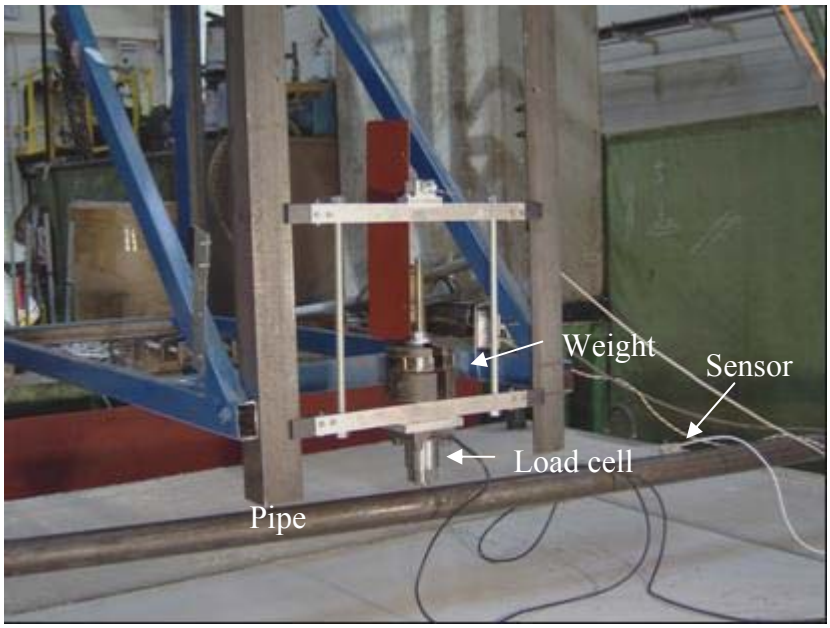

Figure 3.14: Indenter, weight, load cell and sensor

In the first experiment, a spherical indenter of 6mm diameter was used, and this is shown in Figure 3.15. This indenter was originally conical but, after about 3-4 drops had strain hardened and stabilised into the shape shown. Three different

weights 1.5kg, 6.5kg and 11.5kg, were dropped from heights of 0.5m, 1m and 1.5m each test being repeated three times.

Figure 3.15: Spherical indenter

In the second experiment a fresh conical indenter, of 6mm base diameter and 6.5mm in height, as shown in Figure 3.16, was used for each experiment. Two weights (6.5 and 11.5kg) were used, each dropped from two heights, 0.5m and 1m. In this experiment, the indenters were mounted on a load cell (Novatech F218), capable of resolving impact loads up to 40 tonne with a time resolution of 500Hz.

Finally, to study the effect of indenter shape on the signature of the AE signal after several impacts, a third set of experiments were repeated five times using a weight of 11.5kg dropped from 1m height with a single indenter, starting with a conical indenter shape.

Figure 3.16: Conical shape indenter

3.4.5 Three Point Bending Test

In a final series of tests segments of the small diameter pipe were prepared for destructive testing in 3-point bending using a universal testing machine. Two sensors were mounted on segments of pipe of nominal length of 1.9m, each sensor being positioned 0.25m away axially from the mid-span and opposite a machined notch, as shown in Figure 3.17. Five different notch sizes of varying depth and constant length to depth ratio (10.3) were used as shown in Table 3.2.

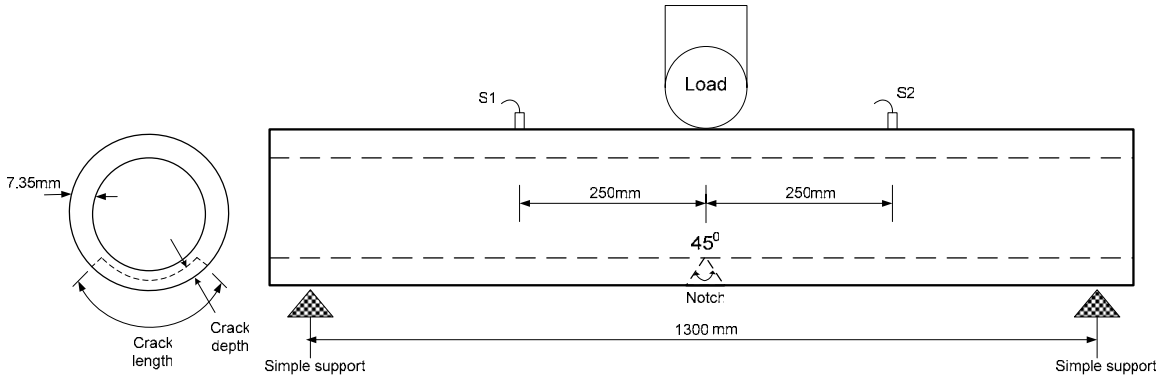

Figure 3.17: Schematic layout of three point bending test and initiated crack position

Pipe No.	Defect length (mm)	Defect depth (mm)
1	30.9	3
2	41.2	4
3	51.5	5
4	61.8	6
5	76	7.35 (through-wall)

Table 3.2: Length and depth of machined notches

The notches were loaded in 3-point bending using a 50kN universal testing machine, as shown in Figure 3.18, with a crosshead speed of 1.66 mm/s (Figure 3.19). The pipes were mounted on two simple supports 1.3m apart and 0.3m high and those, along with the indenter mounted in the crosshead, were coated with rubber to reduce noise. Also, a Linear Variable Displacement Transformer (LVDT) was mounted on the rig to measure displacement of the crosshead. The outputs of

the two AE sensors, the LVDT, and the machine load cell were connected to a 4-channel data acquisition card for simultaneous recording.

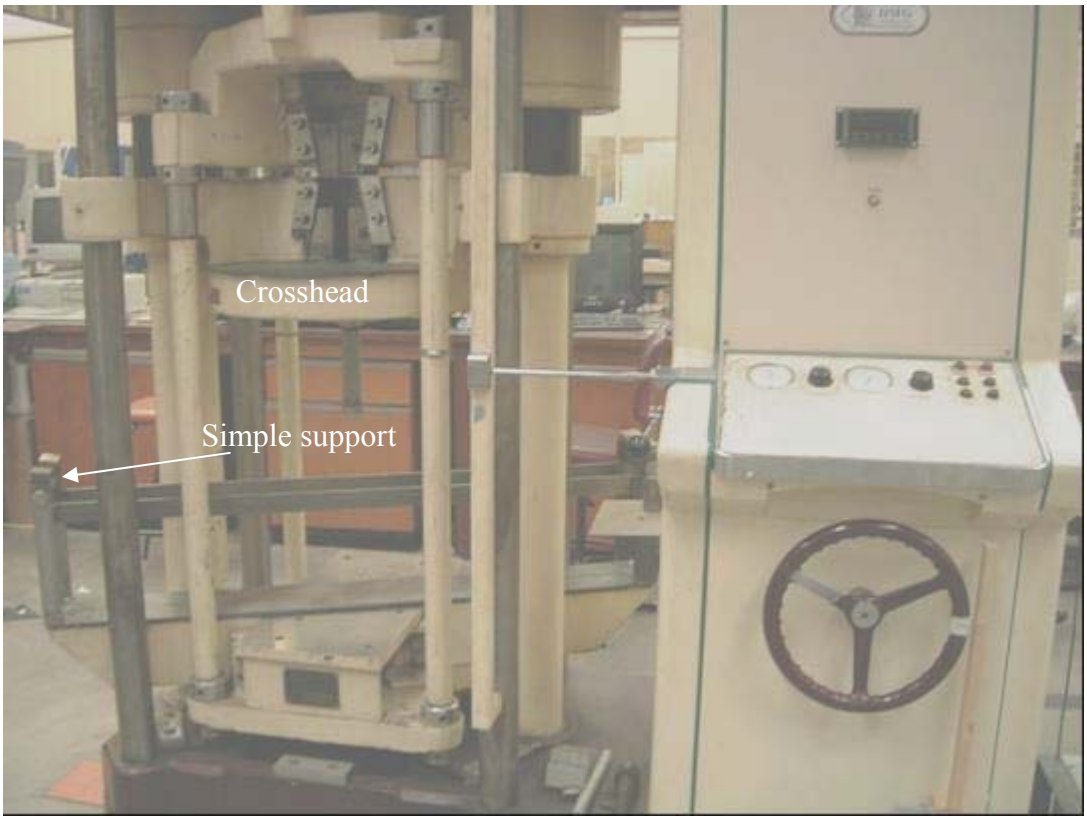

Figure 3.18: Universal testing machine

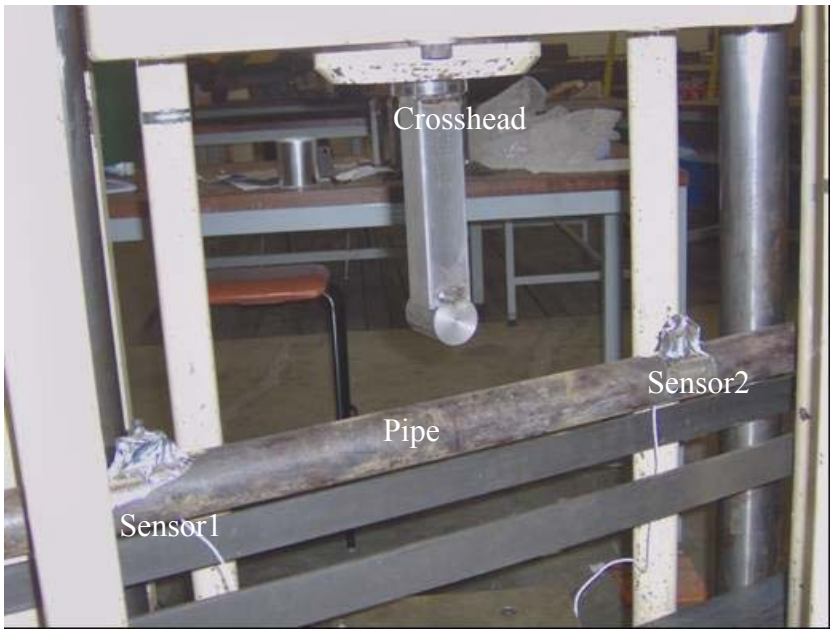

Figure 3.19: Three point bend test setup

3.5 Summary of Experiments

Table 3.3 summarises all experiments carried out on the pipes, and pipe sections. The experiment type, source type, number of sensors and their positions, along with the number of records are also shown in the table. The results of these experiments are analysed and discussed in the following four chapters.

No.	Experiment types	Source types	No. of sensors used	No. of sensor positions	No. of records per position
1	**Plain pipe experiments**				
	1.1 Long length to diameter ratio on large pipe	Pencil	2	13	10
	1.2 Long length to diameter ratio on small pipe	Pencil	2	13	10
	1.3 Short length to diameter ratio on large pipe	Pencil	4	4	10
2	**Internal and external environment effects**				
	2.1 Four different external and internal conditions	Pencil	2	13	10
	2.2 Six different external conditions, air internal	Pencil	2	13	10
3	**Continuous and semi-continuous sources**				
	3.1 Continuous AE source on pipe of 5.5m long	Continuous compressed air	2	50	1
	3.2 Continuous AE source on 18m pipe	Continuous compressed air jet	2	18	5
	3.3 Semi-continuous AE source on 18m pipe	Semi-continuous compressed air jet	2	18	5
4	**Impact test**				
	4.1 Effect of dropped weights of 1.5kg, 6.5kg and 11.5kg from heights of 0.5m, 1m and 1.5m	One spherical indenter	1	1	3
	4.2 Effect of fresh indenter for dropped weights of 6.5kg and 11.5kg from heights 0.5m and 1m	Four sharp conical indenters	1	1	1
	4.3 Effect of indenter shape for dropped weight of 11.5kg from height 1m	One indenter	1	1	5
5	**Three point bending test**				
	5.1 Different machined notches of 3, 4, 5, 6mm, and through-wall	Crack extension	2	1	2000

Table 3.3: Summary of all experiments carried out

Chapter 4: Plain Pipe Experiments using Simulated Source

4.1 Introduction

This chapter discusses the results of the simulated source tests on plain pipe as a means of establishing some key propagation characteristics of different lengths and diameter of pipe. The chapter concentrates on the temporal aspects of AE wave propagation and specifically on determining the arrival times of propagating waves generated from a simulated source in a simple pipe configuration. Hence, identifying the "wave modes" and speeds increases the accuracy of source location, although it might be pointed out that most of the published wave mode analysis has been developed for plane waves, and so only applies reasonably at relatively large distances from the source due partly to the influence of curvature of the wavefront at short distances, but also because separation due to velocity differences becomes clearer as distance increases [28]. Time-, frequency- and time-frequency domain analysis techniques are used in this chapter to derive features of the detected AE signals which can then be used to obtain accurate arrival time estimates.

4.2 Experimental Results

The main objective of the AE analysis in this chapter is to identify and characterise the AE waves propagating along steel pipes of different length to diameter ratios. For all these transmission tests, raw AE signals were acquired at a sampling rate of 5 MHz for a fixed period of 10 ms (50000 points), and ten repeats were carried out of each test.

4.2.1 Time Domain

Figures 4.1a, 4.1b, 4.1c and 4.1d show typical raw AE sensor signals captured at S2 on the large diameter pipe for relatively short and relatively long distances, respectively, from the source. As can be seen, at longer distances, the arrival of

various “waves” can be clearly seen, specifically a relatively low amplitude, high speed wave (Wave 1) and a relatively high amplitude, low speed wave (Wave 2). Some authors have suggested that Wave 1 is an extensional Lamb Wave mode, and Wave 2 is a flexural wave [28, 35]. It can be seen that here it is difficult to separate the waves from each other, particularly at shorter distances.

4.2.2 Frequency Domain

The analogue filter on the pre-amplifier ensures that the frequency content of the AE signals is between 0.1 and 1MHz, although the sensors themselves have a sensitivity which varies with frequency across this range. Nevertheless, changes in frequency content were detectable in some signals rendering some analysis worthwhile, and the frequency content was therefore calculated in terms of power spectral density using Welsh’s method [102].

Figure 4.2 shows a typical frequency domain plot of a raw AE signal at a relatively long distance from the source (5m). Notwithstanding the resonant nature of the sensor, it is clear that the energy is carried mostly in two fairly narrow bands centred on frequencies of around 150 KHz and 340 KHz.

4.2.3 Combination of Time and Frequency Domains

Figure 4.3a shows, for large diameter pipe, how the frequency content of a typical signal (at a relatively short distance) varies with time, where the amplitude in the frequency domain at each time step has been normalised to the same total energy in order to counteract the effect of reducing total energy with time. Clearly, apart from a modest change in spectrum at very short times (probably associated with the difference between Waves 1 and 2, although these are difficult to separate in the time domain), there is little change in spectral content with time. At long times the signal amplitude reduces to noise levels which have a high frequency component. Figures 4.3b shows similarly normalised frequency-time plots for longer distances where there is a substantial reduction in the component of the signal at higher

frequencies. Also, the frequency patterns at shorter times show Wave 1 (low amplitude, fast) to be associated with lower frequencies than is Wave 2.

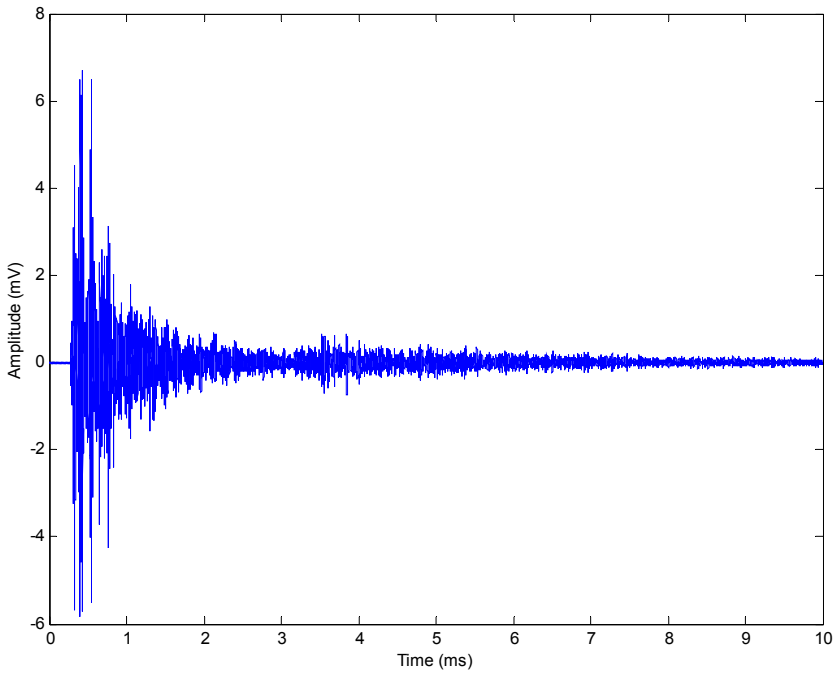

a)

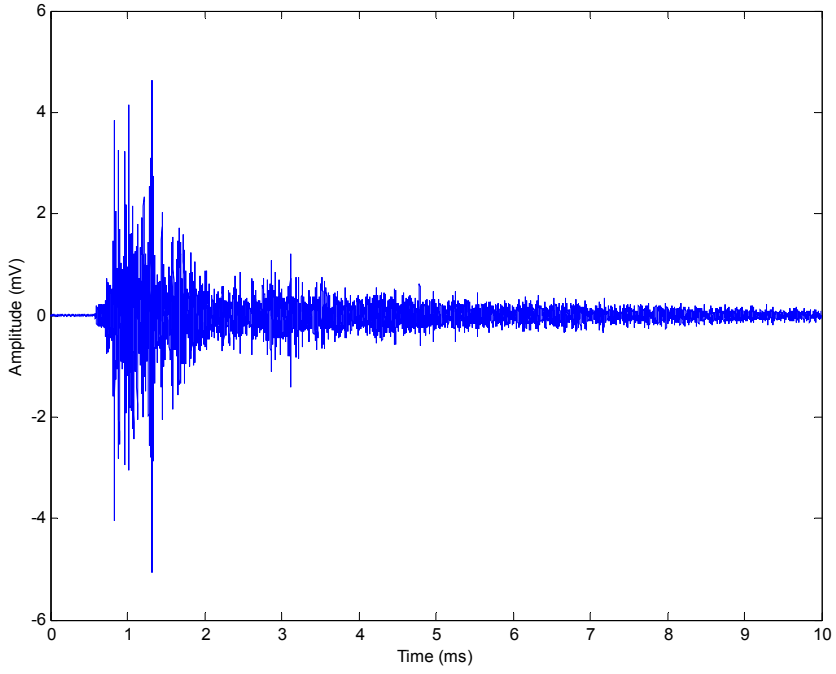

b)

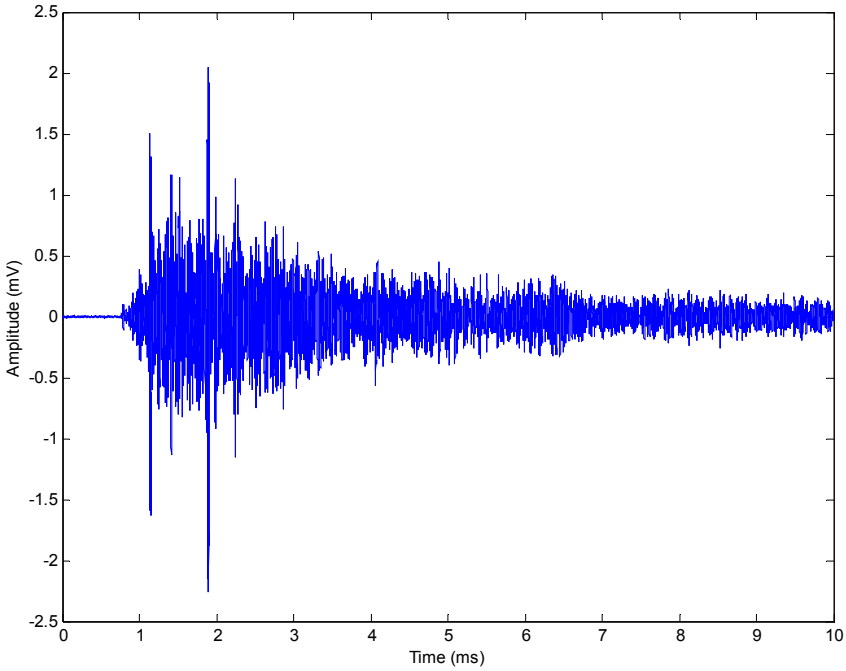

c)

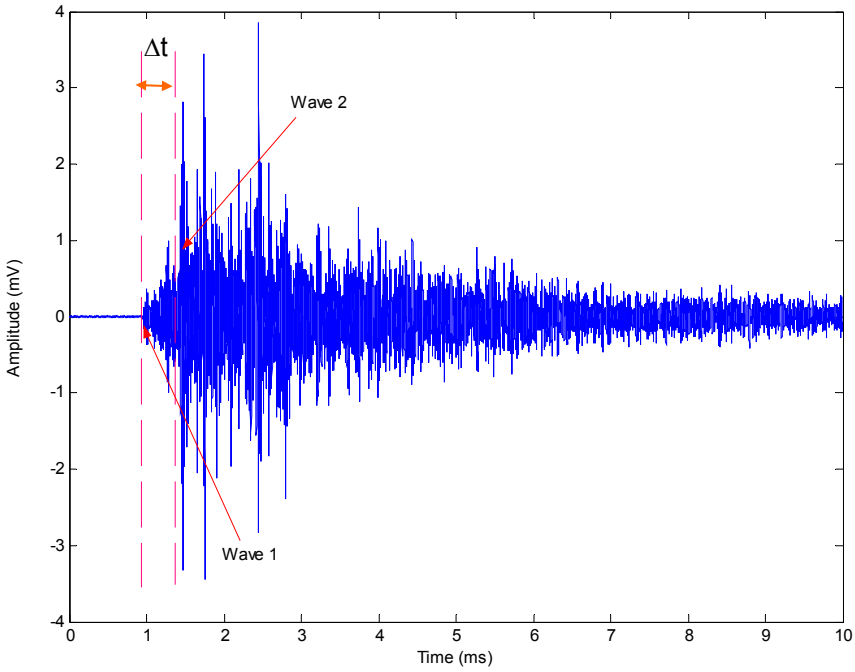

d)

Figure 4.1: Typical raw AE signals acquired at a) 0.4m, b) 2m, c) 3m and d) 4m from S2, for large diameter pipe

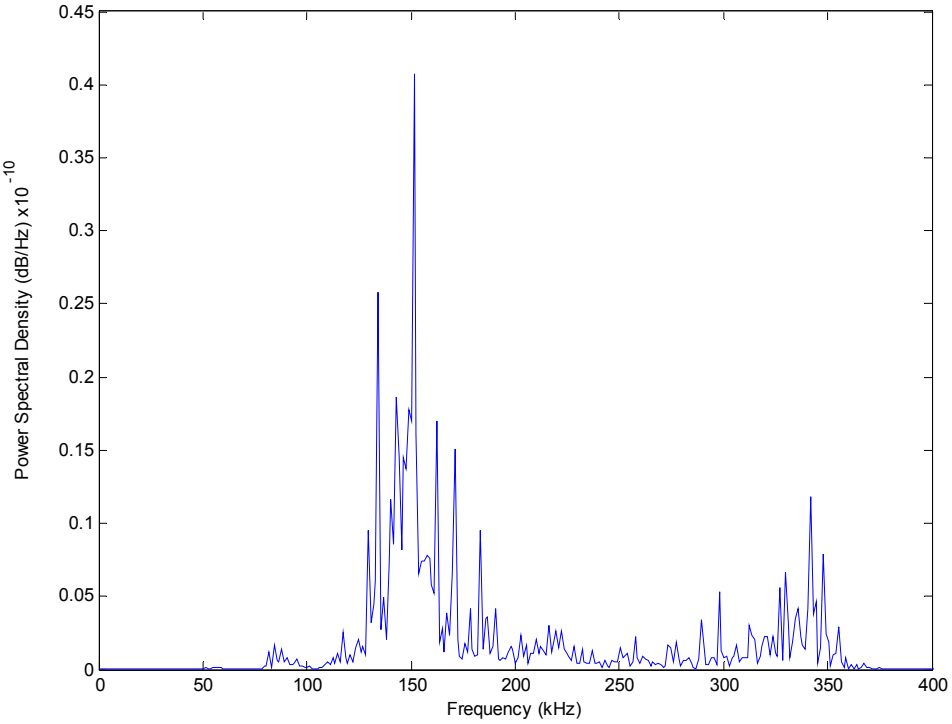

Figure 4.2: Typical frequency domain for raw AE signal at 5m for large diameter pipe

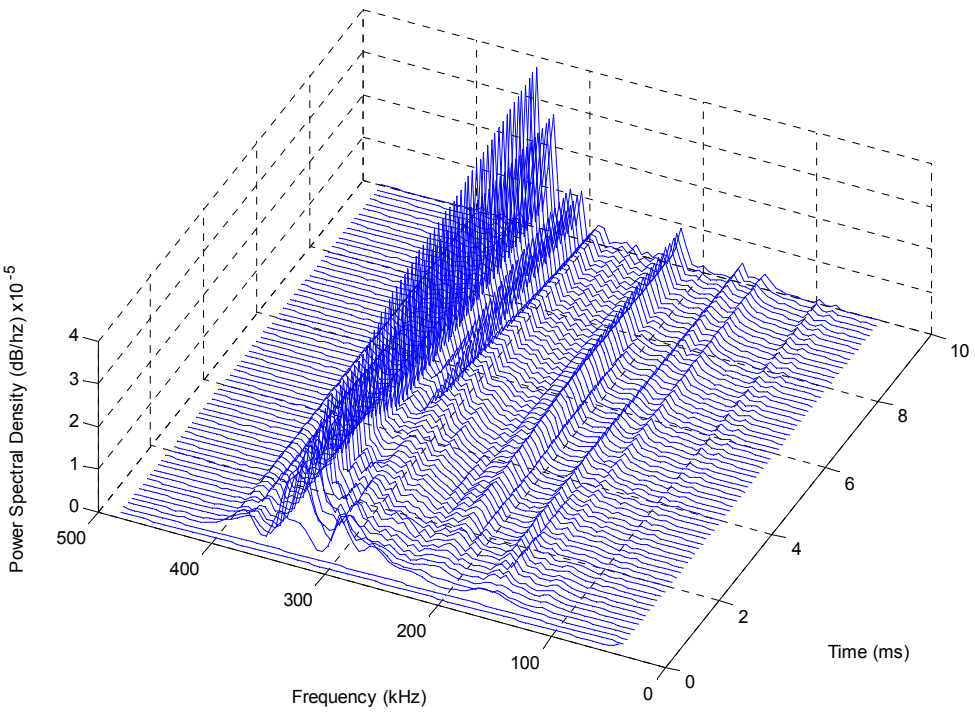

Figure 4.3a: Normalized frequency-time plot for signal acquired at 0.4 m

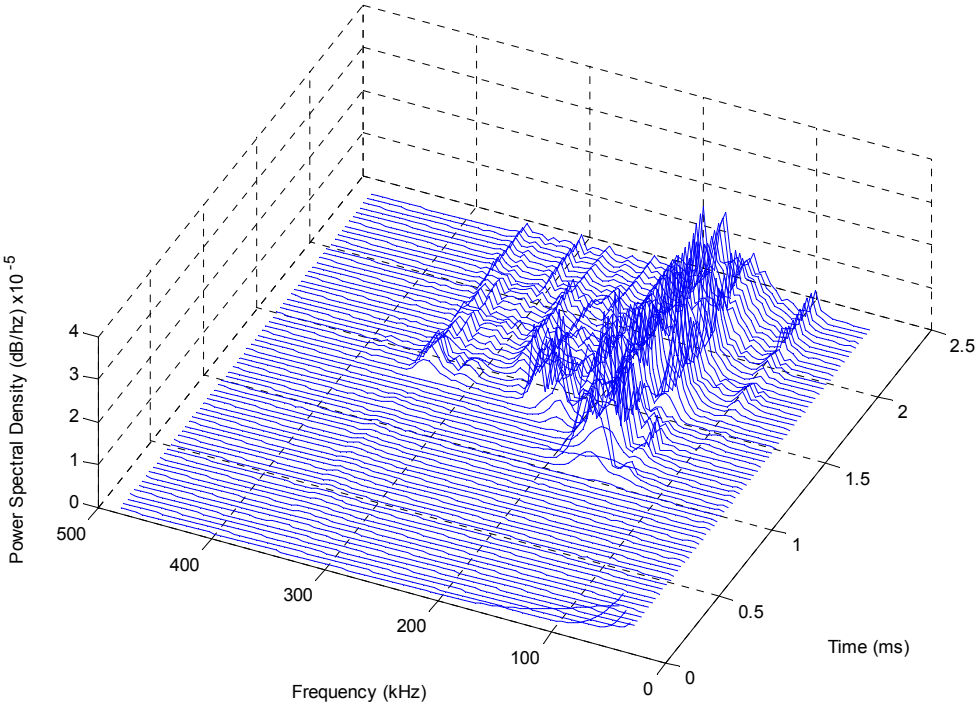

Figure 4.3b: Normalized frequency-time plot for signal acquired at 4 m

In the AE raw time domain it is difficult to distinguish between the wave modes (if indeed there are two, and two only) in an objective way. For the large diameter pipe, a sharp (Chebyshev I) high-pass filter was applied at 340 kHz to isolate the high frequency component, which seems to be almost absent in Wave 1, and the root square taken of the resulting filtered (low amplitude) and raw signals (high amplitude), shown in Figure 4.4 for the case of the source at 4m away from the sensor. Although this rather severe filter removes a substantial component of Wave 2, it is still possible to identify its arrival time and compare it with the arrival time for Wave 1 obtained from the unfiltered signal.

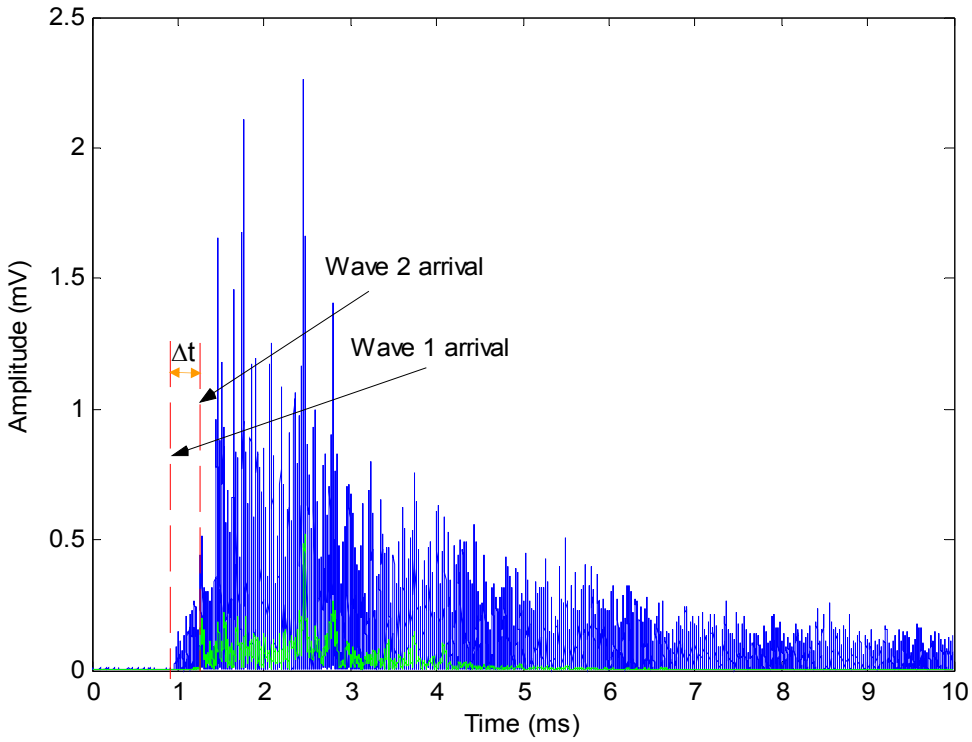

Figure 4.4: Comparison between the arrival of raw signal (Wave 1) and filtered signal (Wave 2) at 4m for large diameter pipe

As mentioned in Chapter 2, the wave speed of AE propagation in structures can be treated theoretically as a variety of pure modes implying simple sources and structures [28], even though the theoretical approach considers the structure to be a homogeneous elastic continuum and without attenuation effects, which may not be applicable to pipes in real applications [20, 33, 103, 104]. Table 4.1 show wave speed data for varies types of wave type in steels.

Ultimately, the wave speed (V) determined experimentally from an AE signal using sensors positioned on the surface of a pipe with a known separation (x) depends on the measurement of the arrival time difference between the signals (Δt). In condition monitoring, automatic techniques are preferable since they allow large amounts of data to be dealt with and avoid subjective judgement.

Material	**Wave speed (ms^{-1})**		
	Longitudinal wave	**Shear wave**	**Surface wave**
Steel	5900	3200	3000

Table 4.1: AE wave speeds for steel [40]

In order to provide a bench-mark for the automatic techniques, a simple experiment was carried out on the large diameter pipe to estimate "manually" the two mode speeds, using an array of four sensors pitched axially at 1m from each other. Ten pencil lead breaks at 10cm from the trigger (S1) were carried out, and the two speeds determined using the 340 kHz cut-off described above, yielding the averaged results shown in Figure 4.5

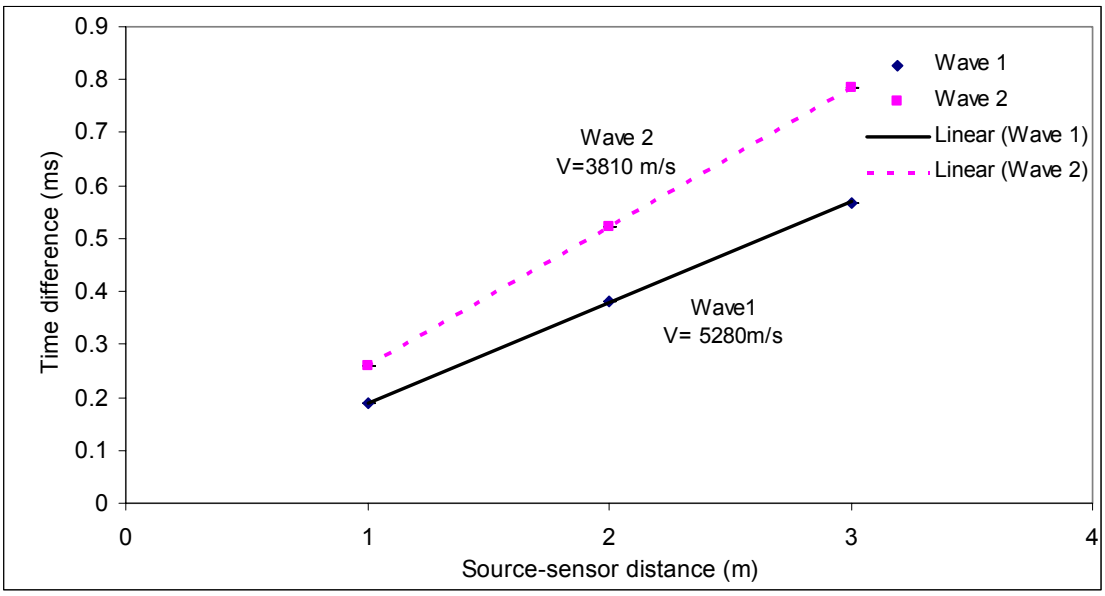

Figure 4.5: Manual wave speed estimation

4.3 Automatic Arrival Time Estimation Techniques

In this section two new methods of identifying wave arrival times and hence potential source location will be presented, and these will be compared with more conventional approaches and the "manual" estimation described above. The first new technique is based on a sliding window determination of the energy distribution across the spectrum, and the second uses cross-correlation combined with wavelet decomposition. These methods are then compared with more conventional cross-correlation and threshold techniques and also with a method based on the Gabor WT.

4.3.1 The Sliding Window Energy Technique

In this technique, a Chebyshev type I filter of the type and effect shown in Figure 4.4 is applied, and the energy ratio of the high-pass (f> 340 kHz) to low-pass bands (f <340 kHz) calculated as a function of time. Figure 4.6 shows this energy ratio calculated for every 20 μs up to 3 ms, for source-sensor distances of 0.4, 2 and 4m. As can be seen by comparison with the corresponding time series (Figures 4.1 and 4.3), the energy ratio falls sharply when Wave 1 arrives. After a period of time, which increases with distance, the energy ratio begins to increase again, which is taken to signify the arrival of the slower, higher frequency Wave 2. These two observations permit an automatic determination of arrival times of the fast and slow waves by detecting the two edges where the energy ratio drops and rises again, the latter of which is shown in the inset in Figure 4.4 for the sensor at 4m from the source.

Figures 4.7a and 4.7b show the arrival times so determined for Waves 1 and 2 for the larger diameter and smaller diameter pipes respectively, yielding velocities which are similar to the manual estimates. Figure 4.8 shows the approach applied to short source-sensor distances and, as can be seen, discrimination between Waves 1 and 2 is very difficult, although values could, in principle, still be obtained.

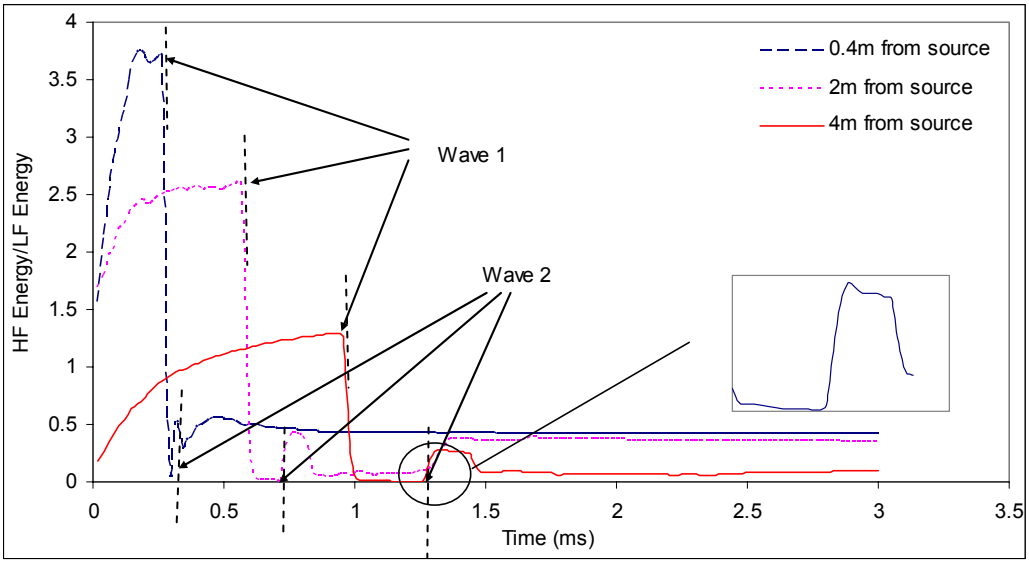

Figure 4.6: Windowed energy ratio (above and below 340kHz) in the time domain for larger diameter pipe, and long source-sensor distances

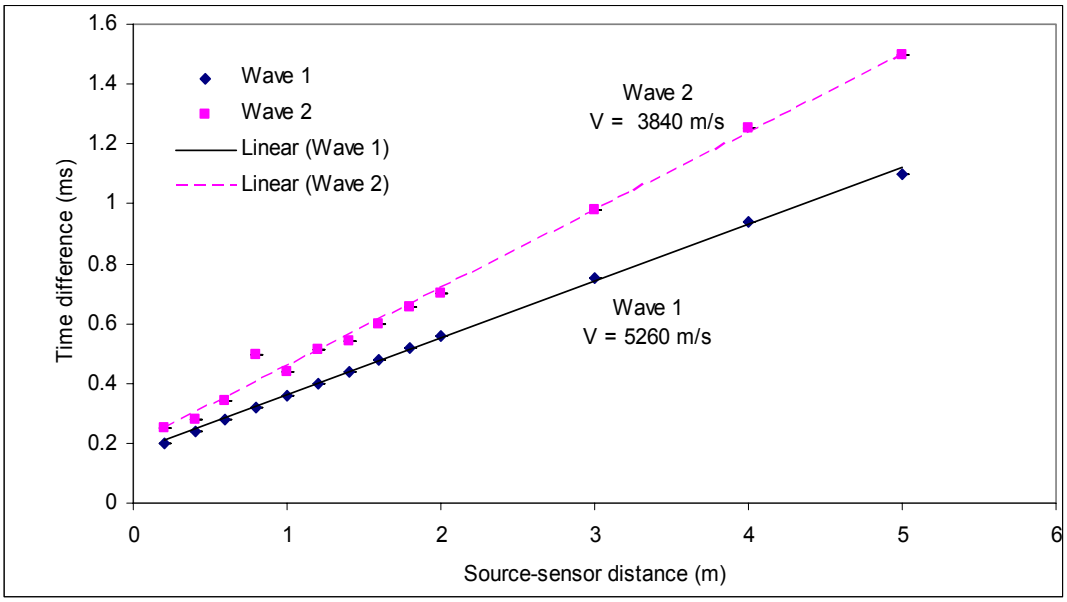

Figure 4.7a: Arrival times for larger diameter pipe, and long source-sensor distances

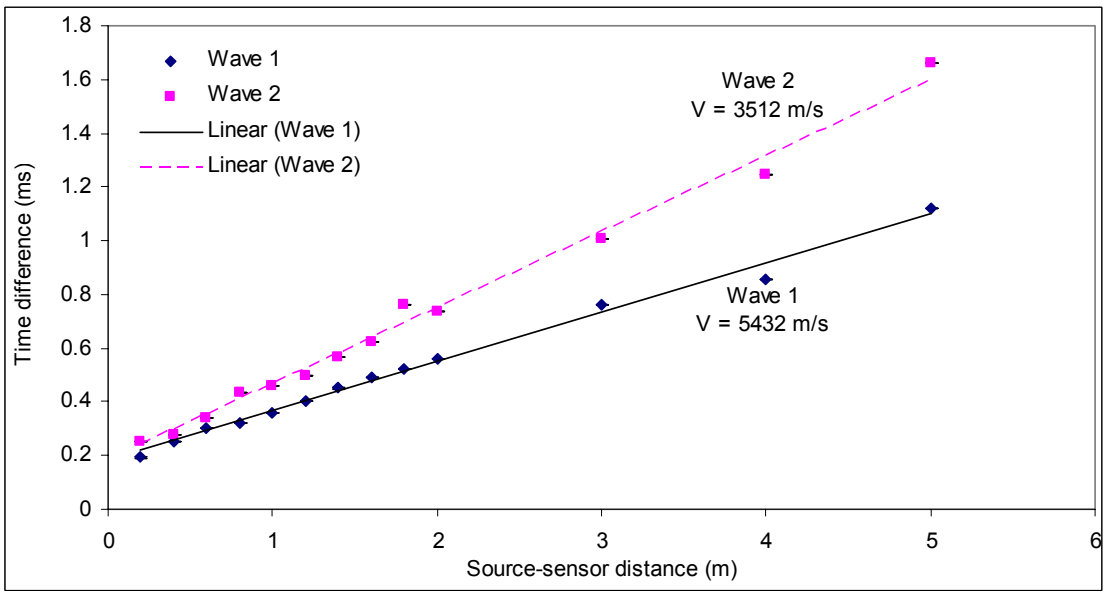

Figure 4.7b: Arrival times for smaller diameter pipe, and long source-sensor distances.

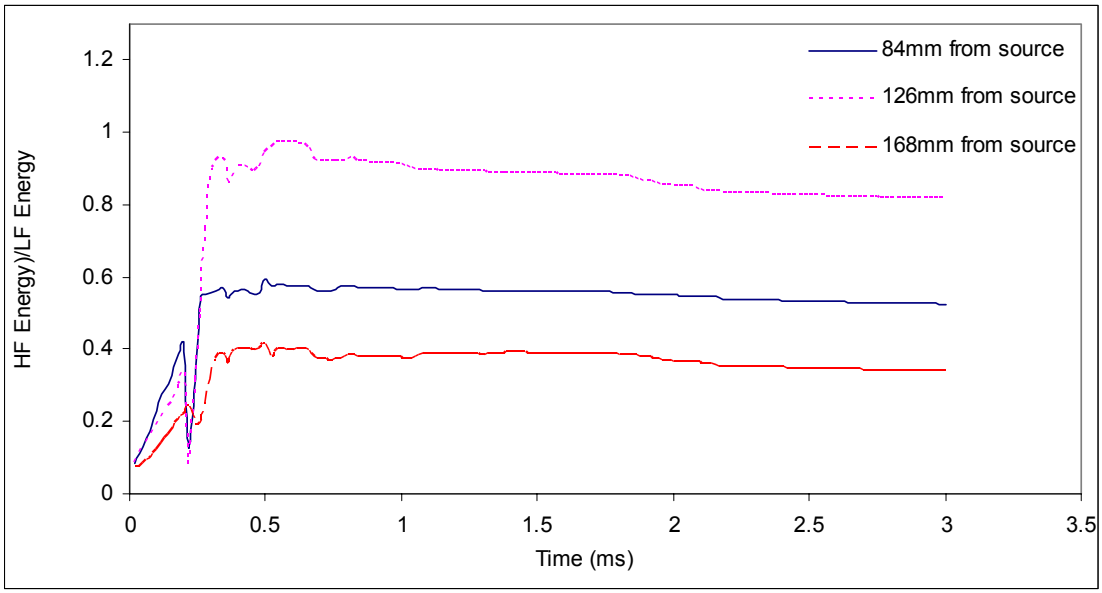

Figure 4.8: Windowed energy ratio (above and below 340kHz) in the time domain for larger diameter pipe, and short source-sensor distances

4.3.2 Cross-correlation of Decomposed Signals

A Daubechies Wavelet of order 1 was used to decompose the signal to level one using a proprietary package (MATLAB), into an Approximation component (which, for convenience, is associated with Wave 1, although, as seen earlier, a much more aggressive filter is needed to isolate this component) and a Detail (Wave 2) component. Then a conventional cross-correlation technique was used to identify the arrival times for each level, as seen in Figure 4.9 for long length to diameter ratios. The technique was also applied to the signals after high-pass filtering at 340 kHz and the results for Wave 1 and Wave 2 are shown in Table 4.2.

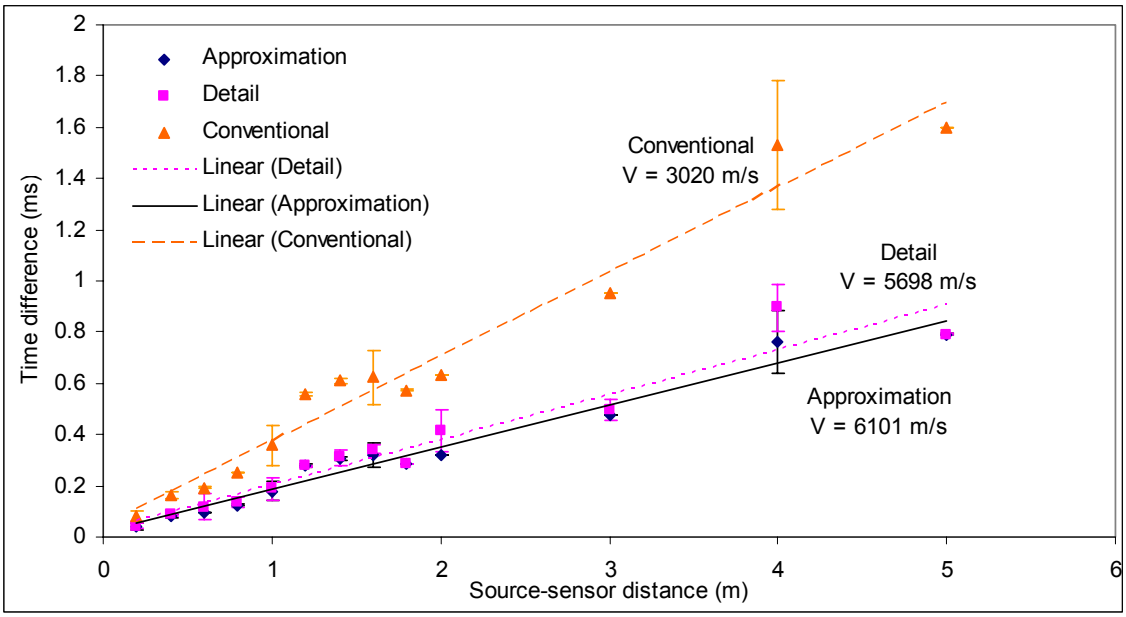

Figure 4.9: Arrival times using wavelet decomposed signal and cross-correlation for smaller diameter pipe and long length to diameter ratio

Wavelet Signal	**Wave 1**		**Wave2**	
	Approx.	**Detail**	**Approx.**	**Detail**
Velocity ms^{-1} (Long distance – large diameter)	5984	4958	4649	4644
Velocity ms^{-1} (Short distance – large diameter)	6830	8680	4304	4344
Velocity ms^{-1} (Long distance – small diameter)	6101	5698	6402	6752

Table 4.2: Velocity of Level 1 decomposed signals for short and long distances

4.3.3 Threshold Method

In this method the arrival times of Waves 1 and 2 are determined by using the unfiltered signal to determine the arrival time of Wave 1 and then using the high-pass Chebyshev filter type I for Wave 2. As can be seen in Figures 4.10 and 4.11, the arrival time estimates are sensitive to the threshold chosen and, in this case, 0.03 of maximum amplitude of the filtered signal was used to detect automatically the arrival time of Wave 2, and 0.015 of maximum amplitude of the raw signal was used for Wave 1. This technique identifies the Wave 1 speed to be 5370 ms^{-1} for the large diameter pipe and 5219 ms^{-1} for the small diameter pipe, both of which

are close to the manually estimated speed. For Wave 2, speed estimates were 4520 ms^{-1} for the large diameter pipe and 4022 ms^{-1} for the small diameter pipe.

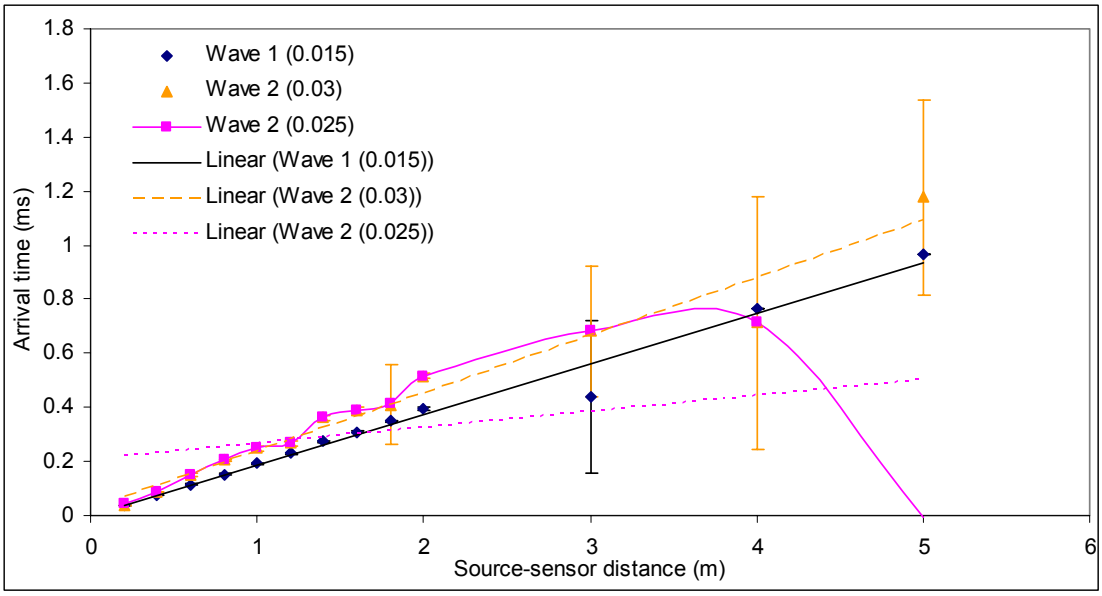

Figure 4.10: Arrival time estimation using threshold method for larger diameter pipe

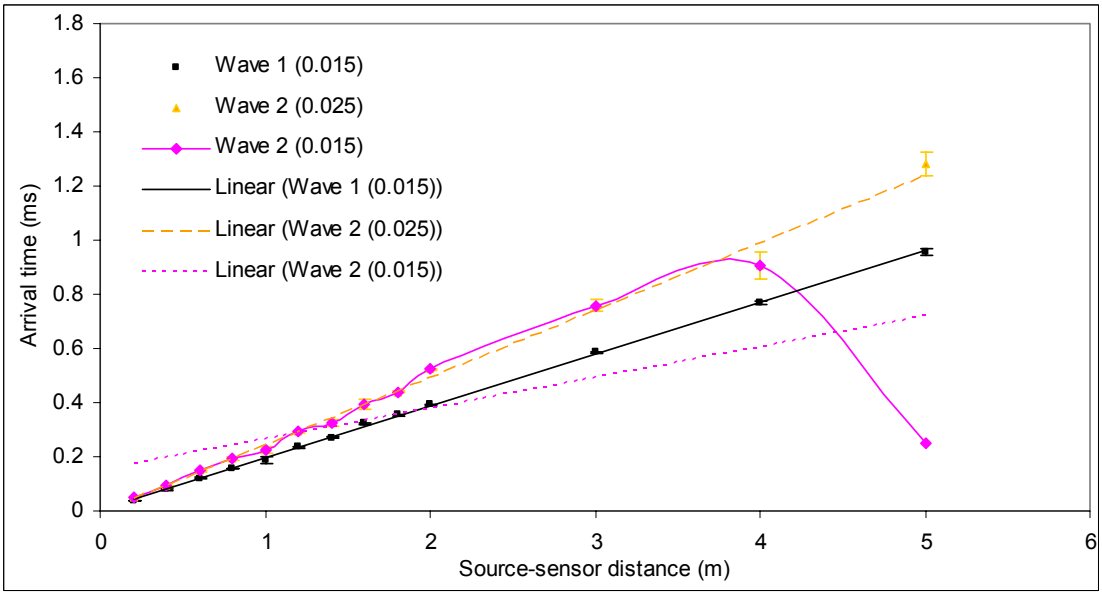

Figure 4.11: Arrival time estimation using threshold method for smaller diameter pipe

4.3.4 Cross-correlation Method

This technique essentially maps two signals to each other over the time domain and returns a time delay corresponding to the maximum in the cross-correlation function. To estimate the AE "signal speed", the square root of the square (absolute) of the raw AE signal was calculated and then the cross-correlation function calculated using a proprietary package (MATLAB). As can be seen in Figures 4.12a and 4.12b, the cross-correlation functions between the trigger sensor and the remote sensor are relatively sharp, with an easily identifiable peak.

Figure 4.13 shows the arrival times for all signals recorded on the large and small diameter pipes, respectively, and might be noted that these yield rather lower speeds than other techniques. Because this technique makes explicit use of the trigger sensor signal, is unlikely to separate out effectively Waves 1 and 2.

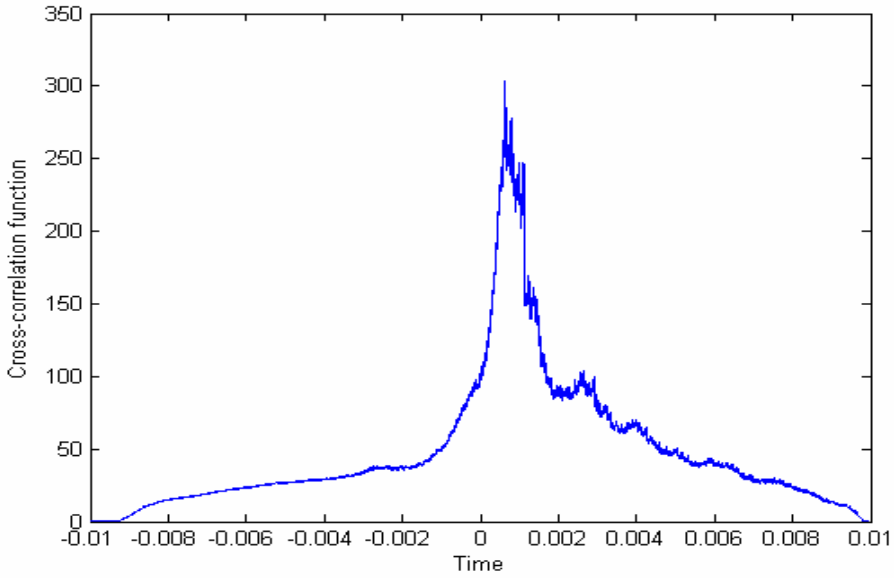

Figure 4.12a: Cross-correlation function between S1 and S2 at 2m from source

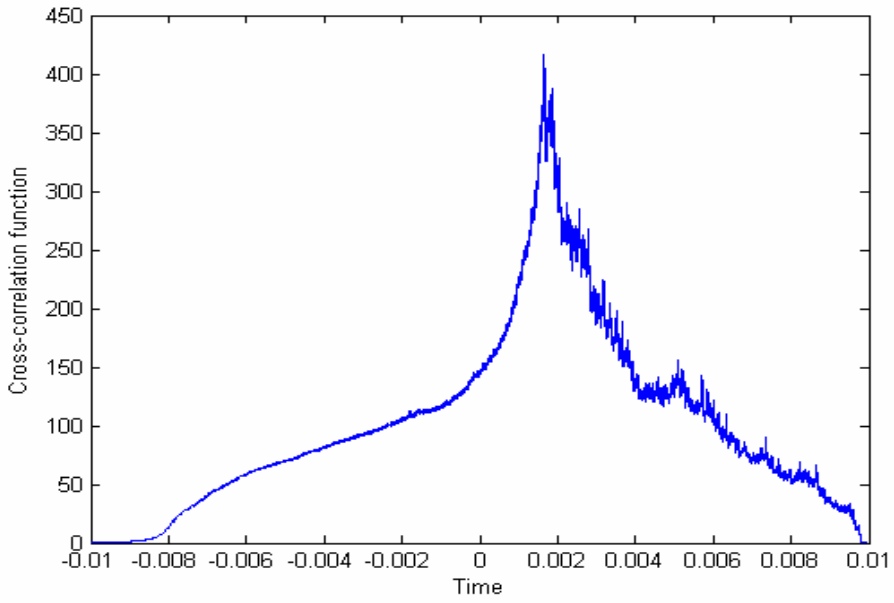

Figure 4.12b: Cross-correlation function between S1 and S2 at 5m from source

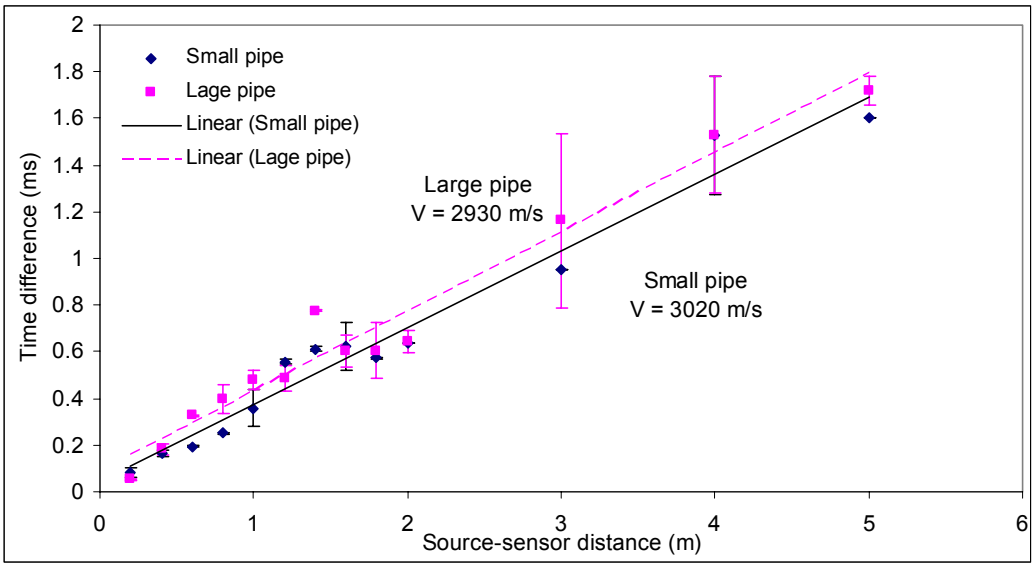

Figure 4.13: Arrival time estimation using cross-correlation method for small and large diameter pipes

4.3.5 Gabor Wavelet Transform

To examine this time-frequency approach, Gabor WTs were calculated using proprietary software (AGU-Vallen Wavelet), specifically developed for AE analysis. The program has a Gabor function as the "mother" wavelet based on the Gaussian function. Figure 4.14 shows a plan view on the time-frequency plane of

the WT magnitude at two different distances. Arrival times were taken as the highest peak in each of the two main frequency bands at around 170 kHz and 340 kHz.

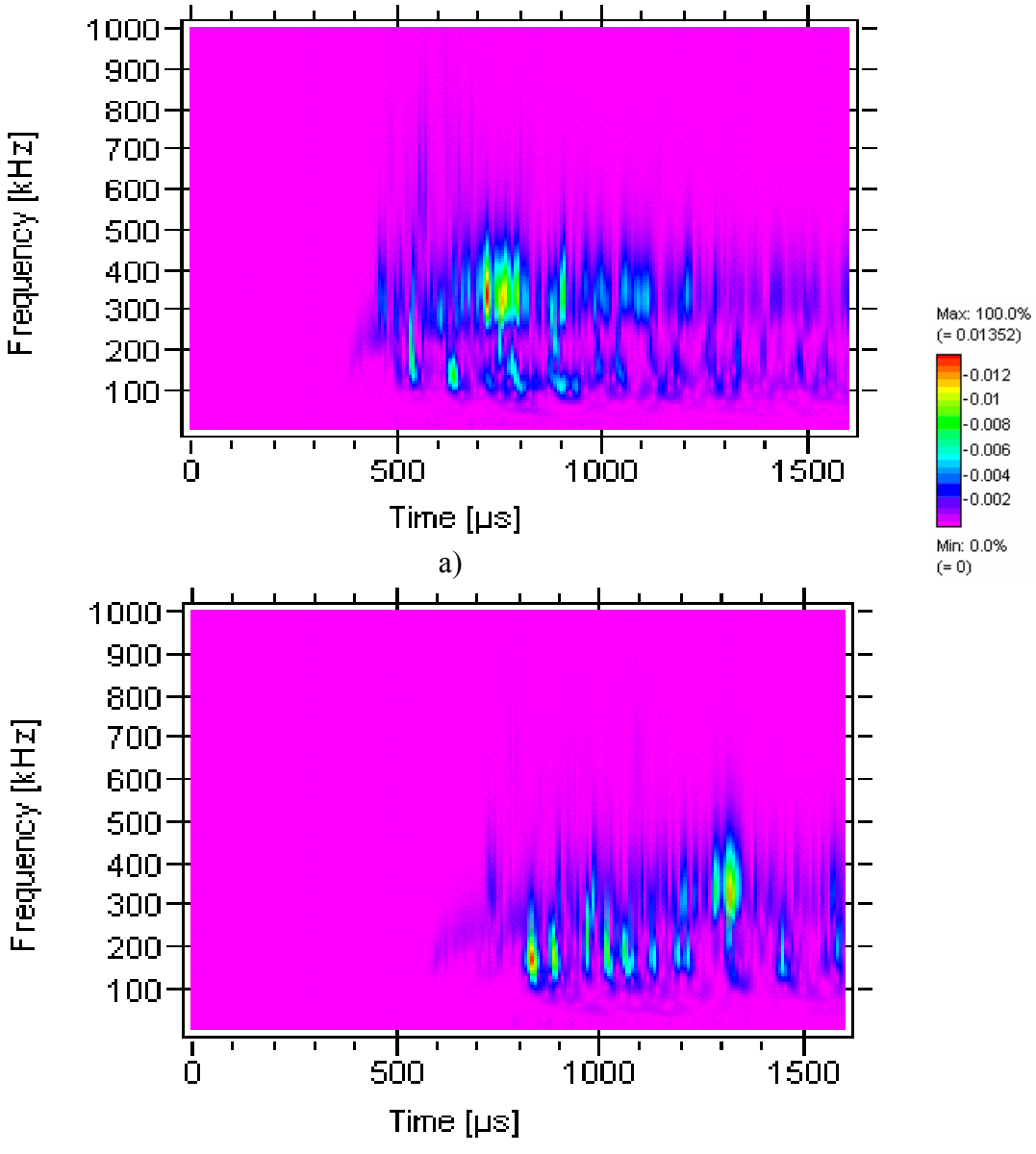

Figure 4.14: Gabor WT calculated (a) at 1 m distance from S2 and (b) at 2 m distance from S2 for large diameter pipe

The arrival times for all signals recorded on the large and small diameter pipes were again used to determine apparent wave speeds and the results are shown in Figure 4.15. Because this technique makes explicit use of the trigger sensor signal and essentially compares the whole time series, it is not possible to separate out

effectively Waves 1 and 2 [61], although it has the advantage over unfiltered cross-correlation that there is some separation in the frequency axis.

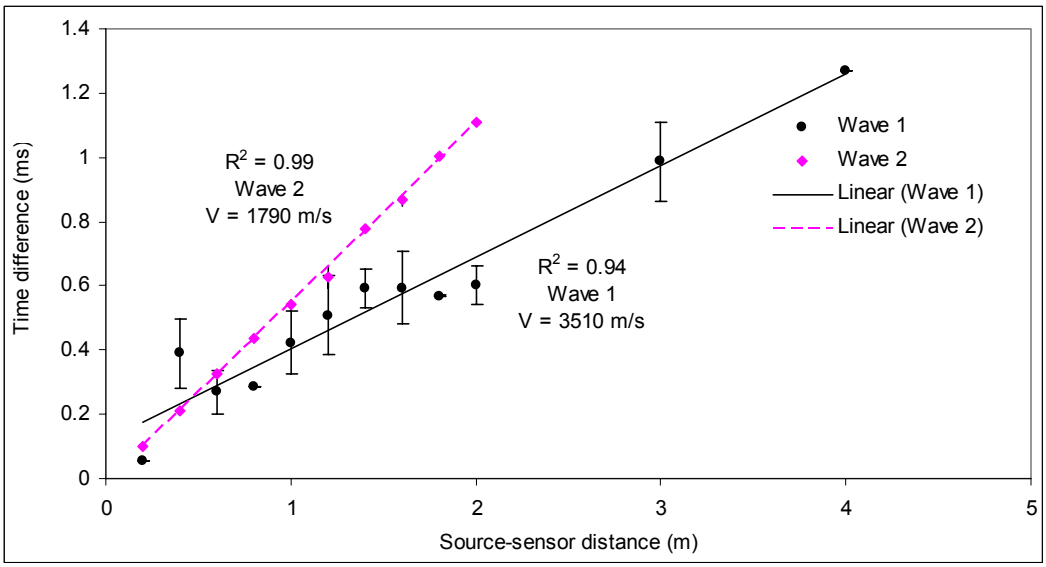

Figure 4.15: Arrival times calculated from WT magnitude for larger diameter pipe

4.4 Discussion

The various methods yield a variety of wave velocities as shown in Table 4.3. Taking the manual estimate as a benchmark (albeit on a different set of data), it is clear that the windowed energy technique gives the most reliable method of estimation of velocity for the two waves over longer lengths, despite the fact that the threshold technique is essentially an automatic version of the manual technique. This is probably because using a simple threshold requires a certain amount of judgement which is difficult to automate in terms of threshold level. The threshold technique is, however, the most effective at short distances, mainly because there is only a single part to the signal and there is no need to deal with multiple arrival times.

Although the wavelet decomposition combined with cross correlation improved on the conventional cross correlation technique, the wavelet transform approximation signal with cross-correlation produces relatively high estimates of velocity for each of the two components, whereas the simple cross-correlation produces relatively low estimates. Cross-correlation techniques are the only ones of those used here

which do not explicitly deal with arrival times and have, as an inherent assumption, that the entire group (filtered or not) is travelling with a given velocity, which is not true of dispersive waves.

The Gabor WT used here did not produce results consistent with the other methods, part of the difficulty being evident in Figure 4.13, where multiple peaks are present in the transform in both frequency bands. The choice of appropriate peaks in the Gabor WT is a matter which has been dealt with in detail by Ding *et al* [61] and this might explain the relative variations in "Wave 1" and "Wave 2" results (as measured by R^2) shown in Figure 4.14. The complexity of the waveform found on plain pipes appears to make it difficult to identify particular peaks, rendering this technique of limited use in such applications.

Source to sensor distance-diameter	**Long - large**		**Short - large**		**Long - small**	
Wave type	1	2	1	2	1	2
Manual estimation	5280	3810	4757	3091	5263	3407
WT & cross-correlation	5984	4649	6830	4394	6101	6402
Windowed energy	5263	3840	-	-	5219	3512
Cross-correlation	2930		3403		3020	
Threshold	5370	4520	5097	3576	5219	4022
Gabor WT	3510	1790	3150	1792	3227	2669

Table 4.3: Practically estimated wave speeds (ms-1)

A confirmatory experiment was carried out in order to assess the relative accuracy of the various methods in an actual source location exercise. The larger diameter pipe was set up with the sensors placed 4m apart and ten pencil leads broken at distances of 2, 3 and 3.6m from S1. In order to provide a final, longer source-sensor distance, S1 was then moved 1m to the end of the pipe so that the source was at 4.8m from S2. Each of the techniques was applied to locate the source and an averaged location calculated ($\bar{x}_m$). It should be noted that the threshold was set at 60 % of the maximum amplitude of the raw AE signal at 2m and was then

decreased to 20 %. The mean error with respect to the actual location x_{act} was then determined from:

$$\%Error = \frac{\Sigma \left| x_{act} - \bar{x}_m \right| \big/ x_{act}}{n} \times 100 \tag{4.1}$$

where n is the number of observations (in this case, four).

The results in Table 4.4 show all of the techniques except that based on the Gabor WT to give good location accuracy, the windowed energy technique giving the lowest error. Despite the fact that they use an averaged velocity, the cross-correlation techniques work quite well, the WT technique performing somewhat better than the conventional cross-correlation. It is expected that, as distances become even longer, the changed balance in amplitude between Waves 1 and 2 will make a straight cross-correlation less reliable. It is worth noting that the senses of the errors in each case are not random; rather, each technique either under- or over-estimates the source-sensor distance systematically. It is also evident that techniques which put greatest reliance on Wave 1 tend to over-estimate distance and vice versa, so the cause of this variation may be a small error in the Wave 1 and/or Wave 2 speeds.

Actual distance from sensor 2	**2 m**	**3 m**	**3.6 m**	**4.8 m**	**Error**
WT & cross-correlation	2	2.9	3.5	4.6	2.5%
Windowed energy	2.05	3.05	3.63	4.87	1.5%
Cross-correlation	2	2.89	3.44	4.45	4%
Threshold	2.04	3.3	3.79	4.81	4%
Gabor WT	1.68	3.9	3.63	4.04	16%

Table 4.4: Automatic techniques to estimate source sensor distance using Wave 1

When two separate arrival times and speeds can be identified, there is an option to use a single sensor as the sole, as mentioned in section 2.2.3.1, or supporting, means of source location. The arrival time difference Δt between a wave propagating at speed V_1 and one propagating at V_2 for a sensor at a distance x from

the source can be calculated using Equation 2.15. Using the windowed energy technique to estimate the time difference between Wave 1 and Wave 2 and using the speeds indicated in Table 4.3, the distances shown in Table 4.5 could be calculated.

Actual distance from sensor 2	**2 m**	**3 m**	**3.6 m**	**4.8 m**	**Error**
Windowed energy	2.6	3.12	3.69	4.85	9.4%

Table 4.5: Source distance from Sensor 2 estimated using windowed energy technique and time difference between Waves 1 and 2

Because the first wave to arrive is of relatively low amplitude, it is important to consider relative attenuation of the two components for application to long pipes. AE energy attenuation can be conveniently described by an exponential decay function using Equation 2.11 which can be rearranged [17, 20]:

$$\ln(E) = \ln E_0 - kx \tag{4.2}$$

Figure 4.16 shows the energy per unit time of raw AE for the time period between Wave 1 and Wave 2 arrivals, and, for the same length of time after the arrival of Wave 2, plotted on a semi-log basis as suggested by Equation 4.2. Although there is quite a lot of scatter (mostly at the shorter distances where it is difficult to separate the two components) it appears that Wave 1 is marginally less heavily attenuated with distance than is Wave 2, the two trend lines in Figure 4.15 crossing at about 70m. This observation gives some confidence that techniques which rely on the detection of Wave 1 should be operable even at long distances provided that there is a detectable signal at all.

The high-pass filter at 340 kHz, which is used for most of the techniques in this chapter, was essentially determined by inspection, and it is useful to consider how the threshold might be determined in cases where the structure and/or sensor are different, and which may lead to different frequency domain characteristics. Accordingly, for a subset of the data, a sliding high pass filter was applied, along with a fixed threshold of 0.03 of the maximum amplitude to determine the arrival times of the unfiltered (Wave 1) and filtered (Wave 2) components as a function of

cut-off frequency. The results, shown as arrival time difference (Wave 2 – Wave 1) are shown in Figure 4.17 for source-sensor distances of 0.2m, 2m and 4m, and it can be seen that there is a region of high-pass cut-off between 300-350 kHz at which a stable separation of arrival time is achieved. Such a technique could be easily automated in order to cope with different sensors and/or structures and/or dispersion at longer distances.

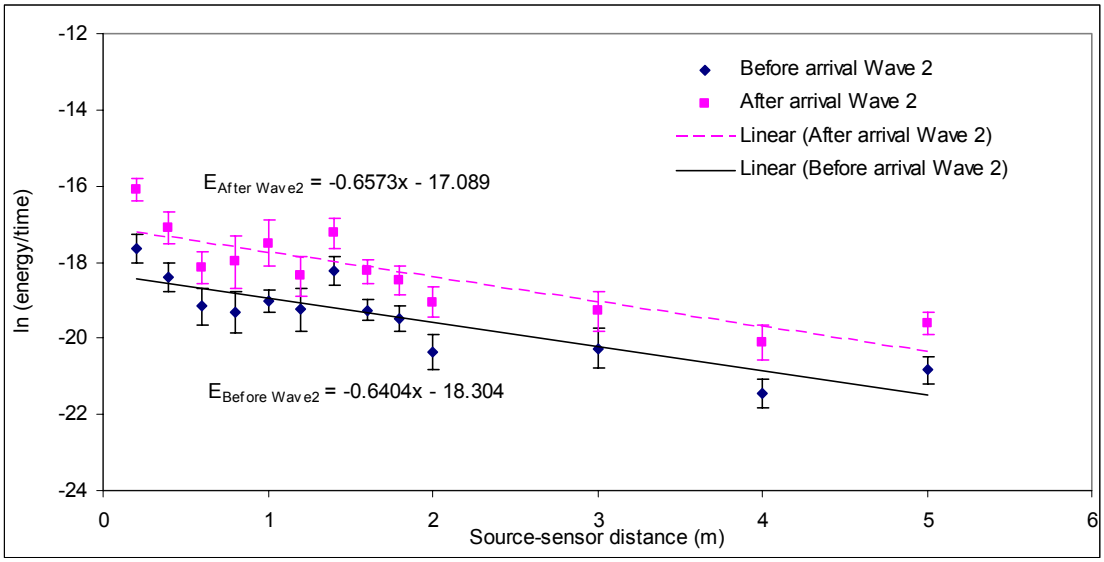

Figure 4.16: Energy of raw AE for time period between Wave 1 and Wave 2 before and after arrival of Wave 2 for large diameter pipe

Finally, it has been assumed inherently throughout the source location study that waves are travelling axially along the pipe and that circumferential distances are negligible with respect to axial distances. The work of Barat *et al* [47] can be used to assess the error involved in this assumption using their formula for the distance between two points θ_1, z_1 and θ_2, z_2 on the surface of a cylinder (Figure 4.18):

$$L = \sqrt{R^2(\theta_1 - \theta_2)^2 + (z_1 - z_2)^2} \tag{4.3}$$

The effect of the ratio of axial separation to radius of the cylinder $K=z_1-z_2/R$ can be examined, taking $\theta_1 = 0$:

$$\frac{L}{R} = \sqrt{\theta_2^2 + K^2} \tag{4.4}$$

which is plotted in Figure 4.19, for values of θ up to π radians for values of K from 1 to 10. The relative difference of the true and axial separations can be seen by the values at θ_2=0 and θ_2= π for each value of K. As can be seen, the error is about 5% at K=*10*, 10% at K=7 and 50% at K= 3. Therefore, in long pipes (L/R>10) the maximum error is about the same as repeated in Table 4.4. For the large diameter pipe the error for source-sensor distances of 20cm and 2m are about 80% and 0.05% respectively, while, for the small diameter pipe, it is about 7% and 0.0005% respectively.

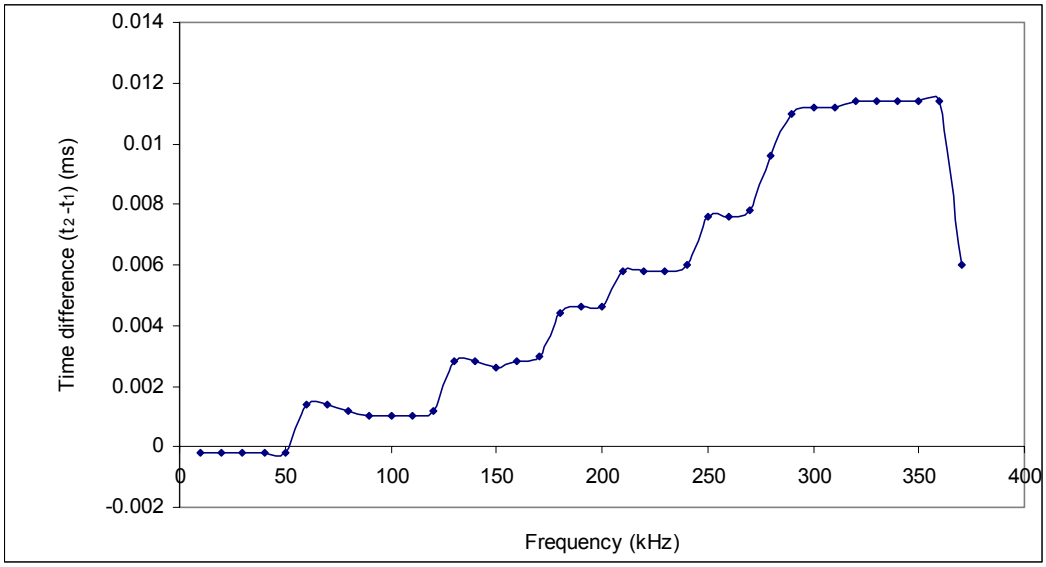

a) 0.2m

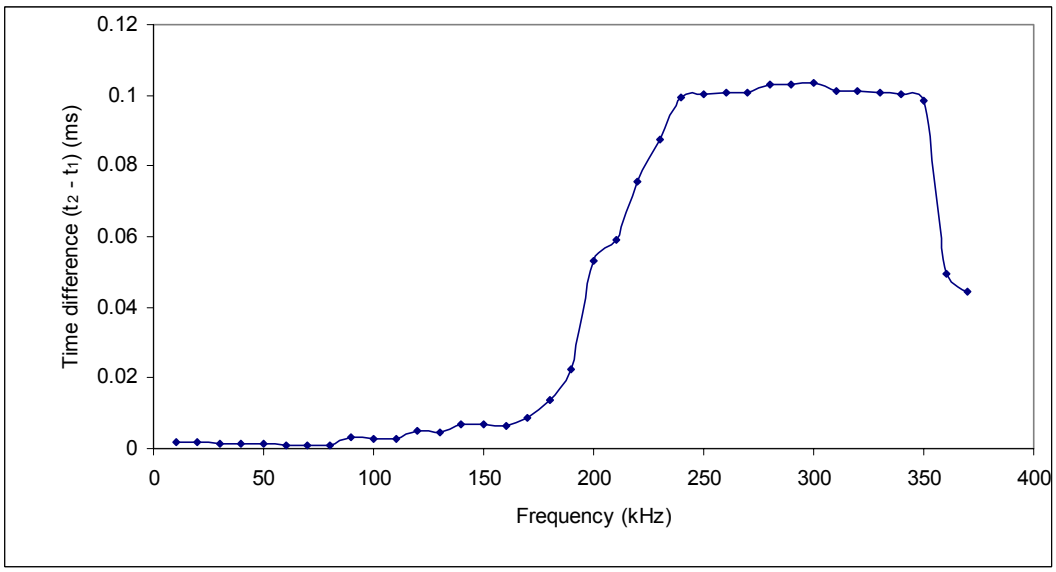

b) 2m

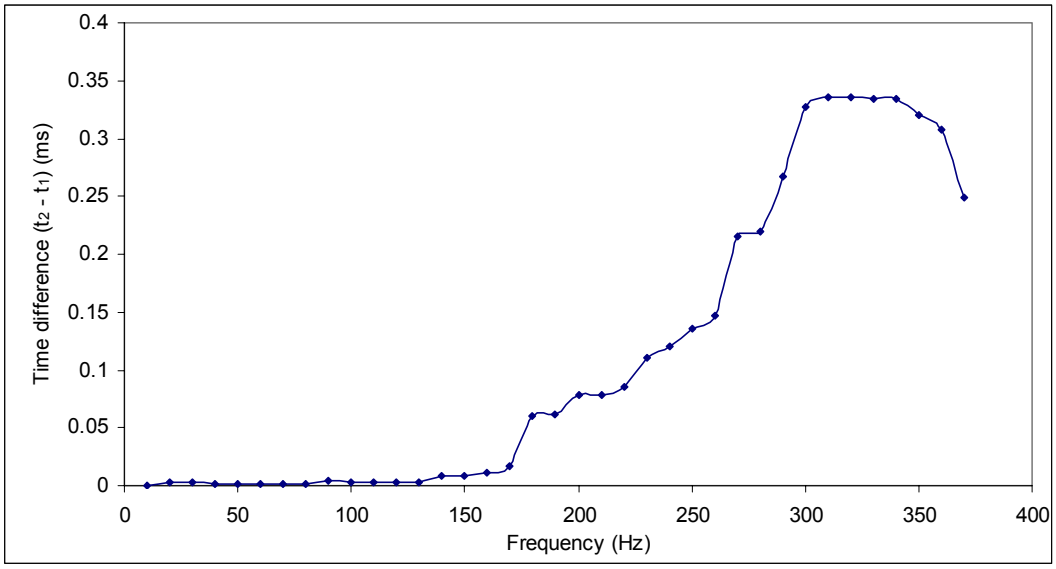

d) 4m

Figure 4.17: Arrival time estimation between Wave 1 and Wave 2 for large diameter pipe using sliding filter

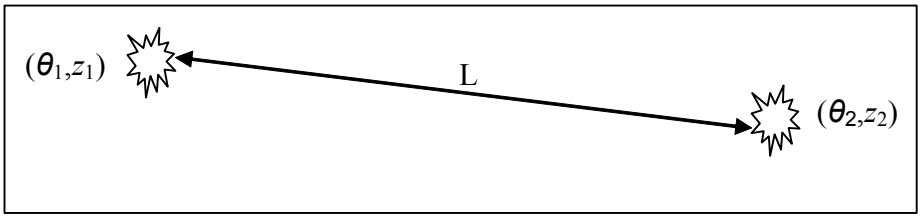

Figure 4.18: Axial and surface separations of two points on a cylindrical surface

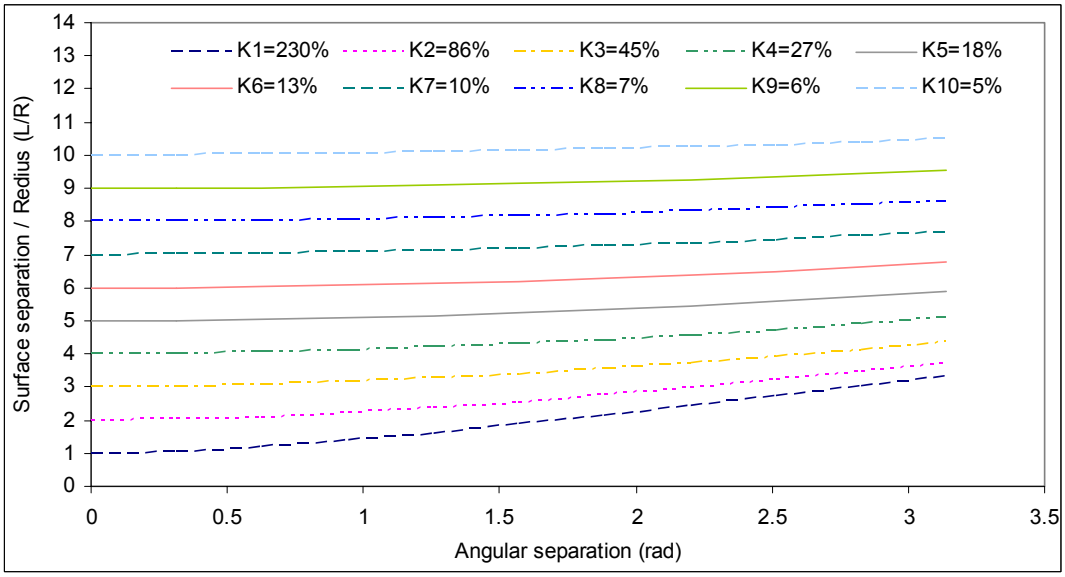

Figure 4.19: Surface and axial separations on a cylindrical surface

4.5 Summary

It has been seen that simple impulsive sources produce a signal in long steel pipes which can conveniently be split into a slow and a fast component, and that it is difficult to distinguish between these at short source-sensor distances. The implication is that simple techniques are quite adequate for source location in pipes where the sensor is close to the source, but that independent measures can be obtained at longer distances. Also, it has been shown that two-dimensional source locations algorithms should be used when source-sensor distance is less than about five times the pipe diameter.

The windowed energy technique relies on changes in the balance of high and low frequency components of the signal as a function of time to determine arrival times and, in a separate source location exercise, was shown to be the most accurate of the techniques investigated. The next most successful technique also relies upon the frequency balance, and utilises a very sharp filter to remove Wave 1 so that arrival times can be estimated for both waves based on the unfiltered and filtered signals.

Chapter 5: Effect of Internal and External Environment

5.1 Introduction

This chapter describes and discusses the results of the various tests using simulated sources on pipes with different internal and external media. The focus here is on AE wave attenuation and time-of-flight along the pipe in different environmental conditions. The analysis is based mostly on relatively simple statistical signal processing techniques, and the signals are first reviewed in the time-, frequency- and time-frequency domains to establish features for detailed analysis.

The main objective of the analysis was to understand the effects of internal and external environment on propagation of AE to supplement that developed in the previous chapter. As for Chapter 4, all experiments used a simulated pencil lead source, and raw AE signals were acquired at a sampling rate of 5 MHz for a fixed period of 10 ms (50000 points). All of the results recorded here relate to the smaller diameter pipe.

5.2 General Observations

In this section, a brief overview of the data is given in order to establish those features of the signals which can be used for later analysis.

5.2.1 Time Domain

Figure 5.1 shows typical time evolutions of the raw AE signals for the four interface conditions captured at S2 for one position relatively close to the sensor and one relatively far from the sensor. As can be seen, for the long source-sensor distance for each condition, a faster-moving component again appears in the signal (Wave 1), and this component is of higher relative amplitude (compared with the main wave) the fewer air interfaces there are on the pipe. Also, for signals recorded

both close to and far from the source, the signal amplitude in the main wave is generally of lower amplitude and is more quickly damped, the fewer air interfaces there are. These observations are consistent with energy being lost by transmission into the water and wet sand more easily than to air, which is to be expected because of the closer impedance matching of steel with water. The main, slower component (Wave 2) seems to be more affected by this than the initial, faster component as shown in Figures 5.2 and 5.3.

5.2.2 Frequency Domain

Figures 5.4, 5.5 and 5.6 show typical frequency domain plots for relatively short and relatively long distances from the source for the various internal and external environments. As before, it is clear that, at relatively long distances (5m), the energy is carried mostly in two fairly narrow bands centred on frequencies of around 170 KHz and 340 KHz, although, at short distances, quite a number of spectral peaks are evident.

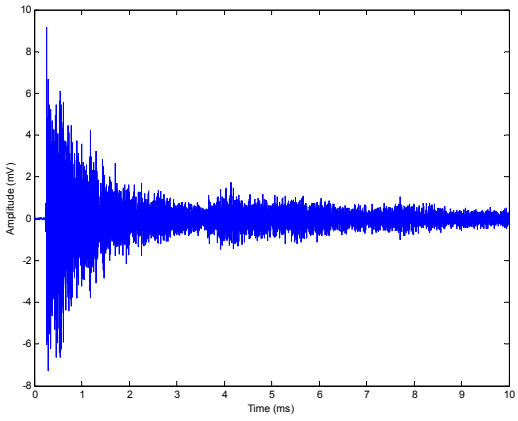

a: Air-air at 0.2 m

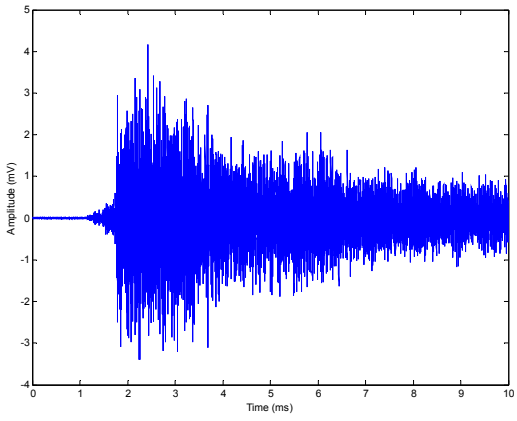

b: Air-air at 5 m

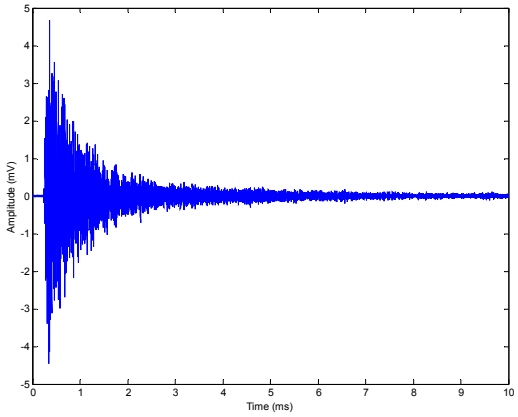

c: Water-air at 0.2 m

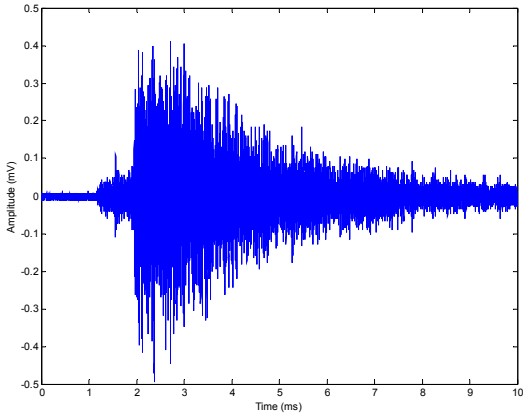

d: Water-air at 5m

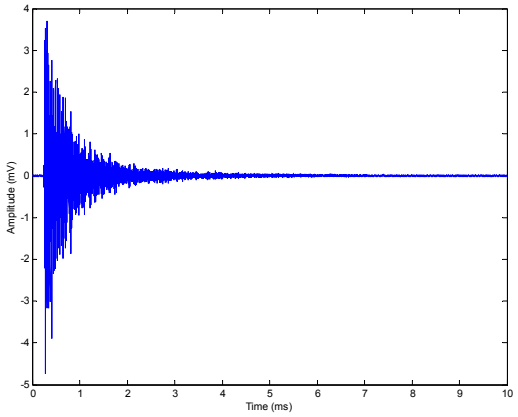

e: Air-wet fine sand (20% water) at 0.2m

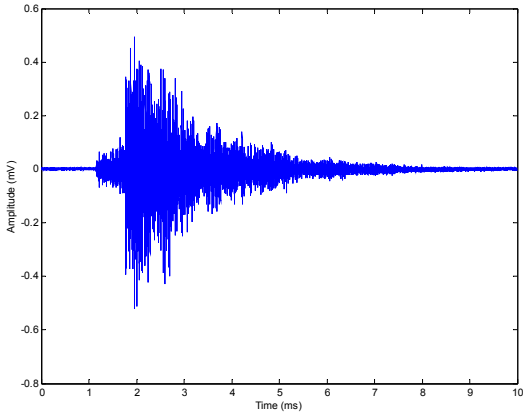

f: Air-wet fine sand (20% water) at 5m

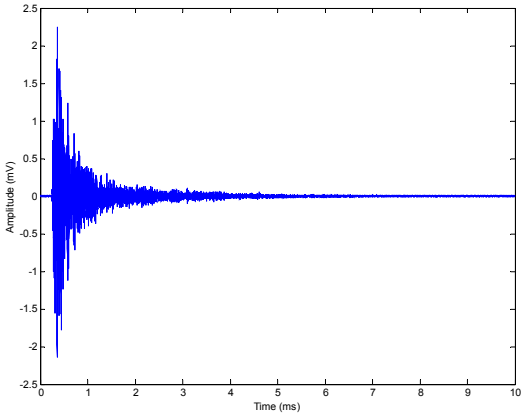

g: Water-wet fine sand (20% water) at 0.2m

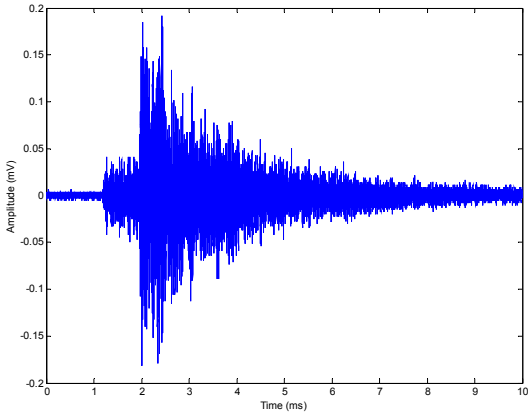

h: Water-wet fine sand (20% water) at 5m

Figure 5.1: Typical AE time series at S2 for various internal-external conditions recorded at 0.2m and 5m from the simulated source

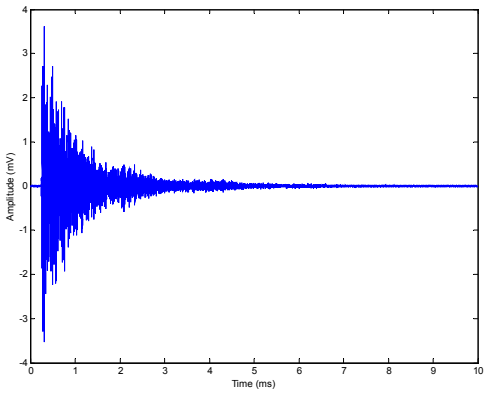

a: Dry sand at 0.2m

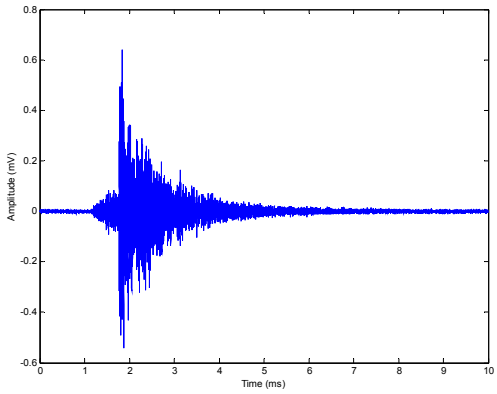

b: Dry sand at 5m

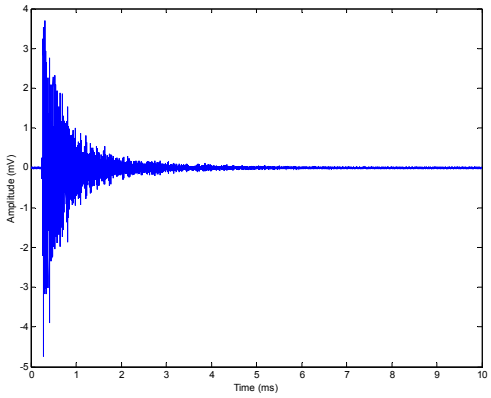

c: Wet sand (20% water) at 0.2m

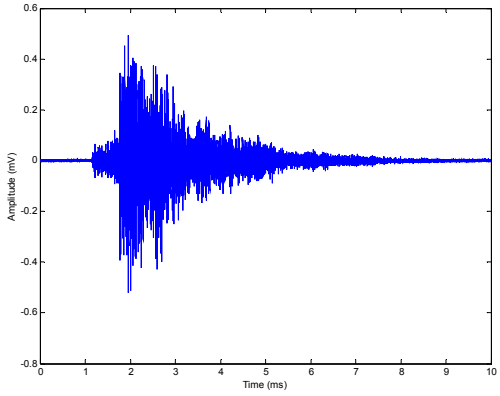

d: Wet sand (20% water) at 5m

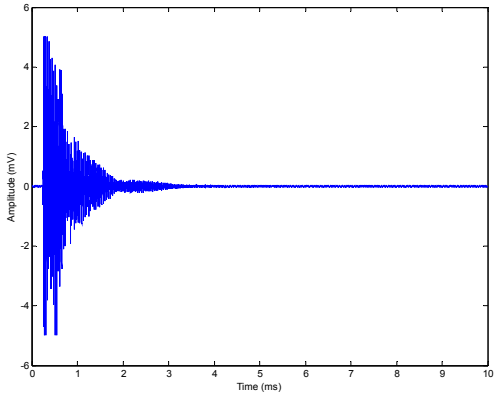

e: Soaked sand (27% water) at 0.2m

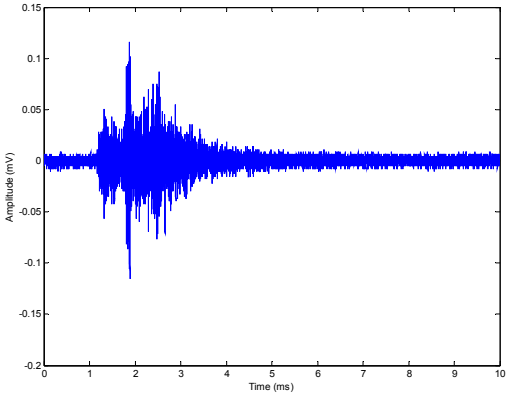

f: Soaked sand (27% water) at 5m

Figure 5.2: Typical AE time series at S2 for various conditions of external small size sand and internal air recorded at 0.2m and 5m from the simulated source

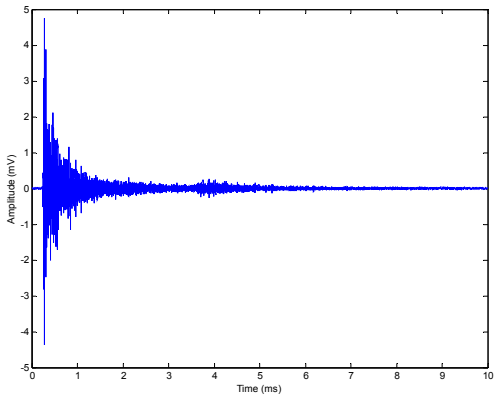

a: Dry sand at 0.2m

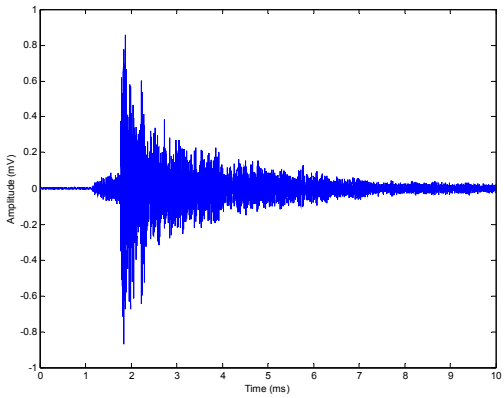

b: Dry sand at 5m

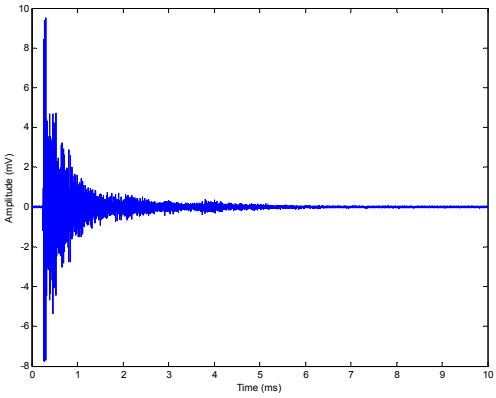

c: Wet sand (13% water) at 0.2m

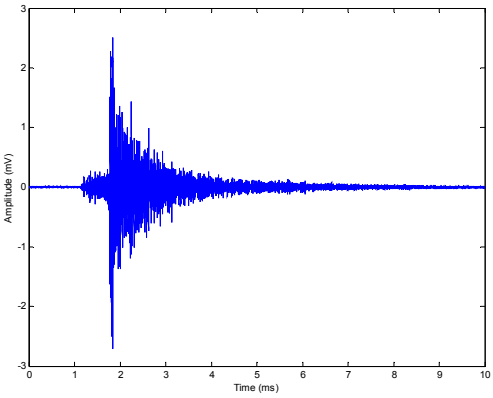

d: Wet sand (13% water) at 5m

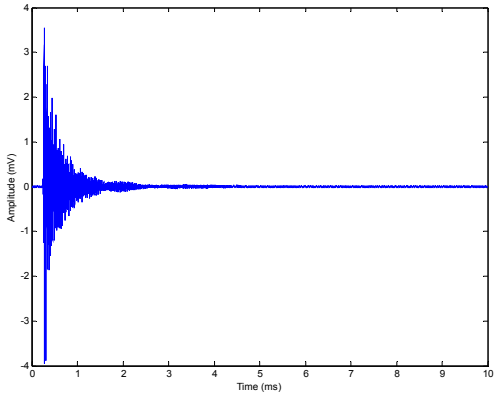

e: Soaked sand (20% water) at 0.2m

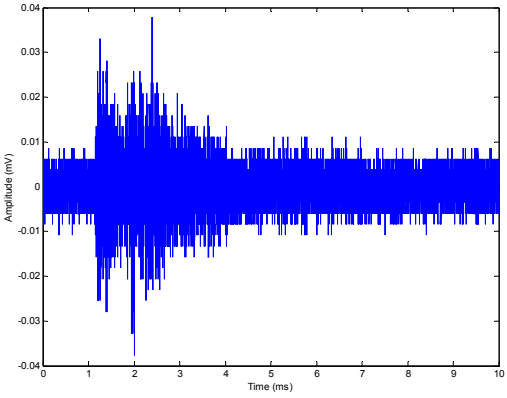

f: Soaked sand (20% water) at 5m

Figure 5.3: Typical AE time series at S2 for various conditions of external coarse sand and internal air recorded at 0.2m and 5m from the simulated source

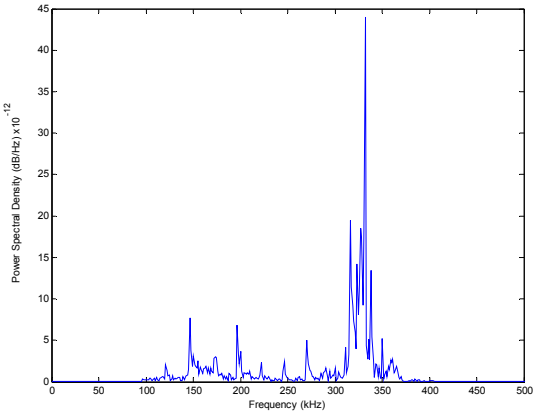

a: Air-air at 0.2 m

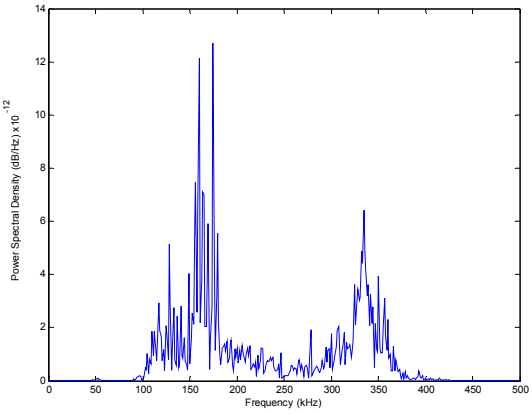

b: Air- air at 5 m

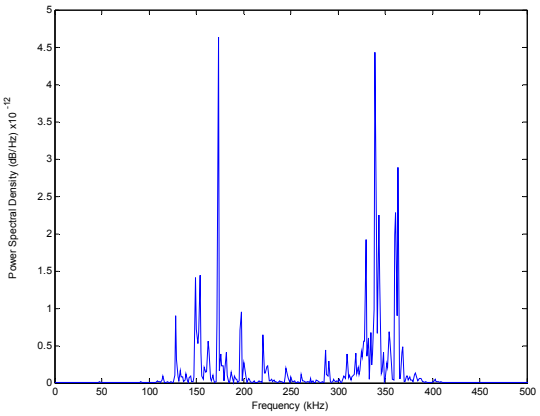

c: Water-air at 0.2 m

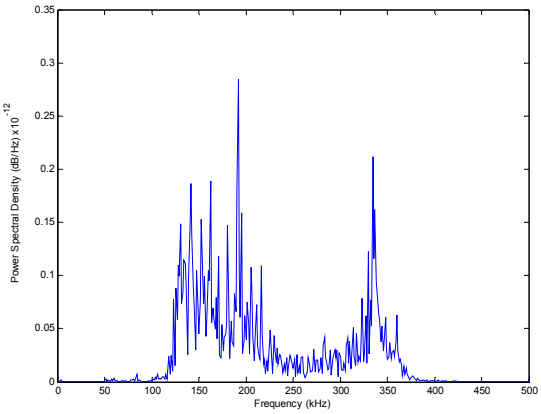

d: Water-air at 5 m

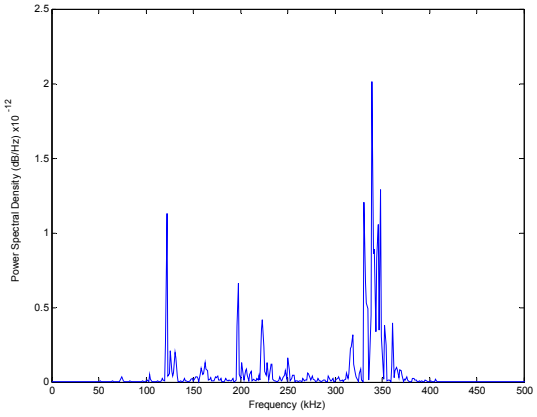

e: Air-wet fine sand (20% water) at 0.2m

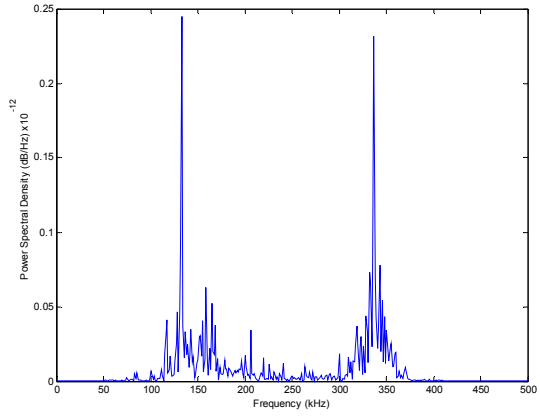

f: Air-wet fine sand (20% water) at 5m

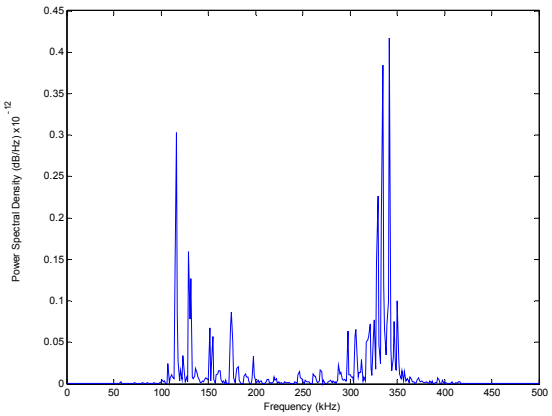

g: Water-wet fine sand (20% water) at 0.2m

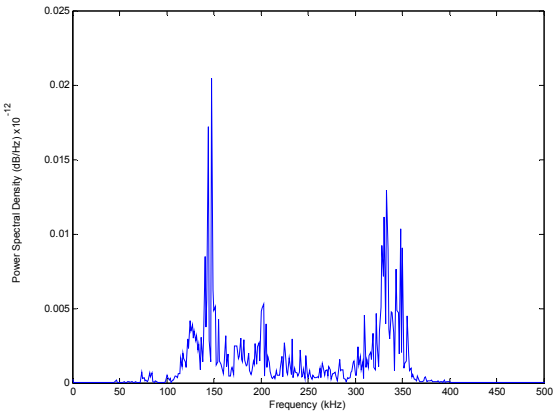

h: Water-wet fine sand (20% water) at 5m

Figure 5.4: Typical AE frequency spectra for various internal-external conditions recorded at 0.2m and 5m from the simulated source

5.2.3 Time-Frequency

Figure 5.7 shows how the frequency content of a typical signal varies with time, the air-air configuration being the benchmark for other configurations, where the amplitude in the frequency domain at each time step has been normalised to the same total energy in order to counteract the effect of reducing total energy with time. These figures show similar features to Figure 4.3 (for large diameter pipe) in that there is a difference in spectral content between the earlier part of each signal and the later part. Also, there appears to be a general shift from higher frequencies to lower frequencies as source-sensor distance increases.

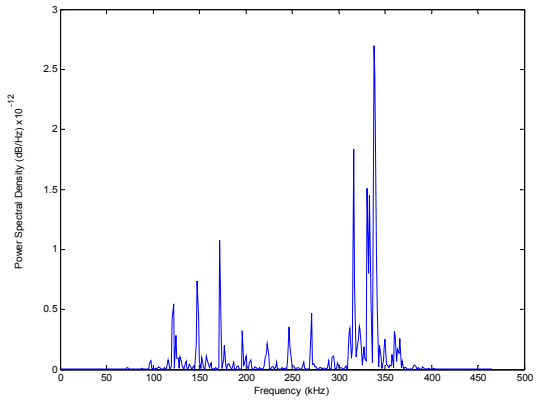

a: Dry sand at 0.2

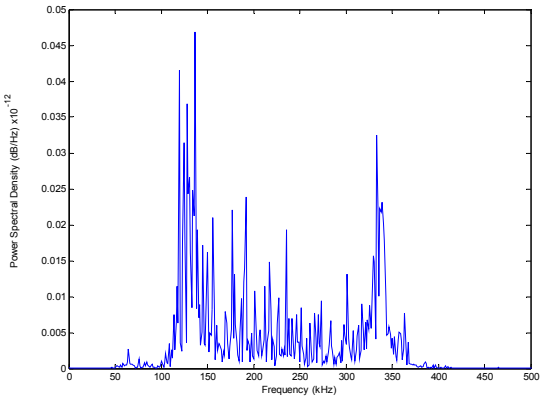

b: Dry sand at 5m

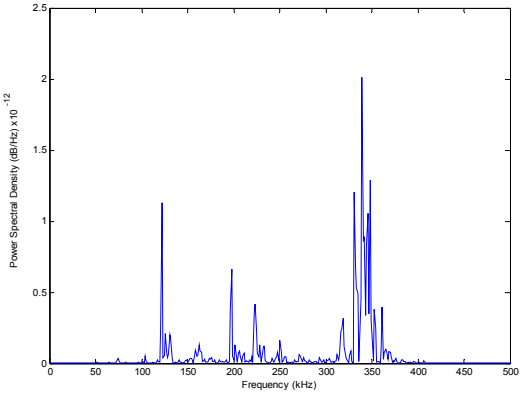

c: Wet sand (20% water) at 0.2m

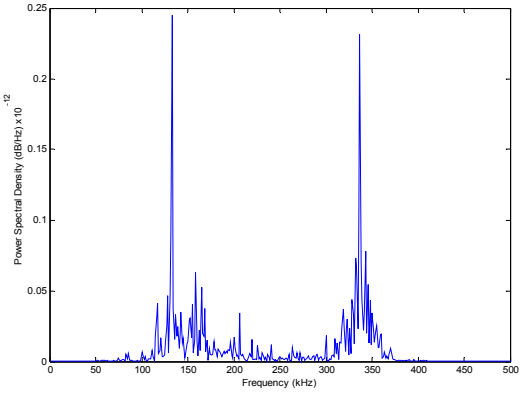

d: Wet sand (20% water) at 5m

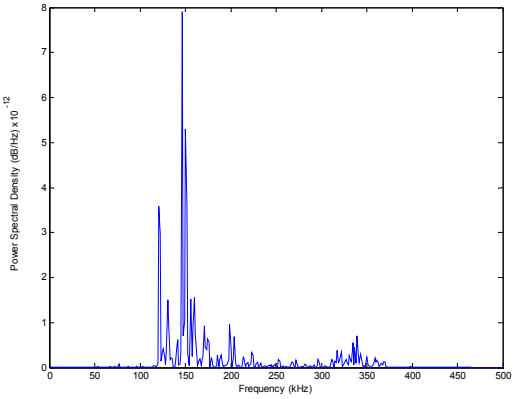

e: Soaked sand (27% water) at 0.2m

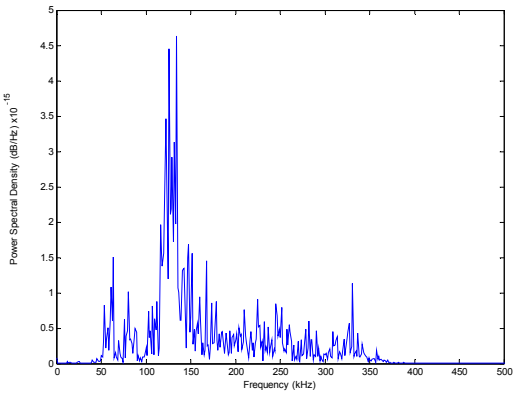

f: Soaked sand (27% water) at 5m

Figure 5.5: Typical AE frequency spectra for various conditions of external fine sand and internal air recorded at 0.2m and 5m from the simulated source

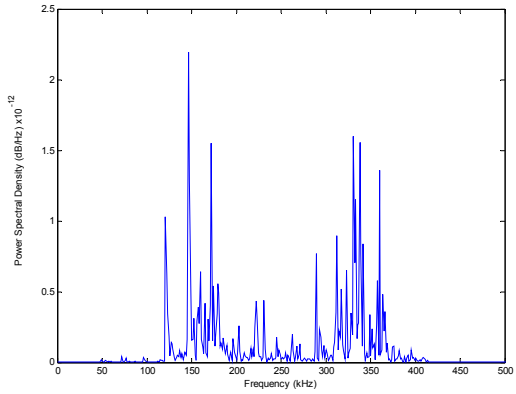

a: Dry sand at 0.2

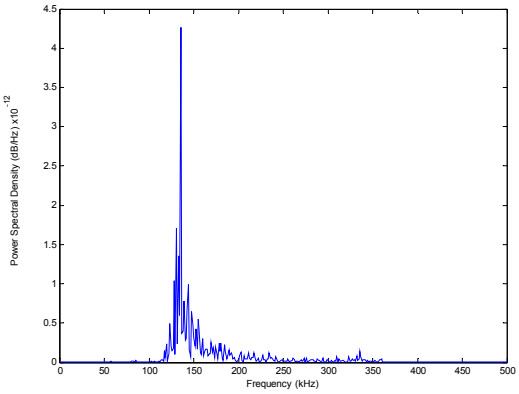

b: Dry sand at 5m

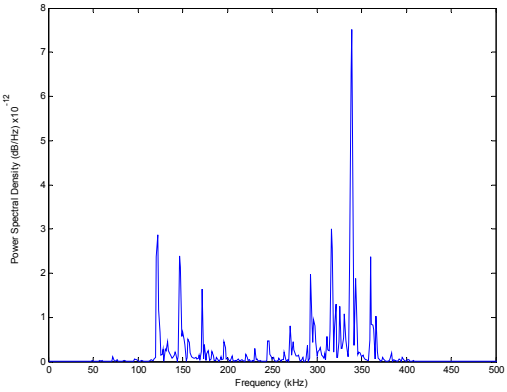

c: Wet sand (13% water) at 0.2m

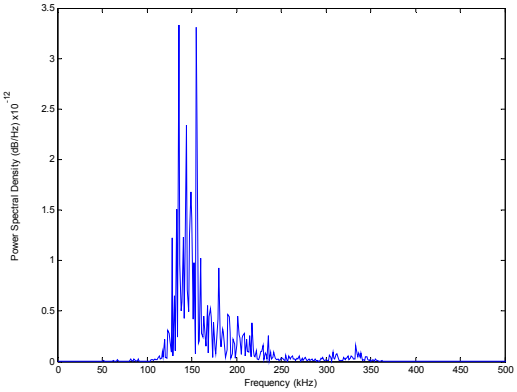

d: Wet sand (13% water) at 5m

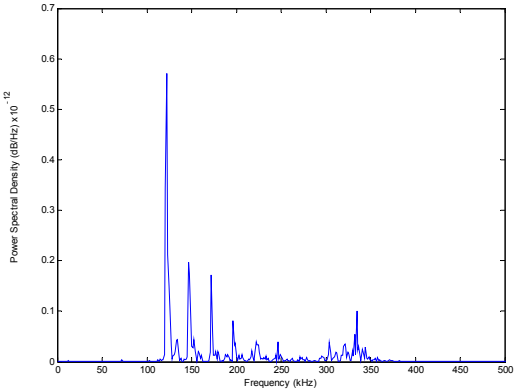

e: Soaked sand (20% water) at 0.2m

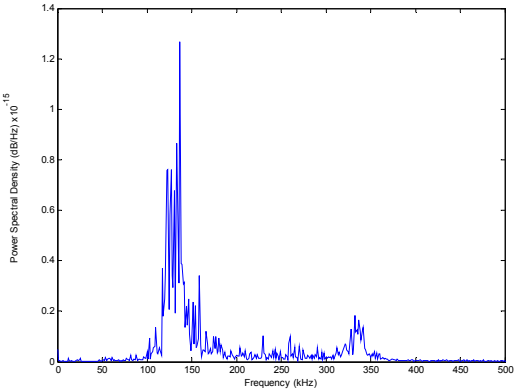

f: Soaked sand (20% water) at 5m

Figure 5.6: Typical AE frequency spectra for various conditions of external coarse sand and internal air recorded at 0.2m and 5m from the simulated source

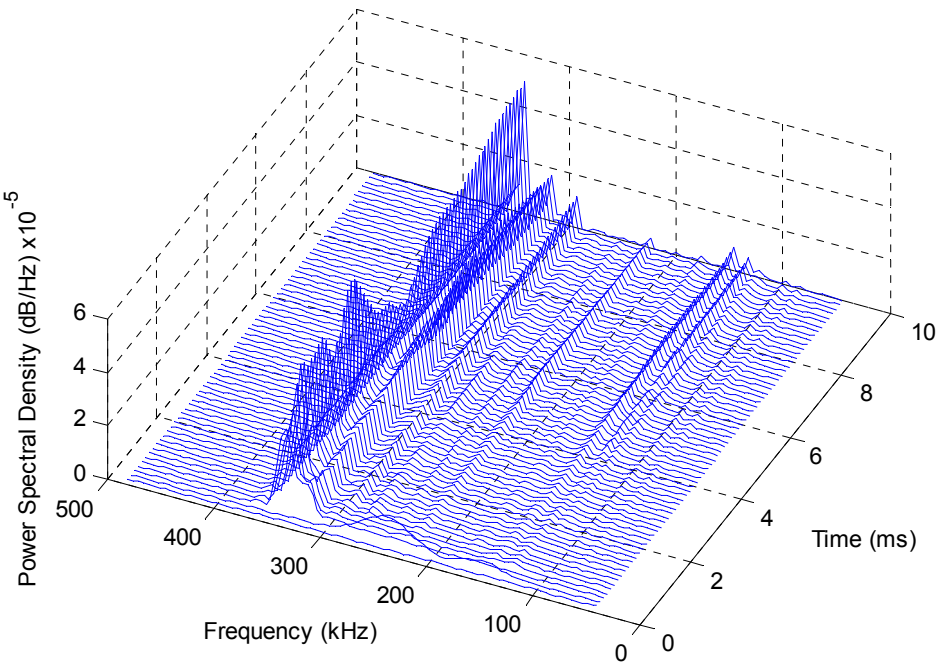
Power Spectral Density (dB/Hz) x10^-5
6
4
2
0
500
400
300
200
100
0
Frequency (kHz)
0
2
4
6
8
10
Time (ms)

a: 0.2m

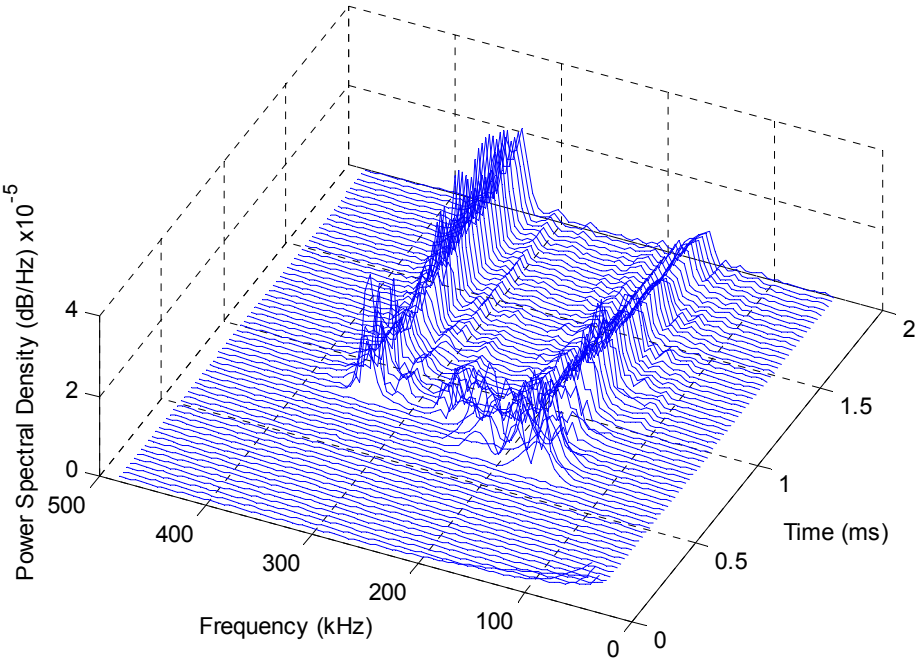
Power Spectral Density (dB/Hz) x10^-5
4
2
0
500
400
300
200
100
0
Frequency (kHz)
0
0.5
1
1.5
2
Time (ms)

b : 2m

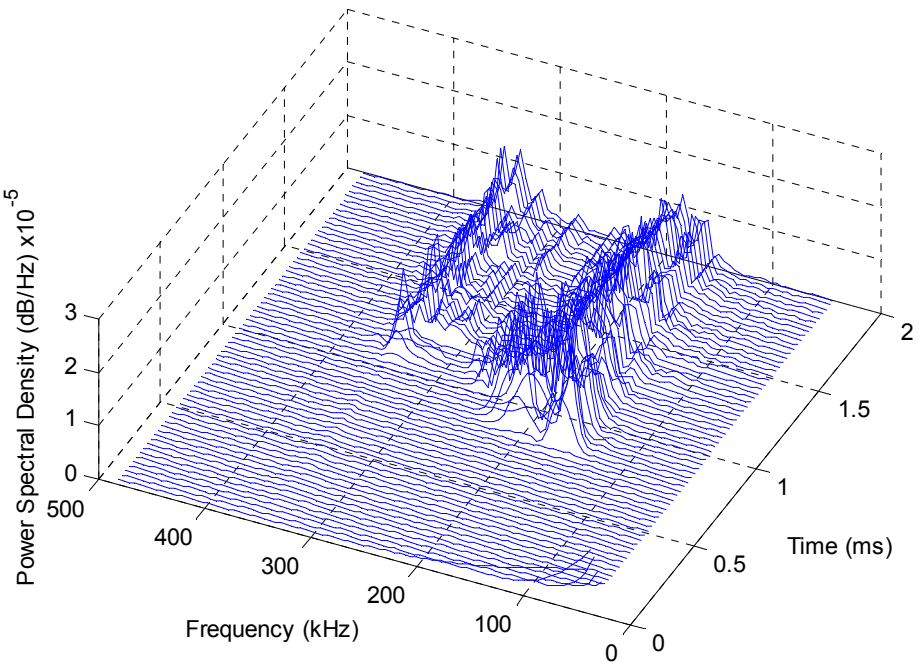

c: 3m

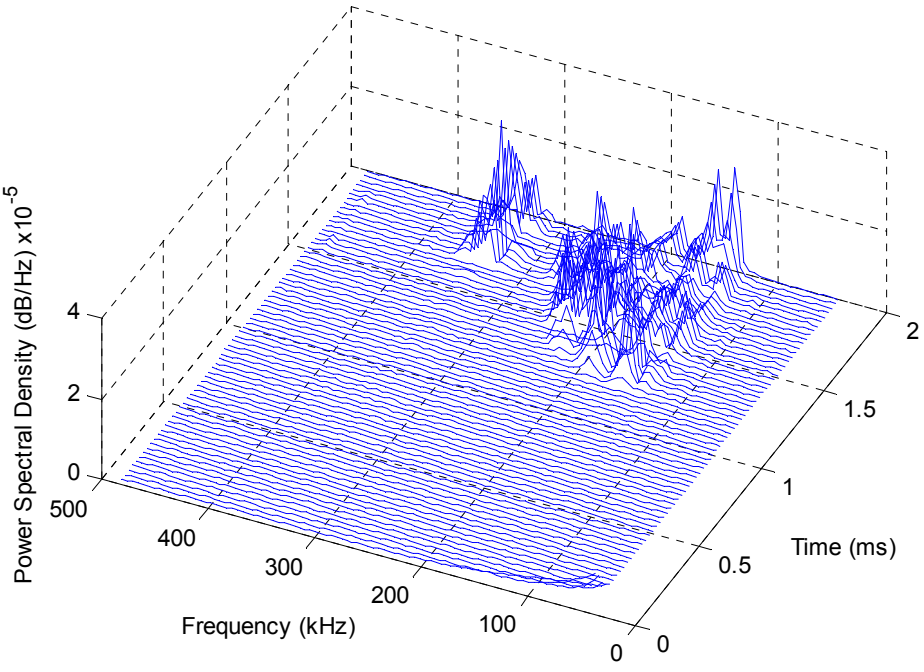

d: 5m

Figure 5.7: Normalized frequency-time plot for air-air condition at various distances

5.3 Signal Analysis: Effects of Internal and External Interfaces

From the preceding section, it can be seen that the AE signal is affected by both the internal and external environments, observable in the time domain and the frequency domain.

In Chapter 4, on similar pipe with air as the internal and surrounding medium, it was shown that, at longer distances, the signals can be split into a relatively low frequency, high speed wave (Wave 1) and a relatively high frequency, low speed wave (Wave 2), and it was pointed out that some authors have suggested that Wave 1 is an extensional wave and Wave 2 is a flexural wave. The waves were separated using a sharp filter at 350 kHz in order to improve the accuracy of arrival time estimation. In this chapter, it is also of interest to separate the components this time with a view to examining the relative attenuation of each in different internal or external environments.

5.3.1 Time Domain Analysis

Figure 5.8 illustrates a signal thresholding technique applied to the square root of the square of the raw signal in order to split the components in the time domain. To identify the start and end of the two waves in the time domain, the first crossing, corresponding to the start of Wave 1 (t_1) was set at 200% of the maximum noise amplitude (established over the first 200μs of the signal), and the start of Wave 2 (t_2) at the average between the maximum amplitude and the amplitude at t_1. The signal was terminated in the time domain at t_3 when it crossed a threshold in the downward direction set at the maximum amplitude for the last 200μS of the signal. Although this technique is far from rigorous, it does provide a means of dividing up the signals into objectively determined time windows.

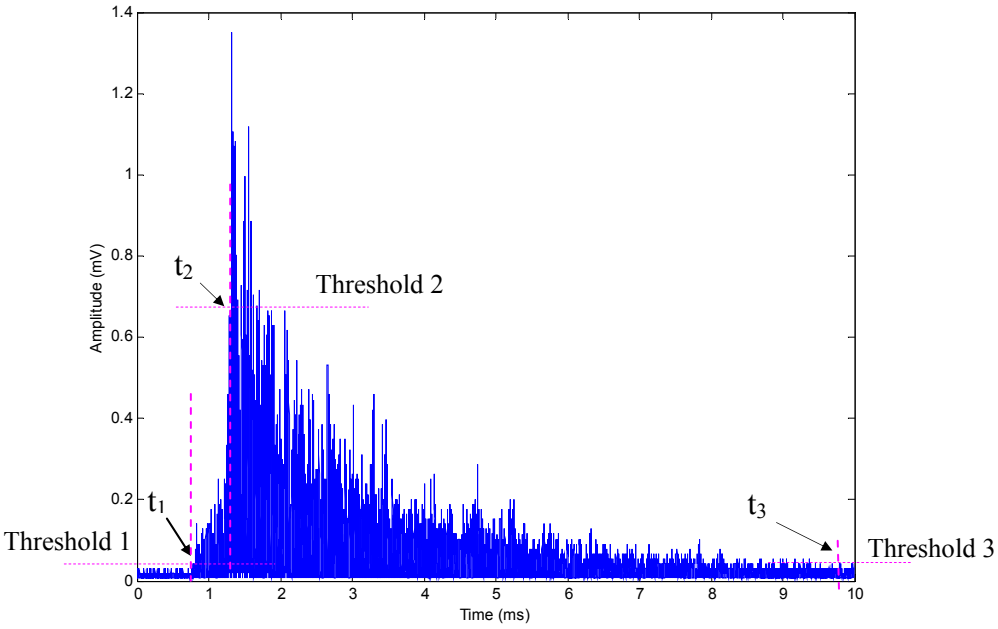

Figure 5.8: Square root of squared raw signal with the thresholds used to identify the arrival times for Wave 1 and 2 and the end of the signal

Figures 5.9 – 5.11 show the relative durations of Wave 1 and Wave 2 according to the foregoing criteria. Clearly, the duration of Wave 1 increases approximately linearly with source-sensor distance and the slope decreases a little with amount of water in the environment. Supposing that Waves 1 and 2 have distinct velocities:

$$t_2 - t_1 = x\left(\frac{1}{V_2} - \frac{1}{V_1}\right) \tag{5.1}$$

and it can be seen (Figure 5.9) that V_2 or V_1, or both, change with the internal and external environment. The degree of wetness of the sand does not appear to change V_1 and V_2, except possibly in the case of soaked sand where the behaviour becomes erratic (Figures 5.10a and 5.11a). For all conditions the duration of Wave 2 falls off gently with source-sensor distance and this is expected to be due largely to attenuation.

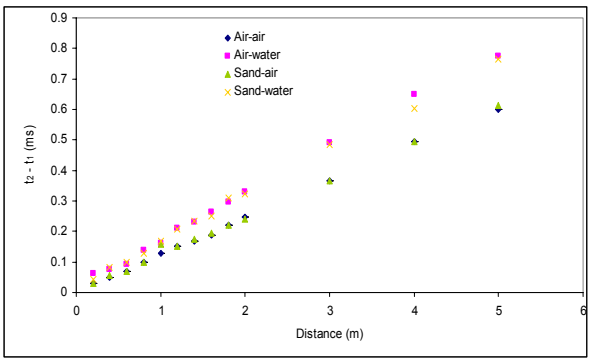

a: Wave 1

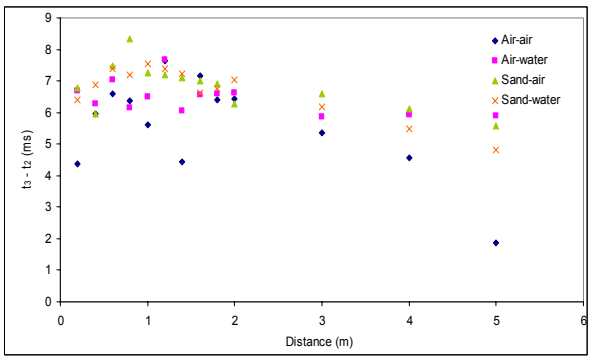

b: Wave 2

Figure 5.9: Durations of Wave 1 and Wave 2 in the time domain for different external (air and wet sand) and internal environments (air and water)

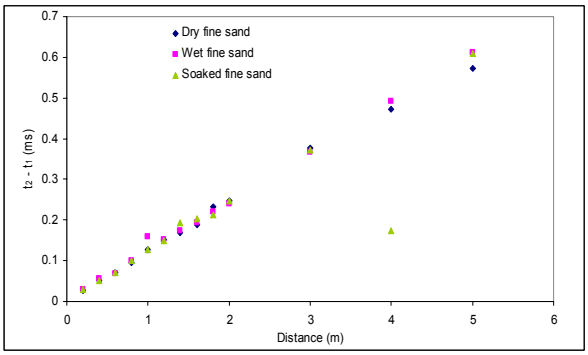

a: Wave 1

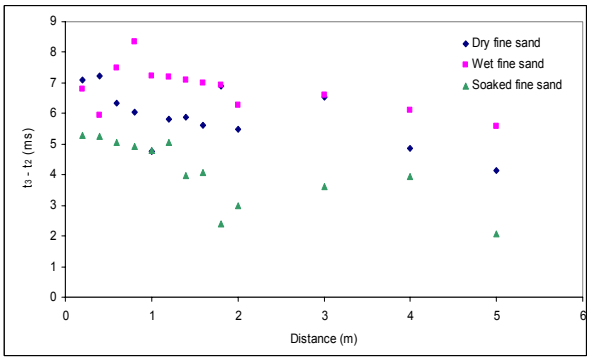

b: Wave 2

Figure 5.10: Durations of Wave 1 and Wave 2 in the time domain for different conditions of external fine sand and internal air

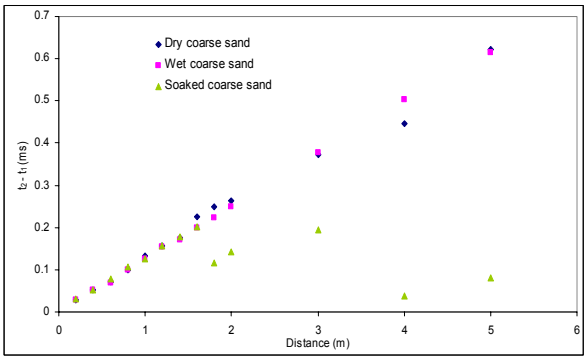

a: Wave 1

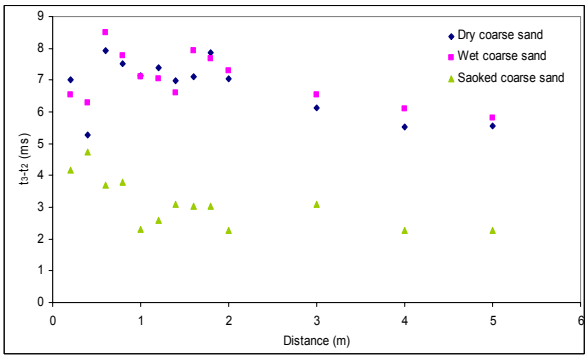

b: Wave 2

Figure 5.11: Durations of Wave 1 and Wave 2 length in the time domain for different conditions external coarse sand and internal air

5.3.2 Frequency Analysis

In section 5.2.2 two frequency bands were identified, and, in order to carry out some analysis, two bands between 100 and 200 kHz and between 300 and 350 kHz were chosen. Figure 5.12 summarises the frequency content in the two bands for relatively short and long source- sensor distances. These figures show significant differences in relative attenuation of high and low frequency components between the different environments. For example, when the pipe has air inside and outside (Figures 5.12 (a) and (b)), there appears to be a reverberant effect with a return time of around 4ms, corresponding approximately to the length of the pipe. Also, the higher frequency component appears to be more heavily attenuated than the lower. The introduction of water to the internal or external environment reduces considerably the low frequency component of Wave 2 even at relatively short distances. In contrast, the low frequency component, which makes up most of Wave 1, seems to be rather less heavily attenuated the more water there is in the environment.

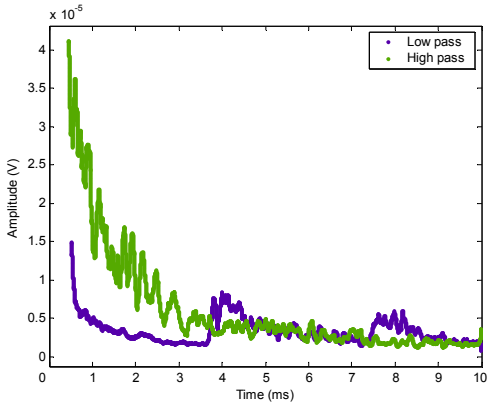

a: Air-air at 0.2m

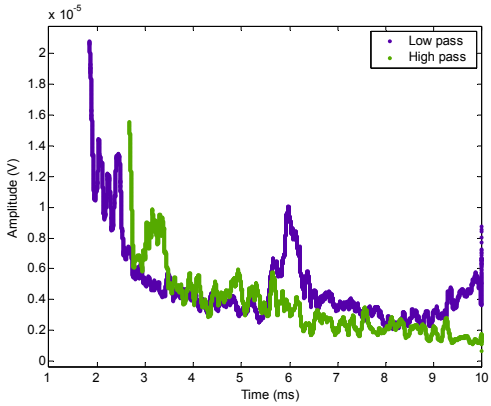

b: Air-air at 5m

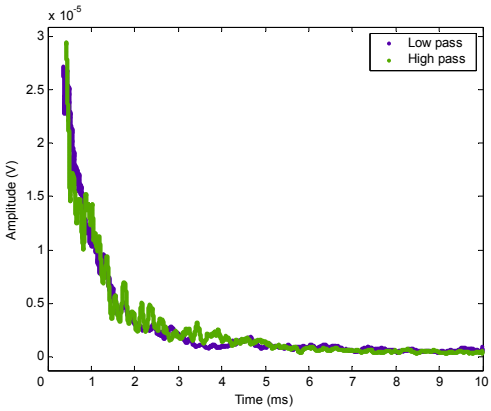

c: Water-air at 0.2m

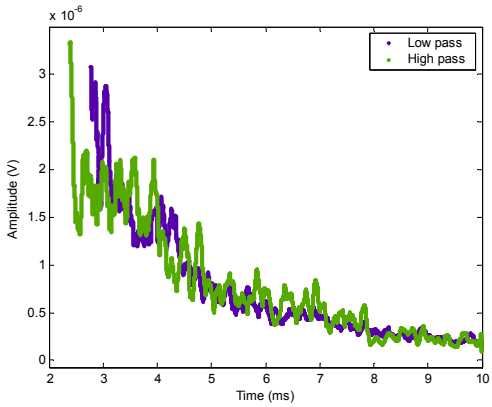

d: Water-air at 5m

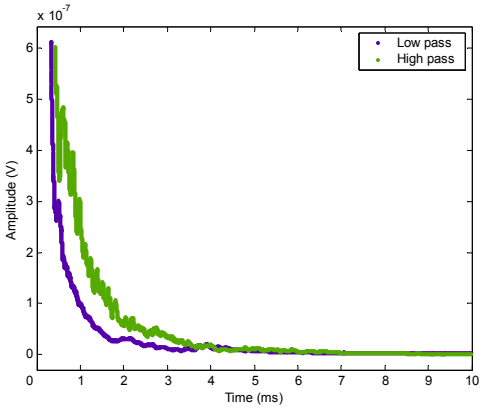

e: Air-wet fine sand (20% water) at 0.2m

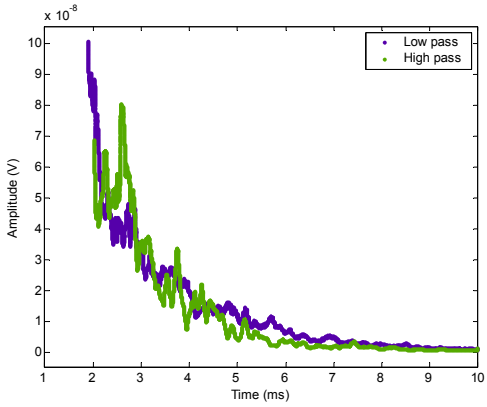

f: Air-wet fine sand (20% water)at 5m

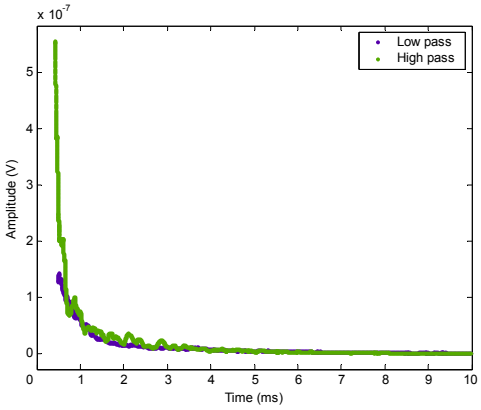

g: Water-wet fine sand (20% water) at 0.2m

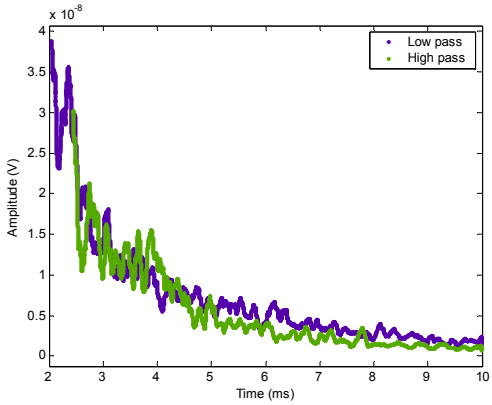

h: Water-wet fine sand (20% water) at 5m

Figure 5.12: Amplitude attenuation for internal-external conditions recorded at 0.2m and 5m from S2, high band (300-350 kHz) and low band (100-200 kHz)

5.3.3 Energy Analysis

The variation in the energy of the signal with distance from the source can be encapsulated in a simple model which takes account of external and internal conditions, where the energy from the source can be seen as being propagated in two types of wave, one travelling over the surface carrying energy E_2, and another travelling through the bulk carrying energy E_1, as shown in Figure 5.13. Without going into the detail of possible surface or bulk modes, it might be expected that the attenuation factor, k, for the surface component would depend on the external environment, whereas that for the bulk component should be independent of environment, the interfacial attenuation depending upon the number of reflections at internal and external surfaces which, in turn, would increase in an approximately

linear fashion with source-sensor distance. Thus, the attenuation Equation (2.11) might be modified to the following:

$$E(x) = E_1(x) + E_2(x) \tag{5.2}$$

This can be expressed as

$$E(x) = [m \cdot n]^{ax} E_{0,1} e^{-k_1 x} + E_{0,2} e^{-k_2 x} \tag{5.3}$$

where k_2, m and n are dependent upon the impedance matching between steel and the external (k_2 and m) and internal (n) environments, and k_1, a, $E_{0,1}$ and $E_{0,2}$ would not be expected to change for a given pipe configuration and source type. Since we are dealing with (at least) two different types of wave, we might expect these waves to have different frequency profiles, and to have different group velocities. Therefore filtering and time-windowing may also need to be used in determining the parameters above.

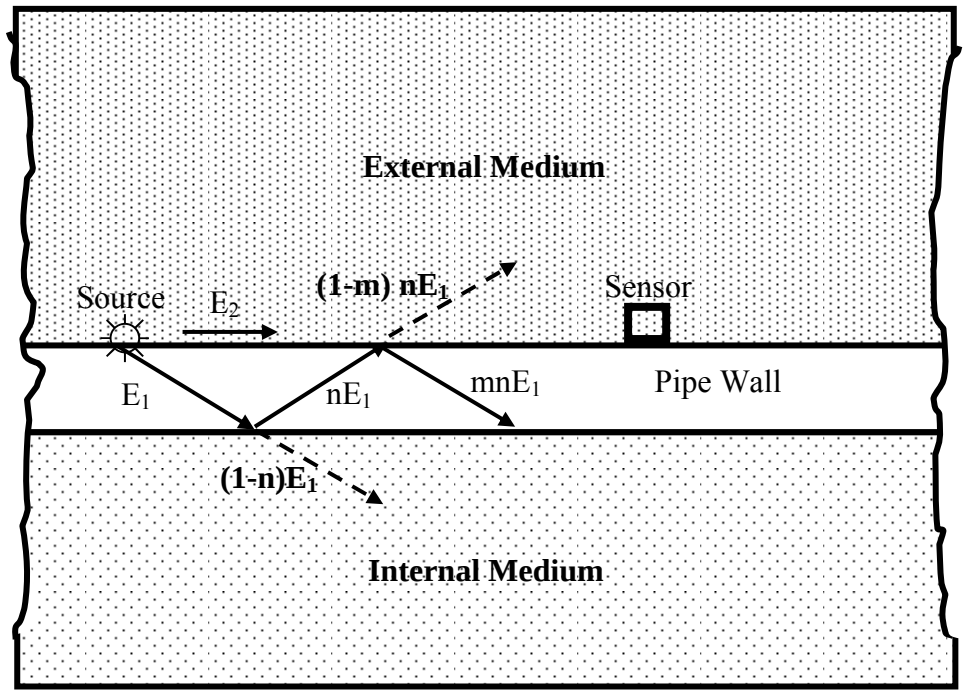

Figure 5.13: Schematic of propagation model

Figures 5.14 - 5.16 show the total energy for all environment conditions, the air-air case showing the least attenuation and water in either the internal or external

environment increasing it. The attenuation was also calculated separately for each of the frequency bands (100-200 kHz and 300-350 kHz) and the results are shown in Tables 5.1 to 5.3. These tables show attenuation to increase with the amount of water in the environment, and for the soaked sand to be a little less effective than water inside, the fine sand being more effective than the coarse sand for a given degree of wetness. Also, the higher frequency band is in all cases more heavily attenuated than the lower.

5.4 Automatic Arrival Time Estimation

In this section, the four main techniques for automatic arrival time estimation presented in Chapter 4 are applied. Therefore, for each of the four conditions, the sliding window technique, conventional cross-correlation and cross-correlation combined with wavelet decomposition are used to identify the arrival times of the raw AE signal. Also, the threshold technique was used combined with a sharp, 340 kHz Chebyshev I filter to identify separate arrival times for each of the components. Finally, the Gabor WT is re-examined in this section to determine whether the additional attenuation improves its results.

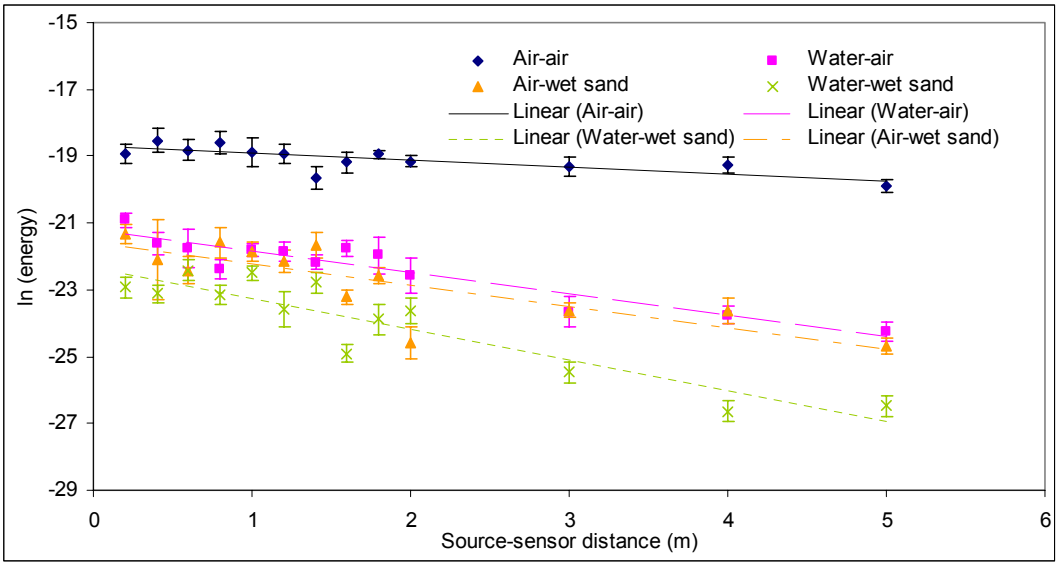

Figure 5.14: Attenuation curves for different external (air and wet sand) and internal environments (air and water)

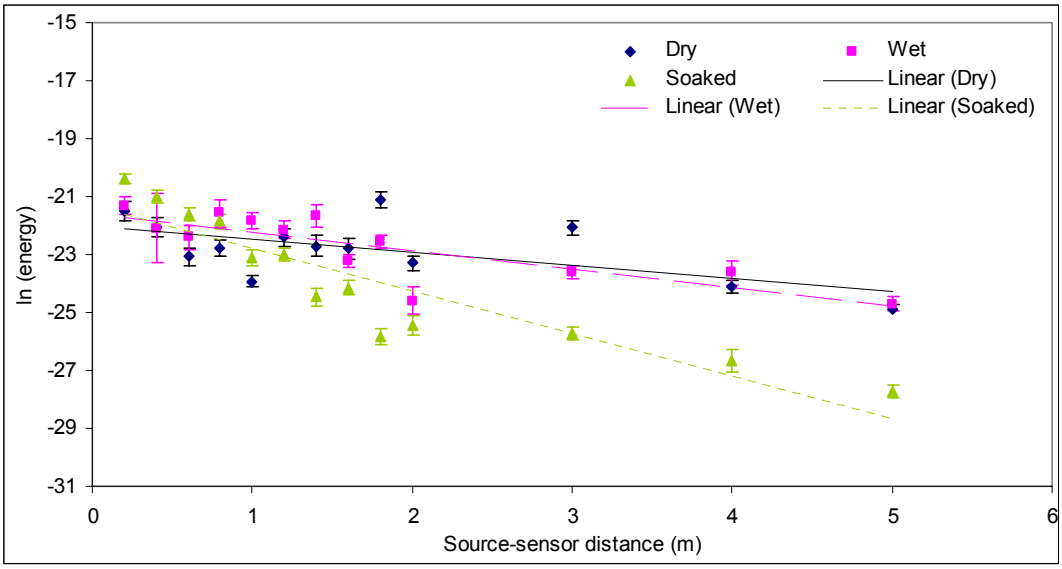

Figure 5.15: Attenuation curves for different conditions of external fine sand and air internal

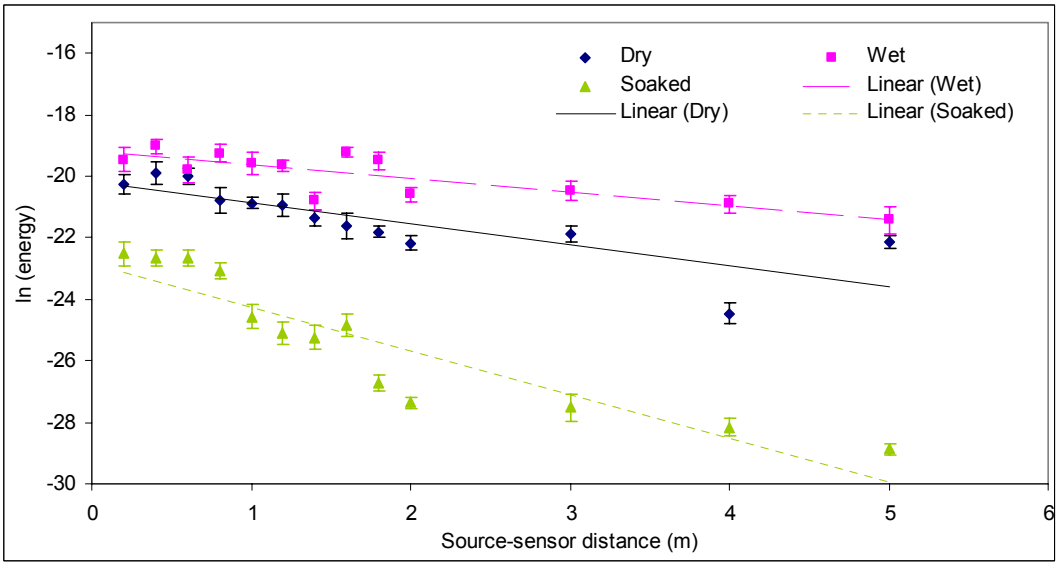

Figure 5.16: Attenuation curves for different conditions of external coarse sand and air internal

Frequency band	**Raw**			**100 – 200 kHz**		**300 – 350 kHz**	
	E_o ($\times 10^{-9}$)	(k)	(R^2)	(k)	(R^2)	(k)	(R^2)
Air-Air	8	0.21	0.61	0.014	0.004	0.36	0.86
Water-air	0.6	0.64	0.88	0.58	0.85	0.68	0.9
Air-wet fine sand	0.5	0.65	0.68	0.49	0.56	0.75	0.72
Water-wet fine sand	0.2	0.92	0.83	0.8	0.68	0.98	0.9

Table 5.1: Attenuation data for raw and filtered signals for different external (air and fine wet sand) and internal environments (air and water)

Frequency band	Raw			100 – 200 kHz		300 – 350 kHz	
	E_o (×10^{-9})	(k)	(R^2)	(k)	(R^2)	(k)	(R^2)
Dry	0.3	0.45	0.37	0.33	0.21	0.60	0.52
Wet	0.5	0.65	0.68	0.49	0.56	0.75	0.72
Soaked	0.6	1.46	0.83	1.4	0.81	1.78	0.90

Table 5.2: Attenuation data for raw and filtered signals for different conditions external fine sand and air internal

Frequency band	Raw			100 – 200 kHz		300 – 350 kHz	
	E_o (×10^{-9})	(k)	(R^2)	(k)	(R^2)	(k)	(R^2)
Dry	2	0.68	0.66	0.57	0.52	0.99	0.87
Wet	5	0.43	0.68	0.25	0.37	0.81	0.91
Soaked	0.1	0.84	1.42	1.31	0.82	1.75	0.87

Table 5.3: Attenuation data for raw and filtered signals for different conditions external coarse sand and air internal

5.4.1 Cross Correlation Technique

To estimate the AE "signal speed" using cross correlation, the square root of the square of the raw AE signal was calculated and then the cross-correlation function calculated as described in Chapter 4. As can be seen in Figure 5.18, the cross-correlation functions between the trigger sensor and the remote sensor are quite different, at long distances, for the four conditions, but all give a clear peak, the peak tending to be sharper when there is water in the environment.

The peak, and hence the time difference can be estimated automatically, Figure 5.19 shows the arrival times for all signals recorded for each of the four conditions, along with the corresponding effective "signal speeds". The arrival times for all signals recorded in the other conditions, were also used to determine apparent wave speeds and the results are summarized later (Tables 5.6 and 5.7).

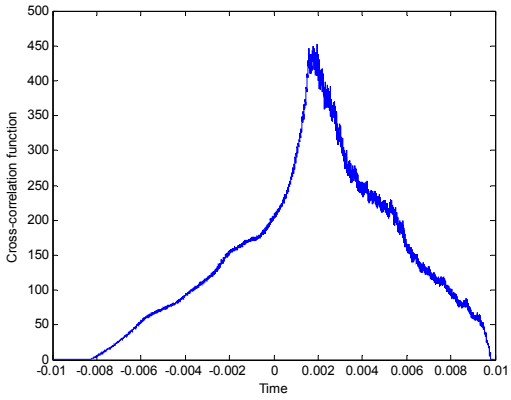

a: Air-air

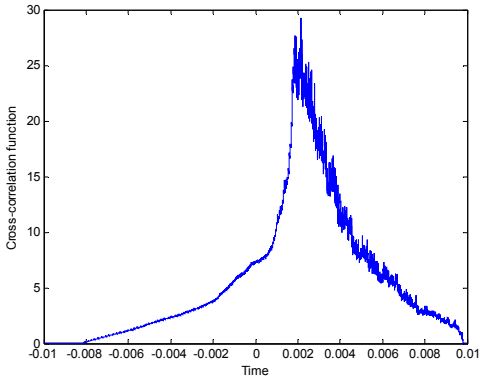

b: Water-Air

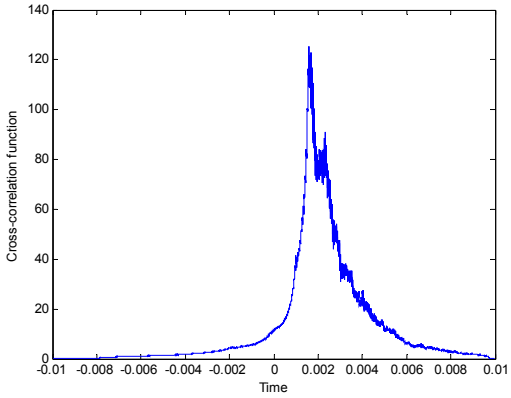

c: Air-wet fine sand

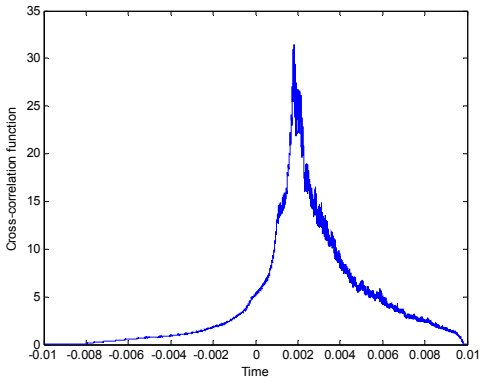

d: Water-wet fine sand

Figure 5.18: Cross-correlation function between Sensor 1 and Sensor 2 for different internal-external environment conditions at 5m

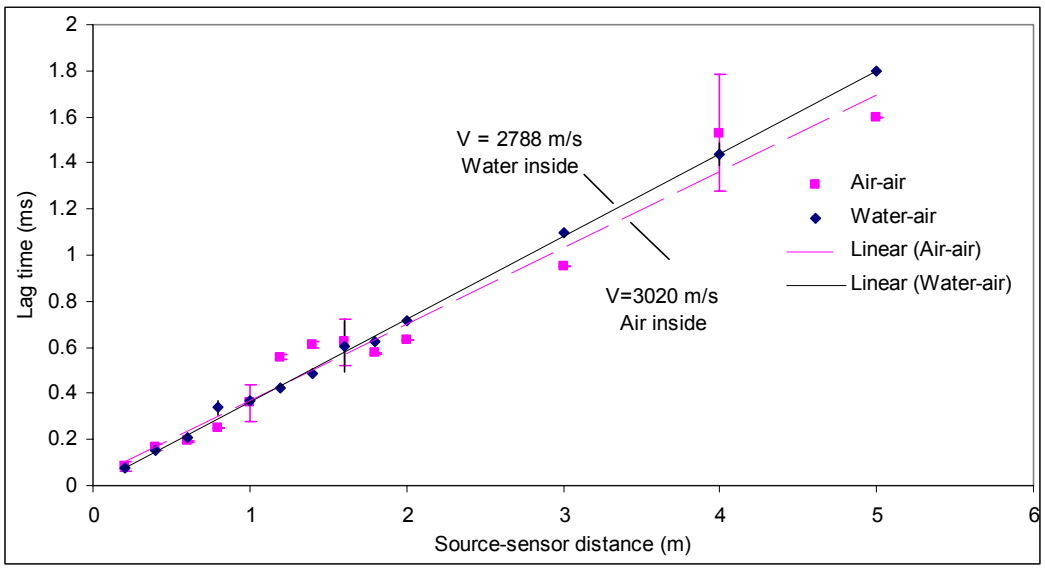

a: Pipe surrounded by air

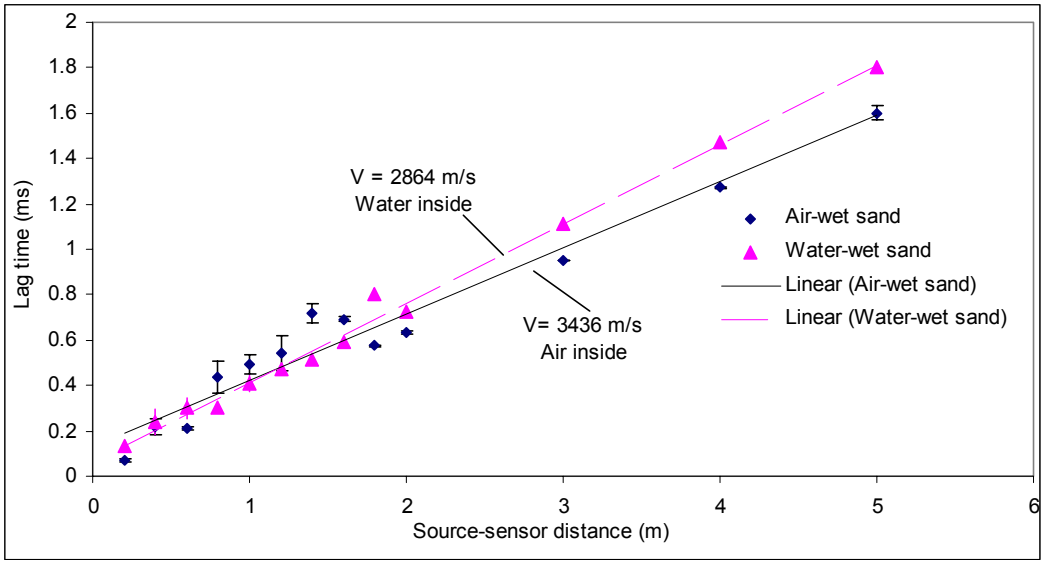

b: Pipe buried in wet fine sand

Figure 5.19: Cross-correlation "wave speeds" for various internal-external environment conditions

5.4.2 Cross Correlation with Wavelet Decomposition

A Daubechies wavelet packet transform was used next to decompose the raw AE signal to one level of detail and one approximation as described in Chapter 4. Then, cross-correlation, as applied in section 5.5.1, was used to determine the arrival time of the Approximation and Detail components of the decomposed signal, Figure 5.20. The technique was also applied for all other conditions and the results are summarized later (Tables 5.6 and 5.7).

5.4.3 Threshold Technique

As discussed at the end of Chapter 4, separation of Waves 1 and 2 is possible between 300 and 350 kHz and so a band-pass filter in this range was applied to isolate the high frequency components and the root square taken of the resulting filtered and raw signals, shown, for example in Figure 5.21. As before, the arrival time estimates are sensitive to the threshold chosen and these used are shown in Figure 5.22. The results for other conditions are summarized later (Tables 5.6 and 5.7).

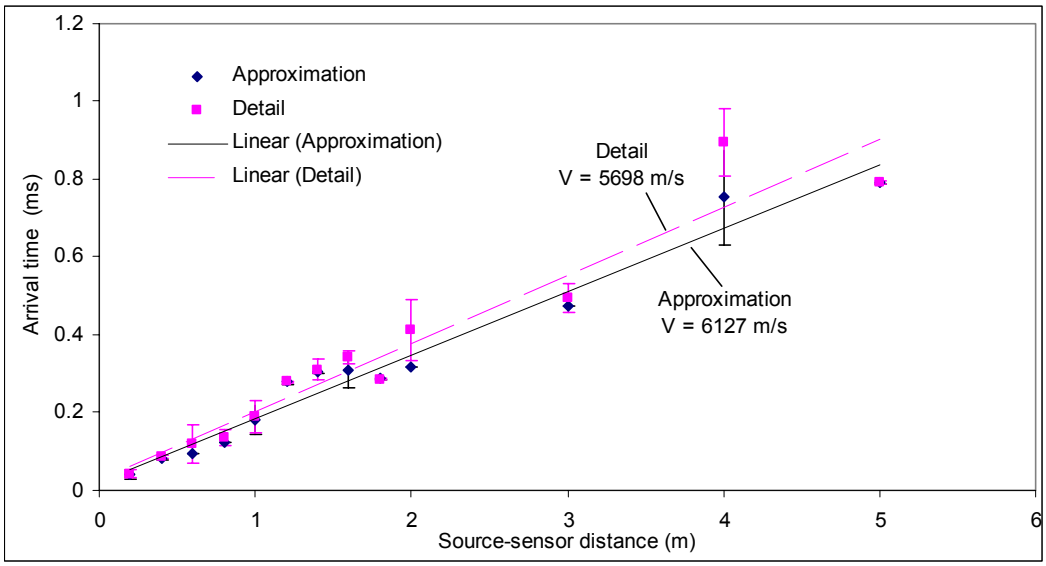

a: Air-air

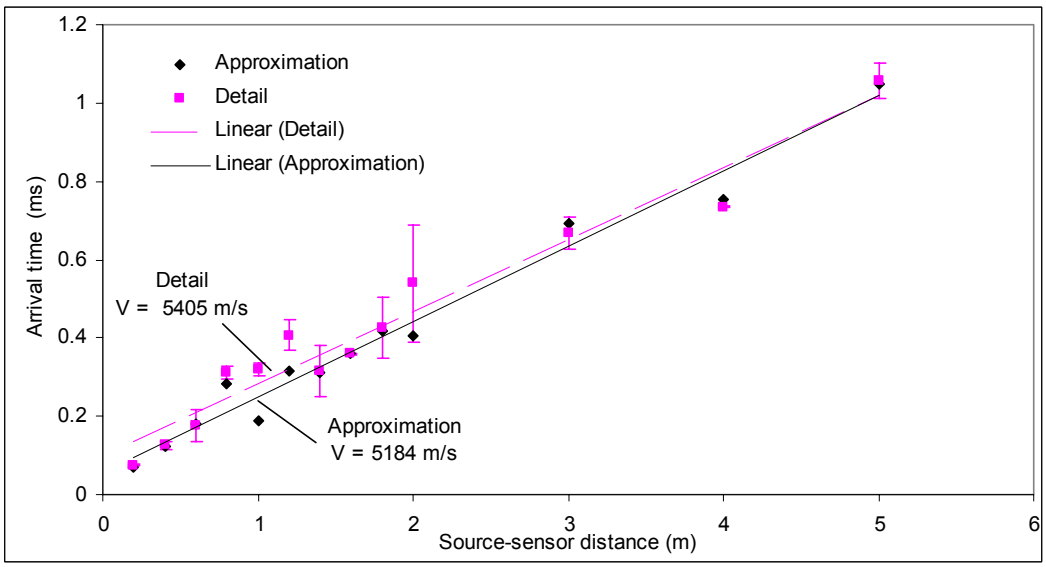

b: Air-water

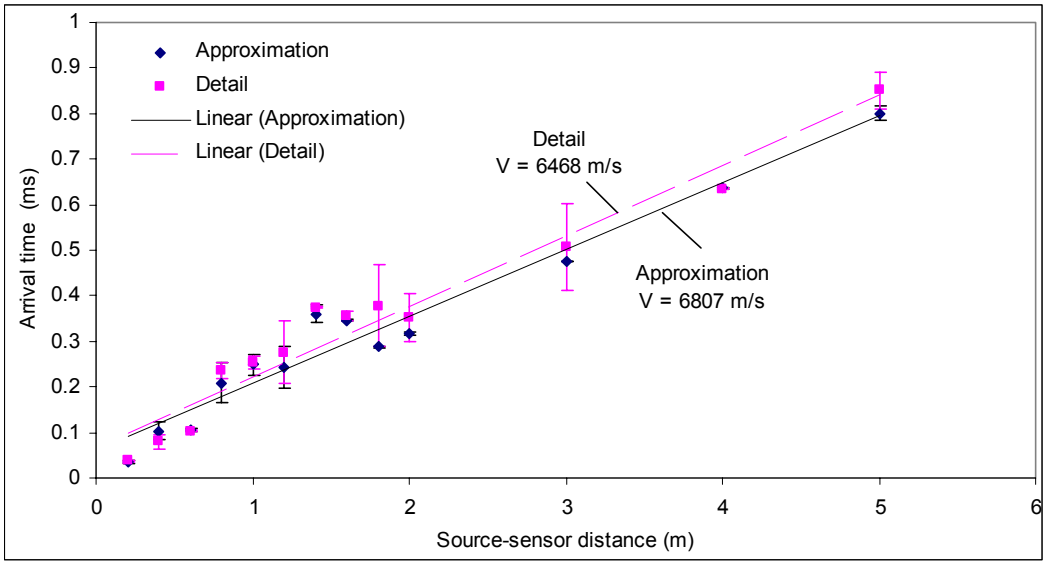

c: Air-find wet sand

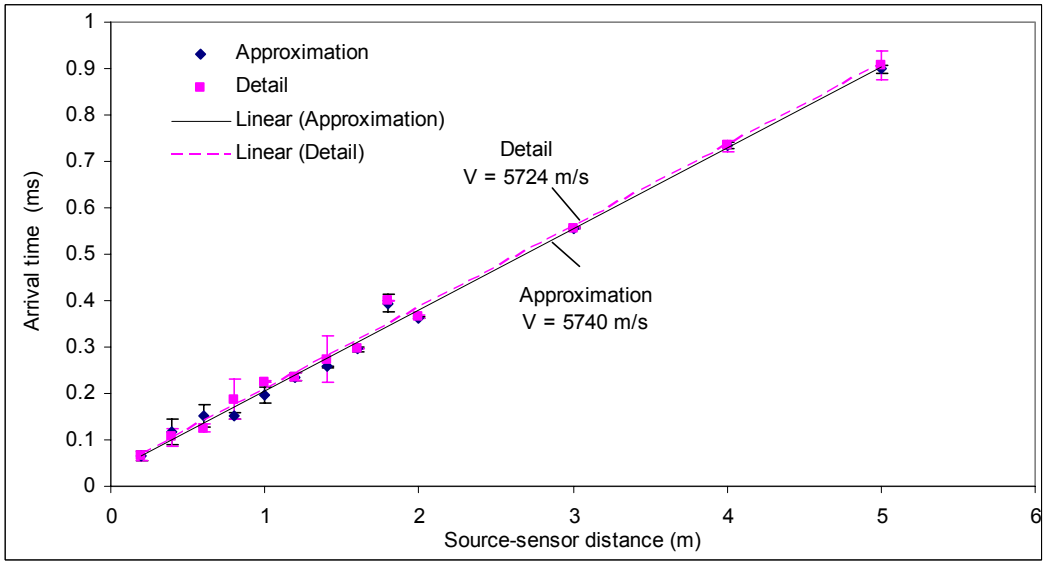

d: Water-wet fine sand

Figure 5.20: Wave speed for various internal-external environment conditions using cross-correlation and wavelet decomposition

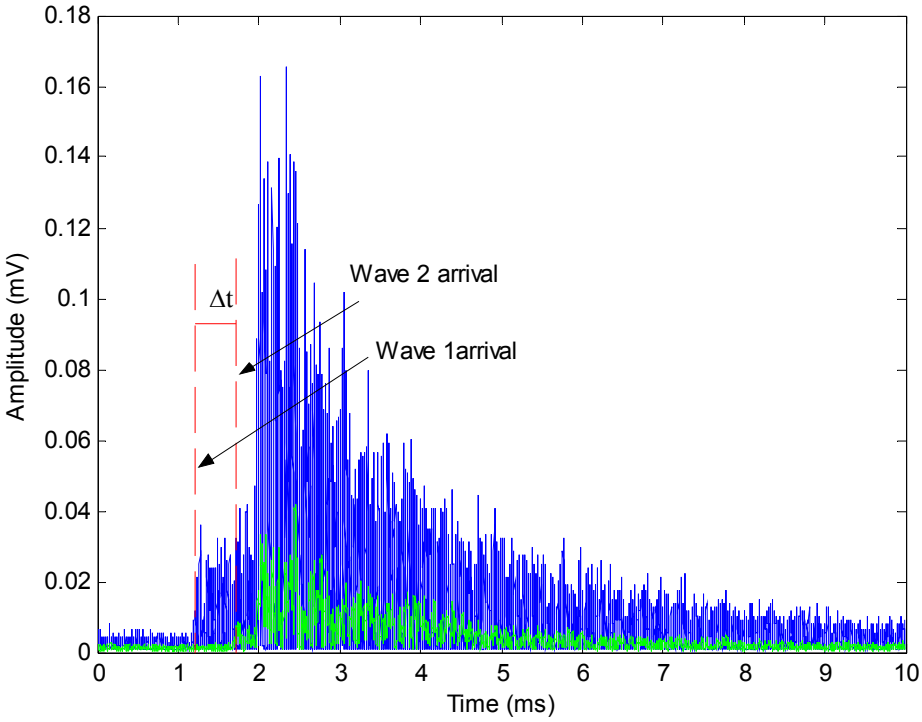

Figure 5.21: Comparison between the arrival of raw signal (Wave 1) and filtered signal (Wave 2) at 5m for water inside and wet fine sand outside

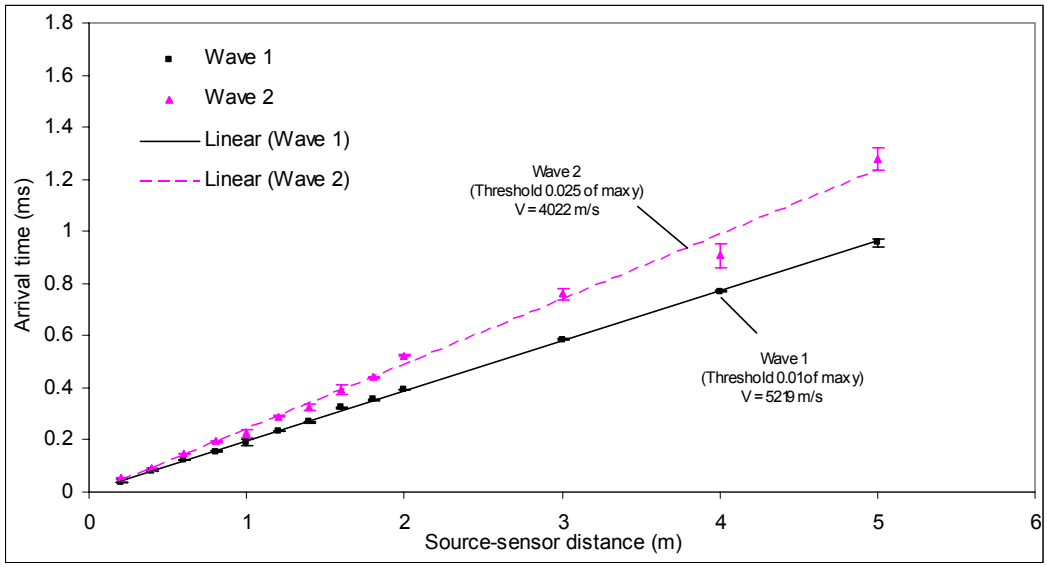

a: Air-air

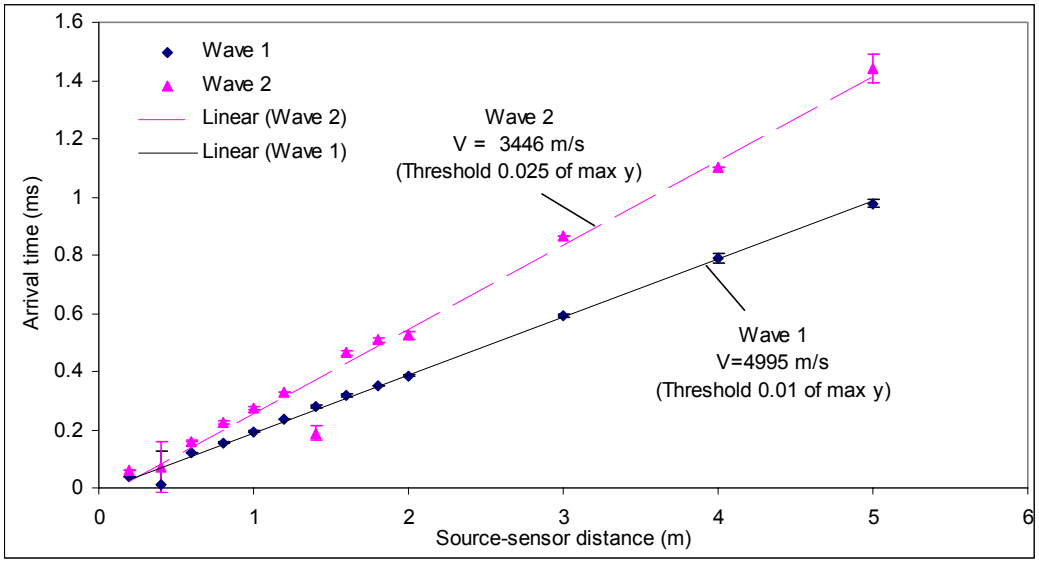

b: Water-air

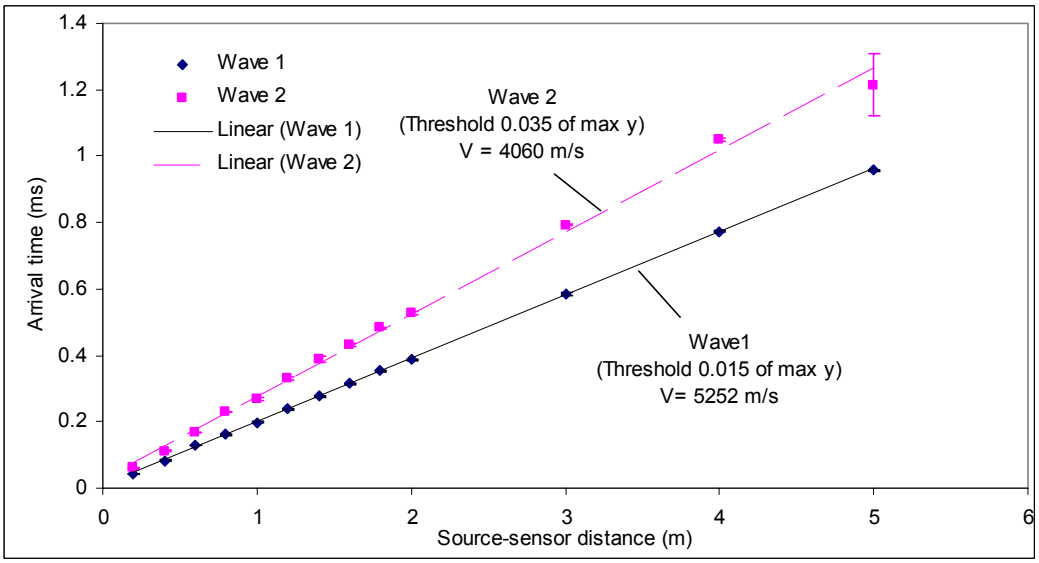

c: Air-wet fine sand (20% water)

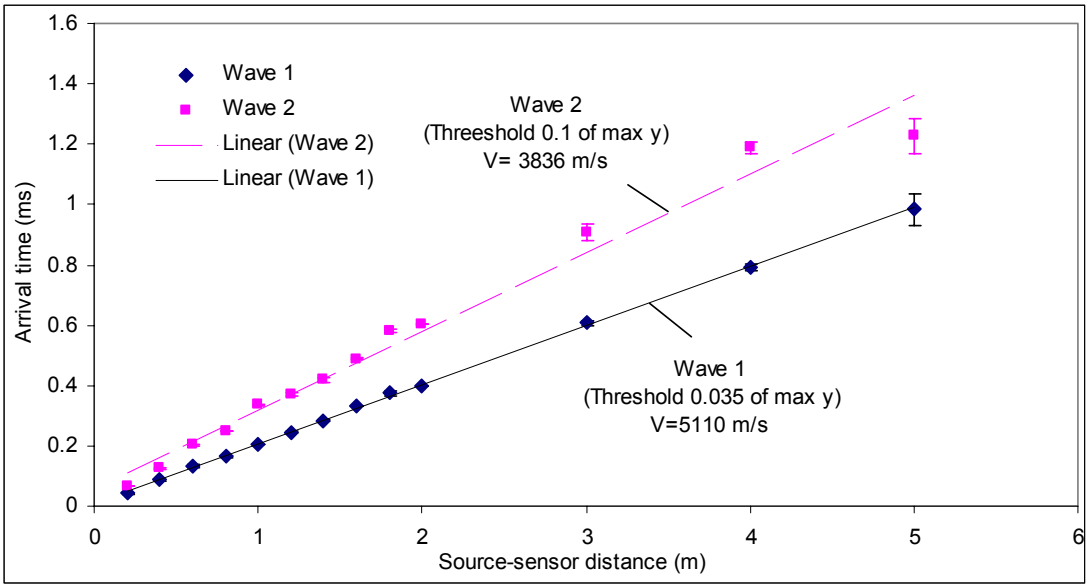

d: Water-wet fine sand (20% water)

Figure 5.22: Arrival time estimation by threshold method with various internal-external environment conditions

5.4.4 The Sliding Window Energy Technique

The sliding window technique described in Chapter 4 was also applied to all external and internal environment conditions. As before, the energy ratio of the high-band (300-350 kHz) to low-band (100-200 kHz) was calculated as a function of time. Figure 5.23 shows this energy ratio calculated for every 20μs up to 3ms, for source-sensor distances of 0.2, 2 and 5m for the first set of external and internal environments. As before, the energy ratio falls sharply when Wave 1 arrives, and, after a period of time which increases with distance, the begins to increase again, which is taken to signify the arrival of Wave 2. Figure 5.24 shows the resulting arrival times plotted against source-sensor distance along with the corresponding wave speeds. These, and the wave speeds for the other conditions, are summarized later (Tables 5.6 and 5.7).

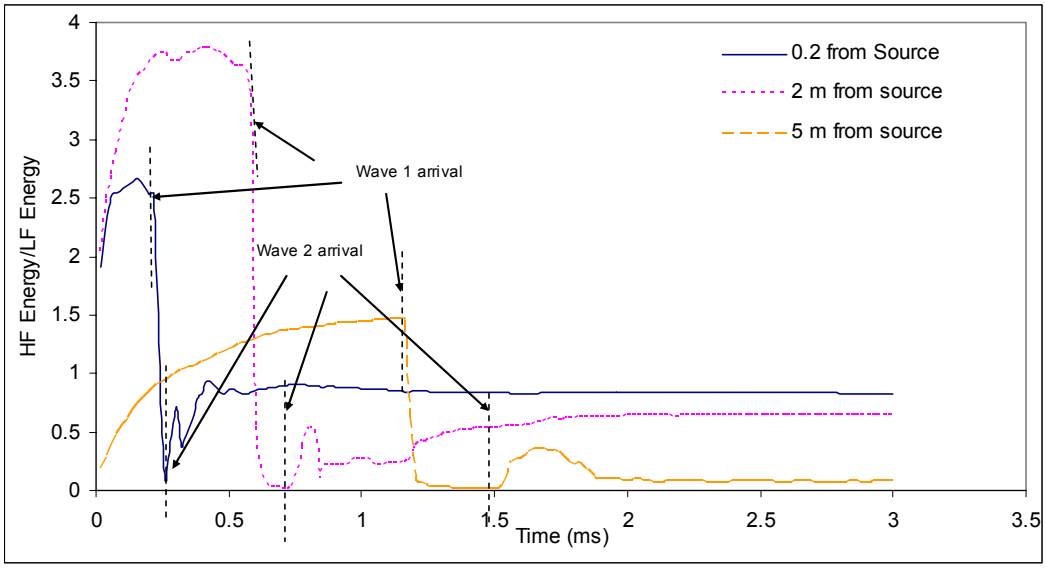

a: Air-air

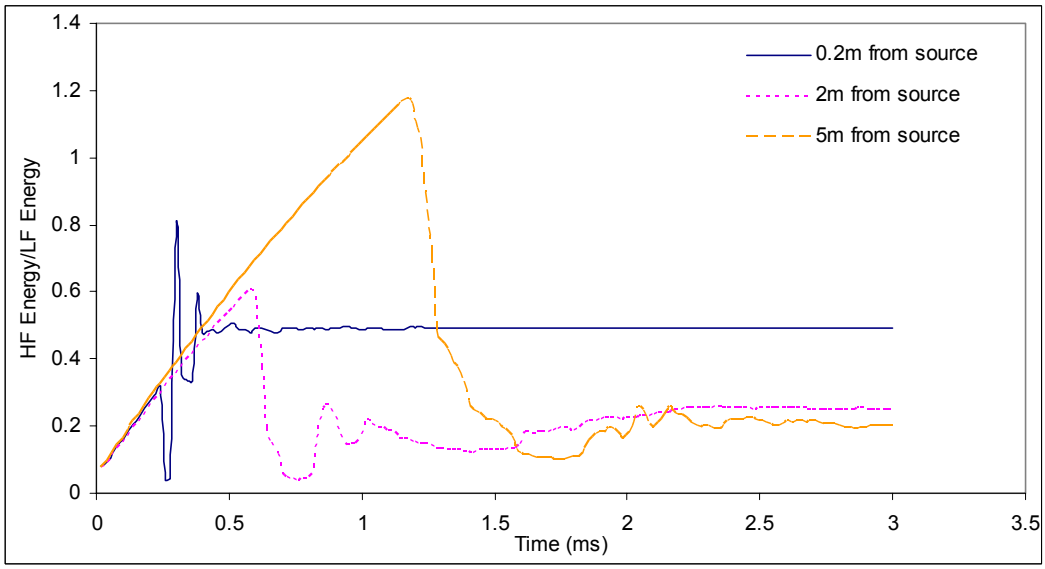

b: Water-air

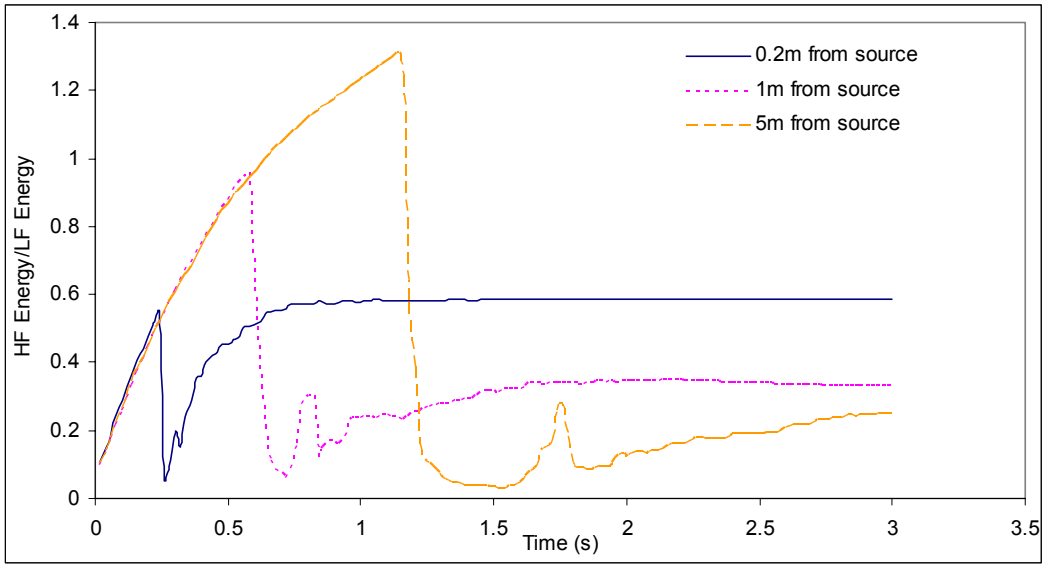

c: Air-wet fine sand

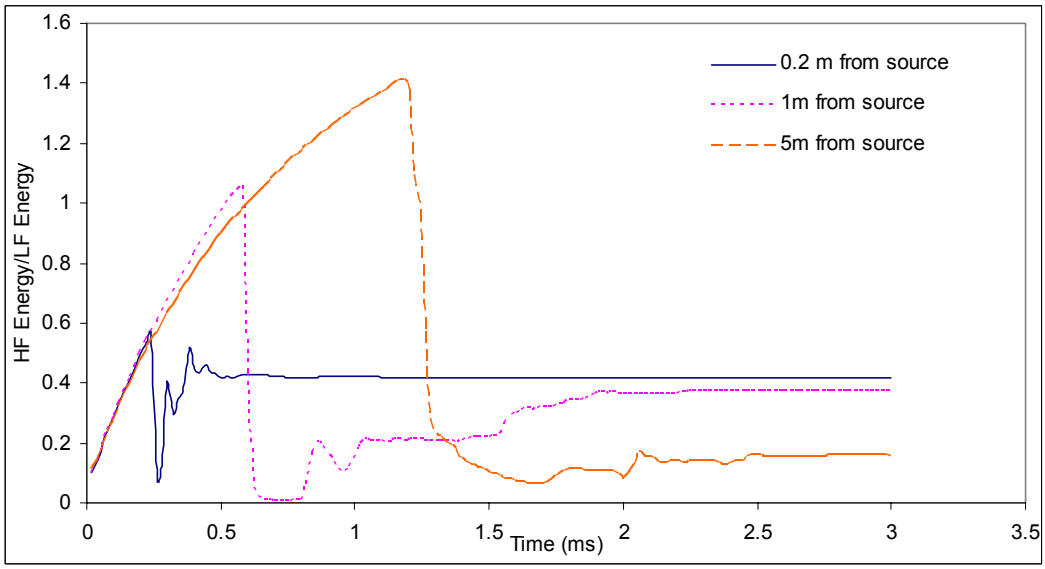

d: Water-wet fine sand

Figure 5.23: Windowed energy ratio (high band to low band) in the time domain for various internal-external environment conditions

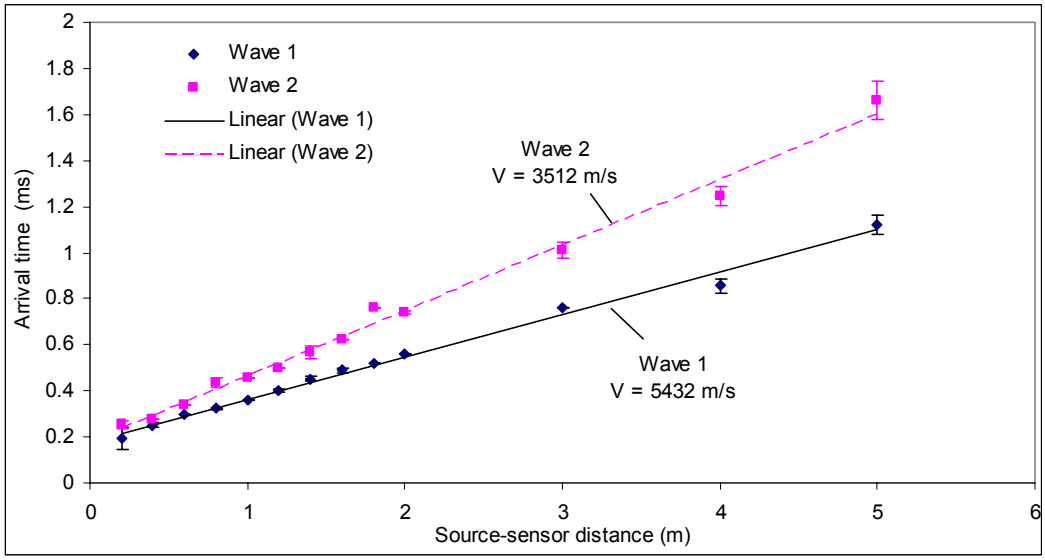

a: Air-air

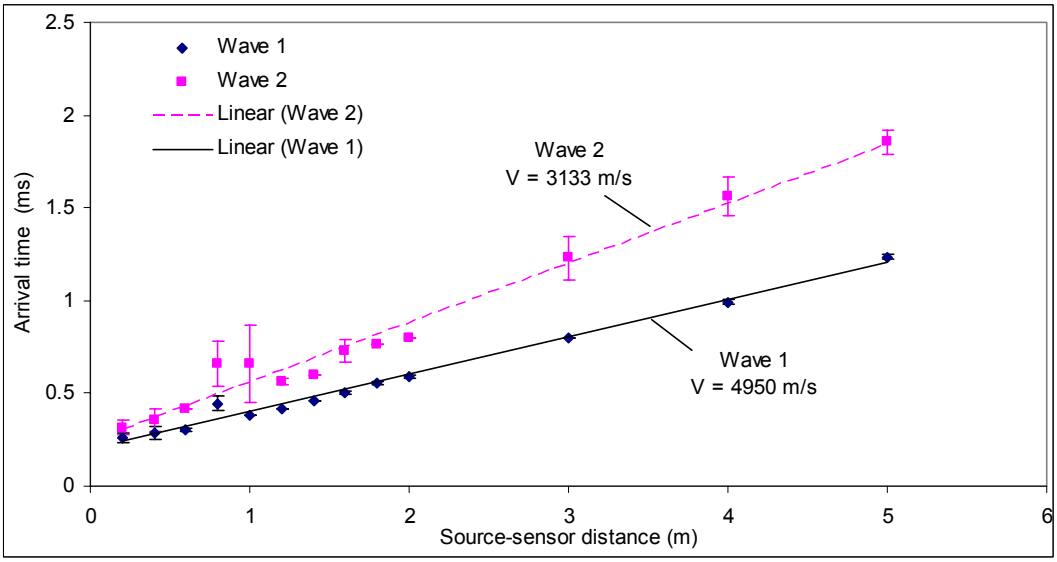

b: Water-air

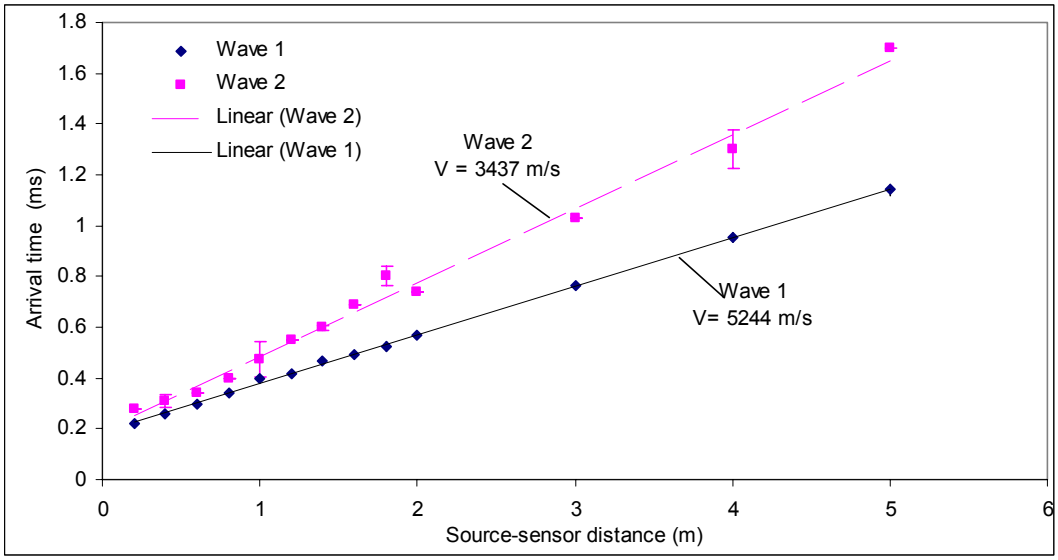

c: Air-wet fine sand

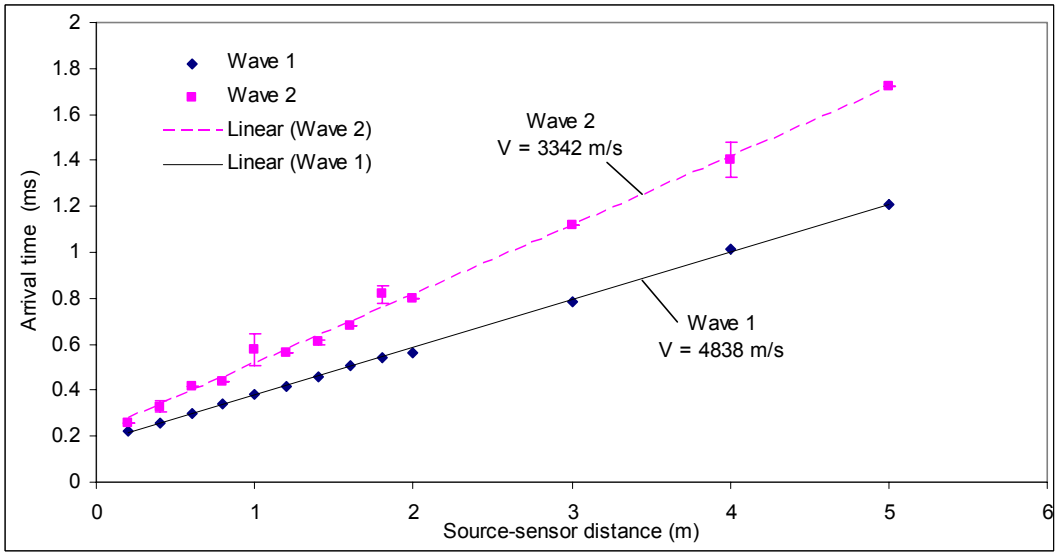

d: Water-wet fine sand

Figure 5.24: Wave speed estimation by energy windowing method for various internal-external environment conditions

5.4.4 Gabor Wavelet Transform

As before, arrival times were taken as the highest peak of the Gabor WT in each of the two main frequency bands at around 170 kHz and 340 kHz and the results are shown in Figure 5.25. The arrival times for all other conditions were also calculated and the results corresponding wave speeds shown in Tables 5.6 and 5.7. As can be seen, the performance of the Gabor WT is little better than it was for the plain pipe

and the problem is again due to there being multiple peaks in the transform at a given frequency.

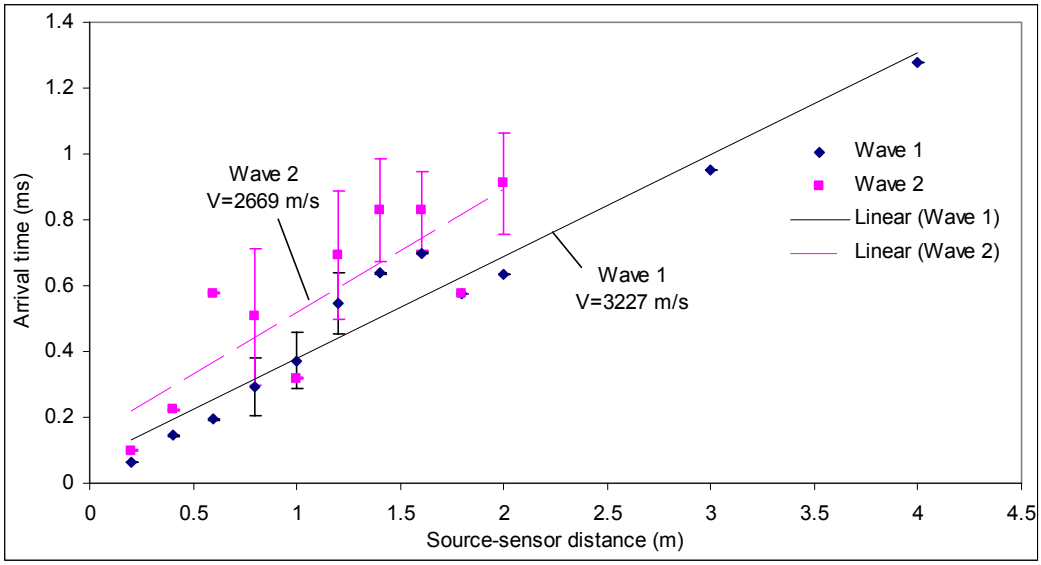

a: Air-air

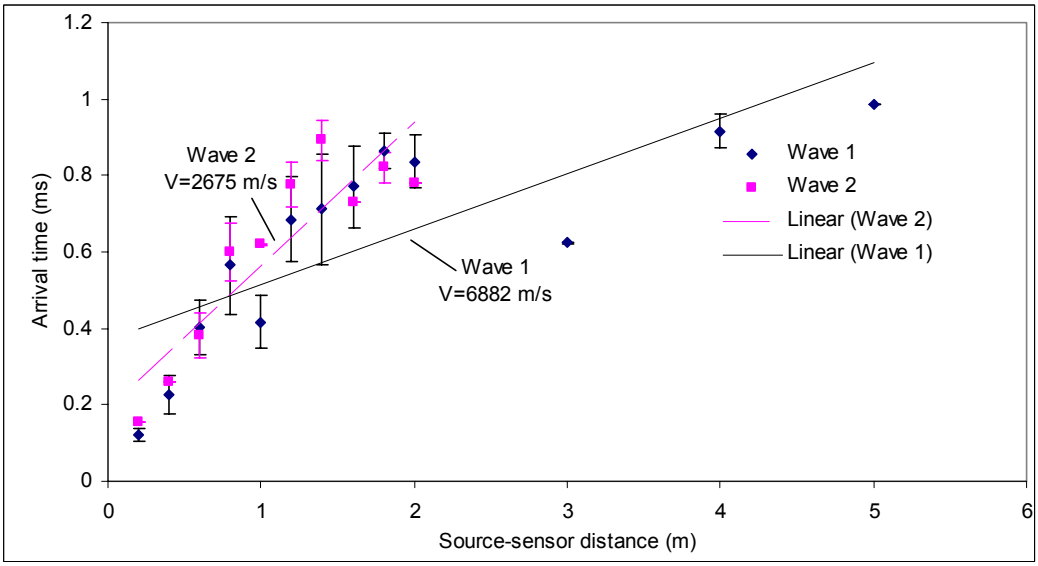

b: Water-air

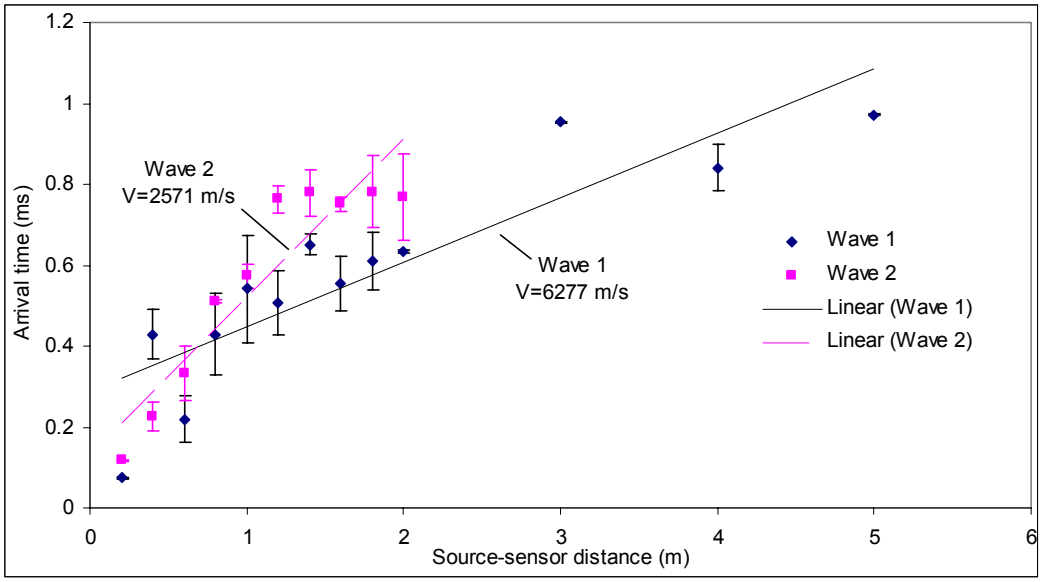

c: Air-wet fine sand

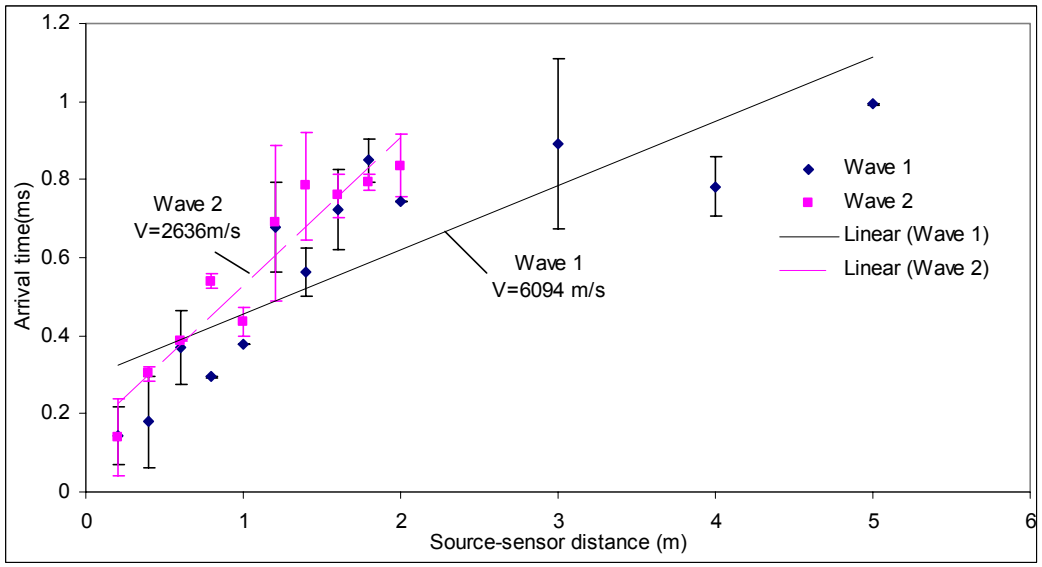

d: Water-wet fine sand

Figure 5.25: Wave speed estimation using Gabor WT for various internal-external environment conditions

5.5 Discussion

5.5.1 Attenuation

As can be seen in Tables 5.1 to 5.3 the internal and external environments have a considerable effect on the attenuation of both Wave 1 and Wave 2. As illustrated in

Figure 5.13, AE energy can be considered to be partly reflected and partly transmitted at boundaries as the wave propagates along the pipe. Leaving aside, for simplicity, possible mode conversions at the boundary, the proportion of energy reflected depends on the relative acoustic impedances of the two media and calculated values for relevant media are given in Table 5.4. It is clear from these values that the signal is almost totally reflected at air interfaces, while it faces less reflection in water, which can explain the attenuation behaviour of the various environments.

Z_2 / Z_1	**Air**	**Water**	**Dry sand**
Steel	0.999	0.87	0.97

Table 5.4 Calculated reflection coefficients at steel interfaces

The data in Table 5.4 can be used to determine the coefficients of Equation 5.3 for the four internal-external interface conditions, $m = n = 1$ for air-steel and assuming that $m = n = 0.87$ for other conditions:

$$E_1(x) = E_{0,1}e^{-k_1 x} + E_{0,2}e^{-k_2^{air} x} \tag{5.4}$$

$$E_2(x) = (0.87)^{ax} E_{0,1}e^{-k_1 x} + E_{0,2}e^{-k_2^{air} x} \tag{5.5}$$

$$E_3(x) = (0.87)^{ax} E_{0,1}e^{-k_1 x} + E_{0,2}e^{-k_2^{water} x} \tag{5.6}$$

$$E_4(x) = (0.87 \times 0.87)^{ax} E_{0,1}e^{-k_1 x} + E_{0,2}e^{-k_2^{water} x} \tag{5.7}$$

where $E_1(x)$ is total energy for air-air condition;

$E_2(x)$ is total energy for water-air condition;

$E_3(x)$ is total energy for air-wet sand condition; and

$E_4(x)$ is total energy for water-wet sand condition.

To find a, the above equations can rearranged to give:

$$E_1(x) - E_2(x) = (1 - 0.87^{ax})E_{0,1}e^{-k_1 x} \tag{5.8}$$

and

$$E_3(x) - E_4(x) = (1 - 0.87^{ax})0.87^{ax} E_{0,1} e^{-k_1 x} \tag{5.9}$$

Dividing Equation 5.8 by 5.9 and taking the logarithm of both sides gives:

$$\ln\left[\frac{E_1(x) - E_2(x)}{E_3(x) - E_4(x)}\right] = F_1(x) = -ax\ln(0.87) \tag{5.10}$$

Plotting the averaged data points for E_1, E_2, E_3 and E_4 treated to yield Figure 5.26 gives a value of a of around 1.5, although the intercept is not zero and the straight line fit is poor.

Using the derived value of a, Equations 5.8 and 5.9 can be rearranged to yield:

$$\ln\left[\frac{E_1(x) - E_2(x)}{1 - 0.87^{ax}}\right] = F_2(x) = \ln(E_{0,1}) - k_1 x \tag{5.11}$$

and

$$\ln\left[\frac{E_3(x) - E_4(x)}{(1 - 0.87^{ax})0.87^{ax}}\right] = F_3(x) = \ln(E_{0,1}) - k_1 x \tag{5.12}$$

As can be seen from Figure 5.27, $F_2(x)$ and $F_3(x)$ yield similar values of k_1, but values of $E_{0,1}$ which differ by a factor of about 4.

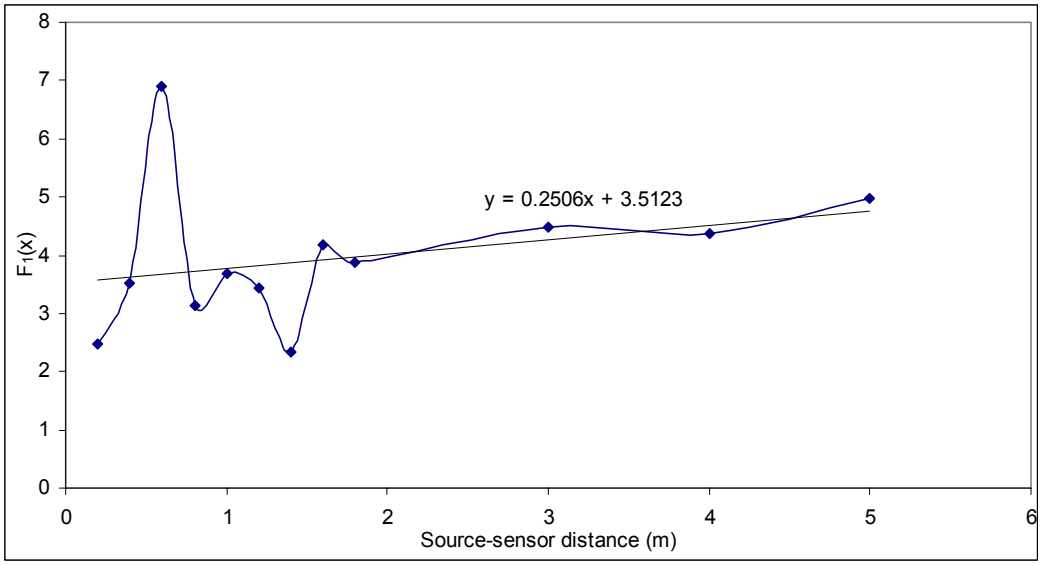

Figure 5.26: Determination of a

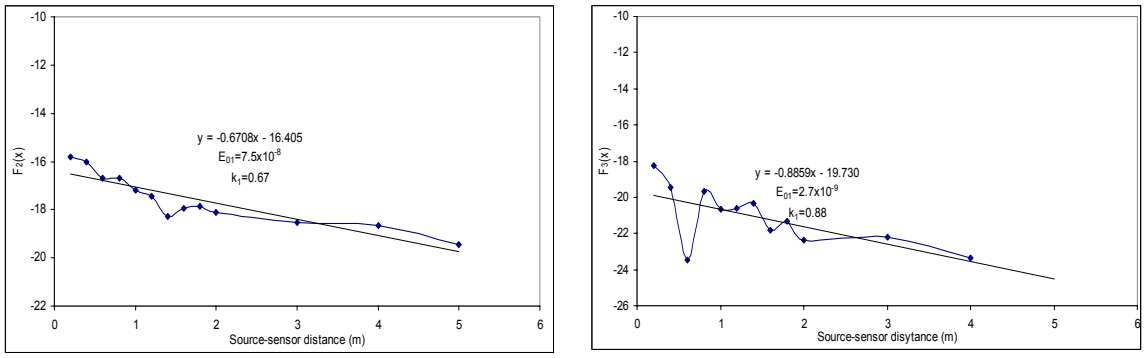

a) b)

Figure 5.27: Determination of E0,1 and k1

Taking the lower value of $E_{0,1}$ (2.7×10^{-9}) and the average value of k (0.7), four functions can be derived to reveal the residual attenuation associated with $E_{0,2}$, k_2^{air} and k_2^{water}:

$$E_1(x) - E_{0,1}e^{-k_1 x} = F_4(x) = E_{0,2}e^{-k_2^{air}x} \quad (5.13)$$

$$E_2(x) - (0.87)^{ax} E_{0,1}e^{-k_1 x} = F_5(x) = E_{0,2}e^{-k_2^{air}x} \quad (5.14)$$

$$E_3(x) - (0.87)^{ax} E_{0,1}e^{-k_1 x} = F_6(x) = E_{0,2}e^{-k_2^{water}x} \quad (5.15)$$

$$E_4(x) - (0.87)^{2ax} E_{0,1}e^{-k_1 x} = F_7(x) = E_{0,2}e^{-k_2^{water}x} \quad (5.16)$$

and these are shown in Figure 5.28.

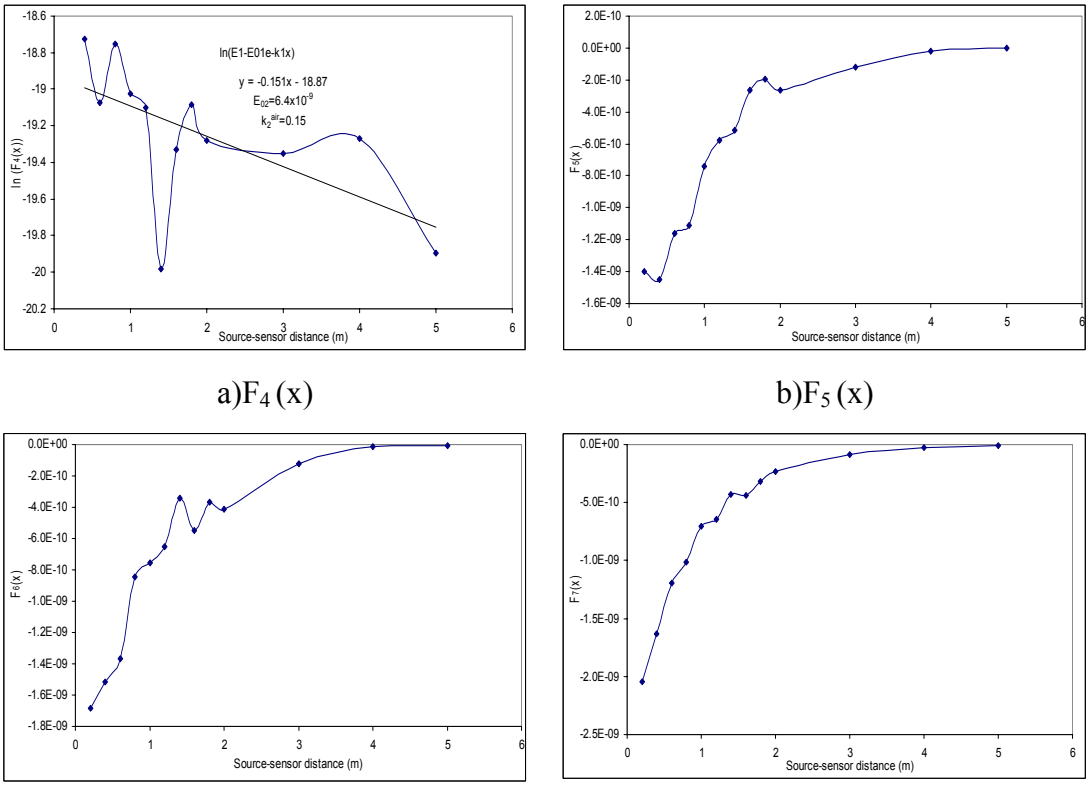

a)F_4 (x) b)F_5 (x)

c)F_6 (x) d)F_7 (x)

Figure 5.28: Plotting results to find E0,2 and k2

As can be seen, only F_4 (x) yields positive values, the remainder being slightly negative, which implies that the attenuation behaviour can be adequately described without surface propagation.

It has to be acknowledged that the forgoing analysis is under-constrained, since the evaluation of k_1 and $E_{0,1}$ first may have affected the results. Furthermore, it is based on the assumption that $m = n$ in Equation 5.5, although allowing a difference would further reduce the constraint on evaluation of the parameters. Finally, acknowledging a critical angel and\or permitting mode conversions at interfaces would rarely introduce yet more unknown parameters.

The attenuation, and particularly the effects of interfaces, can also be examined by imagining the energy to be moving along sound rays (Figure 5.29), losing energy at each reflection according to an absorption coefficient of the surface, and reflecting according to Snell's law [105, 106].

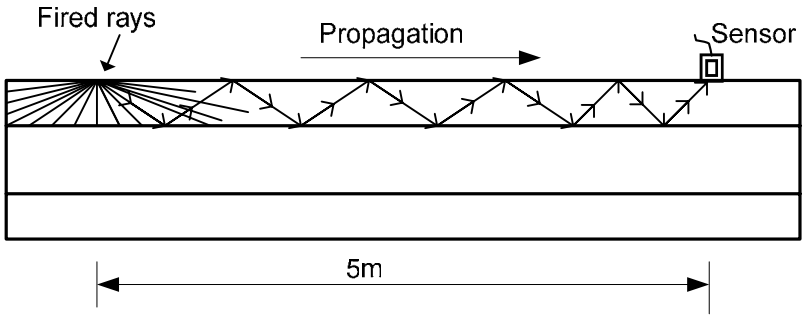

Figure 5.29: Schematic drawing for propagations of fired rays in pipe wall

Energy loss (attenuation) due to reflection at boundaries and absorption were built into a solid model of the pipe [106], and rays fired randomly in all directions from a "source" collecting the number of hits at "sensors" using a reflection coefficient, R_c, and an material damping, c, so that the overall energy due to each hit, E_h, can be expressed:

$$E_h = E_0(e^{-cx'})R_c^{N_r} \tag{5.17}$$

where E_0 is a unit source of energy, c is the material (internal) damping; N_r is the number of reflections and x' is the actual path length of the ray (as opposed to the source-sensor distance). It should be pointed out that this model only considers internal rays. The number of rays fired, N_f, and the number of rays hitting the sensor, N_h, is recorded using an algorithm, which also calculates the energy of each ray at the time it hits, modifying the value of N_h to account for number of reflections and path length, x', yielding a modified hit count which is less than unity. Hypothetically, it can be assumed that the modified hit-ratio ($\Sigma N_h'/\Sigma N_f$) will be directly proportional to the measured AE energy ratio at a given distance, so that the attenuation equation becomes [106]:

$$\ln\left(\frac{E}{E_0}\right) = \ln\left(\frac{\Sigma N_h'}{\Sigma N_f}\right) = e^{-k^* x} \tag{5.18}$$

The model has been examined using three different numbers of fired rays, 225, 400 and 625, using the calculated (from Figure 5.27) attenuation factors, k_1, of 0.67 and

0.88, reflection coefficients, R_c, of 0.87 and 1, a simulation elapsed time of 1.5ms and a propagation speed of 5200ms^{-1}. The sensors were positioned axially in a similar way to the experiments, the sensors being positioned at 0.2m from the source up to 5m with 0.2m spacing between the sensors.

The number of fired rays has an effect on the results as shown in Figure 5.30, the results for 625 giving a better R^2. Due to computational limitations, it was not possible to examine the effect of number of iterations. Also, the results were not significantly changed with changing the reflection coefficient.

Generally, the simulations show that the estimates made of k_1 are little high, since there is a significant contribution (even over the limited length of the simulation period) from reflected rays. The limited effect of R_c on attenuation can be explained by the fact that the simulation will have stopped before all but the most direct rays reach the sensor.

5.5.2 Wave Speed

Tables 5.5, 5.6 and 5.7 summarise the wave speeds determined by the methods described earlier, and it is clear that the apparent speed, and hence any source location, will depend upon how arrival time has been determined. However, some consistent observations are possible across all of the methods with the exception of these using the Gabor WT for the air-air condition, which suffers from the same difficulty with multiple peaks as was reported in Chapter 4. Taking air-air as the base case, the introduction of water into the pipe always results in a reduction of apparent wave speed, whereas the introduction of wet fine sand on the outer surface, often results in an increase in apparent wave speed, although this is quite small according to some of the methods. The introduction of sand outside to the case of water inside also results in a modest increase in apparent wave speed, except in the WD method where the increase is substantial. The degree of wetness and coarseness of the sand have no consistent effect on wave speed within or between the techniques.

The various methods yield a variety of wave velocities as shown in Tables 5.5 to 5.7. From this chapter, and Chapter 4, it is clear that all of the techniques except simple cross-correlation can be used to obtain speeds of more than one component of the signal although the means of separation of the components differ. Of these, the identification of the first peak in the Gabor WT at a given frequency is perhaps the least reliable, and the threshold technique requires some judgement in the setting of thresholds which can be difficult to automate.

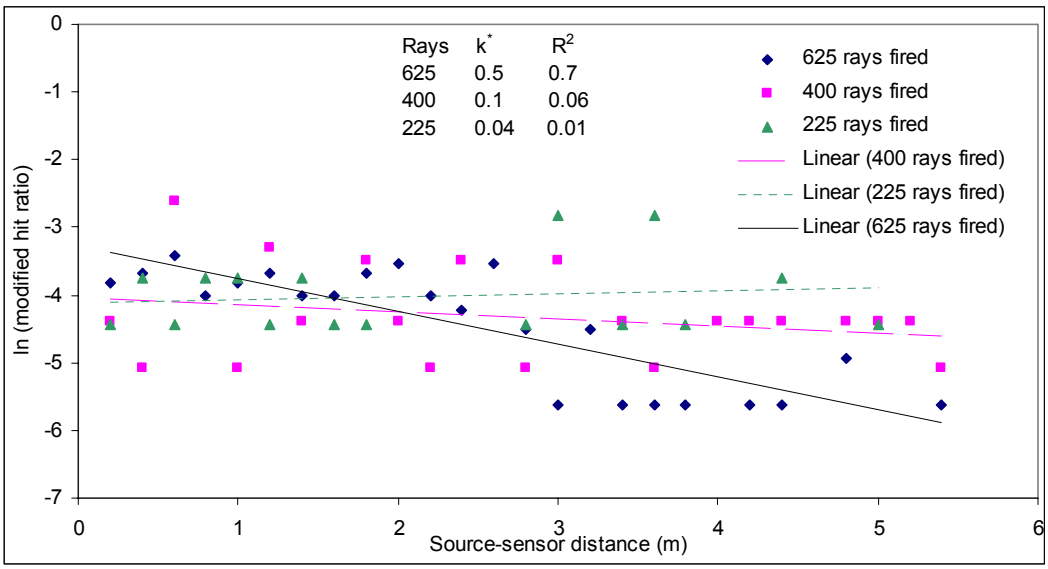

a)

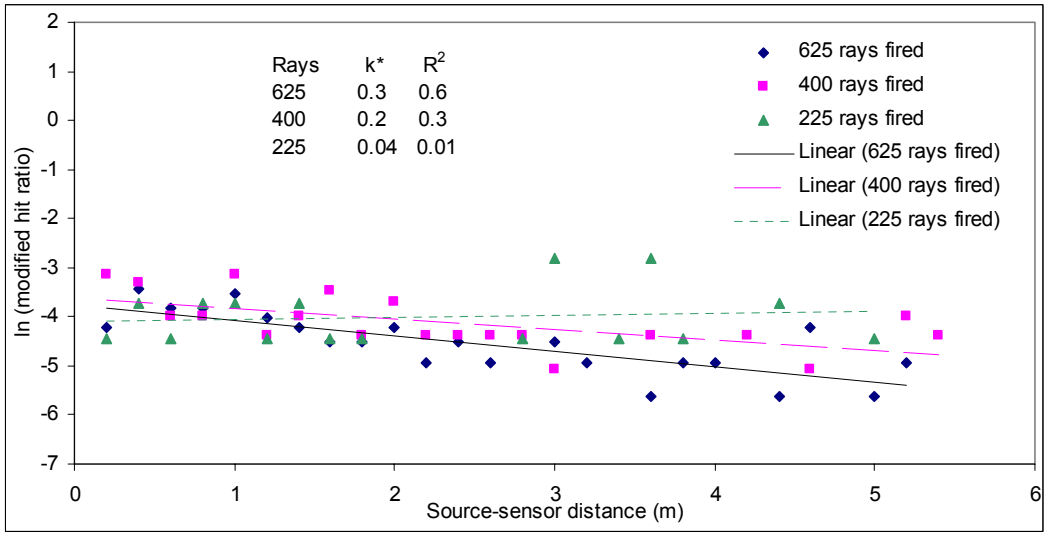

b)

Figure 5.30: Ray tracing of different number of rays fired for material damping of a) 0.67 and b) 0.88

Internal-external environment		Air-air	Water-air	Air-wet fine sand	Water-wet fine sand
Simple x-c		3020	2788	3403	2864
WD and x-c	**Approximation**	6598	5184	6468	5724
	Detail	6127	5405	6807	5740
Threshold Wave 1		5219	4995	5252	5110
Threshold Wave 2		4022	3446	4060	3836
Windowed energy Wave 1		5432	4950	5244	4838
Windowed energy Wave 2		3512	3133	3437	3342
Gabor WT 170kHz		3227	6882	6277	6094
Gabor WT 340kHZ		2669	2675	2571	2636

Table 5.5: Summary of apparent wave speeds ms^{-1} for various internal-external environment conditions (WD: Wavelet Decomposition, x-c: Cross-correlation, WT: Wavelet Transform)

External environment sand		Dry	Wet	Soaked
Simple x-co		3217	3403	3218
WD and x-co	**Approximation**	6476	6468	6261
	Detail	6460	6807	6258
Threshold Wave 1		4452	5252	5460
Threshold Wave 2		3728	4060	3670
Windowed energy Wave 1		5037	5244	5012
Windowed energy Wave 2		3310	3437	3121
Gabor WT 170kHz		5414	6277	5043
Gabor WT 340kHZ		3068	2571	3870

Table 5.6: Summary of apparent wave speeds ms^{-1} for different external environment conditions of fine sand (particle size 180 micron) (WD: Wavelet Decomposition, x-c: Cross-correlation, WT: Wavelet Transform)

External environment sand		Dry	Wet	Soaked
Simple x-c		3141	3161	3291
WD and x-c	**Approximation**	6265	6357	6414
	Detail	6329	6325	5110
Threshold Wave 1		4600	4080	5900
Threshold Wave 2		4415	3730	3330
Windowed energy Wave 1		5076	5208	5097
Windowed energy Wave 2		3197	3257	2870
Gabor WT 170kHz		5327	4393	4425
Gabor WT 340kHZ		2052	2291	3133

Table 5.7: Summary of apparent wave speeds ms^{-1} for different external environment conditions of coarse sand (particle size 2000 micron) (WD: Wavelet Decomposition, x-c: Cross-correlation, WT: Wavelet Transform)

5.6 Summary

In this chapter AE propagation has been studied for discontinuous simulated sources for a range of internal and external conditions. It has been found that apparent speeds of components of the waves depend upon the environment and that the added attenuation brought about by water in the internal and external environment can be explained in terms of reflections at the interfaces.

The following chapter considers sources which are extended over time and examines the extent to which the findings of the Chapter 4 can be applied to such sources.

Chapter 6: Continuous and Semi-Continuous AE Signals

6.1 Introduction

This chapter discusses methods applicable to continuous and semi-continuous AE signals. A continuous AE signal was generated by applying a gas jet to the metal surface and time-based features were introduced by pulsing the jet using a solenoid valve. Continuous AE signals are difficult to analyse unless they have a clear temporal structure and this was the reason for pulsing the jet. The focus of the analysis was to estimate distortions in the time and frequency domains and to examine how attenuation compares with a discontinuous on a plain pipe. Some tests were done on a 5m length pipe, raw AE signals being acquired at a sampling rate of 5 MHz for a fixed period of 10 ms (50000 points), and others on a pipe of 18m length, where the raw AE signal was acquired at a sampling rate of 5 MHz for a fixed period of 100 ms (500000) points.

6.2 General Observations

Figures 6.1a and 6.1b, and Figure 6.2a and 6.2b show typical raw AE signals captured at S2 for continuous and semi-continuous sources. As can be seen, at longer distances, the signal is significantly attenuated. Figures 6.3a and 6.3b, and Figures 6.4a and 6.4b show corresponding normalized spectra of raw AE signals again for continuous and semi-continuous sources. Here, there is clearly substantial relative attenuation of the higher frequency component of the spectrum as distance from the source increases. Figure 6.5 shows this effect on a more continuous basis as a normalized plot.

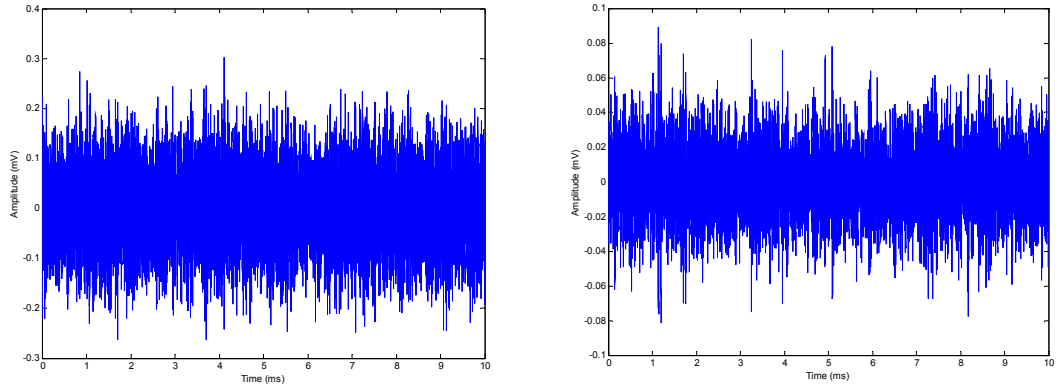

a) 0.1m b) 5m

Figure 6.1: The continuous AE time series at S2 for 5m long pipe

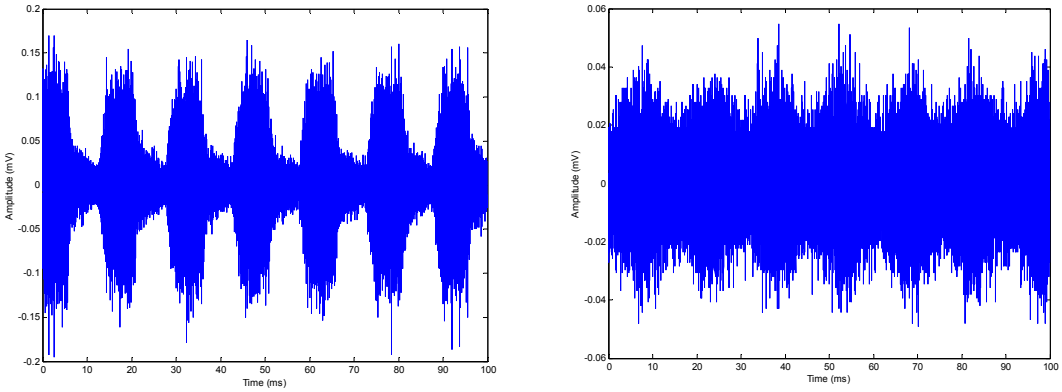

a) 0.2m b) 10m

Figure 6.2: Typical semi-continuous AE time series at S2 for 18m long pipe

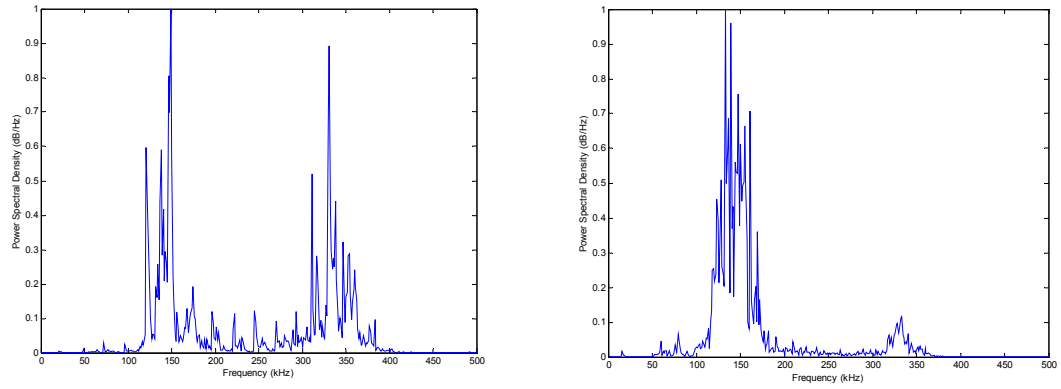

a) 0.1m b) 5m

Figure 6.3: Normalized continuous AE frequency spectra at S2 for 5m long pipe

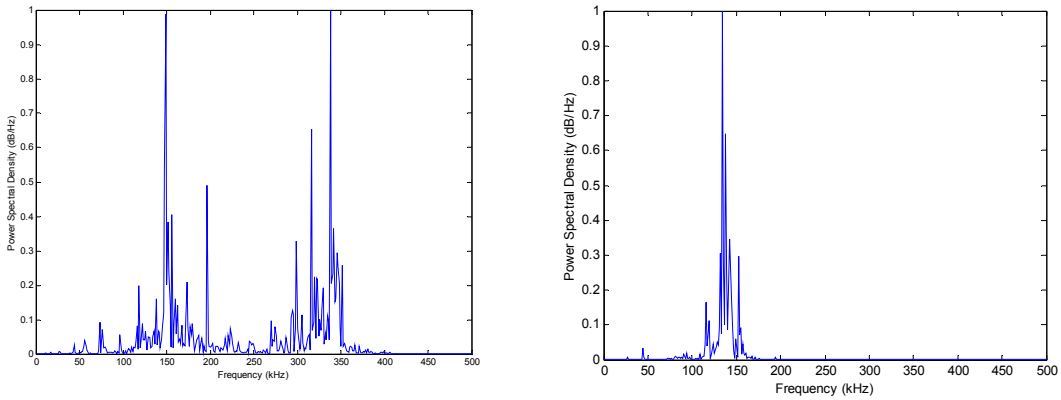

a) 0.2m b) 5m

Figure 6.4: Normalized semi-continuous AE frequency spectra at S2 for 18m long pipe

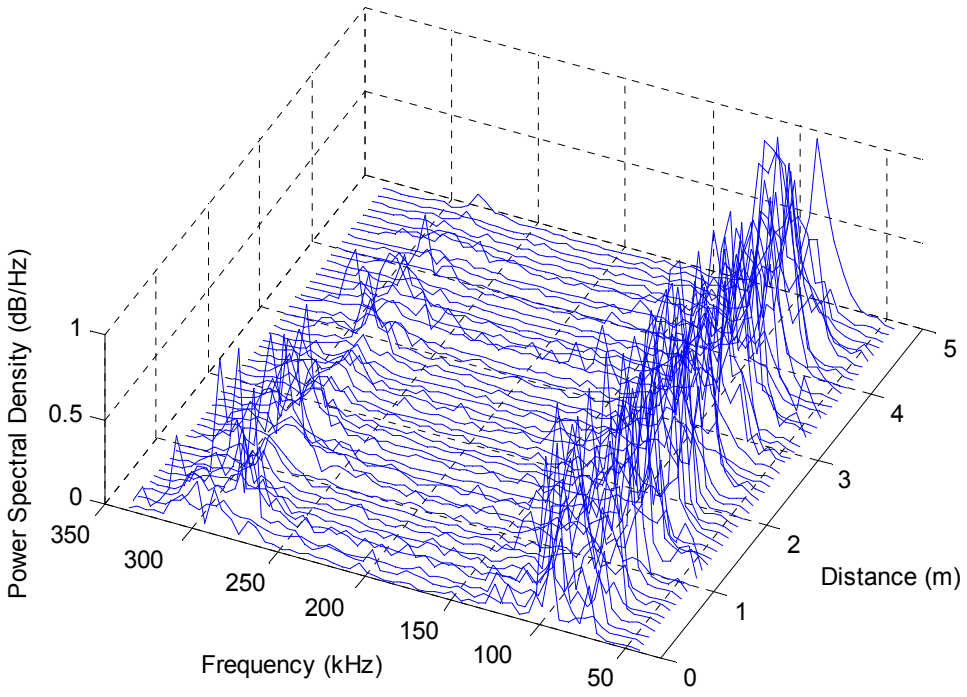

Figure 6.5: Normalized frequency-distance plot for signal acquired for continuous source for 5m long pipe

6.3 Attenuation

For signals which have no reference time, attenuation may be the only way to locate a source and, as discussed in the last two chapters, splitting the wave into

components which may have differing attenuation characteristics could help to improve identification and location accuracy.

In Figures 6.3 and 6.4, it is clear that much of the energy is in two bands between 100 and 200 kHz, and 300-350 kHz. Accordingly, the signal was filtered using a band pass (Chebyshev I) filter between 100 and 200 kHz (low component), and 300-350 kHz (high component) for the continuous and semi-continuous signals, and the energy was calculated for the raw and filtered signals, as shown in Figures 6.6 to 6.8. As can seen, the low frequency component shows comparable behaviour to the raw signal, while the high frequency component is more heavily attenuated for all cases. The slope for the raw and low frequency components suggest very little attenuation even at longer distances.

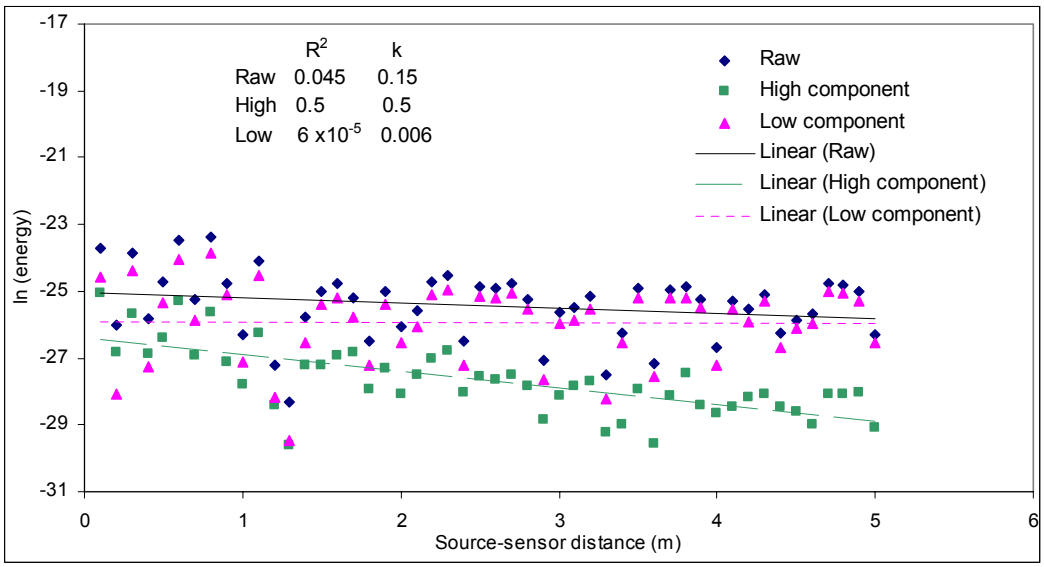

Figure 6.6: Energy calculated for the raw and band pass filtered, low (100-200), high (300-350 kHz), continuous AE signal for 5m long pipe

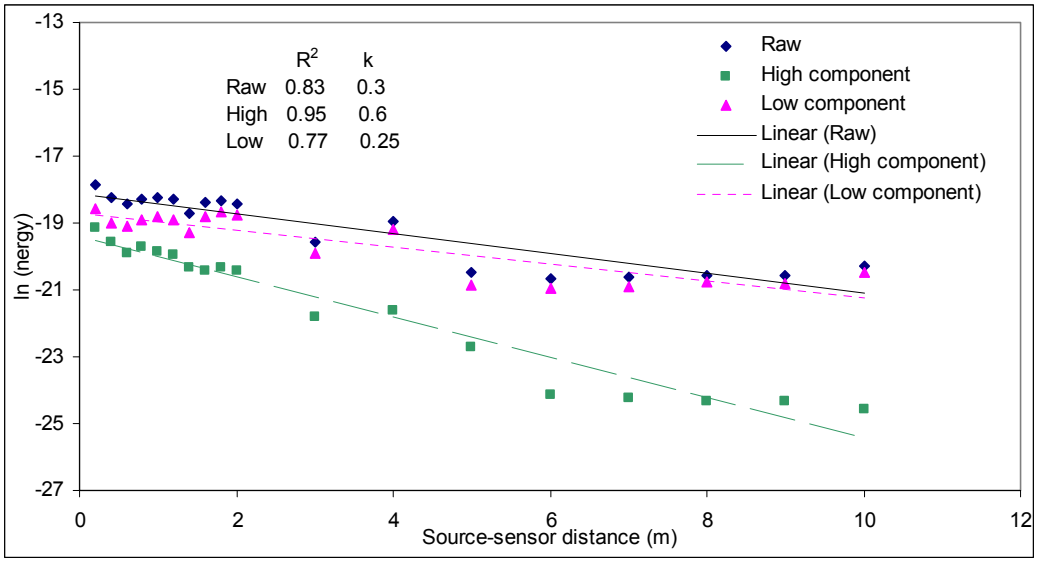

Figure 6.7: Energy calculated for the raw and band pass filtered, low (100-200), high (300-350 kHz), continuous AE signal for 18m long pipe

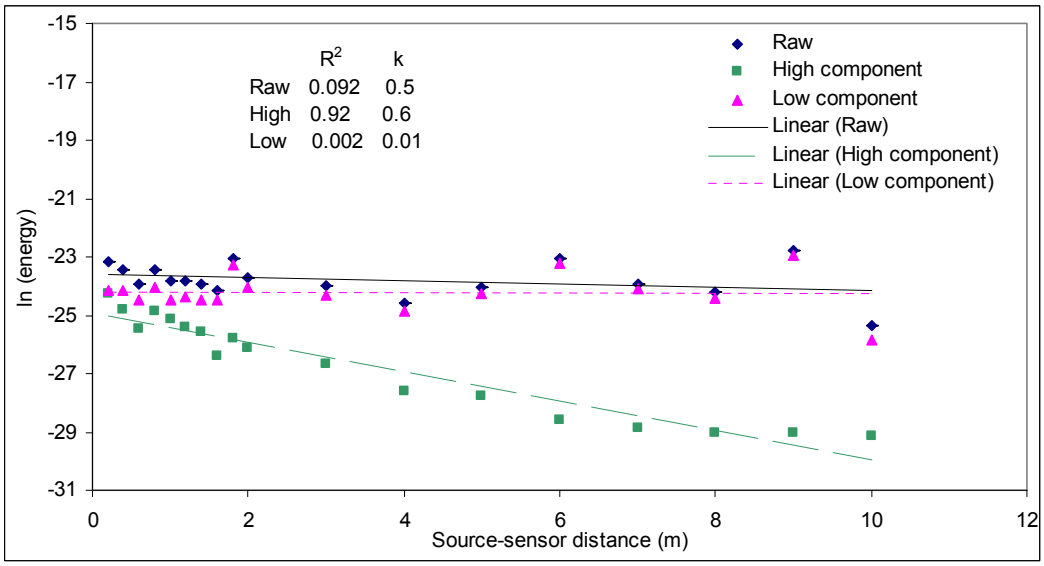

Figure 6.8: Energy calculated for the raw and band pass filtered, low (100-200), high (300-350 kHz), semi-continuous AE signal for 18m long pipe

In Figure 6.9, the energy of the high frequency component has been normalized to the total energy, in order to reduce the effect of variation of the source and, as can be seen, this only leads to minor improvements in correlation factor, if at all. As can be seen in Figure 6.9b that the attenuation for the semi-continuous signal is greater than the continuous signal and, by comparison with the findings in Chapter 4 and 5, both are greater than the factors for discontinuous sources. This would tend to suggest that there is a dispersive element to AE propagation in which cannot be accounted by simple filtering and further strengths the approach of identifying

wave types in the time domain. Unfortunately, such an approach cannot be taken with continuous sources which limit the accuracy even for energy-based methods of source location.

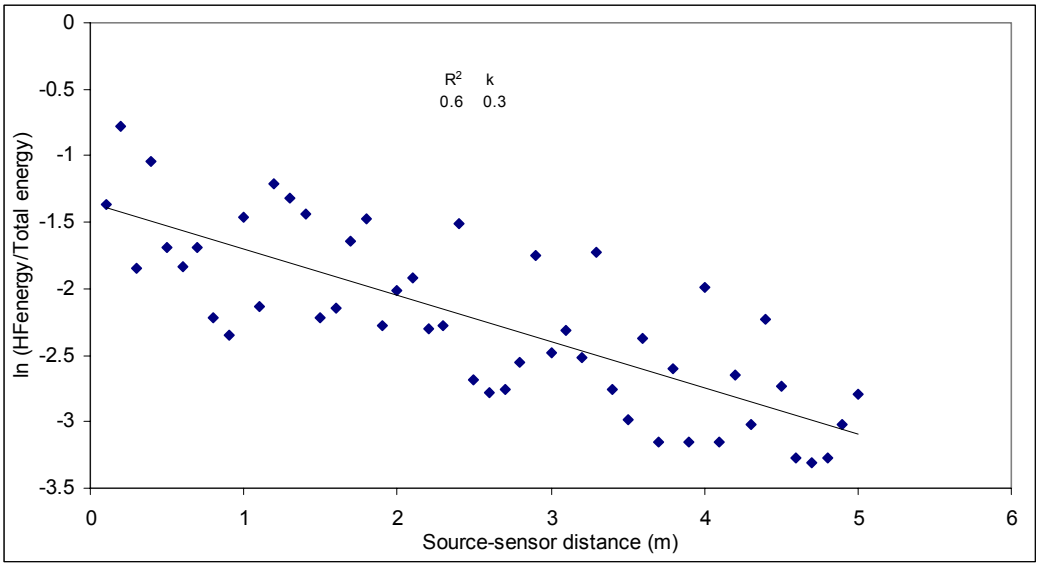

a) Continuous AE signal

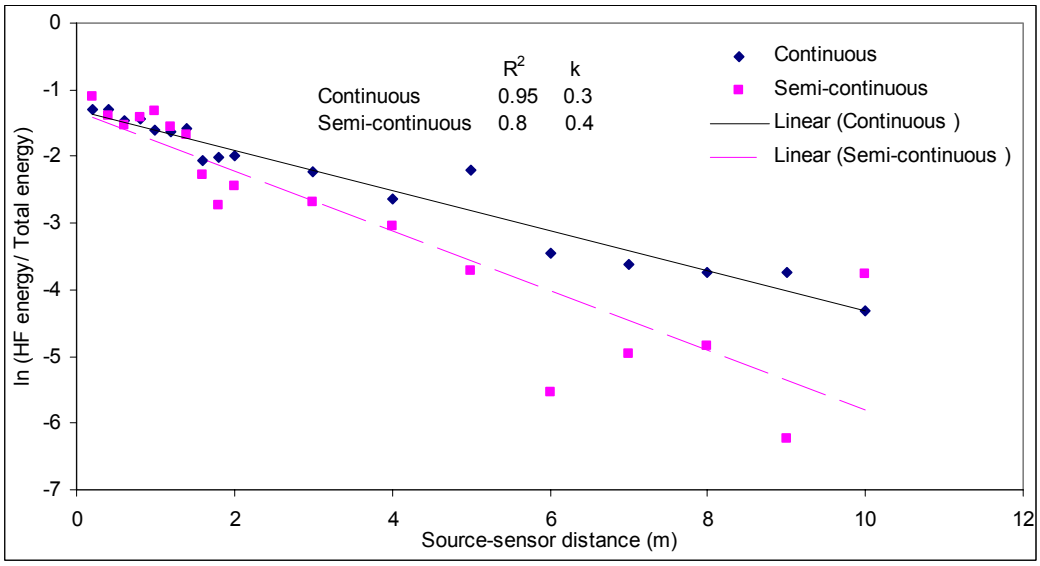

b) Semi-continuous and continuous AE signal

Figure 6.9: Normalized energy versus source sensor distance for high frequency component for a) 5m and b)18m long pipes

6.4 Source Location

The location of sources with no temporal structure can be estimated only, as discussed in section 2.2, by using Equation 2.11, which can be rearranged:

$$x = -\frac{1}{k}\ln\left(\frac{E}{E_o}\right) \tag{6.1}$$

where x is the source-sensor distance, which can therefore be found provided that at least two sensors are available (Section 2.2.3.3).

As noted in the last two chapters, source location can be achieved by using cross-correlation provided that the signals have some temporal structure. Also, as seen above, filters can be used to improve performance and Chapter 4 has shown that a sharp 340 kHz filter makes a clear separation between Wave 1 and Wave 2. Therefore, the signals of the type shown in Figure 6.2 were filtered and correlated with the corresponding filtered trigger signal, Figures 6.10 and 6.11 showing typical results for the high-pass and low-pass components. Clearly, at longer distances, the high-pass filtered component does not given a clear peak and this is consistent with its higher degree of attenuation.

Figure 6.12 shows the cross-correlation function peaks times for each of the source-sensor distances. Clearly, the low-pass component of the signal gives a more consistent measure of speed although the value is rather different to those found for discontinuous sources. Next, the discontinuous signals were band-pass filtered between 100 and 200 kHz and Figure 6.13 shows a typical cross-correlation for this. The peak is far clearer in this case, with secondary peaks associated with the out-of-phase pulses. Figure 6.14 shows the time lags plotted against distance and it is clear that this filter gives a good estimation of velocity although the value is again lower than for discontinuous sources.

Finally, in order to check if any temporal structure is detectable for the continuous source, cross-correlation functions were determined for these as well. Some examples are shown in Figure 6.16 and it is clear that these give null results.

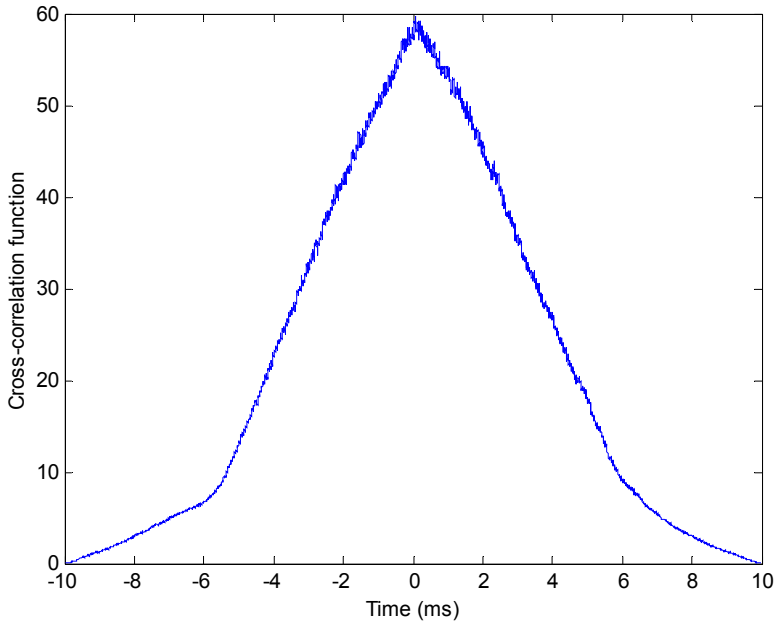

a: 0.2 m

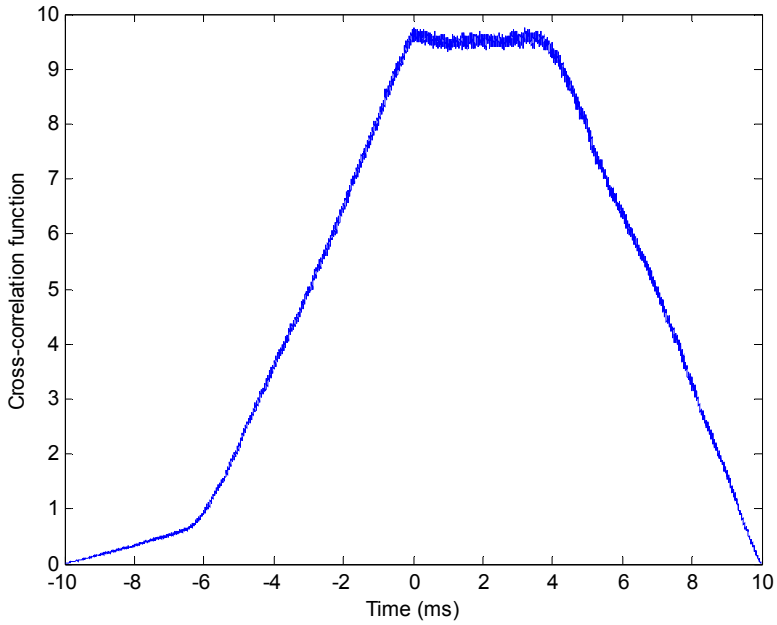

b:10m

Figure 6.10: Cross-correlation function for high pass filter for semi-continuous signal on 18m long pipe

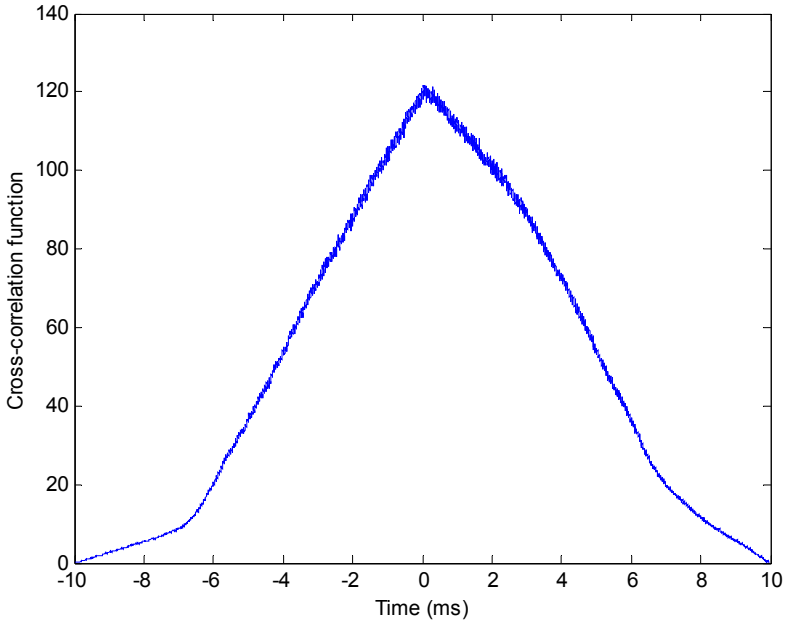

a: 0.2m

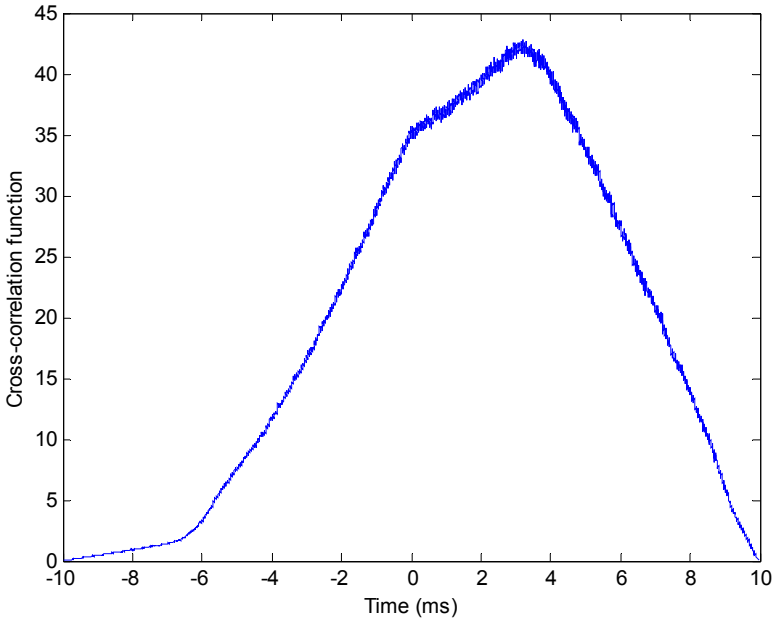

b: 10m

Figure 6.11: Cross-correlation function for semi-continuous signal on 18m long pipe

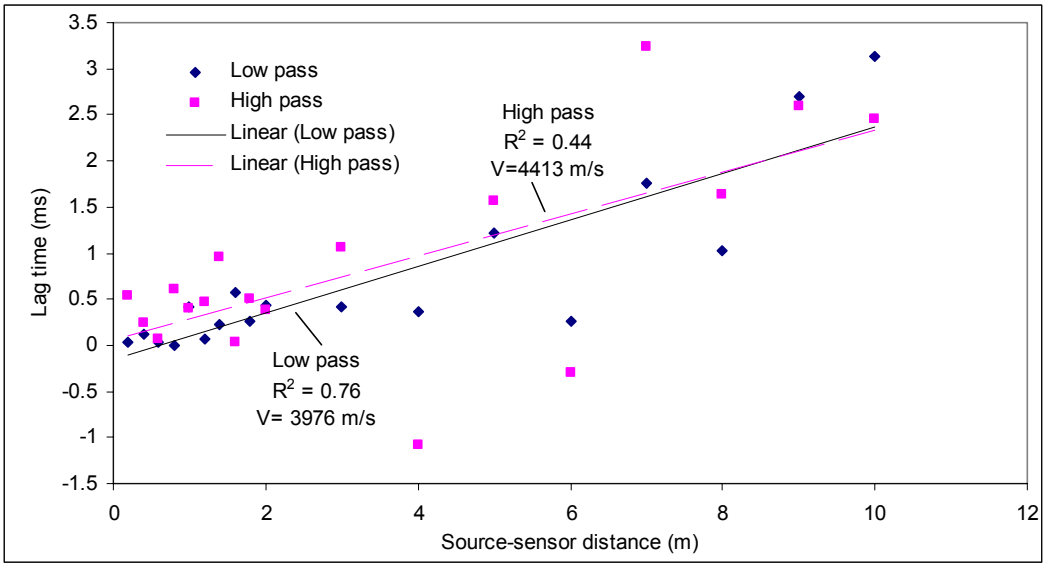

Figure 6.12: Arrival time estimation for high and low pass filter for semi-continuous source for pipe 18m length

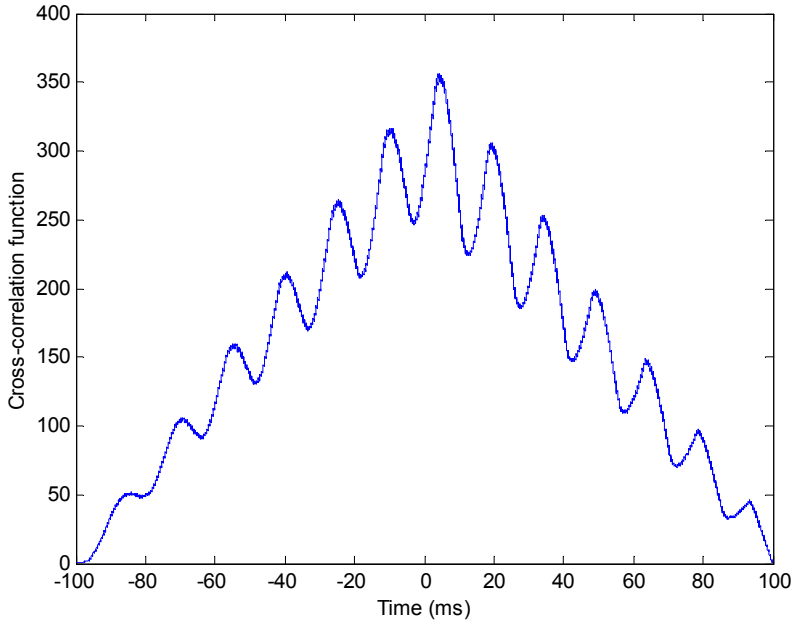

Figure 6.13: Cross-correlation function at 10m from semi-continuous source band pass filtered between 100 and 200kHz for pipe of length 18m

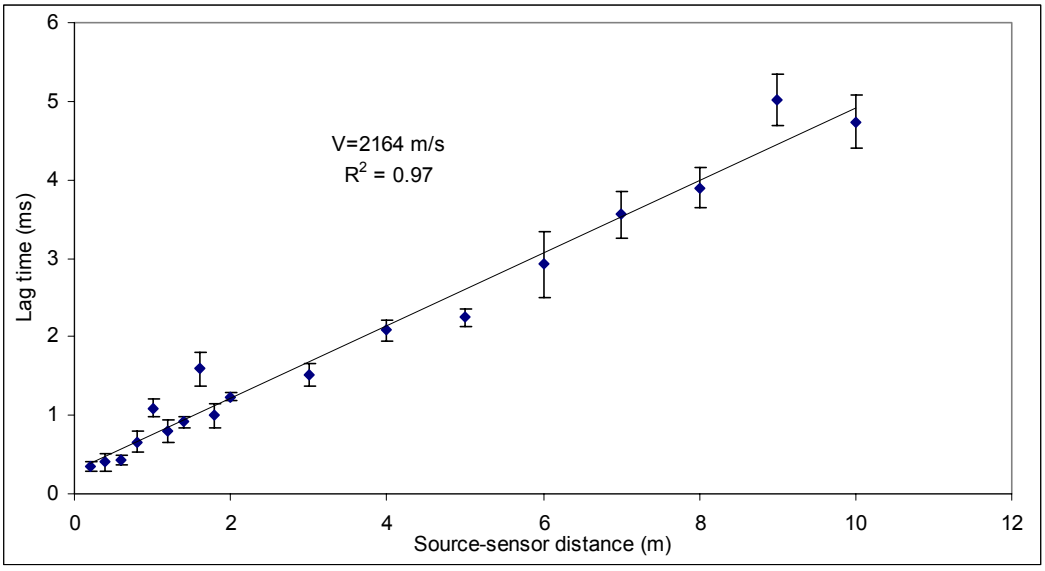

Figure 6.14: Arrival time estimation for band pass filtered (100 to 200kHz) for semi-continuous source for of pipe length 18m

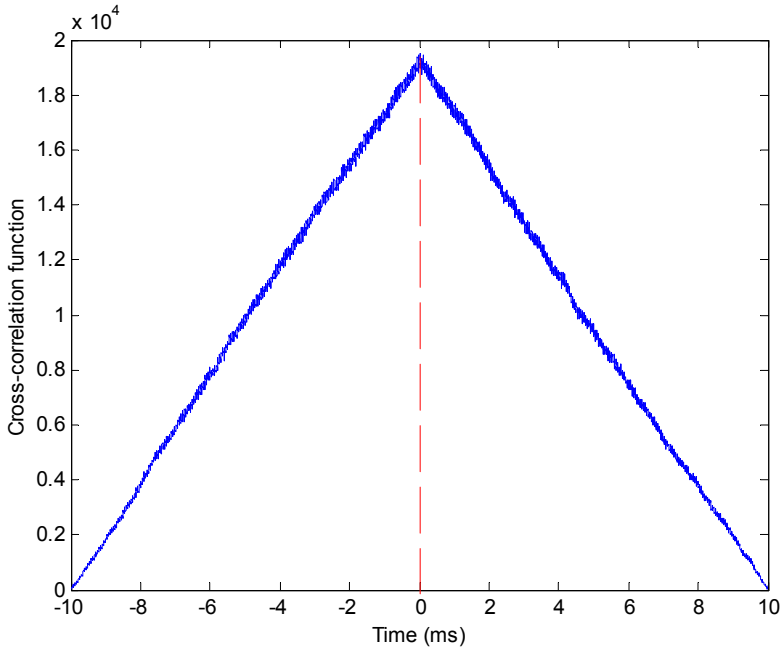

a) 0.2m

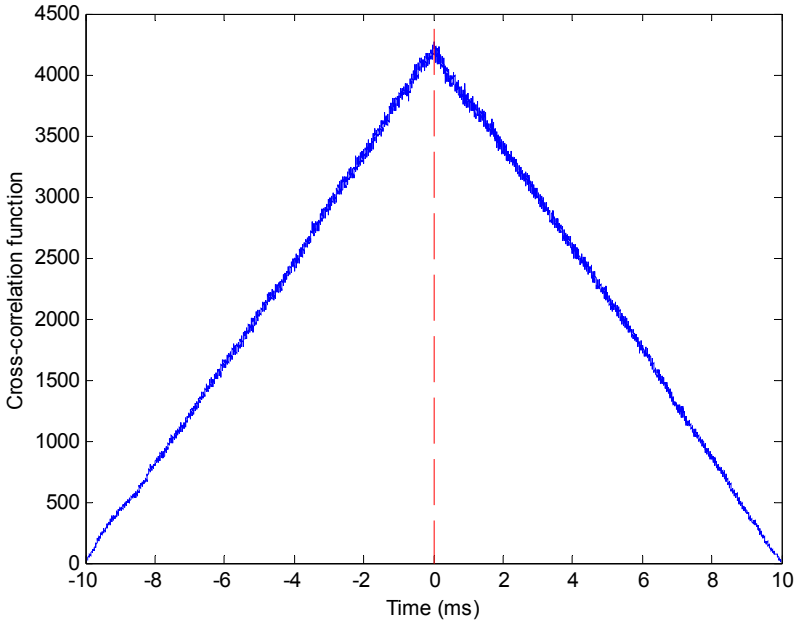

b) 5m

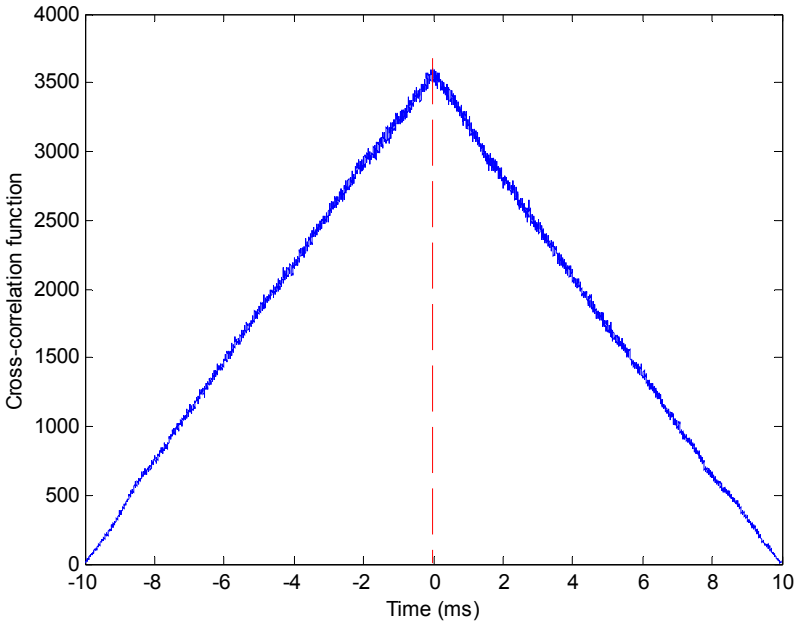

c) 10m

Figure 6.15: Cross-correlation functions for continuous AE sources

6.5 Discussion

Attenuation techniques appear to be suitable for location of continuous and semi-continuous AE sources, and can be improved by filtering. To examine this in more detail a series of experiments were carried out in order to assess the relative

accuracy of the attenuation methods in an actual source location exercise. The small pipe, 48.4mm diameter and 5m long, was set up with the two sensors placed 5m apart and a continuous source produced at distances of 2, 3 and 4m from S2, using S1 as the trigger, with the sensors and source axially aligned. The raw, band pass, and filtered normalised AE energy were then used to locate the source and an averaged location ($\bar{x}_m$) calculated, using Equation 4.2. Using the parameters from Figures 6.6 and 6.9a, the location of the source was calculated and the results are recorded in Table 6.1. As can be seen, removing the relatively un-attenuated component in a continuous source improves the accuracy of location.

Actual distance from Sensor 2	**2m**	**3m**	**4m**	**Error %**
Raw signal	1.02	4.89	0.8895	76.9
Band-pass	2.32	4.228	3.44	37.6
Band-pass/raw signal (normalised)	2.43	3.5	4.08	13.36

Table 6.1: Energy technique using band pass filtering between 300 and 350 kHz to locate the continuous AE source on 5m long pipe

Whereas the energy technique works best with the attenuated components of the signal, cross-correlation works best for the un-attenuated component. However, cross-correlation will only work if there is some temporal structure to the signal, as is the case in the pulsed continuous source.

6.6 Summary

It has been seen here that the factors affecting continuous source location are whether or not it has any temporal structure and whether or not specifically attenuated components can be identified.

The last three chapters have dealt with simulated sources, which have strictly controlled temporal characteristics and are applied at a single point on the pipe. The next chapter is concerned with simulation of more realistic sources which do not have known temporal characteristics.

Chapter 7: Real AE Sources

7.1 Introduction

The focus of this chapter is to examine the behaviour of real sources, where the temporal and, to an extent, spatial distribution of the AE source is less controlled than in the case of the simulated sources in the previous two chapters. The sources chosen are impact from dropped weights and quasi-static crack spreading under 3-point bending. The precise nature of the sources was not known *a priori* but was expected to include impact and plastic deformation of the surface of the pipe in the first series of experiments, and crack-opening and local general plastic deformation in the second series. Analysis techniques are developed in this chapter to extract significant features of the AE signal associated with real sources, based mostly on techniques using energy in the time domain, taking account of the propagation characteristics established in the previous two chapters.

7.2 Impact Test Results

The following subsections cover the three experiments carried out to study the effects of different weights, heights and shapes of indenter on relatively long pipes. For all tests, raw signals were acquired at a sampling rate of 5 MHz for a fixed period of 20ms, and the energy content determined using time domain and frequency domain processing

7.2.1 Spherical Indenter Tests

In these tests, one spherical indenter was dropped from three different heights each using three different weights, each condition being repeated three times on a fresh area of the surface located 1m away from the sensor. A typical impact crater on the pipe surface is shown in Figure 7.1 and impressions were taken for later measurement. The indentation depth and diameter were measured and the volume

determined considering the crater to be a spherical cap using a well-known formula from spherical geometry, the resulting values being shown in Table 7.1. No measurable deformation could be seen for the 1.5kg weight dropped from heights of 0.5m and 1m, and the remaining dimensions were measured to an accuracy of ± 0.25mm using contact devices. Whereas the impressions could, undoubtedly, be measured more accurately, there are, as will be seen later, other sources of variation in the dynamic interaction that make this unnecessary.

Figure 7.1: Typical impact crater of 6mm diameter and 0.83mm depth on pipe surface for 11.5kg load dropped from 1.5m height using spherical indenter

Weight (kg)	**Height (m)**		
	0.5	**1**	**1.5**
1.5	Non measurable	Non measurable	1.06
6.5	5.3	5.2	5.6
11.5	8.85	9.06	11.9

Table 7.1: Volume (mm^3) of spherical indentation on pipe surface for various weights dropped from various heights

To determine the kinetic energy (KE) of the carriage and weight, the speed was measured using a 240 frame/s high speed camera for the 1.5kg weight dropped from the three different heights. Although, in principle, the mass of a dropped object has no effect on the speed when dropped from a given height, the friction in the carriage guideway may introduce a mass-independent retarding force. This

friction can be assumed to be constant for all tests and can be determined from the following equation:

$$F_g - F_f = ma \tag{7.1}$$

where F_f is the total friction force;

$F_g = g.m$;

a is acceleration; and

m is the mass of the dropped object.

Since the carriage starts from rest, the impact velocity, v is given by:

$$v = \sqrt{2as} \tag{7.2}$$

and hence the kinetic energy at impact:

$$KE = \frac{1}{2} m v^2 \tag{7.3}$$

Values of calculated impact energy, along with the relevant potentional energy ($m.g.h$) which assumes no friction losses, are shown in Table 7.2. Figure 7.2 shows the indentation volume plotted against the calculated kinetic energy of impact, and it is clear that a relationship exists.

Weight (kg)	**Height (m)**		
	0.5	**1**	**1.5**
1.5	2.6 (7.3)	5.5 (14.7)	9.7 (22)
6.5	27 (32)	54.5 (64)	83 (95.6)
11.5	51.4 (56.4)	101.4 (113)	156.6 (169)

Table 7.2: Kinetic (and potential) energies (J) for weights dropped from different heights

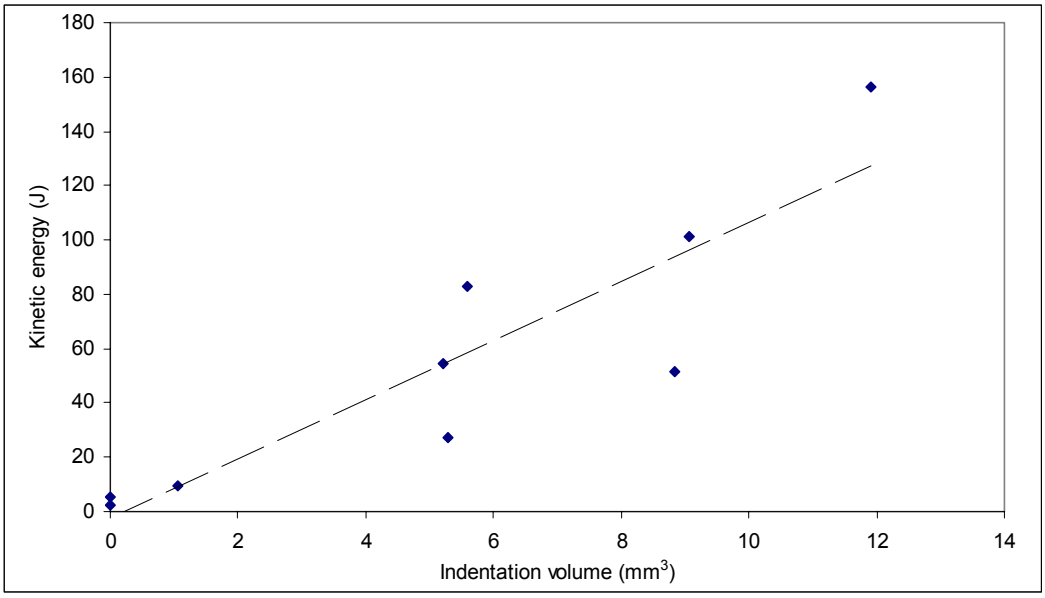

Figure 7.2: Kinetic energy and volume of surface indentation (crater) for various weights dropped from various heights

Typical raw AE signals obtained from the impact tests for 1.5kg, 6.5kg and 11.5kg dropped from different heights are shown in Figures 7.3, 7.4 and 7.5 respectively. For the 1.5kg weight dropped from all heights and 6.5kg dropped from 0.5m, it is difficult to discern the initial impact, whereas, for the remainder, a clear gap can be seen between around 2ms and a return time which appears to vary with impact energy. Figure 7.6 shows normalized spectra of the AE signals for 1.5kg and 11.5kg dropped from 1m, and it can be seen that only a relatively broad band low frequency component appears at around 100 kHz.

On the basis of the above inspection and to understand the changing AE signal with time, the cumulative energy was determined by adding discrete elements evaluated over a time window of 20μs and the average of the resulting evolutions are plotted in Figures 7.7, 7.8 and 7.9 for the first 10ms of the signal. For the heaviest weight (Figure 7.9), there is a clear stratification of energy, even within the first 10ms, four distinct phases being discernible with boundaries at t_1, t_2, t_3 and t_4. These phases become less easy to discern as the kinetic energy falls (Figures 7.7 and 7.8), but it is possible to extract some features from the curves, the simplest being the return time (t_4) and the slope of AE energy evolution with time in Phase III, which can be ascertained for some of the conditions, the results being shown in Figures 7.8 and 7.9.

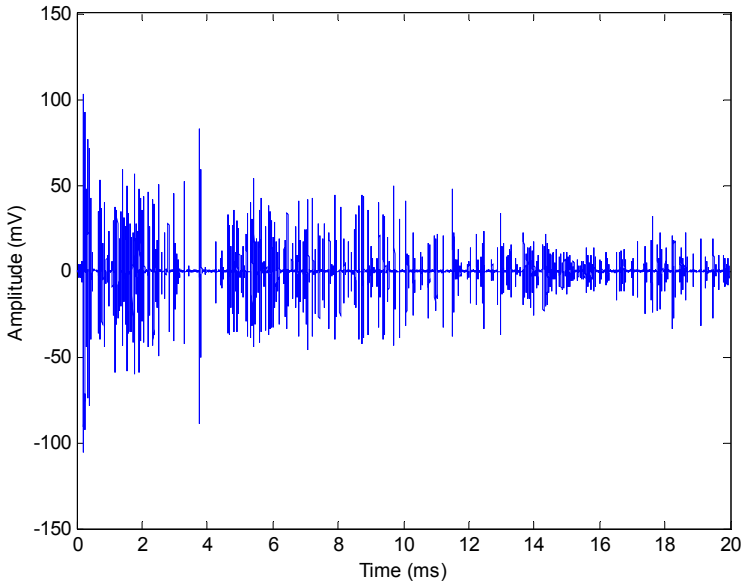
150
100
50
0
-50
-100
-150
Amplitude (mV)
0
2
4
6
8
10
12
14
16
18
20
Time (ms)

a:0.5m

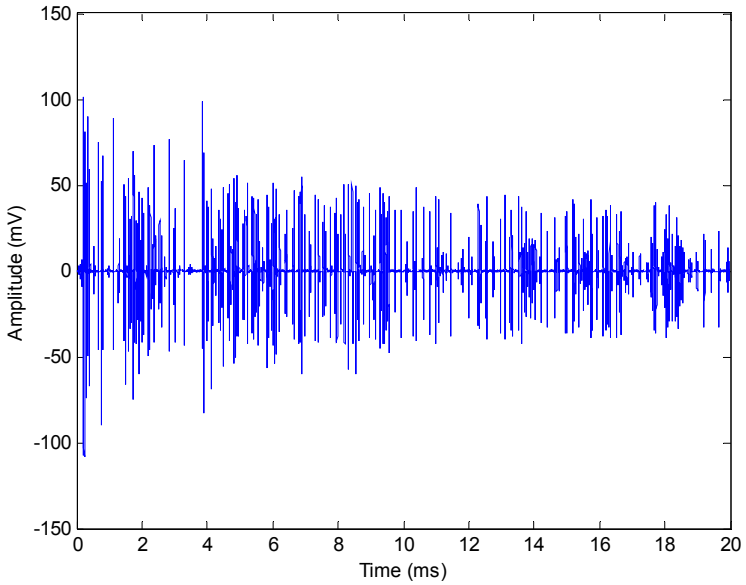
150
100
50
0
-50
-100
-150
Amplitude (mV)
0
2
4
6
8
10
12
14
16
18
20
Time (ms)

b:1m

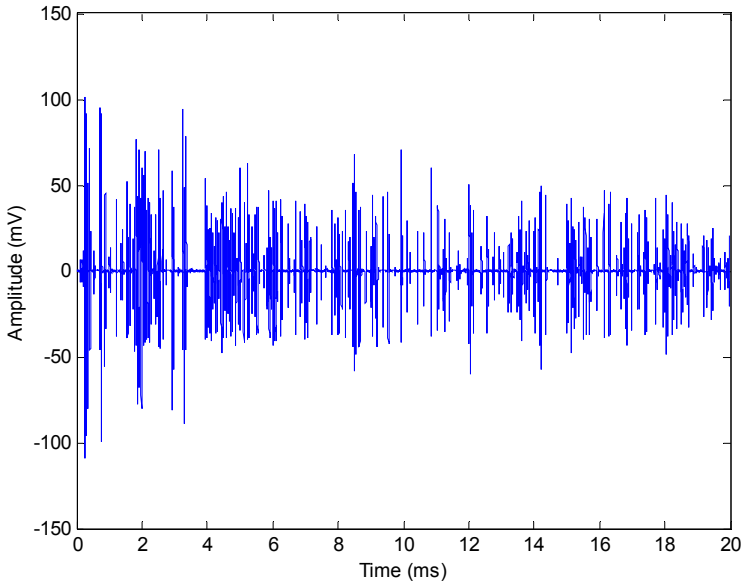

c:1.5m

Figure 7.3: Typical raw AE signal for 1.5kg dropped from different heights

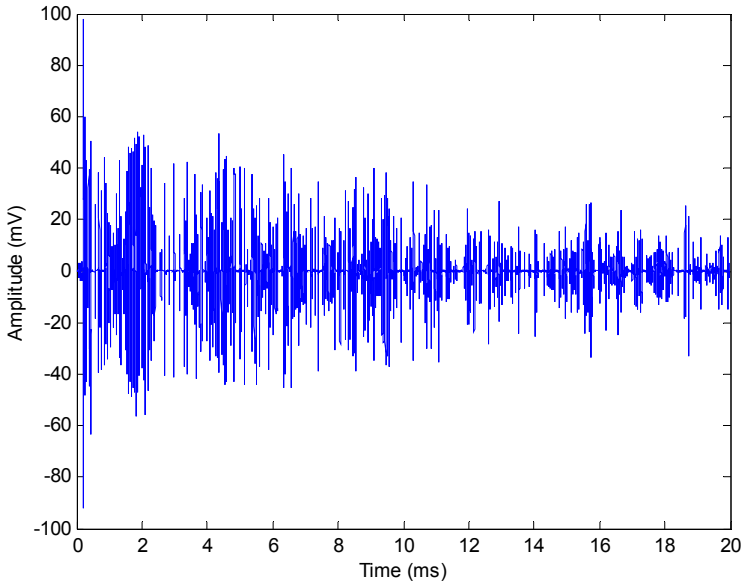

a:0.5m

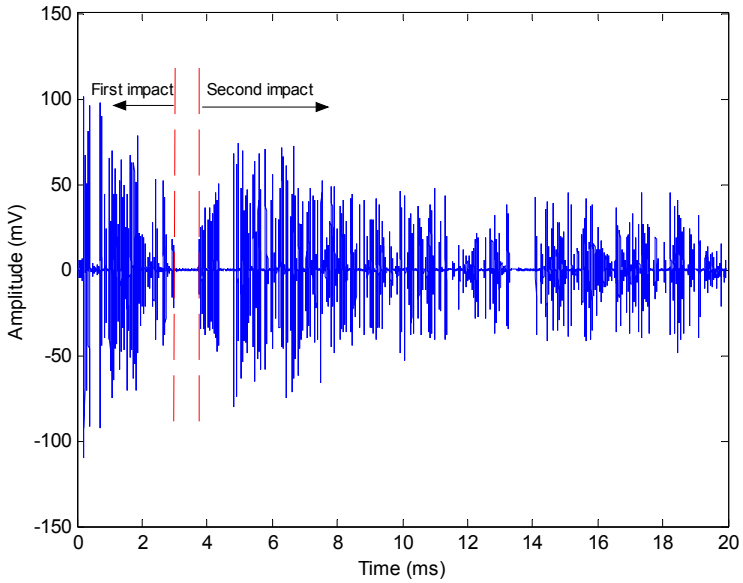

b:1m

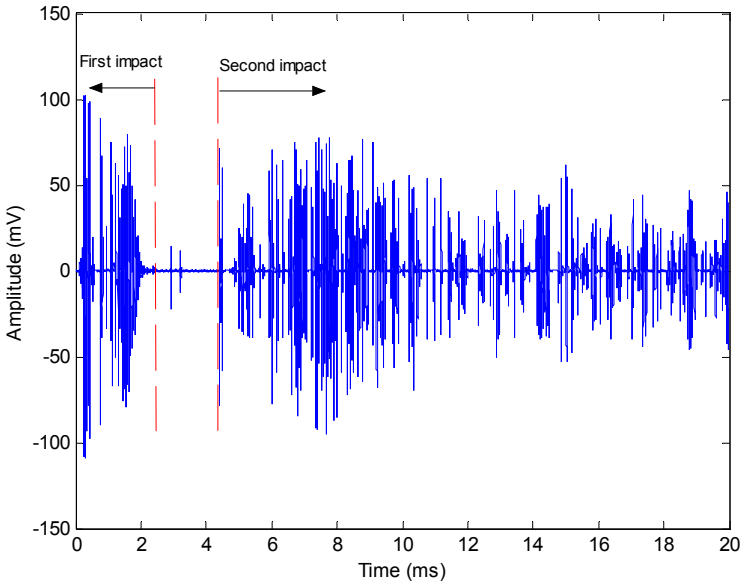

c:1.5m

Figure 7.4: Typical raw AE signal for 6.5kg dropped from different heights

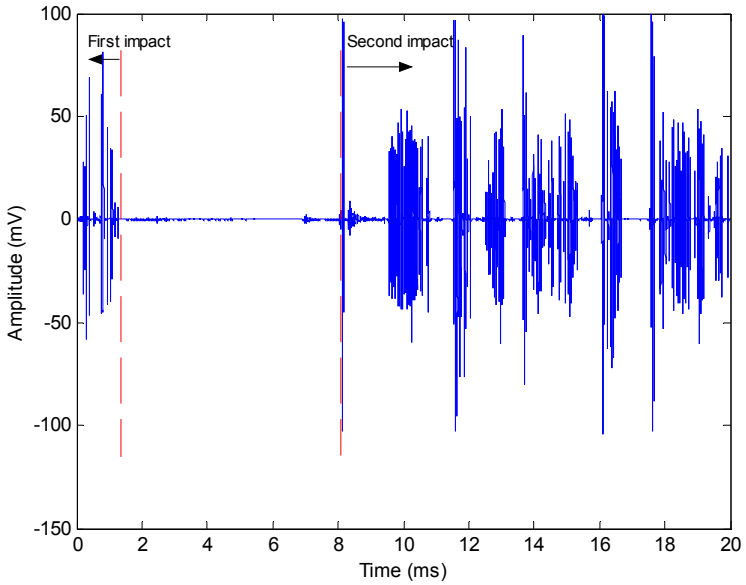
First impact
Second impact
Amplitude (mV)
Time (ms)
100
50
0
-50
-100
-150
0
2
4
6
8
10
12
14
16
18
20

a:0.5m

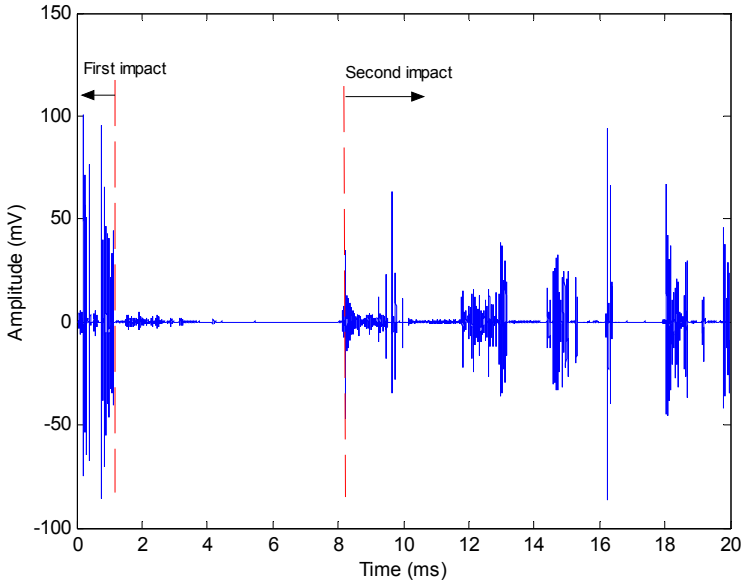
First impact
Second impact
Amplitude (mV)
Time (ms)
150
100
50
0
-50
-100
0
2
4
6
8
10
12
14
16
18
20

b:1m

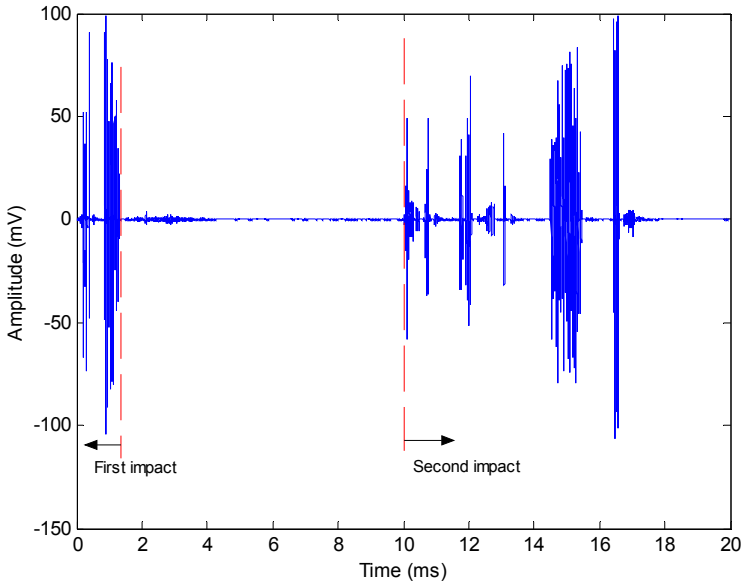

c:1.5m

Figure 7.5: Typical raw AE signal for 11.5kg dropped from different heights

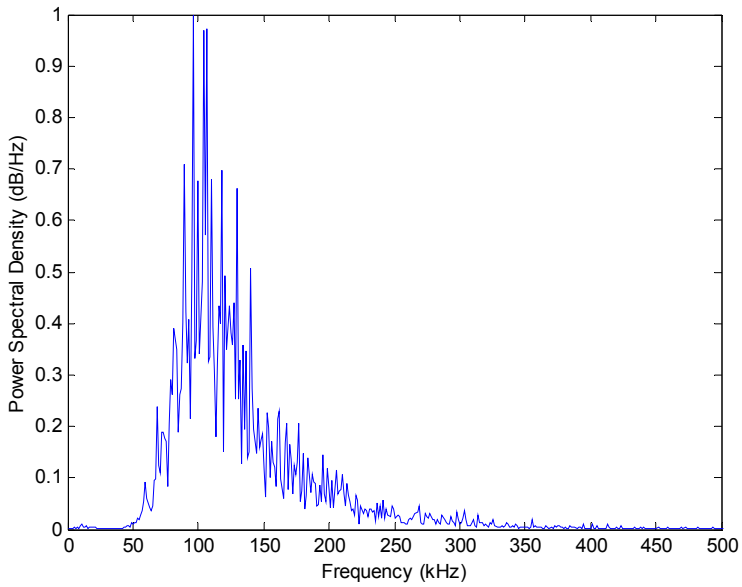

a: 1.5kg

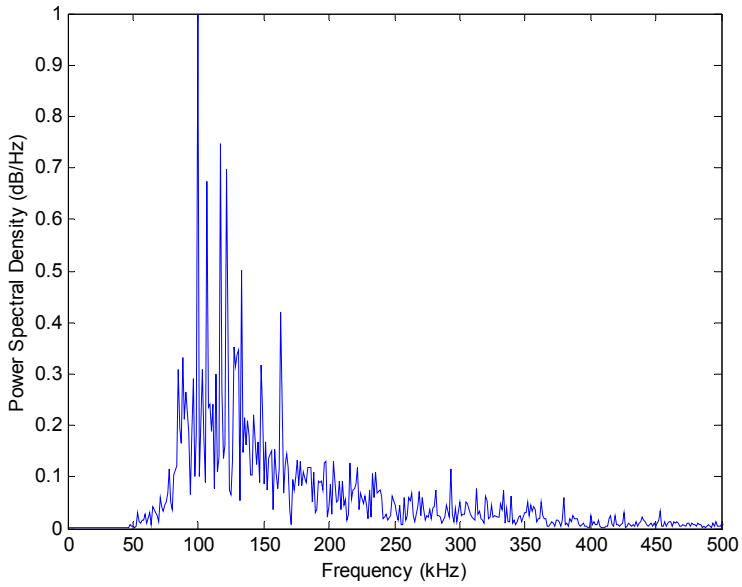

b: 11.5kg

Figure 7.6: Typical normalized frequency for 1.5kg and 11.5 kg dropped from 1.5m

As a working hypothesis, it can be supposed that the first impact happens during Phases I and III and that Phase IV represents a second impact after the indenter has bounced off the surface and then returned. Accordingly, the energy of Phases I and II, Phase III and all three phases is plotted against the impact kinetic energy in Figures 7.10 to 7.12, respectively, although it might be noted that the data for 1.5kg dropped from 0.5m and 1m, and 6.5kg dropped from 0.5m did not show clear enough separation of phases to be included in these plots. The AE is not directly related to KE, except when considering each mass separately, the AE energy seemingly depending on the height independently of the kinetic (or potential) energy. Similarly, the relationship between AE and indentation volume, as shown in Figures 7.13 to 7.15, exhibited a clear relationship only when the masses were considered separately. In contrast, the return time (t_4), shown in Figure 7.16, does show a clear relationship to kinetic energy for those conditions where t_4 can be determined. Taken together, these observations indicate that there is a dynamic relationship between the indenter and pipe and that, whereas the AE is probably related to the impact energy, a clearer way of separating first impact from recoils needs to be determined.

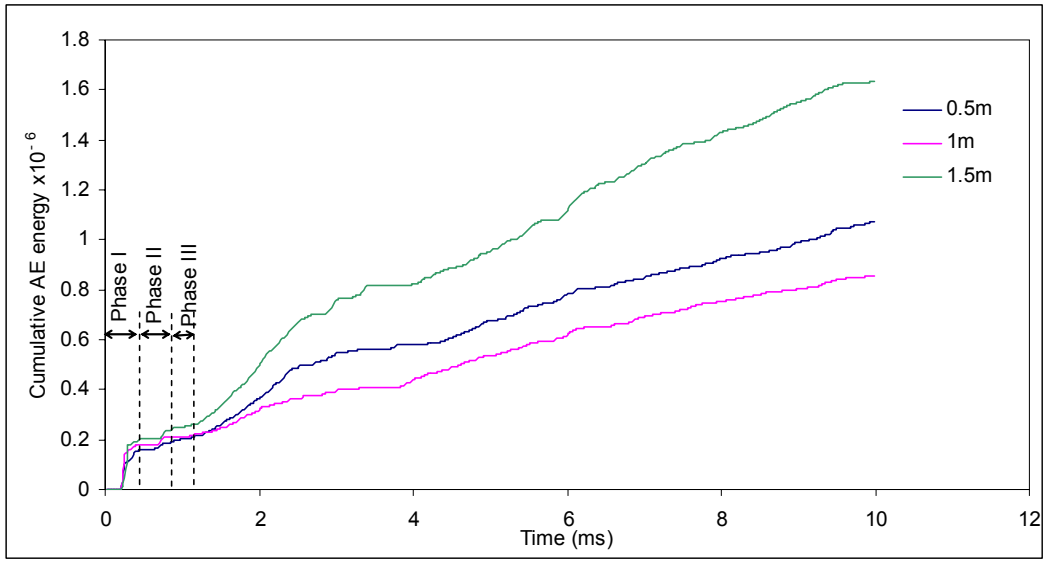

Figure 7.7: Cumulative AE energy for 1.5kg dropped from different heights using spherical indenter

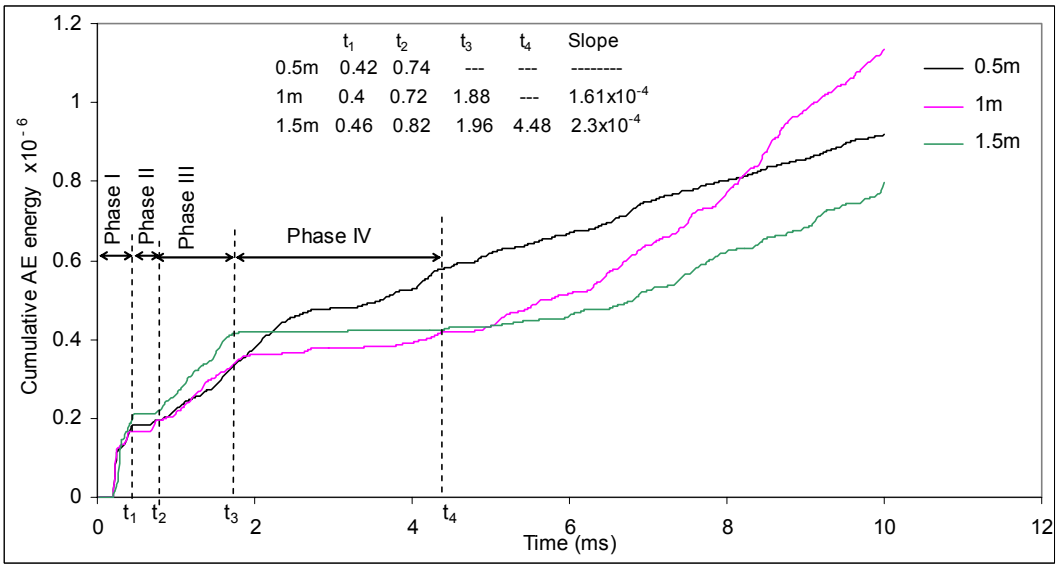

Figure 7.8: Cumulative AE energy for 6.5kg dropped from different heights using spherical indenter

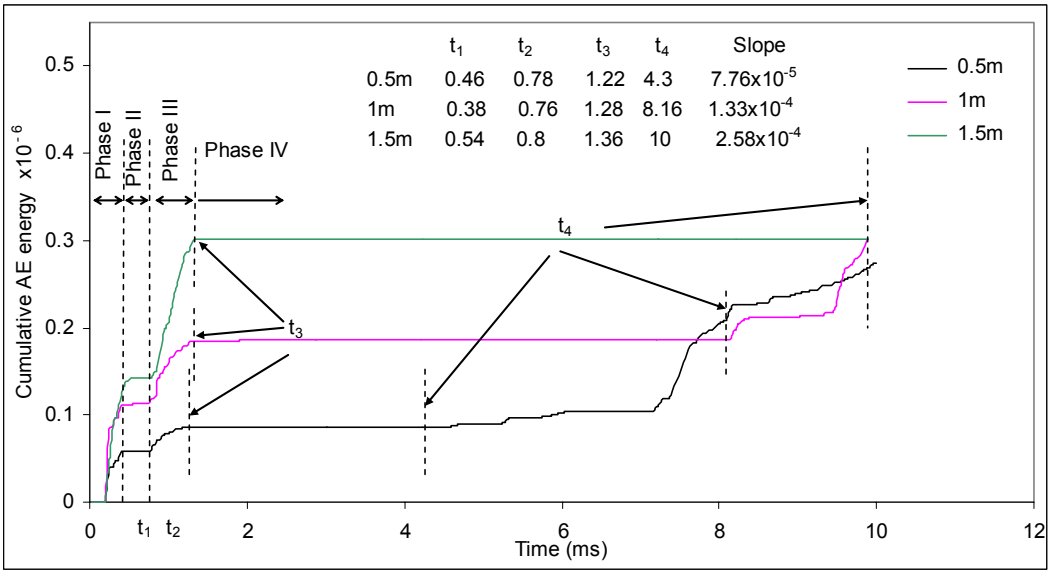

Figure 7.9: Cumulative AE energy for 11.5kg dropped from different heights using spherical indenter

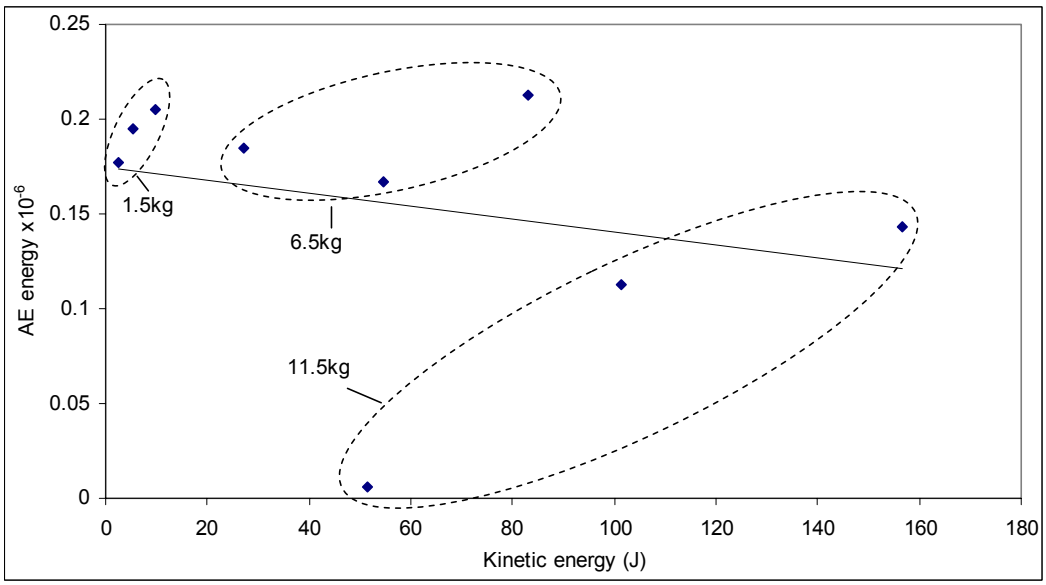

Figure 7.10: Kinetic energy and AE energy for Phases I and II using spherical indenter

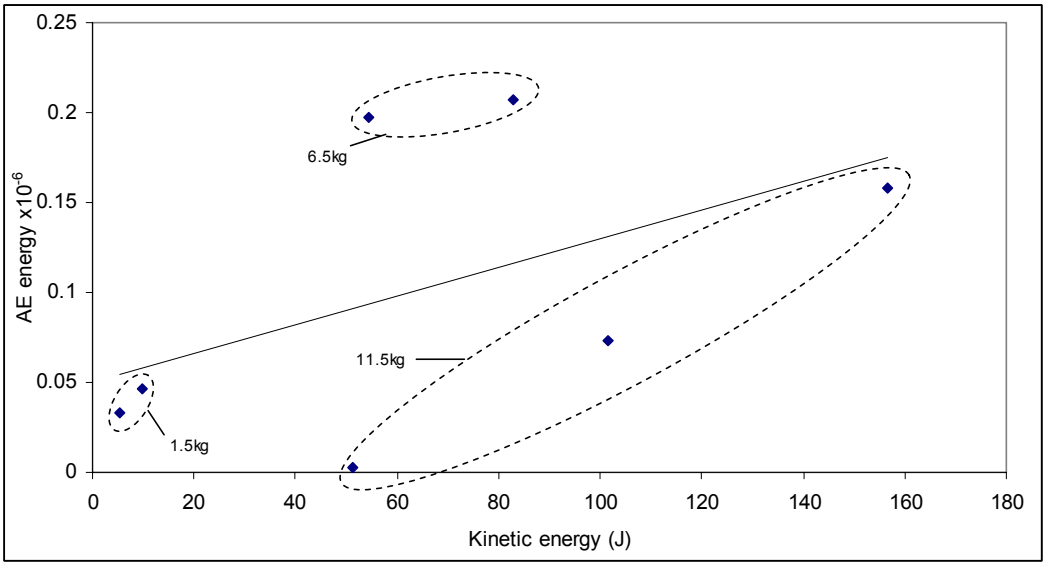

Figure 7.11: Kinetic energy and AE energy for Phase III using spherical indenter

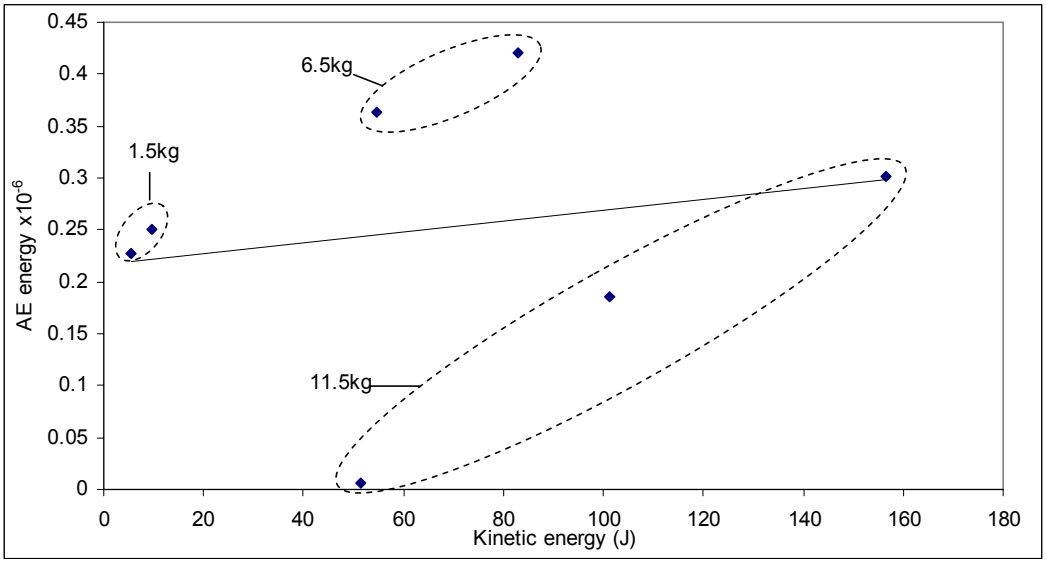

Figure 7.12: Kinetic energy and AE energy for Phases I, II, III and IV using spherical indenter

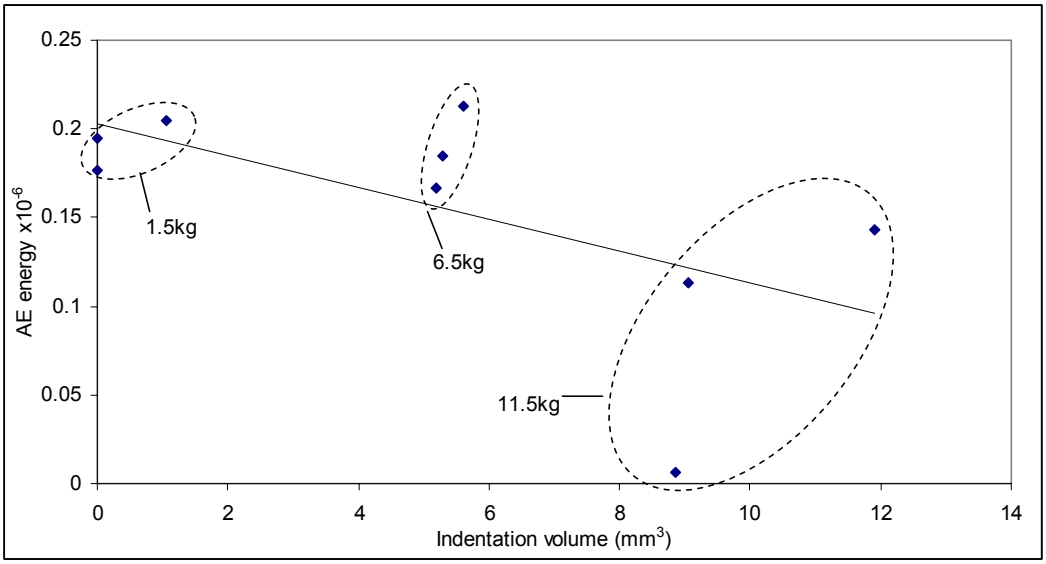

Figure 7.13: Indentation volume and AE energy for Phases I and II using spherical indenter

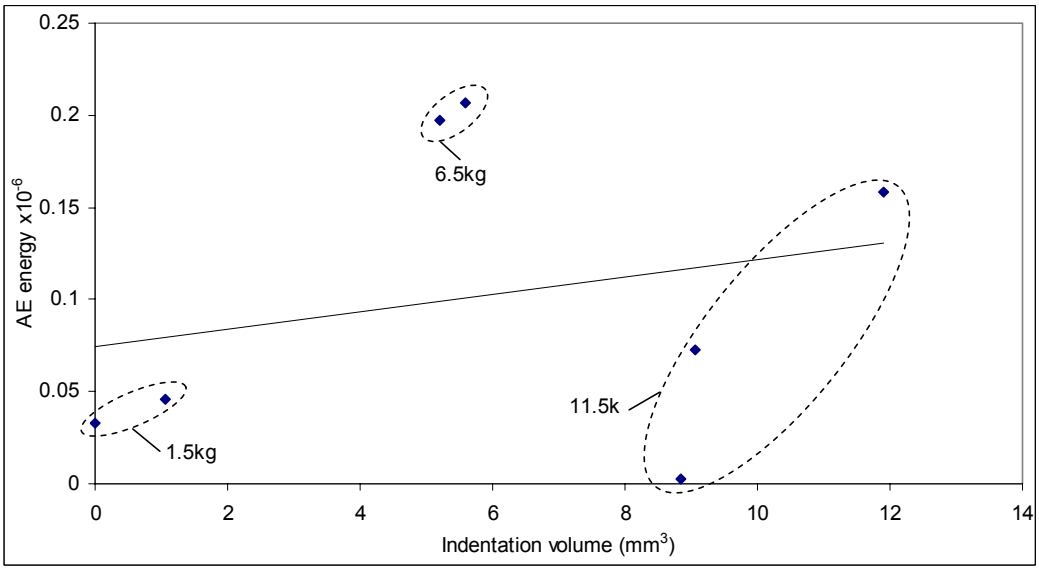

Figure 7.14: Indentation volume and AE energy for Phase III using spherical indenter

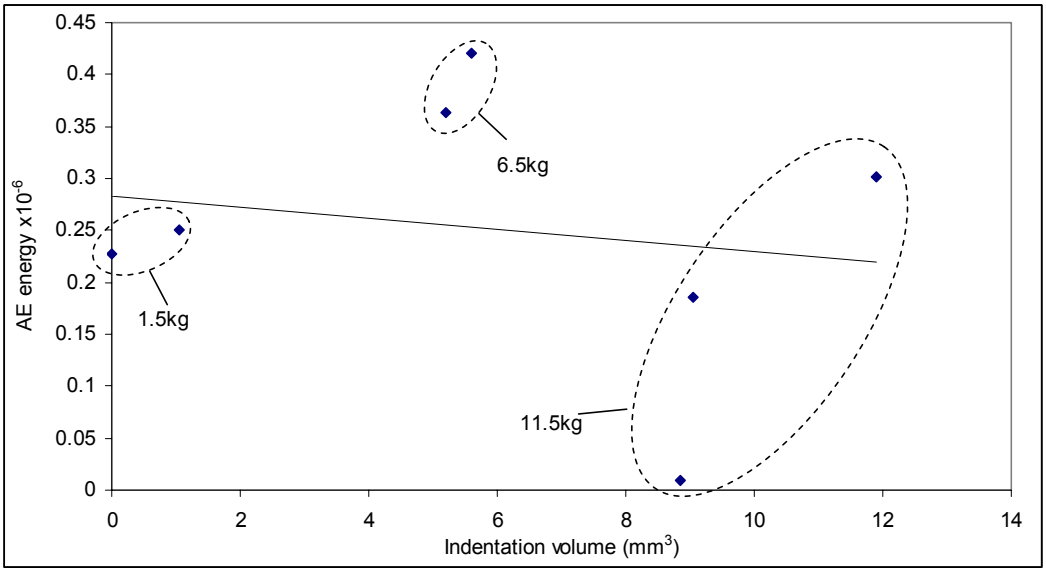

Figure 7.15: Indentation volume and AE energy for Phases I, II, III and IV using spherical indenter

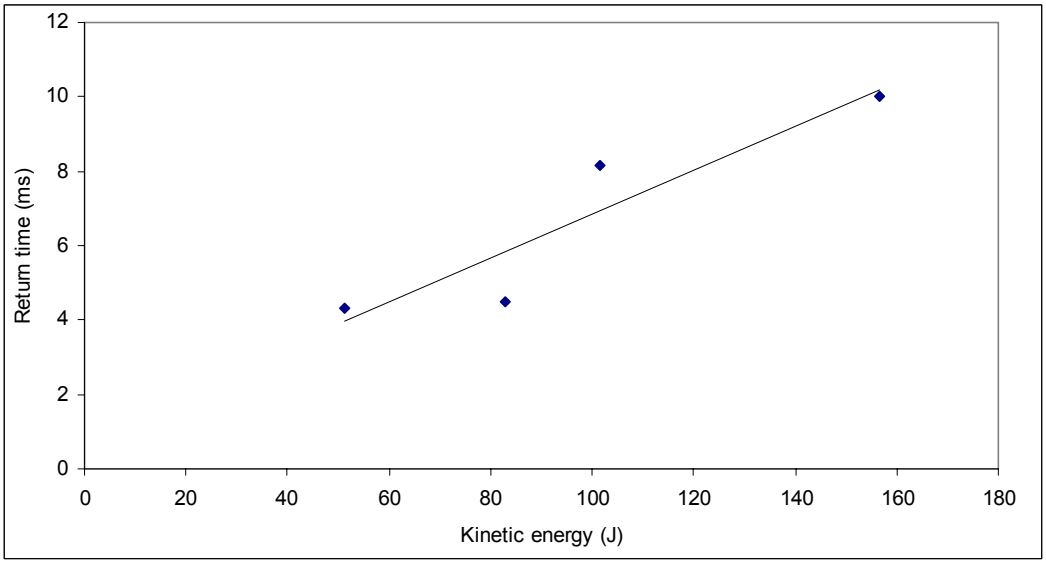

Figure 7.16: Kinetic energy and return time (t_4) using spherical indenter

7.2.2 Conical Indenter Tests

Only two weights and two heights were used with conical indenters, although, in this test, the indenter was mounted on the load cell, and the resulting measured forces are shown in Figure 7.17. It is clear from Figure 7.18 that the height of the first peak is related to the kinetic energy of the indenter. In these tests, the surface indentation was insignificant although the deformation of the indenter was not, as

shown in Figure 7.19. Accordingly the volumetric strain of the indenter was determined and is plotted against kinetic energy in Figure 7.20, showing that maximum load, kinetic energy and volumetric strain are related.

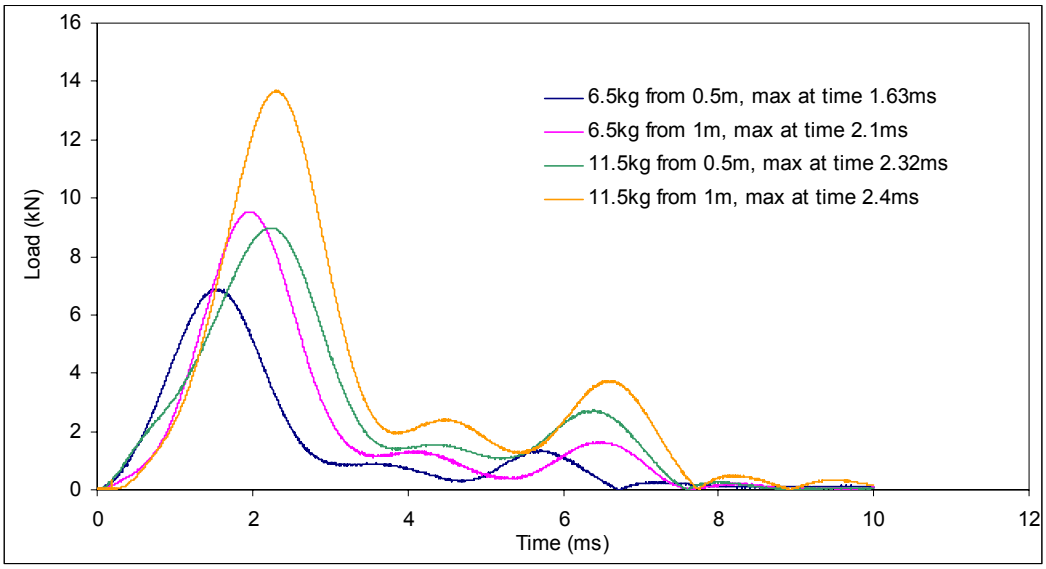

Figure 7.17: Loads for different weight and heights using conical indenter

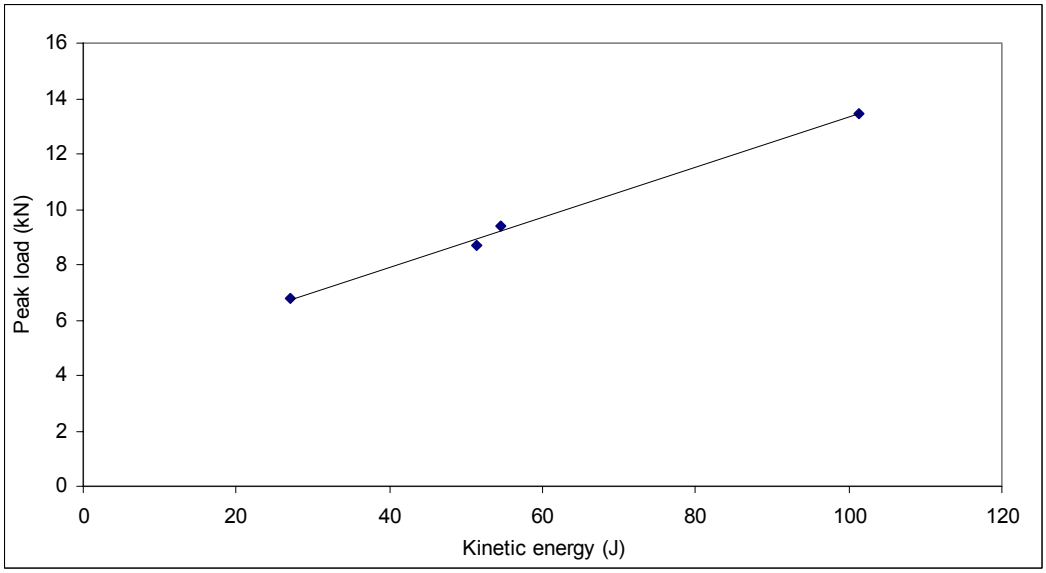

Figure 7.18: Impact load and kinetic energy using conical indenter

Figure 7.19: Conical indenters after impact, a) 6.5kg (0.5m), b) 6.5kg (1m), c) 11.5kg (0.5m) and d) 11.5kg (1m)

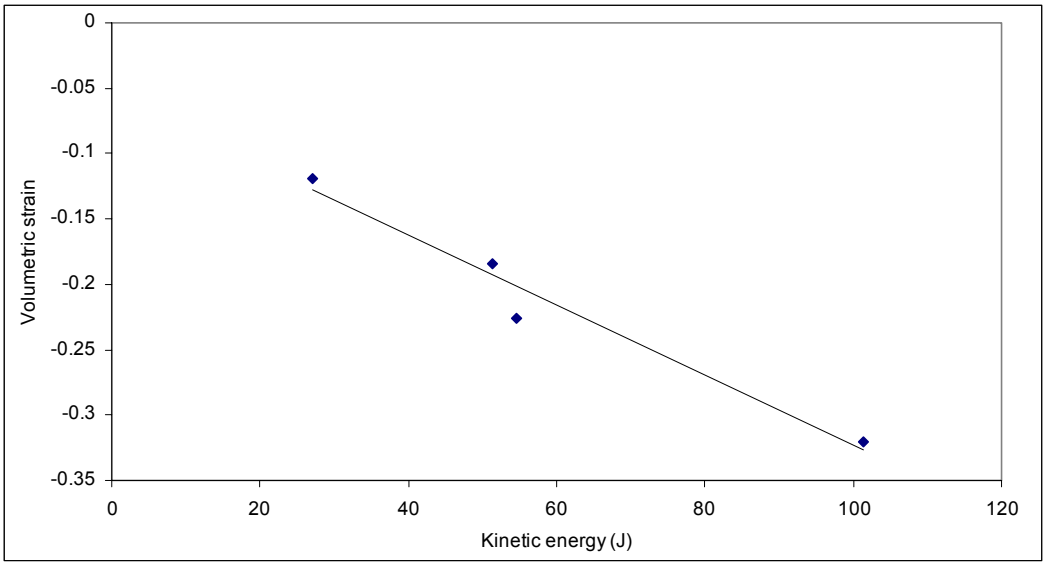

Figure 7.20: Kinetic energy and volumetric strain using conical indenter

Figures 7.21 and 7.22 show typical raw AE signals, where the first impact can be clearly seen, its termination corresponding to the peak in the force curves (Figure 7.17). As before, the cumulative energy has been determined using discrete time windows of 20μs, and the results are plotted in Figure 7.23. Here, Phases I, II, and III are difficult to distinguish although the end of Phase III can be identified clearly on each curve. Accordingly, the load curve (Figure 7.17) was used to identify the time of impact, and the area up to maximum load was determined and plotted against the cumulative AE up to same time for maximum load, as shown in Figure 7.24. Figure 7.25 shows the return time (t_4), plotted against kinetic energy. These observations show that the relationship between impact energy and AE energy is

not simple where the expected relationship between kinetic energy, volumetric strain and impulsive force, is shown only for the drop heights, pointing to an uncontrolled experimental variable affecting the AE energy. This could include uncontrolled loss of sensor coupling due to the impact or, more likely, inconsistent coupling between the indenter and the metal surface, given that most of the AE is being generated in the indenter as opposed to on the pipe for the spherical indenter.

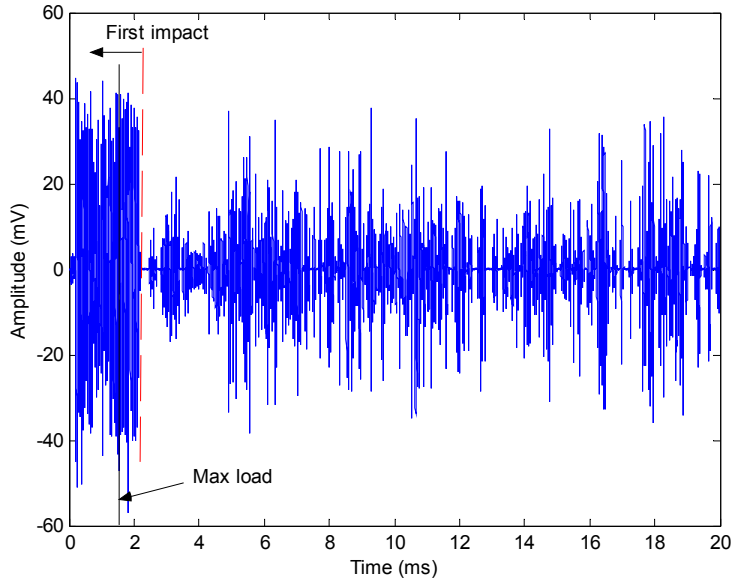

Figure 7.21: Raw AE signal for 6.5kg dropped from 0.5m using conical indenter

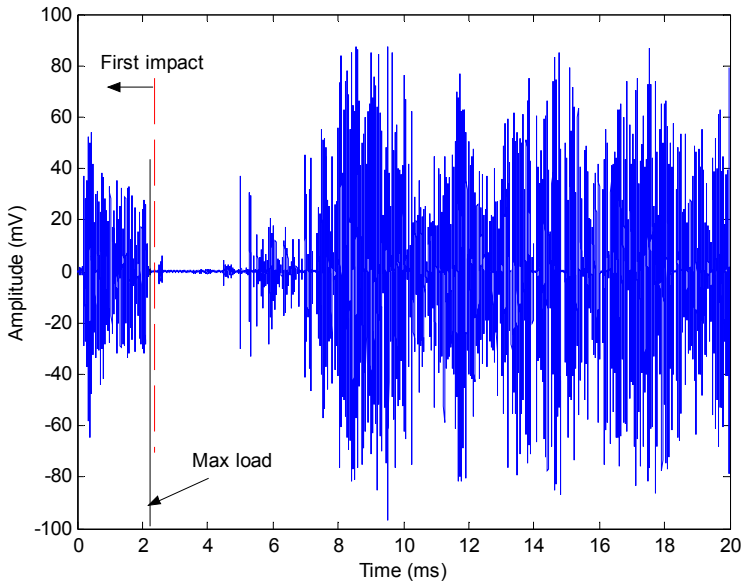

Figure 7.22: Raw AE signal for 11.5kg dropped from 1m using conical indenter

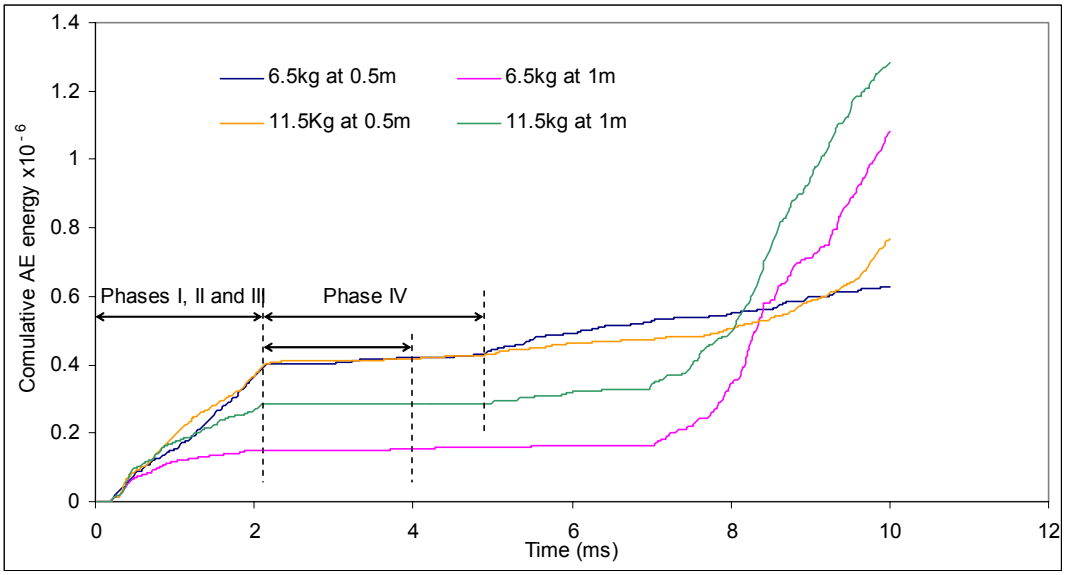

Figure 7.23: Cumulative AE energy for different weights and heights using conical indenter

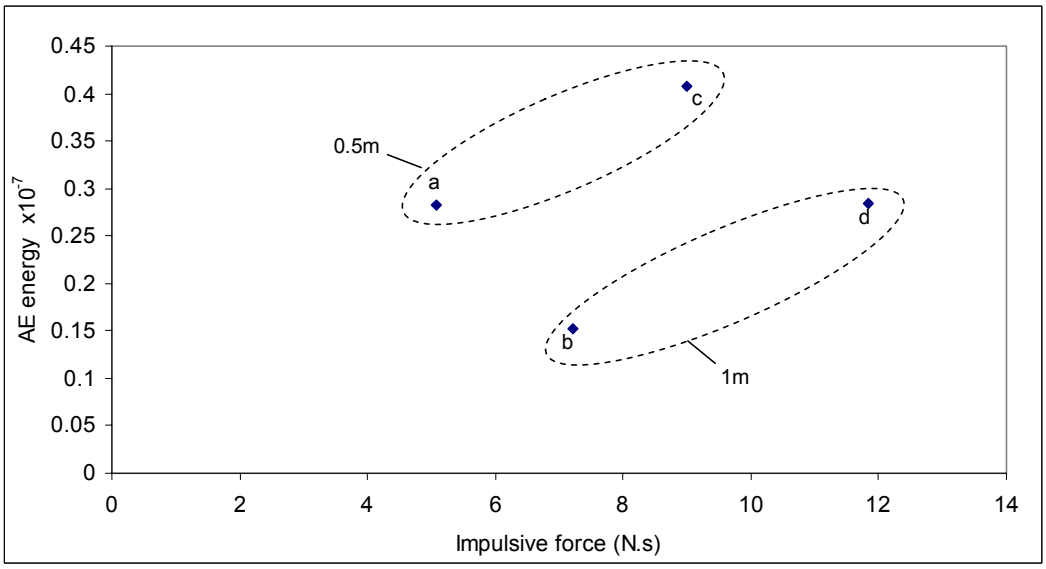

Figure 7.24: AE energy and impulsive force for Phases I, II, III and IV using conical indenter, a) 6.5kg (0.5m), b) 6.5kg (1m), c) 11.5kg (0.5m) and d) 11.5kg (1m)

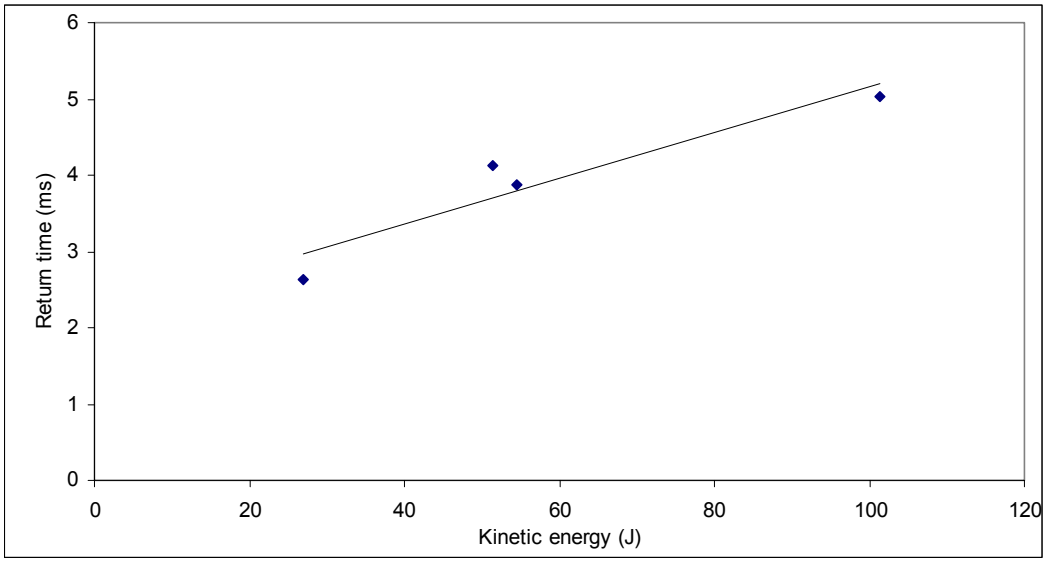

Figure 7.25 : Kinetic energy and the return time (t_4) using conical indenter

7.2.3 Effect of Indenter Shape

From the last two sections it can be seen that the AE signature of impact is affected by changing the indenter shape, as shown, for example in Figures 7.4b and 7.21. To investigate this effect systematically, a fresh conical indenter was dropped from the same height with the same weight a total of five times, and the indenter shapes before and after the experiment is shown in Figure 7.26. Figure 7.27 shows the effect of indenter shape on the raw AE signal, where it can be seen that the density (if not the amplitude) of events for the first impact using the fresh conical indenter is greater than that once the cone has been crushed, and the return time is much shorter for the first drop, probably because the crushing absorbs energy. Figure 7.28 shows the cumulative AE evolution for first drop to be qualitatively different from the remaining four, which all have a plateau after about 0.6ms, regaining the slope after about 0.8ms. The heights of the Phase IV plateau also seem to change between the tests, although there is no systematic order to the changes. It is therefore, concluded that, once an indenter has been used once, the contribution of crushing of the cone to the AE ceases to be significant in comparison with the contribution from deformation of the surface of the pipe. Figure 7.29 shows the first and second plateaux for the cumulative AE evolutions shown in Figure 7.28. It is clear that neither plateau shows a systematic variation with number of drops, although it is possible that drop 4 shows the maximum combination of indenter

crushing and surface determination. It is equally possible, however, that there is a variability in the results due to random effects.

Figure 7.26: Indenter shape before and after five impact tests (not: photograph do not show the same indenter)

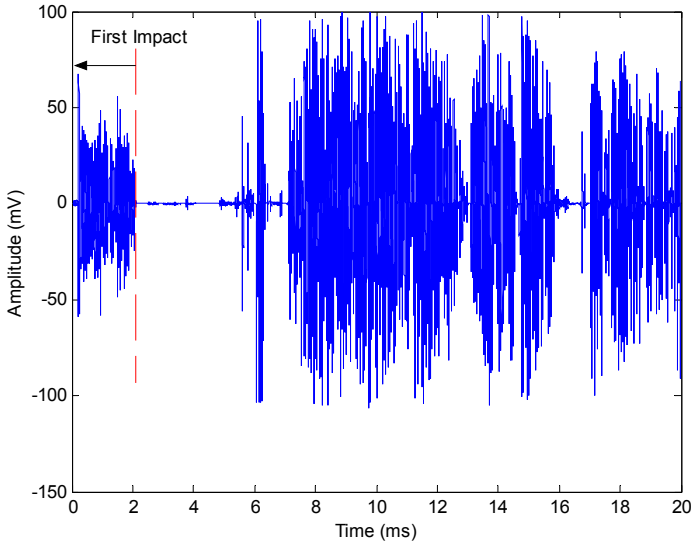

a) Test 1 (conical indenter)

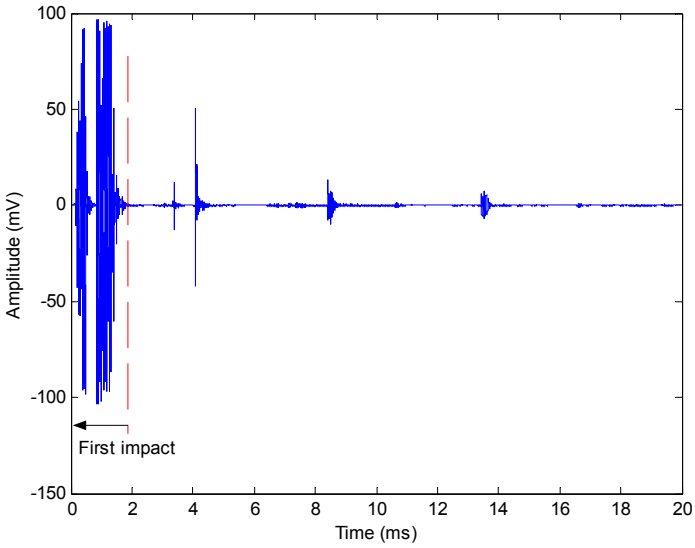

b) Test 3

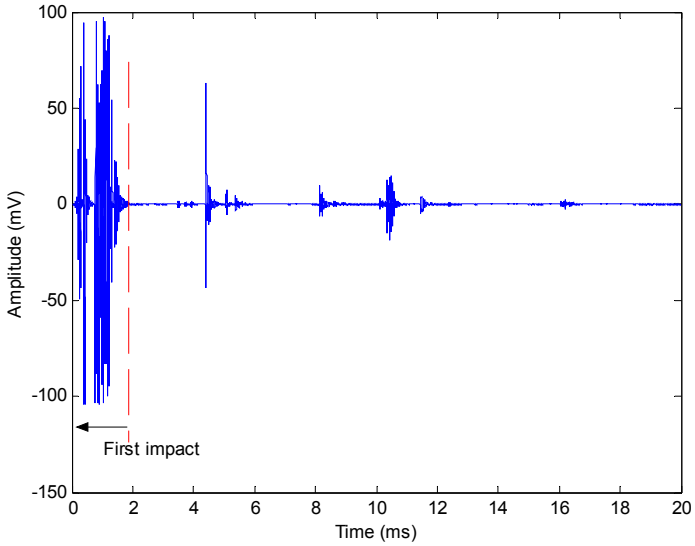

c) Test 5

Figure 7.27: Typical raw AE signals for 11.5kg dropped from 1m height using one indenter

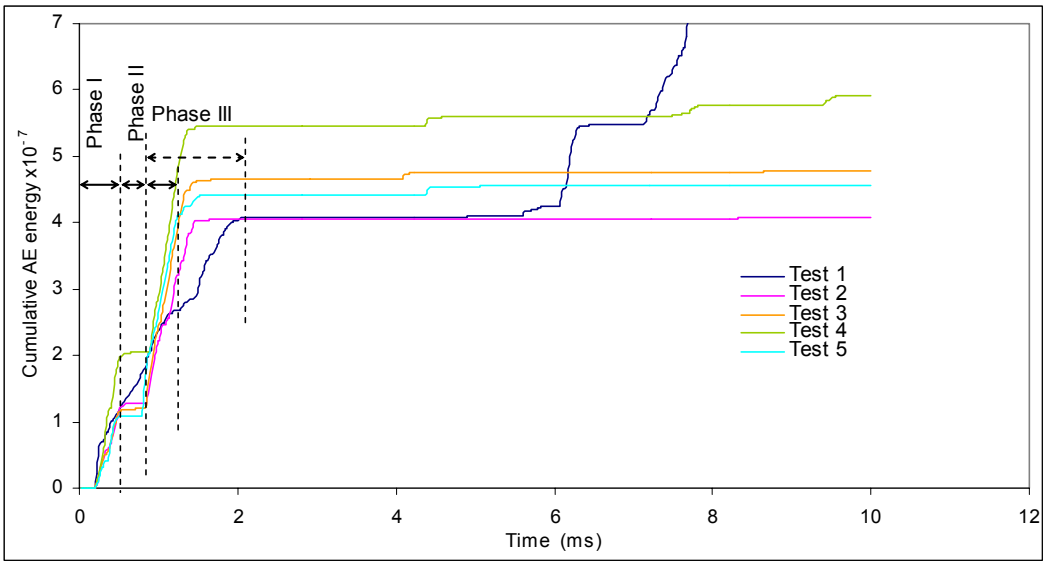

Figure 7.28: Cumulative AE energy for 11.5kg dropped from 1m using one indenter

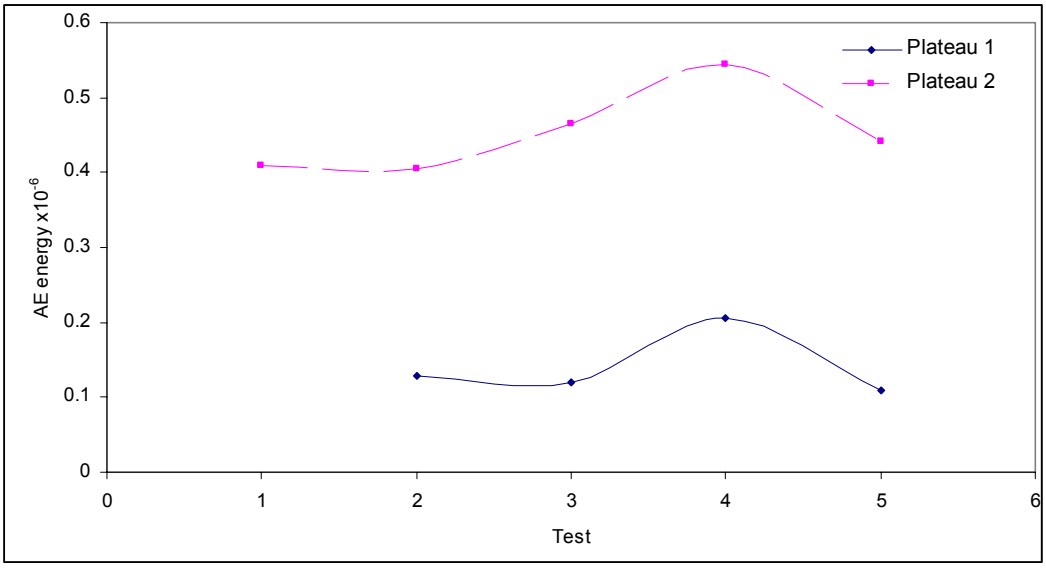

Figure 7.29: AE energy for Phases I, II, and III for all tests

7.3 Three Point Bending Test Results

In the three-point bend test, the load is applied at mid-span, so that the bending moment M in the plane of load application is:

$$M = \frac{Pl}{4} \tag{7.4}$$

where P is the applied load; and

l is the distance between the (simple) supports.

Figure 7.30 shows the notch geometry of a circumferential external defect on a cylinder under bending for which the collapse moment, for $\beta < \frac{\pi}{1+\eta}$ is given by [107]:

$$S_r = \frac{M}{4R^2 h\sigma_f} = \cos\left(\frac{(1-\eta)\beta}{2}\right) - \frac{(1-\eta)\sin\beta}{2} \tag{7.5}$$

where M is the bending moment for plastic collapse (kN.m);

R is the cylindrical radius (m);

h is the wall thickness;

σ_f is the flow stress which can be taken as the average of the tensile and yield strengths (MPa);

Table 7.3 shows the calculated moment to cause collapse and the geometry of the ligament area for the five experiments.

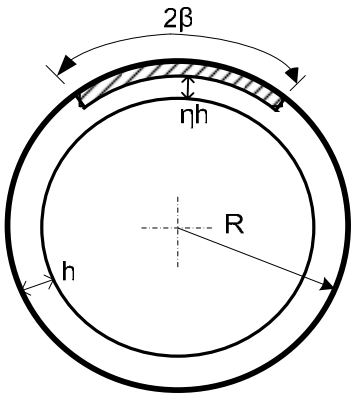

Figure 7.30: Geometry of surface circumferential crack

	Collapse moment (kN.m)	**Ligament length (mm)**	***ηh* (mm)**
Pipe 1	4.75	30.9	4.35
Pipe 2	4.17	41.2	3.35
Pipe 3	3.47	51.5	2.35
Pipe 4	2.95	61.8	1.35
Pipe 5	1.13	76	zero

Table 7.3: Calculated collapse moment and geometry specifications for the ligament area

The AE from the three point bending tests was recorded for a total of 90 seconds, in 1450 batches of 4 ms at a sampling rate of 5 MHz. A typical raw AE batch is shown in Figure 7.31 and Figure 7.32 shows a normalized frequency domain plot of the same batch. Unlike the indentation tests (Figure 7.5) the energy is now mostly in a high frequency band around 350 kHz, although some peaks are present at 100-150 kHz.

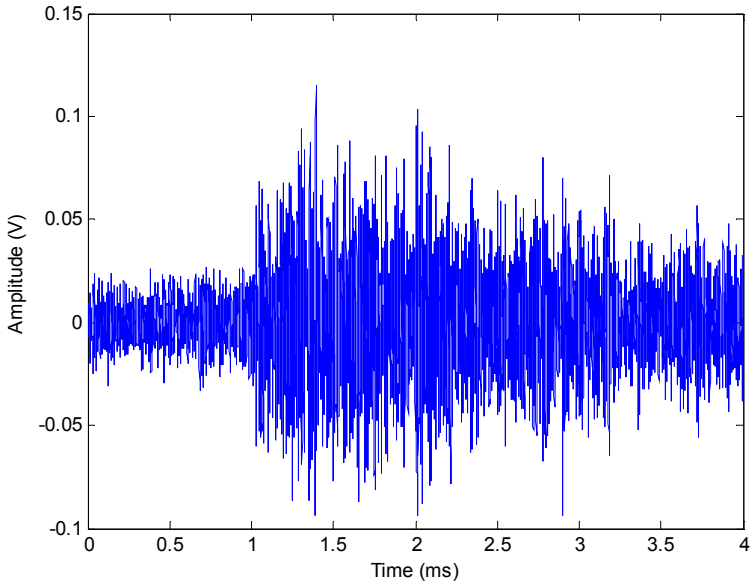

Figure 7.31: AE raw signal in 3-point bending recorded at a deflection of 3.22 mm on Pipe 2

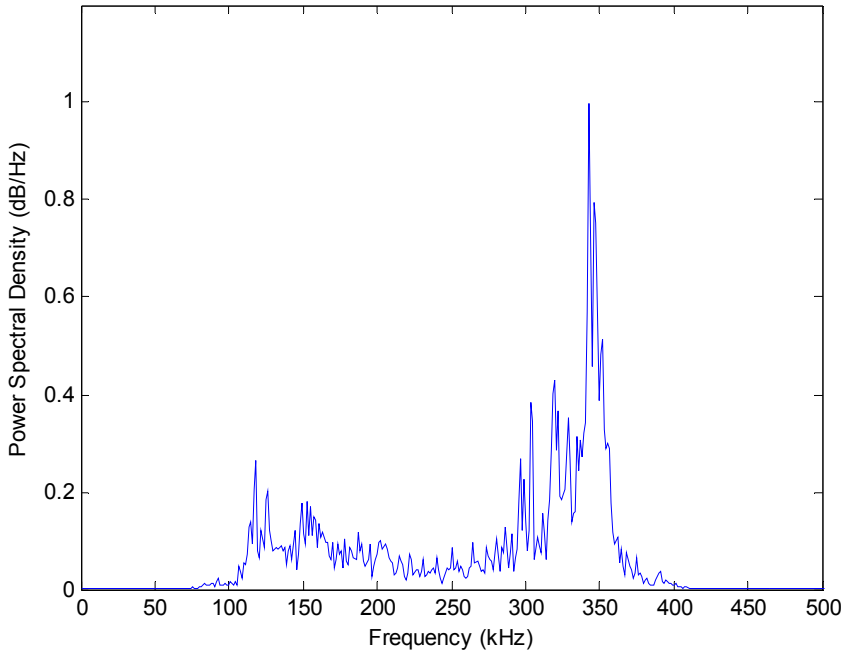

Figure 7.32: Normalized frequency in 3-point bending recorded at a deflection of 3.22 mm on Pipe 2

Figure 7.33 shows a typical two stage failure of one of the pipe samples. As can be seen, the mechanical notch first pops through the wall and subsequently propagates circumferentially around the pipe, the latter having all the features of ductile tearing as opposed to fracture. Figure 7.34 shows the maximum measured moment from the load-deflection curve plotted against the calculated collapse moment from

Equation 7.5. As can be seen, the measure failure moment is generally above that calculated consistent with the slight underestimate of yield stress and its which would be expected when using specifies values. The smaller difference for pipes with smaller defects suggests a shift from failure by plastic collapse to failure by fracture at smaller defect sizes.

Figure 7.35 shows the load-deflection curves for each of the samples, along with the time evolutions of the AE (integrated for each batch of 4ms). The load-deflection curves have a characteristic shape, which has been divided into four zones:

Zone I: Elastic deformation of pipe.

Zone II: Plastic deformation of pipe, expected to be most intense at the root of the notch.

Zone III: Pop-through of notch (fast ductile fracture).

Zone IV: Extension of popped-through crack around circumference (ductile tearing) and plastic deformation of remaining pipe wall ligament.

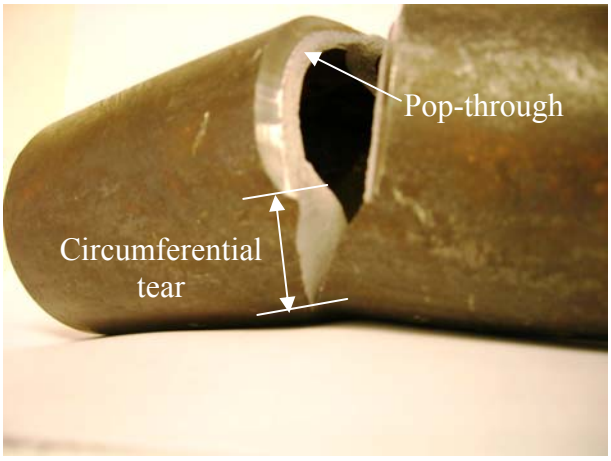

Figure 7.33: Typical pipe failure from 3-point bend test

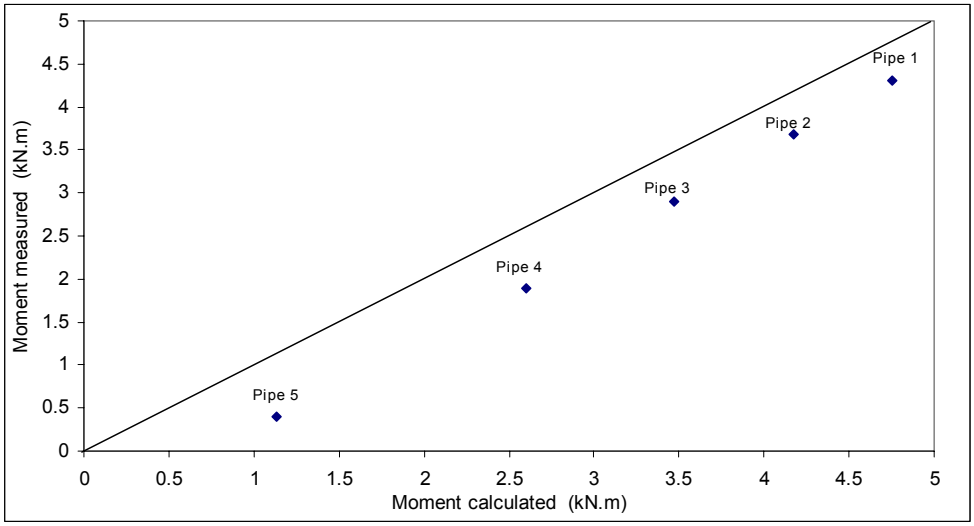

Figure 7.34: Measured and calculated failure conditions for circumferential defects in pipes under bending

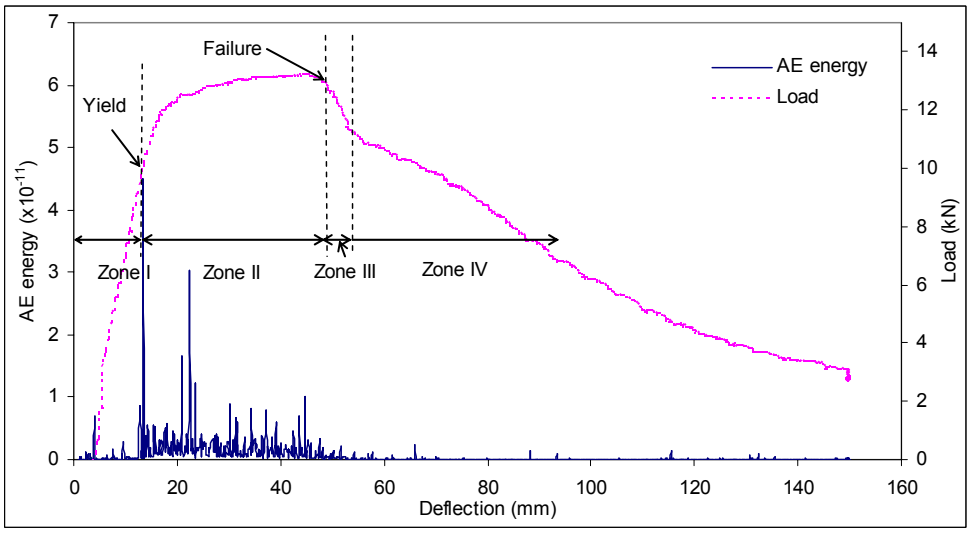

a) Pipe 1

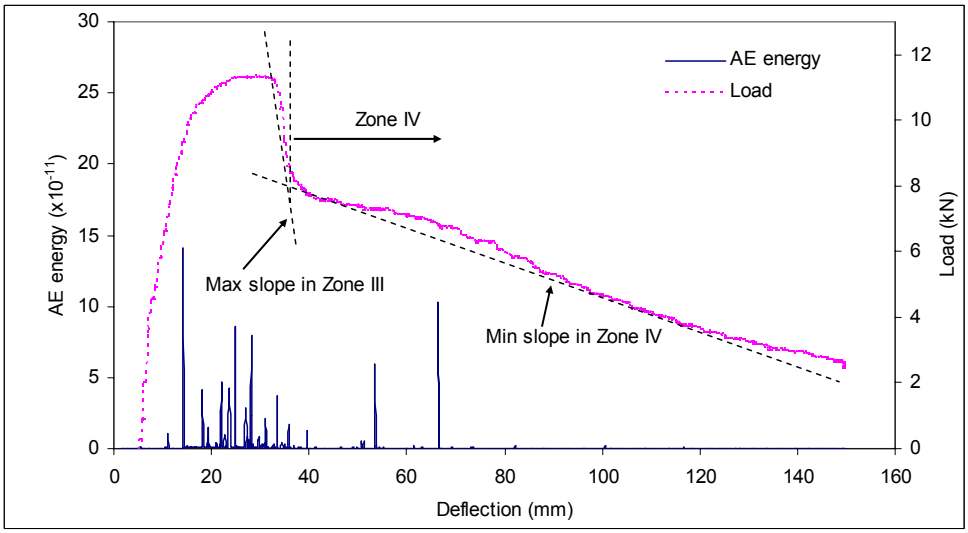

b) Pipe 2

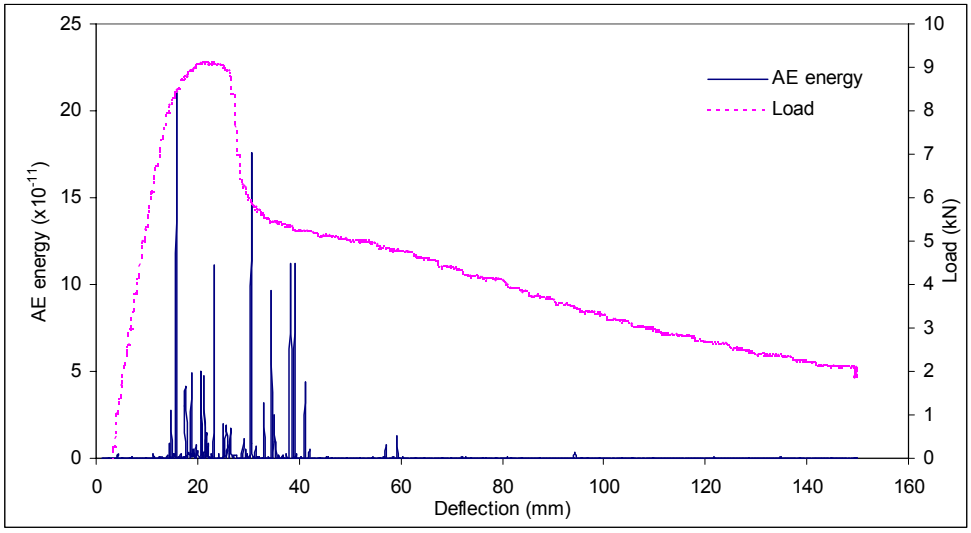

c) Pipe 3

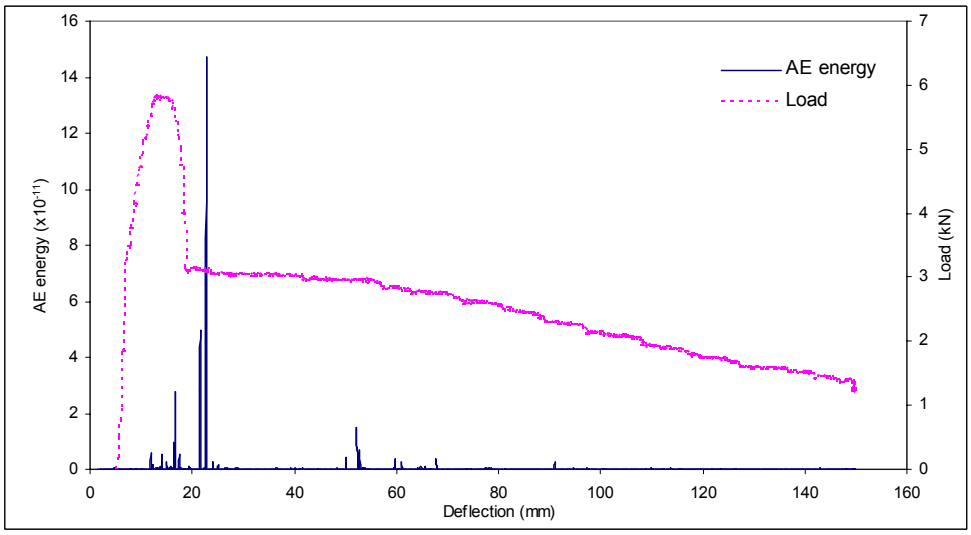

d) Pipe 4

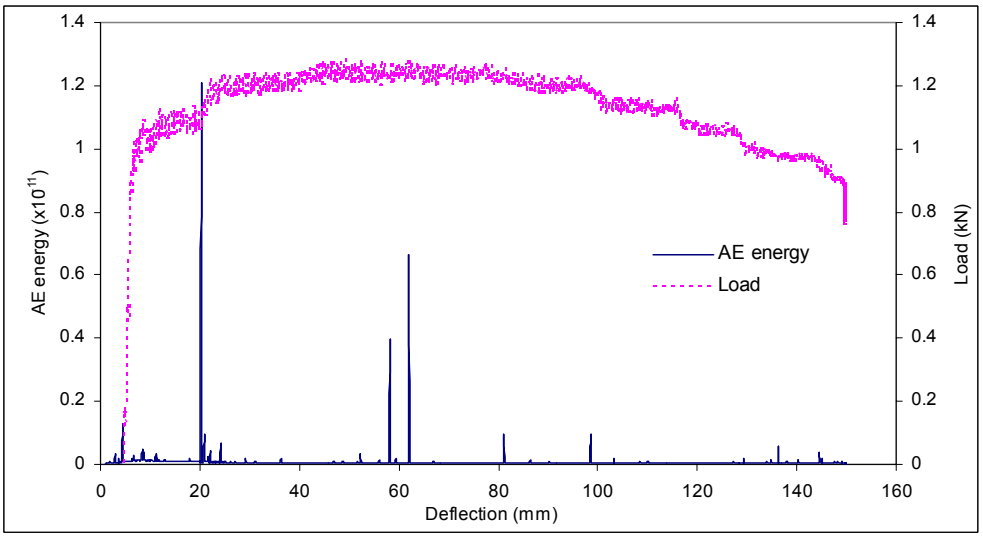

e) Pipe 5

Figure 7.35: The mechanical load and AE batch energy versus deflection for all pipes

The AE energy can be calculated simply by adding the batches of energy for each of the relevant files and the mechanical energy by determining the area under the force-deflection curve. Accordingly, Figures 7.36 and 7.37 show the AE and mechanical energies for the entire test, and then split between that up to maximum load (Zones I and II) and that after maximum load (Zones III and IV). As can be seen, the AE energy for Pipe 3 is at a maximum with regard to total mechanical energy input and that this is associated with the period after maximum load. Taking Zones I and II, it can be seen that, as the defect size increases, the AE energy in Zones I and II does not change very much with mechanical energy until the very large defect sizes, where it drops off sharply. These observations can be explained by the AE being relatively in insensitive to bulk plastic deformation (the main source of resistance to load), but being more sensitive to local deformation, which can be assessed by the stress intensity factor. Accordingly, the Mode I stress intensity factor (K_I) was determined for Zones III and IV using a standard approach:

$$K_I = (Y\sigma)\sqrt{\pi a} \tag{7.6}$$

where a is the notch depth for Zone III (Figure 7.36) and circumferential length for Zone IV (Figure 7.37); and ($Y\sigma$) can be determined (taking into account membrane and bending stress) as follows:

$$Y\sigma = Mf_w(M_m\sigma_m + M_b\sigma_b) \tag{7.7}$$

where M is the bulging correction factor (in this case M=1);

M_m and M_b are magnification factors, determined for Zone III from graphs in [108], and for Zone IV (M_m=M_b= 1);

$\sigma_m = (\sigma_{outer}+\sigma_{inner})/2$ and $\sigma_b=(\sigma_{outer}-\sigma_{inner})/2$ are membrane and bending stress (MPa) respectively; and

$f_w=\{\sec[\pi c/w)(a/B)^{0.5}]\}^{0.5}$ for Zone III, and $\{\sec(\pi a/w)\}^{0.5}$ for Zone IV, where w is π ×diameter and B is wall thickness, as shown in Figures 7.38 and 7.39.

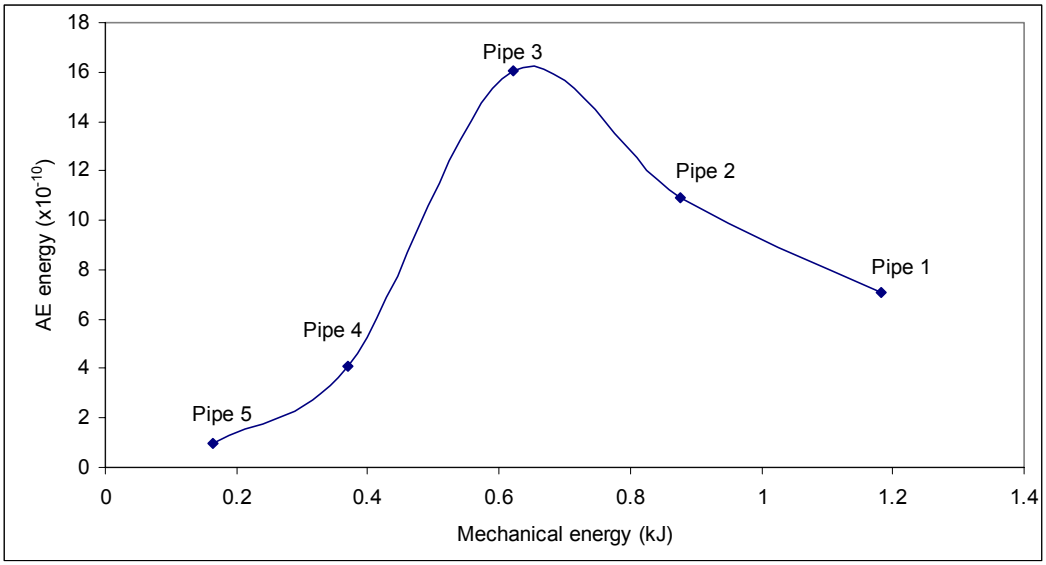

Figure 7.36: The total AE energy and mechanical energy for bend tests

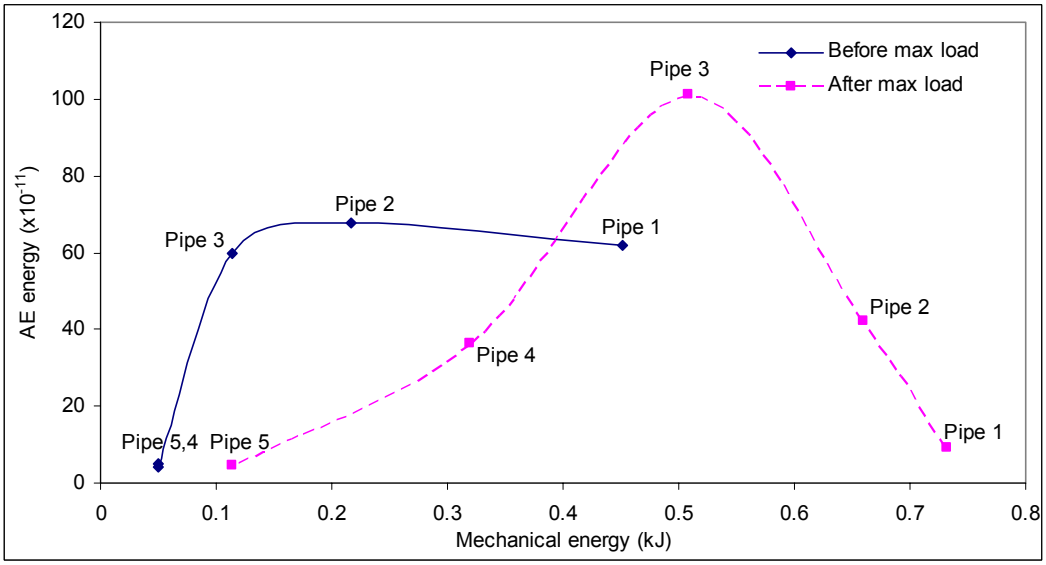

Figure 7.37: The total AE energy and mechanical energy for before and after maximum load

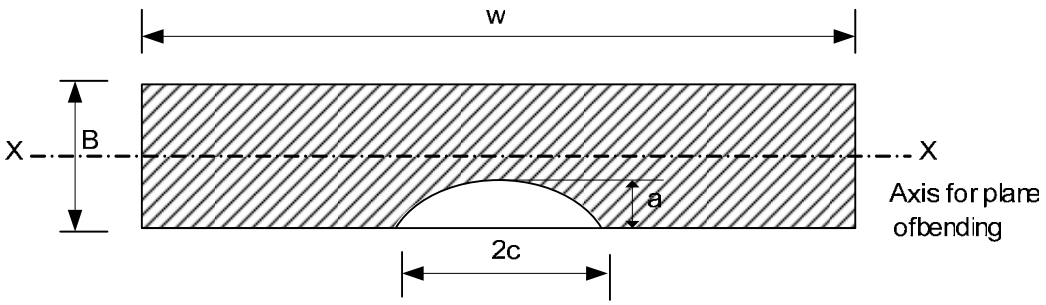

Figure 7.38: Surface flaw geometry for Zone III

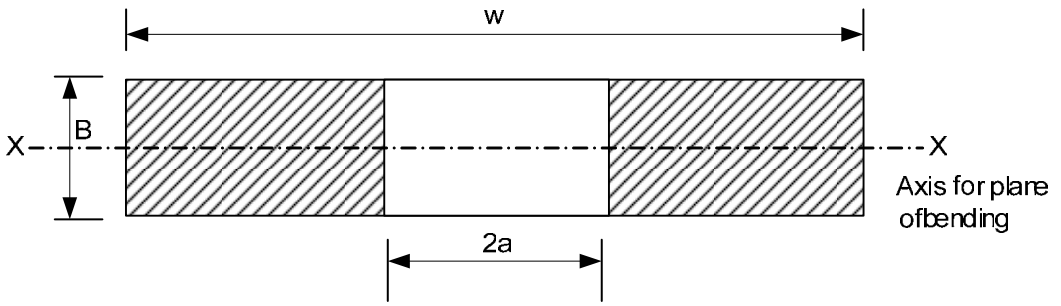

Figure 7.39: Through-thickness flaw geometry for Zone IV

The fracture energy, E_f, associated with the formation of an area, A, can be calculated from the Griffith toughness, G_c, itself related to K_I at fracture:

$$E_f = G_c \times A = \frac{K_I^2}{E} \times A \tag{7.8}$$

where E is the modulus of elasticity. Because the load (and hence stress) at the end of pop-through or ductile tearing is not zero, the energy of fracture was determined for Zone III, E_{III}, and Zone IV, E_{IV}, by:

$$E_{III} = (G_c^1 - G_c^2) \times A_{lig} \tag{7.9}$$

$$E_{IV} = (G_c^2 - G_c^3) \times A_{tear} \tag{7.10}$$

where G_c^1 is the toughness at the start of the fracture process;

G_c^2 is the toughness at the end of Zone III and start of Zone IV;

G_c^3 is the toughness at the end of Zone IV;

A_{lig}, is the area of pop-through; and

A_{tear} is the area of the ductile tear.

Figure 7.40 shows the two components of fracture energy plotted against AE energy and comparison with Figure 7.37 yields some interesting observations. Firstly, the fracture energy, especially in Zone III, is a fairly small proportion of the total mechanical energy and, secondly, this approach still confirms that there is a change in trend between Pipe 1 and Pipe 5, that again occurs at Pipe 3.

To further elucidate this, a plane-stress/plane-strain test was carried out by comparing the apparent value of K_I with the product of the yield stress, σ_y, (here 240 MPa) and the length of the crack front, L:

$$\frac{K_I^2}{\sigma_y^2 L} \tag{7.11}$$

where for pop-through, L is the ligament length given in Table 7.3 and, for circumferential tearing, L is the wall-thickness of the pipe. The resulting values are shown in Table 7.4 and these should be seen in the context that the transition from plane-strain to plane-stress takes place over a range of $K_I^2/\sigma_y^2 L$ from unity to around 3. Therefore, Pipe 3 and 4 only can be considered to be subject to a process of fracture during pop-through, whereas only Pipe 5 is subject to fracture during the circumferential tearing.

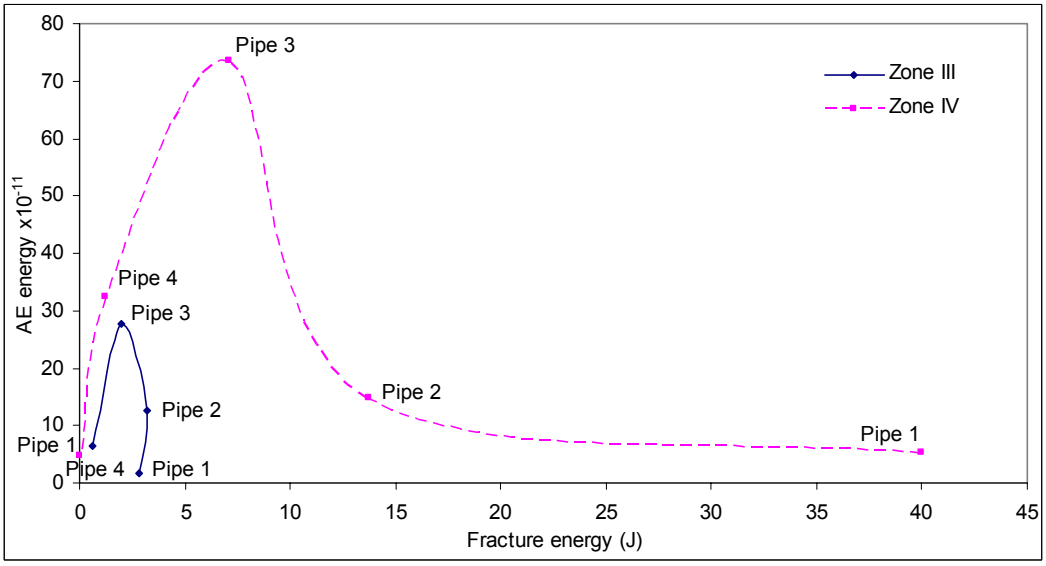

Figure 7.40: Total AE energy and fracture energy for Zones III and IV

	Pipe 1	**Pipe 2**	**Pipe 3**	**Pipe 4**	**Pipe 5**
Pop-through	8.22	3.9	1.9	0.6	--
Circumferential tearing	65.5	34.7	19	5.4	0.9

Table 7.4: Plane-stress/plane-strain tests results from Equation 7.11

Taking values of K_I at failure to be a true measure of K_{Ic} only if $K_I^2/\sigma_y^2 L < 1$ (Pipe 4 for pop-through and Pipe 5 for circumferential tearing) a measure of the degree of plasticity of the fracture can be given by K_I/K_{IC}, which is plotted against AE energy in Figure 7.41 and this can be seen to be consistent with the deviations seen in Figure 7.34.

The behaviour seen in Figure 7.37 can now be explained as follows. In the region before maximum load, the plastic deflection in Pipes 1, 2 and 3 is achieved mostly by general yielding in the pipe wall (K_I/K_{Ic} large), whereas, in Pipes 4 and 5 (K_I/K_{Ic} small) the yielding is more confined to the notch area and this seems to generate less AE energy. After maximum load, there are two types of behaviour, depending on the degree of plasticity of crack extension, and this can be understood by taking Pipes 1, 2 and 3 as one group and Pipes 3, 4 and 5 as another. In the first group, the AE energy is made up of a relatively small component from pop-through, a larger one from circumferential tearing and a third from continued deformation in the pipe wall. Because Pipe 3 has suffered the least general yielding up to maximum load this third component is greater after maximum load than the other two. In pipes 3, 4 and 5, the majority of the AE energy post-maximum load is in Zone IV and this simply increases with the tearing energy, which is linearly related to the mechanical energy.

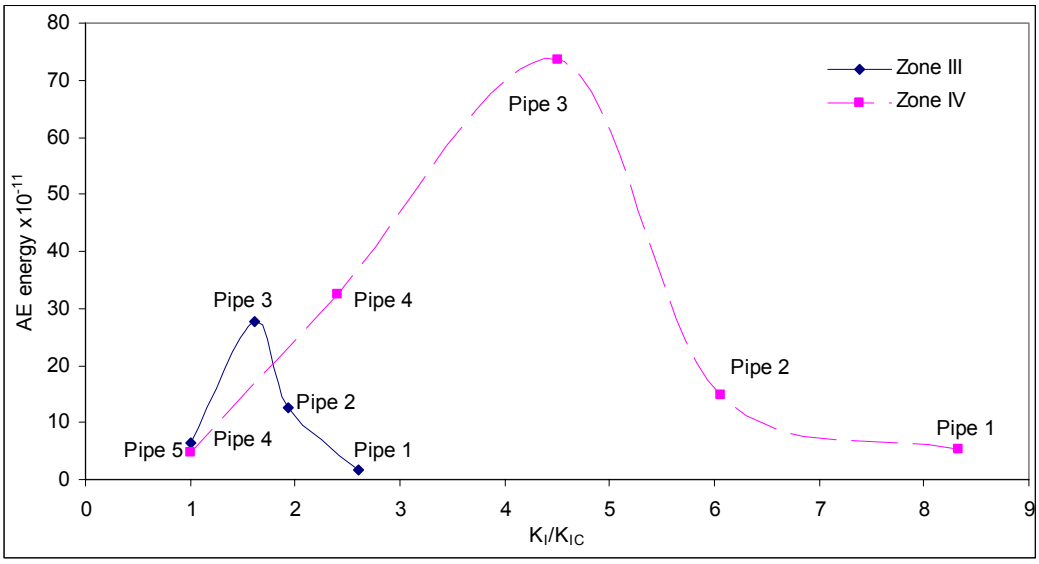

Figure 7.41: AE energy for Zones III and IV against stress intensity factor

7.4 Summary of findings for Real Sources

The work in this chapter has shown that temporal distribution of AE energy can reveal something about sources which are due to mechanical damage to the pipe, and has provided a little information through which different types of damage might be distinguished.

AE due to impact damage tends to manifest itself mostly in low frequencies and impacts produce signals which can be heavily influenced by the nature of the impact and the dynamic response of the pipe. Nevertheless, provided that the primary impact can be isolated from subsequent ones using cumulative AE energy, it would appear that a measure of impact energy (and hence impact damage) is achievable. However, this must remain tentative pending more detailed experiments where the pipe impact dynamics are more clearly controlled.

By contrast, AE due to crack spreading tends to manifest itself mostly in higher frequencies, with contributions from general plastic deformation, and crack spreading by intense plastic deformation and fracture mechanics. The experiments reported here have spanned the plane-stress/plane-strain transition and, as such, have provided two distinct trends with crack size.

Chapter 8: Conclusions and Future Work

8.1 Conclusions

As presented in the preceding chapters, this work has developed techniques to handle discontinuous, continuous and semi-continuous signals produced by simulated AE sources, and real AE sources with uncontrolled temporal structures. Linear sensor arrays have been used in pursuit of the main objectives, which were to improve the precision of source location and to assess the degree of distortion associated with AE wave propagation along a pipe. In particular this research has:

- developed techniques to identify source location on relatively long pipes with a precision of better than 3% using two novel techniques,
- presented an AE attenuation model for understanding the wave propagation in cylinders with different external and internal environments using a combination of simple reflection and transmission laws,
- developed techniques for enhancing the resolution of continuous and semi-continuous sources by using appropriate digital filters with attenuation measurements to remove unwanted components,
- presented methods of correlating the AE energy to impact and crack spreading, improving the understanding of how AE can be used to monitor the mechanical behaviour for pipes under static and dynamic loads.

For long pipes and pipelines, the AE signal is complicated and contains at least two main components, which are travelling at different speeds and are attenuated differently, depending on the environment. Novel techniques have been developed to segment the signals and extract information such as time of flight, wave speeds, attenuation factors, and these have been used to determine the type and location of sources on long steel pipes.

The detailed conclusions from the work with discontinuous simulated sources on plain pipe are:

- It has been shown that simple impulsive sources produce a signal in long steel pipes which can conveniently be split into a slow and a fast component, and that it is difficult to distinguish between these at short source-sensor distances. The implication is that simple techniques are quite adequate for source location in pipes where the sensor is close to the source. However, short source-sensor distances are unlikely in practical most practical situations.
- Because of complexity of the system, it is not necessarily the case that the two components can be identified with two, or only two, modes but other workers using simpler geometries have suggested particular Lamb wave modes. Despite this uncertainty, some progress can still be made on the assumption that the two components can be separated in the frequency domain.
- The apparent wave speed depends on the type of processing that is carried out to determine arrival times, and speed estimates are critically dependent upon the processing method.
- Two novel techniques have been demonstrated to estimate the velocities of the two modes, and hence locate sources in long pipes with an error of less than 3%.
- The windowed energy technique relies on changes in the balance of high and low frequency components of the signal as a function of time to determine arrival times. In a separate source location exercise, it was shown to be the most accurate of the techniques investigated. The other technique also relies upon the frequency balance, and utilises a very sharp filter to remove Wave 1**,** so that arrival times can be estimated for both waves based on the unfiltered and filtered signals.
- The techniques are believed to be generally applicable, but investigation is required as to the balance of the modes identified here as Wave 1 and Wave 2, and have relied on the effectiveness of the 340 kHz cut-off filter, which had to be found by inspection, and which may only apply to the particular sensors used, or indeed to the particular configurations used. However, it has been shown that a method can be developed to automatically determine an appropriate filter cut-off.

- Linear source location is applicable for long distances and this assumption did not produce a significant error in source location for most of the experiments carried out in this work.

The detailed conclusions from the work with discontinuous simulated sources on pipe where the internal and external environments were varied are:

- The transmission of AE from a simulated source is heavily affected by the nature of the internal and external interfaces of a long pipe, specifically if it contains a liquid or a gas, and whether or not it is buried.
- The splitting of the arriving signal into a fast and a slow component allows the isolation of a less-heavily attenuated component (Wave 1) which is less sensitive to changes in the nature of the interface of the pipe.
- Wave 1 is more attenuated when the pipe has water inside, and air or sand outside. Wave 2 is more heavily attenuated than Wave1 for all conditions.
- The apparent wave speed depends on the internal or external environment, Wave 1 being apparently faster in cases of air inside and/or outside the pipe.
- All of the source location techniques suitable for the air-air environment can be applied to the other environments. The Gabor WT technique for source location gives better results with attenuated environments, although still suffers from multiple peaks which make arrival time estimation unreliable.
- An attenuation model has been presented which takes into account internal and external interfaces and involves a surface wave and an internal wave. The application of this model to the data suggests that attenuation can be attributed mostly to the internal wave and to the interface effects along with simple absorption.
- An alternative ray tracing simulation provided similar results although the effect of interfaces was not fully investigated due to computing limitations.

The detailed conclusions from simulated continuous and semi-continuous sources of AE are:

- The energy attenuation technique is the only source location method that can be used with continuous AE sources which have no temporal structure. This technique works best with long pipes, where there is less effect of reflection from boundaries. Thus, the attenuation technique is expected to give better results in more heavily attenuating environments.
- Using a frequency band between 300kHz and 350kHz with the energy attenuation technique improved the continuous AE source location precision to produce an error of less than 14%.
- The cross-correlation technique can be applied to semi-continuous AE sources. This technique is improved by using a band pass filter for the non attenuated components for between 100kHz and 200kHz. Although the temporal structure in the simulated sources was very strong, it can be concluded that fluid dynamic effects in leaks in real pipelines which give rise to any kind of periodicity will improve source location accuracy above what is possible using energy attenuation.

The detailed conclusions from the experiments involving dropped-weight impact and crack spreading under three-point bending (real sources) are:

- The cumulative AE energy can be used to analyse the development of an impact with time. For the heights and weights used here, the impact signatures could be divided into four phases, and the last of these, Phase IV, apparently corresponding to loss of contact between the indenter and the surface.
- The AE energy depends on the kinetic energy of impact, although some dynamic effects in the experiments remain to be fully elucidated.
- The raw AE signal in the dropped-weight test is affected by the shape of the indenter, being different for fresh conical indenters where the plastic deformation is confined to the cone, and for work-hardened indenters, where the plastic deformation is mostly on the surface of the pipe.
- The cumulative AE energy during the 3-point bending test is mostly generated during periods of intense plastic deformation, often the record with the highest AE energy occurring at yield of the pipe section (end of Zone I) and at the commencement of plastic tearing (start of Zone IV). In common with other

workers, it was found that the AE energy was sensitive to where the crack size lay with respect to the plane-stress / plane-strain transition.

- The time domain can therefore evidently be used to distinguish between these particular source types. In addition, there were significant differences in the frequency domain, with impacts showing only one low frequency peak while crack spreading energy had a relatively wide band high frequency peak, with a smaller peak at low frequency.

The general aim of the work has therefore been achieved by contributing to the understanding of AE propagation in cylinders as described by attenuation models, applied to two "waves". The AE energy, wave speed, time of flight and source-sensor distance with different environments have been described and successfully applied for simulated sources. In addition the AE energy evolution corresponding to impact and crack spreading in pipes has also been elucidated.

8.2 Future Work

The following recommendations are suggested for further research:

- The successful application of filtering to the simulated AE burst, continuous and semi-continuous AE for long distances could perhaps be applied to real sources with unknown temporal structures. As a first step, the observed differences in frequency structure of the impact and crack-spreading sources could be used to further understand these sources, perhaps using more controlled dynamic conditions between pipe and indenter and a wider range of pre-crack sizes.
- The sliding window energy and the threshold techniques were found to be the most successful source location techniques for long source sensor distances, and both depend on the filtering above and below 340 kHz. In view of the possibility of different source frequency contents and variable attenuation, there is room to explore a more dynamic filtering technique which permits some adaptation according to the source type, the environment and the source-sensor distance.

- The AE attenuation is clearly affected by internal and external environments, particularly the water content. The modelling of these effects could be studied in more detail by changing the area: length ratio of the pipes and improving the simulation capacity in order to achieve convergence between the results from simulation and those from the more deterministic attenuation model.

References

1. Papadakis, G.A., "*Major Hazard Pipelines: A Comparative Study of Onshore Transmission Accidents",* Journal of Loss Prevention, 1999, **12**, pp. 91-107.
2. Um, J.S. and Wright, R., "*Pipeline construction and Reinstatement Monitoring: Current Practice, Limitations and the Value of Airborn Videography",* The Science of the Total Environment, 1996, **186**, pp. 221-230.
3. Montiel, H., Vilchez, J., Arnaldos, J. and Casal, J., "*Historical Analysis of Accidents in the Transportation of Natural Gas",* Journal of Hazardous Materials, 1996, **51**, pp. 77-92.
4. Verde, C., "*Accommodation of Multi-leak Location in a Pipeline",* Control Engineering Practice, 2005, **13**, pp. 1071-1078.
5. Whitaker, M., Baker, G.R., Westrup, J., Goulding, P.A., Rudd, D.R., Belchamber, R.M. and Collins, M., "*Application of Acoustic Emission to the Monitoring and End Point Determination of a High Shear Granulation Process",* International Journal of Pharmaceutics, 2000, **205**, pp. 79-91.
6. Botten, S.F., "*Prevention of Catastrophic Failure using Acoustic Emission Monitoring",* Journal of Acoustic Emission, 1989, **8**(1-2), pp. 330-333.
7. Hanel, V. and Thelen, W., "*Monitoring Screws under Tensile Load using Acoustic Emission Analysis",* IEE Transactions on Instrumentation and Measurement, 1996, **45**(2), pp. 547-550.
8. Grondel, S., Delebarra, C., Assaad, J., Dupuis, J. and Reithler, L., "*Fatigue Crack Monitoring of Riveted Aluminium Strap Joints by Lamb Wave Analysis and Acoustic Emission Measurement Techniques",* NDT & E International, 2002, **35**, pp. 137-146.
9. Scott, I.G., "*Basic Acoustic Emission"*, Gordon and Breach, New York, 1991.
10. Miller, R. K. and Mclntire, P., "*Nondestructive Testing Handbook. Vol. 5 : Acoustic Emission Testing"*, American Society for Non-Destructive Testing, New York, 1987.

11. Wevers, M., "*Listening to the Sound of Materials: Acoustic Emission for the Analysis of Materials Behaviour",* NDT&E International, 1997, **30**(2), pp. 99-106.
12. Stone, D.E.W. and Dinwall, P.F., "*Acoustic Emission Parameters and Their Interpretation",* NDT International, 1977, **April**, pp. 51-61.
13. Harris, D.O. and Bell, R.L., "*The Measurement and Significance of Energy in Acoustic Emission Testing",* Experimental Mechanics, 1977, **17**(9), pp. 347-353.
14. Wood , B.R.A. and R.W. Harris, "*Structural Integrity and Remnant Life Evaluation of Pressure Equipment from Acoustic Emission Monitoring",* Pressure Vessels and Piping, 2000, **77**, pp. 125-132.
15. Reuben, R. L, "*The Role of Acoustic Emission in Industrial Condition Monitoring",* COMADEM International, 1998, **1**(4), pp. 35-46.
16. Chotard, T., Rotureau, D. and Smith, A., "*Analysis of Acoustic Emission Signature During Aluminous Cement Setting to Characterise the Mechanical Behaviour of the Hard Material",* Journal of the European Ceramic Society, 2005, **25**, pp. 3523-3531.
17. Nivesrangsan, P., Cochrane, C., Steel, J.A. and Reuben, R.L., "*AE Mapping of Engines for Spatially-located Time Series*", *25th European Conference on AE Testing*, Prague, 2002, pp. 1151-1158.
18. Savic, M., "*Detection of Leaks in Vessels*", Patent no. (5675506), USA, 1997.
19. Lee, H.S., Yoon, J.H., Park, J.S. and Yi, Y.M., "*A Study on Failure Characteristic of Spherical Pressure Vessel",* Journal of Materials Processing Technology, 2005, **164-165**, pp. 882-888.
20. Rajtar, J.M. and Muthiah, R., "*Pipeline Leak Detection System for Oil and Gas Flowlines",* Journal of Manufacturing Science and Engineering, Trans. ASME, 1997, **119**, pp. 105-109.
21. Chen, C.M. and Kovacevic, R., "*Joining of A1 6061 Alloy to AISI 1018 Steel by Combined Effects of Fusion and Solid State Welding",* Machine Tools & Manufacture, 2004, **44**, pp. 1205-1214.
22. Zhang, L., Sazonov, V., Kent, J., Dixon, T. and Novozhilov, V., "*Analysis of Boiler-tube Erosion by the Technique of Acoustic Emission: Part I Mechanical Erosion",* Wear, 2001, **250**, pp. 762-769.

23. Opydo, W., "*Study of Elastic Waves of Acoustic Frequencies Generated by Surface Partial Discharges of Solid Insulators in Vacuum",* Vacuum, 2004, **74**, pp. 85-92.
24. Ma, X.Q., Cho, S. and Takemoto, M., "*Acoustic Emission Source Analysis of Plasma Sprayed Thermal Barrier Coatings during Four-point Bend Tests",* Surface & Coatings Technology, 2000, **139**, pp. 55-62.
25. Hamstad, M.A., O'Gallagher, A. and Gary, J., "*A Wavelet Transform Applied to Acoustic Emission Signals: Part 1: Source Identification",* Journal of Acoustic Emission, 2002, **20**, pp. 39-59.
26. Gorman, M.R., "*Plate Wave Acoustic Emission",* Journal of the Acoustical Society of America, 1991, **90**(1), pp. 358-364.
27. Carlin, B., "*Ultrasonics"*, McGraw-Hill, New York, 1960.
28. Pollock, A.A., "*Classical Wave Theory in Practical AE Testing",* Progress in Acoustic Emission III - Japanese Society of Non-Destructive Testing, 1986, pp. 708-721.
29. Giordano, M., Condelli, L. and Nicolais, L., "*Acoustic Emission wave Propagation in a Viscoelastic Plate",* Composite Science and Technology, 1999, **59**, pp. 1735-1743.
30. Pao, Y., Gajewski, R.R. and Ceranolgu, A.N., "*Acoustic Emission and Transient Waves in an Elastic Plate",* Journal of the Acoustical Society of America, 1979, **65**(11), pp. 96-105.
31. Lysak, M.V., "*Development of the Theory of Acoustic Emission by Propagating Crackes in Terms of Fracture Mechanics",* Engineering Fracture Mechanics, 1996, **55**(3), pp. 443-452.
32. Andreykiv, O.Y., Lysak, M.V., Serhiyenko, O.M. and Skalsky, V.R., "*Analysis of Acoustic Emission Caused by Internal Cracks",* Engineering Fracture Mechanics, 2001, **68**, pp. 1317-1333.
33. Surgeon, M. and Wevers, M., "*One Sensor Linear Location of Acoustic Emission Events using Plate Wave Theories",* Materials Science & Engineering A, 1999, **265**(1-2), pp. 254-261.
34. Gorman, M.R. and Prosser, W.H., "*AE Source Orientation by Plate Wave Analysis",* Journal of Acoustic Emission, 1991, **9**(4), pp. 283-288.
35. Holford , K.M. and Carter, D.C., "*Acoustic Emission Source Location",* Key Engineering Materials, 1999, **167-168**, pp. 162-171.

36. Jeong, H. and Jang, Y., "*Fracture Source Location in Thin Plates using the Wavelet Transform of Dispersive Waves",* IEEE Transactions on Ultrasonics, Ferroelectrics and Frequency Control, 2000, **47**(3), pp. 612-619.

37. Hunaidi, O. and Chu, W.T., "*Acoustical Characteristics of Leak Signals in Plastic Water Distribution Pipes",* Applied Acoustics, 1999, **58**, pp. 235-254.

38. NDT Systems, I., Worldwide Excellence in Ultrasonics, *http://www.ndtsystems.com/Reference/Velocity_Table/velocity_table.html*.

39. *http://cgmfileserver.ucdavis.edu/binders/RobotSource/Ultrasound_Tool/02-2%20P%20Imaging%20Table%20and%20Figures.doc*.

40. Nivesrangsan, P., "*Multi-Source, Multi-Sensor Approaches To Diesel Engine Monitoring using Acoustic Emission"*, PhD Thesis, Heriot Watt University, Edinburgh, 2005.

41. Fuller, C.R. and F.J. Fahy, "*Characteristics of Wave Propagation and Energy Distribution in Cylindrical Elastic Shells Filled with Fluid",* Journal of Sound and Vibration, 1982, **81**(4), pp. 501-518.

42. Nivesrangsan, P., Steel, J.A. and Reuben, R.L., "*AE Mapping of Engines for Spatially Located Time Series, Part I: Preliminary studies",* Mechanical Systems and Signal Processing, 2005, **19**(5), pp. 1034-1054.

43. Schoorlemmer, I.H., "*Advanced Real Time Source Location Applications"*, *26th European Conference on AE Testing*, Berlin, 2004, pp. 623-627.

44. Maji, A.K., Satpathi, D. and Kratochvil, T., "*Acoustic Emission Source Location using Lamb Wave Modes",* Journal of Engineering Mechanics, 1997, **123**(2), pp. 154-161.

45. Langhorne, P.J. and Haskell, T.G., "*Acoustic Emission during Fatigue Experiments on First Year Sea Ice",* Cold Regions Science and Technology, 1996, **24**, pp. 237-250.

46. Braginskii, A.B., Medvedev, B.M. and Platkov, A.I., "*Amplitude-Frequency Location Procedure for Acoustic Emission",* Soviet Journal of Nondestructive Testing, 1989, **24**(9), pp. 620-626.

47. Barat, P., P. Kalyanasundaram and Raj, B., "*Acoustic Emission Source Location on a Cylindrical Surface",* NDT & E International, 1993, **26**(6), pp. 295-297.

48. Theobald, P.D., Esward, T.J., Dowson, S.P. and Preston, R.C., "*Acoustic Emission Transducers-Development of a Facility for Traceable Out-of-plane Displacement Calibration",* Ultrasonic, 2004, **43**, pp. 343-350.

49. Colombo, S., Giannopoulos, A, Forde, M.C., Hasson, R. and Mulholland, J., "*Frequency Response of Different Couplant Materials for Mounting Transducers",* NDT & E International, 2005, **38**, pp. 187-193.

50. Wolfinger, C., Arendts, F.J., Friedrich, K. and Drechsler, K., "*Health-Monitoring-System based on Piezoelectric Transducers",* Aerospace Science Technology, 1998, **6**, pp. 391-400.

51. Hsu, N. N. and Hardy, S.C., "*Operation in Acoustic Emission Waveform Analysis for Characterisation of AE Source, Sensors and Structures",* Elastic Waves and Non-destructive Testing of Materials, Trans. ASME, 1978, **29**, pp. 85-106.

52. Stephens, R.W.B. and Pollock, A.A., "*Waveforms and Frequency Spectra of Acoustic Emission",* Journal of the Acoustical Society of America, 1971, **50**(3), pp. 904-910.

53. Powell, L.E. and Dimmick, J.G., "*Apparatus and Method for Testing for Valve Leakes by Differential Signature Method"*, Patent no. (5650943), USA, 1995.

54. Kwan, H.W. and Leach, M.F., "*Characterisation of Cylindrical Particles from their Acoustic Emission",* Ultrasonics, 1985, **23**(5), pp. 233-238.

55. Spall, J.C., Maryak, J.L. and Asher, M.S., "*Neural Network Approach to Locating Acoustic Emission Sources in Non-destructive Evaluation",* Journal of Sound and Vibration, 1998, **211**(1), pp. 133-143.

56. Jemielniak, K., "*Some Aspects of Acoustic Emission Signal Pre-processing",* Journal of Materials Processing Technology, 2001, **109**, pp. 242-247.

57. Cohen, L., "*Time-Frequency Analysis"*, Prentic-Hall PTR, New Jersey, 1995.

58. Cochran, W.T., et al., "*What is Fast Fourier Transform",* IEEE Transactions on Audio and Electroacoustics, 1967, **15**(2), pp. 45-55.

59. Welch, P.D., "*The use of Fast Fourier Transform for the Estimation of Power Spectra: A Method Based on Time Averaging Over Short, Modified*

Periodograms", IEEE Transactions on Audio and Electroacoustics, 1967, **15**(2), pp. 70-73.

60. Cohen, L., "*"Time-frequency Distributions - a Review",* Proceedings of The IEEE, 1989, **77**(7), pp. 941-981.
61. Ding, Y., Reuben, R.L. and Steel, J.A., "*A New Method for Waveform Analysis for Estimating AE Wave Arrival Times using Wavelet Decomposition",* NDT & E International, 2004, **37**(4), pp. 279-290.
62. Grosse, C.U. and Reinhardt, H.W., "*Signal Conditioning in Acoustic Emission Analysis using Wavelets",* NDT.net, 2002, **7**(9), pp. 1-9.
63. Ng, E. and Qi, G., "*Material Fatigue Behaviour Characterisation using the Wavelet-based AE Technique- A Case Study of Acrylic Bone Cement",* Engineering Fracture Mechanics, 2001, **68**, pp. 1477-1492.
64. Jiao, J., He, C., Wu, B., Fei, R. and Wang, X., "*Application of Wavelet Transform on Model Acoustic Emission Source Location in Thin Plates with one Sensor",* Pressure Vessels and Piping, 2004, **81**, pp. 427-431.
65. Venugopal, V. and Foufoula, G. E., "*Energy Decomposition of Rainfall in the Time-frequency-scale Domain using Wavelet Packets",* Journal of Hydrology, 1996, **187**, pp. 3-27.
66. Wu, Y. and Du, R., "*Feature Extraction and Assessment using Wavelet Packets for Monitoring of Machining Processes",* Mechanical Systems and Signal Processing, 1996, **10**(1), pp. 29-53.
67. Wang, Q. and Chu, F., "*Experimental Determination of the Rubbing Location by means of Acoustic Emission and Wavelet Transform",* Journal of Sound and Vibration, 2001, **248**(1), pp. 91-103.
68. Kishimoto, K., Inoue, H., Hamada, M. and Shibuya, T., "*Time Frequency Analysis of Dispersive Waves by Means of Wavelet Transform",* Trans. ASME, Journal of Applied Mechanics, 1995, **62**, pp. 841-846.
69. Qi, G., "*Wavelet-based AE Characterisation of Composite Materials",* NDT & E International, 2000, **33**, pp. 133-144.
70. Yoon, D., Jung, J., Kim, K., Park, P. and Lee, S., "*AE Parameter Analysis for Fatigue Crack Monitoring"*, *the 15th World Conference on Nondestructive Tesfing*, Roma, 2000.

71. Radon, J.C. and Pollock, A.A., "*Acoustic Emission and Energy Transfer During Crack Propagation",* Engineering Fracture Mechanics, 1972, **4**, pp. 295-310.

72. Steven, M., Ziola , S.M. and Gorman, M.R., "*Source Location in Thin Plates using Cross-Correlation",* Journal of the Acoustical Society of America, 1991, **90**(5), pp. 2551-2556.

73. Coulter, J.E., Evans, R.S. and Robertson, M.O., "*Acoustic Emission Leak Source Location"*, Patent no. (4858462), USA*,* 1989.

74. Ziola, S.M. and Gorman, M.R., "*Source Location in Thin Plates using Cross-Correlation",* Journal of the Acoustical Society of America, 1991, **90**(5), pp. 2551-2556.

75. Gorman, M.R., "*Acoustic Emission for the 1990s"*, *Ultrasonics Symposium,IEEE*, Orlando, 1991, pp. 1039-1046.

76. White, P.H., "*Cross Correlation in Structural Systems: Dispersion and Nondispersion Waves",* Journal of the Acoustical Society of America, 1969, **45**(5), pp. 1118-1127.

77. Inoue, H., Kishimoto, K. and Shibuya, T., "*Experimental Wavelet Analysis of Flexural Waves in Beams",* Experimental Mechanics, 1996, **36**(3), pp. 212-217.

78. Buckely, K., Venkatesan, G., West, D. and Kaveh, M., "*Detection and Characterisation of Crack for Failure Monitoring and Diagnostics"*, *Acoustic, Speech, and Signal Processing*, IEEE, Atlanta, 1996, pp. 2738-2741.

79. Robertson, A.I.F., Douglas, R.M., Nivesrangsan, P., Brown, E.R., Steel, J.A. and Reuben, R. L, "*Source Identification using Acoustic Emission on Large Bore Cylinder Liners"*, *26th European Conference on AE Testing*, Berlin, 2004, pp. 637-643.

80. Lozev, M.G., Clemena, G.G., Duke, J.C., Sison, M.F. and Horn, M.R., "*Acoustic Emission Monitoring of Steel Bridge Members"*, Final Report, Transportation Research Council, Virginia, 1997.

81. Stebut, J., "*Multi-mode Scratch Testing-A European Standards, Measurements and Testing Study",* Surface & Coatings Technology, 2005, **200**, pp. 346-350.

82. Boyd, J.W.R. and Varley, J., "*The Uses of Passive Measurement of Acoustic Emissions from Chemical Engineering Processes",* Chemical Engineering Science, 2001, **56**, pp. 1749-1767.

83. Richter, H., Bohmert, J. and Viehrig, W., "*The use of Acoustic Emission to Determine Characteristic Dynamic Strength and Toughness Properties of Steel",* Nuclear Engineering and Design, 1999, **188**, pp. 241-254.

84. Singh, K.S., Srinivasan, K. and Chakraborty, D., "*Acoustic Emission Studies on Metallic Specimen under Tensile Loading",* Materials & Design, 2003, **24**, pp. 471-481.

85. Baudouin, P. and Houbaert, Y., "*The Study of a Uniaxial Deformation Effect on the Magnetic Properties of a Non-oriented Electrical Steel using Acoustic Emission Characterisation",* Journal of Magnetism and Magnetic Materials, 2002, **246**, pp. 247-253.

86. Hao, S., Ramalingam, S. and Klamecki, B.E., "*Acoustic Emission Monitoring of Sheet Metal Forming: Characterisation of the Transducer, the Work Material and the Process",* Journal of Materials Processing Technology, 2000, **101**, pp. 124-136.

87. Carolan, T.A., Kidd, S.R., Hand, D.P. , Wilcox, S.J., P. Wilkinson, Barton, J.S. , Jones, J.C. D. and Reuben, R. L., "*Acoustic Emission Monitoring of Tool Wear During the Face Milling of Steels and Aluminium Alloys using a Fibre Optic Sensor - Energy Analysis",* Proc. I Mech E, Part B Journal of Engineering Manufacture, 1997, **211**(B4), pp. 299-309.

88. Dunegan, H.L., Harris, D.O. and Tetelman, A.S., "*Detection of Fatigue Crack Growth by Acoustic Emission Techniques",* Materials Evaluation, 1970, **28**(10), pp. 221-227.

89. Palmer, I.G. and Heald, P.T., "*The Application of Acoustic Emission Measurements to Fracture Mechanics",* Materials Science & Engineering, 1973, **11**, pp. 181-184.

90. Lindley, T.C., Palmer, I.G. and Richards, C.E., "*Acoustic Emission Monitoring of Fatigue Crack Growth",* Materials Science & Engineering, 1978, **32**, pp. 1-15.

91. Bassim, M.N. and Emam, M.H., "*Acoustic Emission during the Low Cycle Fatigue of AISI 4340 Steel",* Materials Science & Engineering, 1984, **68**, pp. 79-83.

92. Hartbower, C.E., Morais, C.F., Reuter, W.G. and Crimmins, P.P., "*Acoustic Emission from Low-cycle High-stress-intensity Fatigue",* Engineering Fracture Mechanics, 1973, **5**, pp. 765-789.

93. Shi, Z., Jarzynski, J., Bair, S., Hurlebaus, S. and Jacobs, L.J., "*Characterisation of Acoustic Emission Signals from Fatigue Fracture",* Proceedings IMechE, 2000, **214**(C), pp. 1141-1149.

94. Prosser, W.H., Gorman, M.R. and Humes, D.H., "*Acoustic Emission Signals in Thin Plates Produced by Impact Damage",* Journal of Acoustic Emission, 1999, **17**(1-2), pp. 29-36.

95. Gaul, L. and Hurlebaus, S., "*Identification of the Impact Location on A Plate using Wavelets",* Mechanical Systems and Signal Processing, 1997, **12**(6), pp. 783-795.

96. Tonshof, H.K., Jung, M., Mannel, S. and Rietz, W., "*Using Acoustic Emission Signals for Monitoring of Production Processes",* Ultrasonics, 2000, **37**, pp. 681-686.

97. Hou, R., Hunt, A. and Williams, R.A., "*Acoustic Emission of Pipeline Flows: Particulate slurries",* Powder Technology, 1999, **106**, pp. 30-36.

98. Jacob, L.J., "*Characterisation of Acoustic Emission Signals from Mode I Crack",* Journal of Engineering Mechanics, 1991, **117**, pp. 1878-1889.

99. Yoshida, K., Kawano, H., Akematsu, Y. and Nishino, H., "*Frequency Characteristics of Acoustic Emission Wavefoms During Gas Leak*", *26th European Conference on AE Testing*, Berlin, 2004, pp. 321-327.

100. ASTM, "*ASTM E976-99: Standard Guide for Determining the Reproducibility of Acoustic Emission Sensor Response, Annual Book of ASTM Standards"*, Vol. 3.03, pp. 395-403, 1999.

101. *http://www.vallen.de/wavelet/agu.htm*.

102. Welch, P.D., "*The use of Fast Fourier Transform for the Estimation of Power Spectra: A method Based on Time Averaging Over Short, Modified Periodograms",* IEEE Transactions on Audio and Electroacoustics, 1976, **15**(2), pp. 70-73.

103. Schoolemmer, I.H., "*Advanced Real Time Source Location Applications*", *EWGAE*, Berlin, 2004, pp. 623-627.

104. Trofimov, A.I., Brovtsyn, A.K., Gadzhiev, M.S., Konovalov, A.P. and Filatov, A.I., "*Experimental Investigation of the Attenuation of Ultrasonic*

Waves in Liquids with Change of Temperature", Soviet Journal of Nondestructive Testing, 1990, **26**(8), pp. 547-551.

105. Rindel, J.H., "*The Use of Computer Modelling in Room Acoustics",* Journal of Vibroengineering, 2000, **3**(4), pp. 219-224.

106. Lim, T., Nivesrangsan, P., Corney, J. R., Steel, J.A. and Reuben, R. L, "*Predicting AE attenuation within solids by Geometric Analysis"*, *International Conference on Shape Modelling and Applications*, Massachusetts, 2005, pp. 156-162.

107. Miller, A.G., "*Review of Limit Loads of Structures Containing Defects"*, Central Electricity Generating Board, Report no. 2, Berkeley, 1987.

108. BSI, "*BS 7910: Guide on Methods for Assessing the Acceptability of Flaws in Metallic Structures"*, pp. 157-165, 1999.

Appendix A: AE Sensor Calibration Certificates

Figure A.1: AE sensor certificate for sensor 91

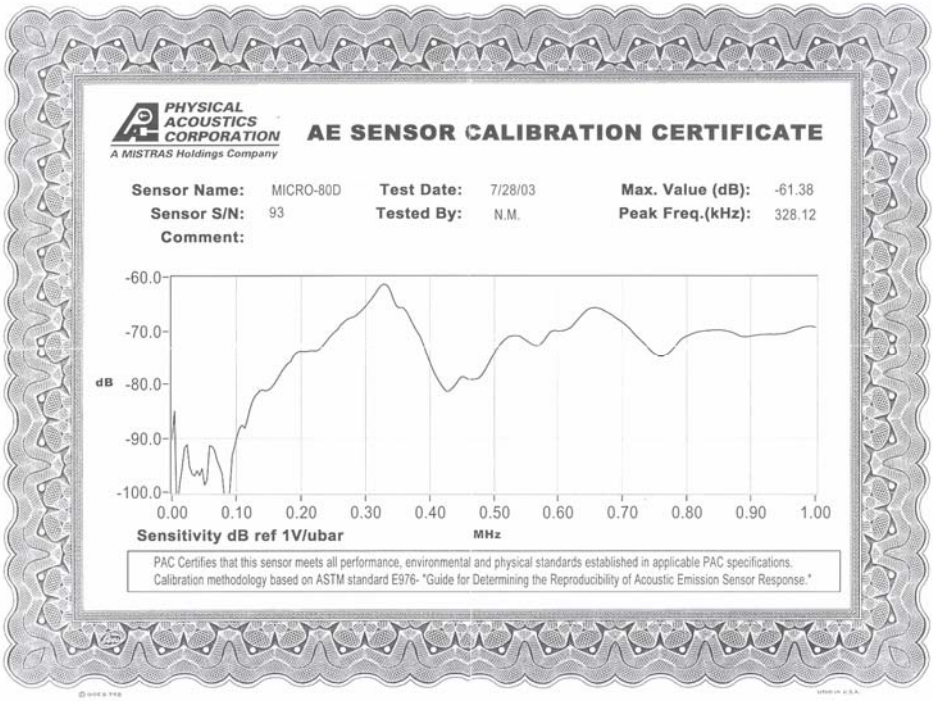

Figure A.2: AE sensor certificate for sensor 93

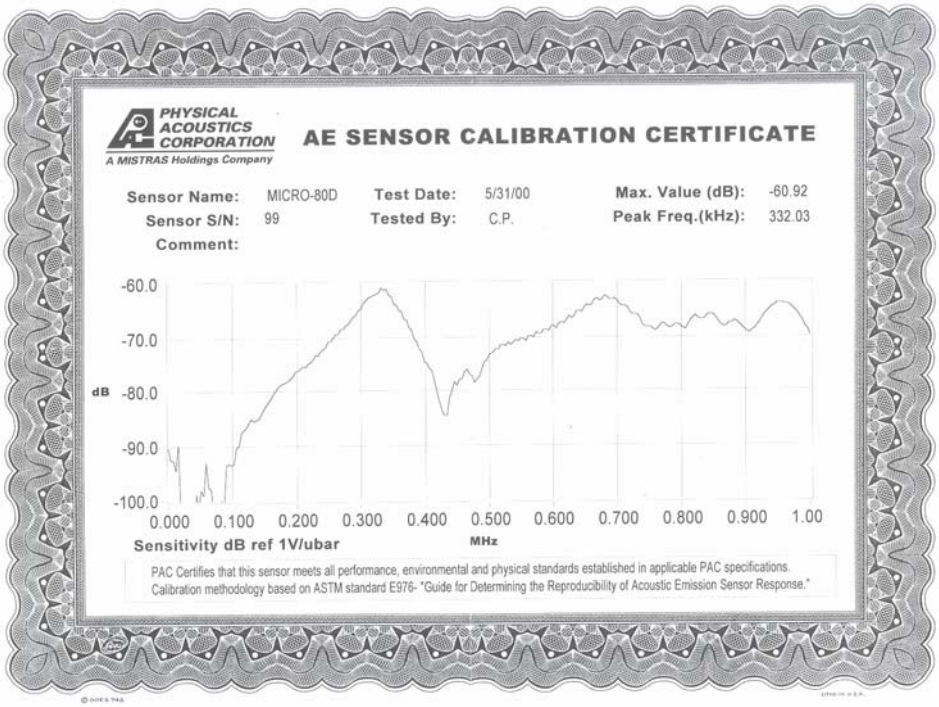

Figure A.3: AE sensor certificate for sensor 99

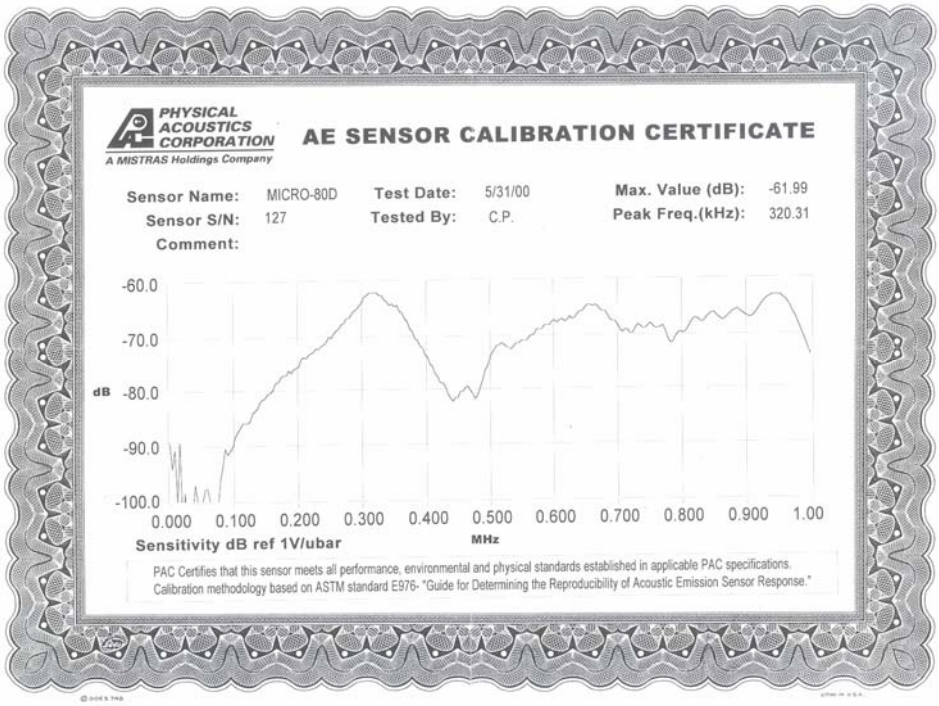

Figure A.4: AE sensor certificate for sensor 127